

DTIC FILE COPY

4

GL-TR-89-0314

AD-A220 117

**Modeling Regional Seismic Waves from
Underground Nuclear Explosion**

Robert W. Clayton
David G. Harkrider
Donald V. Helmberger

California Institute of Technology
Seismological Laboratory
Pasadena, CA 91125

15 May 1989

Final Report
17 March 1987-31 May 1989

APPROVED FOR PUBLIC RELEASE; DISTRIBUTION UNLIMITED

GEOPHYSICS LABORATORY
AIR FORCE SYSTEMS COMMAND
UNITED STATES AIR FORCE
HANSOM AIR FORCE BASE, MASSACHUSETTS 01731-5000

DTIC
ELECTE
APR 3 1990
S B D


90 070

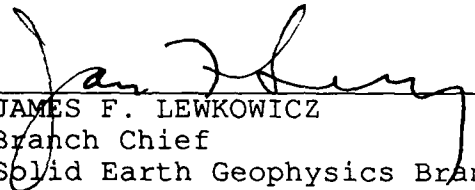
SPONSORED BY
Defense Advanced Research Projects Agency
Nuclear Monitoring Research Office
ARPA ORDER NO.5299

MONITORED BY
Geophysics Laboratory
F19628-87-K-0028


The views and conclusions contained in this document are those of the authors and should not be interpreted as representing the official policies, either expressed or implied, of the Defense Advanced Research Projects Agency or the U.S. Government.

This technical report has been reviewed and is approved for publication.


JAMES F. LEWKOWICZ
Contract Manager
Solid Earth Geophysics Branch
Earth Sciences Division


JAMES F. LEWKOWICZ
Branch Chief
Solid Earth Geophysics Branch
Earth Sciences Division

FOR THE COMMANDER


DONALD H. ECKHARDT, Director
Earth Sciences Division

This report has been reviewed by the ESD Public Affairs Office (PA) and is releasable to the National Technical Information Service (NTIS).

Qualified requestors may obtain additional copies from the Defense Technical Information Center. All others should apply to the National Technical Information Service.

If your address has changed, or if you wish to be removed from the mailing list, or if the addressee is no longer employed by your organization, please notify GL/IMA, Hanscom AFB, MA 01731-5000. This will assist us in maintaining a current mailing list.

Do not return copies of this report unless contractual obligations or notices on a specific document requires that it be returned.

UNCLASSIFIED

SECURITY CLASSIFICATION OF THIS PAGE

REPORT DOCUMENTATION PAGE

1a. REPORT SECURITY CLASSIFICATION UNCLASSIFIED			1b. RESTRICTIVE MARKINGS		
2a. SECURITY CLASSIFICATION AUTHORITY			3. DISTRIBUTION/AVAILABILITY OF REPORT Approved for public release; distribution unlimited		
2b. DECLASSIFICATION/DOWNGRADING SCHEDULE					
4. PERFORMING ORGANIZATION REPORT NUMBER(S)			5. MONITORING ORGANIZATION REPORT NUMBER(S) GL-TR-89-0314		
6a. NAME OF PERFORMING ORGANIZATION California Institute of Tech. Seismological Laboratory		6b. OFFICE SYMBOL (If applicable)	7a. NAME OF MONITORING ORGANIZATION Geophysics Laboratory		
6c. ADDRESS (City, State and ZIP Code) Pasadena, California 91125			7b. ADDRESS (City, State and ZIP Code) Hanscom Air Force Base, Massachusetts 01731-5000		
8a. NAME OF FUNDING/SPONSORING ORGANIZATION Defense Advanced Research Projects Agency		8b. OFFICE SYMBOL (If applicable) NMRO	9. PROCUREMENT INSTRUMENT IDENTIFICATION NUMBER F19628-87-K-0028		
8c. ADDRESS (City, State and ZIP Code) 1400 Wilson Boulevard Arlington, Virginia 22209-2308			10. SOURCE OF FUNDING NOS.		
			PROGRAM ELEMENT NO. 61101E	PROJECT NO. 7A10	TASK NO. DA
11. TITLE (Include Security Classification) Modeling Regional Seismic Waves From Underground Nuclear Explosion					
12. PERSONAL AUTHOR(S) Robert W. Clayton, David G. Harkrider and Donald V. Helmberger					
13a. TYPE OF REPORT Final Report		13b. TIME COVERED FROM 3/17/87 TO 5/31/89		14. DATE OF REPORT (Yr., Mo., Day) 5/15/89	
15. PAGE COUNT 196					
16. SUPPLEMENTARY NOTATION					
17. COSATI CODES			18. SUBJECT TERMS (Continue on reverse if necessary and identify by block number) regional waveforms, seismic modeling, continental-oceanic transition zones, L_g propagation, 2-D modeling of 3D structures, surface waves from tectonic release.		
FIELD	GROUP	SUB. GR.			
19. ABSTRACT <p>The research performed under the contract, during the period 17 March 1987 through 31 May 1989, can be divided into three main topics; modeling regional SH waves that propagate across lateral variations in structure, modeling explosions using 2-D numerical methods, and the effect of differing P and SV source time histories on the generation of Rayleigh and Love waves.</p> <p>In section 1, intermediate-period seismograms recorded at Pasadena of earthquakes occurring along a profile to Imperial Valley are studied in terms of source phenomena versus path effects. Some of the events have known source parameters, determined by teleseismic or near-field studies, and are used as master events in a forward modeling exercise to derive the Green's functions (displacements at Pasadena due to a pure strike-slip or dip-slip mechanism) that describe the propagation effects along the profile. Both timing and waveforms of records are matched by synthetics calculated from two-dimensional velocity models. The best two-dimensional section begins at Imperial Valley with a thin crust containing the basin structure</p>					
20. DISTRIBUTION/AVAILABILITY OF ABSTRACT UNCLASSIFIED/UNLIMITED <input type="checkbox"/> SAME AS RPT. <input type="checkbox"/> DTIC USERS <input type="checkbox"/>			21. ABSTRACT SECURITY CLASSIFICATION UNCLASSIFIED		
22a. NAME OF RESPONSIBLE INDIVIDUAL James Lewkowicz			22b. TELEPHONE NUMBER (Include Area Code) (617)377-3028		22c. OFFICE SYMBOL AFGL/LWH

and thickens towards Pasadena. The detailed nature of the transition zone at the base of the crust controls the early arriving shorter periods (strong motions), while the edge of the basin controls the scattered longer-period surface waves. From the waveform characteristics alone, one can easily distinguish shallow events in the basin from deep events as well as the amount of strike-slip versus dip-slip motions. Those events rupturing the sediments, such as the 1979 Imperial Valley earthquake, can be recognized easily by a late arriving scattered Love wave which has been delayed by the very slow path across the shallow valley structure.

In section 2, the effect of transition regions between continental and oceanic structure on the propagation of L_g waves from continental sources is examined. In particular, the attenuation due to variations in layer thickness in such transition regions is calculated and explained for a suite of simple models. The measured attenuation, due to the geometry of the transition regions between the oceanic and continental structures within a partially oceanic path with source and receiver in a continental structure, is at most a factor of four for frequencies from 0.01 to 1 Hz. This is inadequate to explain the observed extinction of L_g along such paths. This extinction has previously been attributed to the effects of the transition region geometry. The method used to calculate the results presented in this study is developed and its validity and accuracy are demonstrated. Propagator matrix seismograms are coupled into a Finite Element calculation to produce hybrid teleseismic SH mode sum seismograms. These hybrid synthetics can be determined for paths including any regional transition zone or other heterogeneity that exists as part of a longer, mostly plane-layered, path. Numerical results presented for a suite of transition models show distinct trends in each of the regions through which the wavefield passes. The wavefield passes through a continent-ocean transition regions, then a region of oceanic structure, and finally through an ocean-continent transition region. When an L_g wavefront passes through a continent-ocean transition, the amplitude and coda duration of the L_g wave at the surface both increase. At the same time, much of the modal L_g energy previously trapped in the continental crust is able to escape from the lower crust into the subcrustal layers as body waves. The magnitude of both these effects increases as the length of the transition region increases. When the wavefront passes through the region of oceanic structure further energy escapes from the crustal layer, and produces a decrease in L_g amplitude at the surface. The rate of amplitude decrease is maximum near the transition region and decreases with distance from it. When the wavefield passes through the ocean-continent transition region a rapid decrease in the L_g amplitude at the surface of the crust results. The energy previously trapped in the oceanic crustal layer spreads throughout the thickening crustal layer. Some of the body wave phases produced when the wavefield passes through the continent-ocean transition region are incident on the continental crust in the ocean-continent transition region. These waves are predominantly transmitted back into the crust. The other body wave phases reach depths below the depth of the base of the continental crust before reaching the ocean-continent transition and, thus, escape from the system.

In section 3, methods for representation theorem coupling of finite-element or finite difference calculations and propagator matrix method calculations are developed. The validity and accuracy of the resulting hybrid method are demonstrated. The resulting hybrid technique can be used to study the propagation of any phase that can be represented in terms of an SH mode sum seismogram, across regional transition zones or other heterogeneities. These heterogeneities may exist in regions which form subsegments of a longer, mostly plane-layered, path. Examples of structures of interest through which such waves can be propagated using these techniques include, regions of crustal thickening or thinning such as continent-ocean transitions or basins, anomalous bodies of any shape located in the path, and sudden transitions from one layered structure to another. Examples of the types of phase that may be propagated through these structures include Love waves, L_g , S_n , and S_a .

In section 4, we present techniques for modeling explosions realistically using two-dimensional methods in three-dimensional earth models. Although seismic structures are generally three-dimensional(3-D), numerical simulation of wave propagation through laterally heterogeneous media is conceptually simpler and less computationally intensive in two dimensions(2-D). Source expressions for 2-D that have the same radiation patterns as their 3-D counterparts have been derived which can also correct for the differences between 2-D and 3-D wave propagation (Vidale and Helmberger, 1986; Stead and Helmberger, 1988; Helmberger and Vidale, 1988). Because that technique approximately transforms waves from a cartesian 2-D grid to a cylindrically symmetric 3-D world, slightly anisotropic geometrical spreading in 2-D better approximates isotropic spreading in 3-D than simple isotropic spreading in 2-D does. This paper describes a correction to the explosive source expression which reduces energy traveling vertically out of the source region, but leaves unchanged the energy traveling laterally out of the source region. We show that this correction will significantly improve the results of using a 2-D grid to simulate elastic wave propagation from an explosive point source.

The effect of shallow station structure and lateral velocity variation are investigated for records of the Amchitka blasts MILROW and CANNIKIN. The differences between the Mueller-Murphy, Helmberger-Hadley, and von Seggern-Blandford reduced displacement potential (RDP) source representations are smaller than the differences produced by various possible velocity structures. Using a model based on known structure, a better fit is obtained for the records of MILROW, primarily for the surface waves. In addition, a technique is developed to include possible source asphericity. Using this technique, the Amchitka blasts, especially CANNIKIN, show evidence of significant aspherical cavity formation.

In section 5, we present expressions and synthetics for Rayleigh and Love waves generated by various tectonic release models are presented. The multipole formulas are given in terms of the strengths and time functions of the source potentials. This form of the Rayleigh and Love wave expressions is convenient for separating the contribution to the Rayleigh wave due to the compressional and shear wave source radiation and the contribution of the upgoing and downgoing source radiation for both Rayleigh and Love waves. Because of the ease of using different compression and shear wave source time functions, these formula are especially suited for sources for which second and higher degree moment tensors are needed to describe the source, such as the initial value cavity release problem.

A frequently used model of tectonic release is a double couple superimposed on an explosion. One of the purposes of this research is to compare synthetics of this and more realistic models in order to determine for what dimensions of the release model this assumption is valid and whether the Rayleigh wave is most sensitive to the compressional or shear wave source history. The pure shear cavity release model is a double couple with separate P-wave and S-wave source histories. The time scales are proportional to the source region's dimension and differ by their respective body wave velocities. Thus, a convenient way to model the effect of differing shot point velocities and source dimensions is to run a suite of double couple time history calculations for the P-wave and S-wave sources separately and then summing the different combinations.

One of the more interesting results from this analysis is that the well known effect of vanishing Rayleigh wave amplitude as a vertical or horizontal dip-slip double couple model approaches the free surface is due to the destructive interference between the P-wave and SV-wave generated Rayleigh waves. The individual Rayleigh wave amplitudes, unlike the SH-generated Love waves, are comparable in size to those from other double couple orientations. This has important implications to the modeling of Rayleigh waves from shallow dip-slip fault models. Also, the P-wave radiation from double couple sources is a more efficient generator of Rayleigh waves than the associated SV wave or the P-wave from explosions. The latter is probably due to the vertical radiation pattern or amplitude variation over the wave front. This effect should be similar to that of wave front curvature.

FINAL TECHNICAL REPORT
17 March 1987 - 31 May 1989

ARPA Order No.:	5299
Name of Contractor:	California Institute of Technology
Effective Date of Contract:	14 March 1987
Contract Expiration Date:	31 May 1989
Contract Number:	F19628-87-K-0028
Principal Investigators:	Robert W. Clayton (818) 356-6909 David G Harkrider (818) 356-6910 Donald V. Helmberger (818) 356-6998
Program Manager:	James F. Lewkowicz (617) 861-3028
Short Title of Work:	Modeling Regional Seismic Waves From Underground Nuclear Explosions

The views and conclusions contained in this document are those of the authors and should not be interpreted as necessarily representing the official policies, either expressed or implied, of the Defense Advanced Research Projects Agency of the U. S. Government

Sponsored by
Defense Advanced Research Projects Agency (DOD)
Defense Sciences Office, Geophysical Sciences Division
DARPA/DSO Physical Characterization of Seismic Sources
ARPA Order No. 5299
Issued by the Air Force Geophysics Laboratory under
Contract# F19628-87-K-0028

Seismological Laboratory
Division of Geological and Planetary Sciences
California Institute of Technology
Pasadena, California 91125

TABLE OF CONTENTS

Summary_____	VI
1. Modeling regional Love waves: Imperial Valley to Pasadena_____	1
2. Numerical modeling of SH L _g waves in and near continental margins_____	18
3. Seismic representation theorem coupling: synthetic SH mode sum seismograms for non-homogeneous paths_____	43
4. On modeling explosions using 2-D numerical methods_____	62
5. Theoretical Rayleigh and Love waves from an explosion in prestressed source regions_____	115



Accession For	
NTIS GRA&I	<input checked="" type="checkbox"/>
DTIC TAB	<input type="checkbox"/>
Unannounced	<input type="checkbox"/>
Justification_____	
By_____	
Distribution/_____	
Availability Codes	
Dist	Avail and/or Special
A-1	

Summary

The research performed under the contract, during the period 17 March 1987 through 31 May 1989, can be divided into three main topics; modeling regional SH waves that propagate across lateral variations in structure, modeling explosions using 2-D numerical methods, and the effect of differing P and SV source time histories on the generation of Rayleigh and Love waves.

In section 1, intermediate-period seismograms recorded at Pasadena of earthquakes occurring along a profile to Imperial Valley are studied in terms of source phenomena versus path effects. Some of the events have known source parameters, determined by teleseismic or near-field studies, and are used as master events in a forward modeling exercise to derive the Green's functions (displacements at Pasadena due to a pure strike-slip or dip-slip mechanism) that describe the propagation effects along the profile. Both timing and waveforms of records are matched by synthetics calculated from two-dimensional velocity models. The best two-dimensional section begins at Imperial Valley with a thin crust containing the basin structure and thickens towards Pasadena. The detailed nature of the transition zone at the base of the crust controls the early arriving shorter periods (strong motions), while the edge of the basin controls the scattered longer-period surface waves. From the waveform characteristics alone, one can easily distinguish shallow events in the basin from deep events as well as the amount of strike-slip versus dip-slip motions. Those events rupturing the sediments, such as the 1979 Imperial Valley earthquake, can be recognized easily by a late arriving scattered Love wave which has been delayed by the very slow path across the shallow valley structure.

In section 2, the effect of transition regions between continental and oceanic structure on the propagation of L_g waves from continental sources is examined. In particular, the attenuation due to variations in layer thickness in such transition regions is calculated and explained for a suite of simple models. The measured attenuation, due to the geometry of the transition regions between the oceanic and continental structures within a partially oceanic path with source and receiver in a continental structure, is at most a factor of four for frequencies from 0.01 to 1 Hz. This is inadequate to explain the observed extinction of L_g along such paths. This extinction has previously been attributed to the effects of the transition region geometry. The method used to calculate the results presented in this study is developed and its validity and accuracy are demonstrated. Propagator matrix seismograms are coupled into a

Finite Element calculation to produce hybrid teleseismic SH mode sum seismograms. These hybrid synthetics can be determined for paths including any regional transition zone or other heterogeneity that exists as part of a longer, mostly plane-layered, path. Numerical results presented for a suite of transition models show distinct trends in each of the regions through which the wavefield passes. The wavefield passes through a continent-ocean transition regions, then a region of oceanic structure, and finally through an ocean-continent transition region. When an L_g wavefront passes through a continent-ocean transition, the amplitude and coda duration of the L_g wave at the surface both increase. At the same time, much of the modal L_g energy previously trapped in the continental crust is able to escape from the lower crust into the subcrustal layers as body waves. The magnitude of both these effects increases as the length of the transition region increases. When the wavefront passes through the region of oceanic structure further energy escapes from the crustal layer, and produces a decrease in L_g amplitude at the surface. The rate of amplitude decrease is maximum near the transition region and decreases with distance from it. When the wavefield passes through the ocean-continent transition region a rapid decrease in the L_g amplitude at the surface of the crust results. The energy previously trapped in the oceanic crustal layer spreads throughout the thickening crustal layer. Some of the body wave phases produced when the wavefield passes through the continent-ocean transition region are incident on the continental crust in the ocean-continent transition region. These waves are predominantly transmitted back into the crust. The other body wave phases reach depths below the depth of the base of the continental crust before reaching the ocean-continent transition and, thus, escape from the system.

In section 3, methods for representation theorem coupling of finite-element or finite difference calculations and propagator matrix method calculations are developed. The validity and accuracy of the resulting hybrid method are demonstrated. The resulting hybrid technique can be used to study the propagation of any phase that can be represented in terms of an SH mode sum seismogram, across regional transition zones or other heterogeneities. These heterogeneities may exist in regions which form subsegments of a longer, mostly plane-layered, path. Examples of structures of interest through which such waves can be propagated using these techniques include, regions of crustal thickening or thinning such as continent-ocean transitions or basins, anomalous bodies of any shape located in the path, and sudden transitions from one layered structure to another. Examples of the types of phase that may be propagated through these structures include Love waves, L_g , S_n , and S_a .

In section 4, we present techniques for modeling explosions realistically using two-dimensional methods in three-dimensional earth models. Although seismic structures are generally three-dimensional(3-D), numerical simulation of wave propagation through laterally heterogeneous media is conceptually simpler and less computationally intensive in two dimensions(2-D). Source expressions for 2-D that have the same radiation patterns as their 3-D counterparts have been derived which can also correct for the differences between 2-D and 3-D wave propagation (Vidale and Helmberger, 1986; Stead and Helmberger, 1988; Helmberger and Vidale, 1988). Because that technique approximately transforms waves from a cartesian 2-D grid to a cylindrically symmetric 3-D world, slightly anisotropic geometrical spreading in 2-D better approximates isotropic spreading in 3-D than simple isotropic spreading in 2-D does. This paper describes a correction to the explosive source expression which reduces energy traveling vertically out of the source region, but leaves unchanged the energy traveling laterally out of the source region. We show that this correction will significantly improve the results of using a 2-D grid to simulate elastic wave propagation from an explosive point source.

The effect of shallow station structure and lateral velocity variation are investigated for records of the Amchitka blasts MILROW and CANNIKIN. The differences between the Mueller-Murphy, Helmberger-Hadley, and von Seggern-Blandford reduced displacement potential (RDP) source representations are smaller than the differences produced by various possible velocity structures. Using a model based on known structure, a better fit is obtained for the records of MILROW, primarily for the surface waves. In addition, a technique is developed to include possible source asphericity. Using this technique, the Amchitka blasts, especially CANNIKIN, show evidence of significant aspherical cavity formation.

In section 5, we present expressions and synthetics for Rayleigh and Love waves generated by various tectonic release models are presented. The multipole formulas are given in terms of the strengths and time functions of the source potentials. This form of the Rayleigh and Love wave expressions is convenient for separating the contribution to the Rayleigh wave due to the compressional and shear wave source radiation and the contribution of the upgoing and downgoing source radiation for both Rayleigh and Love waves. Because of the ease of using different compression and shear wave source time functions, these formula are especially suited for sources for which second and higher degree moment tensors are needed to describe the source, such as the initial value cavity release problem.

A frequently used model of tectonic release is a double couple superimposed on an explosion. One of the purposes of this research is to compare synthetics of this and more realistic models in order to determine for what dimensions of the release model this assumption is valid and whether the Rayleigh wave is most sensitive to the compressional or shear wave source history. The pure shear cavity release model is a double couple with separate P-wave and S-wave source histories. The time scales are proportional to the source region's dimension and differ by their respective body wave velocities. Thus, a convenient way to model the effect of differing shot point velocities and source dimensions is to run a suite of double couple time history calculations for the P-wave and S-wave sources separately and then summing the different combinations.

One of the more interesting results from this analysis is that the well known effect of vanishing Rayleigh wave amplitude as a vertical or horizontal dip-slip double couple model approaches the free surface is due to the destructive interference between the P-wave and SV-wave generated Rayleigh waves. The individual Rayleigh wave amplitudes, unlike the SH-generated Love waves, are comparable in size to those from other double couple orientations. This has important implications to the modeling of Rayleigh waves from shallow dip-slip fault models. Also, the P-wave radiation from double couple sources is a more efficient generator of Rayleigh waves than the associated SV wave or the P-wave from explosions. The latter is probably due to the vertical radiation pattern or amplitude variation over the wave front. This effect should be similar to that of wave front curvature.

SECTION 1

**MODELING REGIONAL LOVE WAVES: IMPERIAL VALLEY TO
PASADENA**

MODELING REGIONAL LOVE WAVES: IMPERIAL VALLEY TO PASADENA

BY PHYLLIS HO-LIU AND DONALD V. HELMBERGER

ABSTRACT

Intermediate-period seismograms recorded at Pasadena of earthquakes occurring along a profile to Imperial Valley are studied in terms of source phenomena versus path effects. Some of the events have known source parameters, determined by teleseismic or near-field studies, and are used as master events in a forward modeling exercise to derive the Green's functions (displacements at Pasadena due to a pure strike-slip or dip-slip mechanism) that describe the propagation effects along the profile. Both timing and waveforms of records are matched by synthetics calculated from two-dimensional velocity models. The best two-dimensional section begins at Imperial Valley with a thin crust containing the basin structure and thickens towards Pasadena. The detailed nature of the transition zone at the base of the crust controls the early arriving shorter periods (strong motions), while the edge of the basin controls the scattered longer-period surface waves. From the waveform characteristics alone, one can easily distinguish shallow events in the basin from deep events as well as the amount of strike-slip versus dip-slip motions. Those events rupturing the sediments, such as the 1979 Imperial Valley earthquake, can be recognized easily by a late arriving scattered Love wave which has been delayed by the very slow path across the shallow valley structure.

INTRODUCTION

Recent broadband (BB) observations of regional phases at Pasadena, IPAS suggest that these seismic motions are strongly influenced by path effects (Fig. 1). The top two traces contain the BB displacements produced by two San Miguel events rotated into tangential and radial directions. The event on the bottom is roughly 50 times larger than the upper foreshock. The next few sets of traces display simulations of what these motions would produce on conventional instruments operated by the Seismological Laboratory at various times. The long-period Wood-Anderson (wa.lp), operated during the 40's and 50's, produced the primary data set used in the stress-drop study by Thatcher and Hanks (1973).

The similarity of these two events across the various frequency-bands is a rather common occurrence (Bent *et al.*, 1989) and emphasizes the role of propagation in regional phases. If we knew the mechanism of the smaller foreshock, we probably could make some good estimates of the faulting parameters of the main events by using the well-known empirical Green's function approach (Hartzell, 1978). This approach has proven very useful in strong-motion simulations of main events from their aftershocks by assuming that the aftershock and the main event have the same mechanisms. The strength of this procedure lies in eliminating the path effects by assuming they are included in the small event record automatically. The main problem in applying this method regionally is that it is difficult to find an aftershock or foreshock with the same orientation as the main event at the appropriate depth and range.

Generally we do not know the mechanisms of many of these moderate aftershocks because they are too large for local arrays and too small for global networks. In addition, waveforms of different aftershocks are often so different, even if they are

MODELING REGIONAL LOVE WAVES

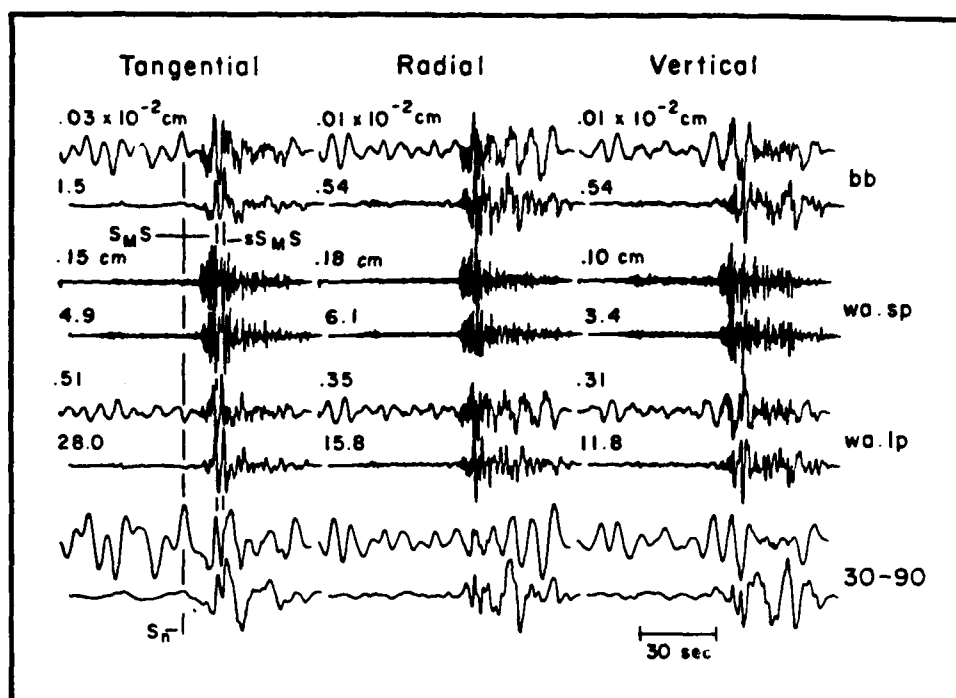


FIG. 1. The upper trace of each pair is a small foreshock, $M = 3.2$. The lower trace is a $M = 5.3$ foreshock at a similar location. Comparing the amplitudes one can see that the larger event is richer in longer periods as expected. The wa.lp simulation corresponds to instruments operated in the 40's and 50's.

spatially close to each other, that it is not easy to determine which aftershock can be used as an empirical Green's function to simulate the main event. Examples of this category of events are the series of aftershocks of the 1979 Imperial Valley earthquakes recorded on the Press-Ewing (30-90) of Pasadena (Fig. 2). We would like to call attention to the three aftershocks labeled A, B, and C, where motions for all three events are about the same size on the vertical (UP) component but distinctly different on the horizontals (EW and NS). Differences in waveforms are also apparent on all three components. Since the paths from the Imperial Valley to Pasadena are essentially the same for the three events, we would conclude that the source characteristics (depths and faulting parameters such as strike, dip, and rake) must be different. As we will discuss shortly, event A is probably a mid-depth normal dip-slip event, whereas event B is a shallow normal dip-slip event. Event C is a deep strike-slip event.

In order to study these seismograms in detail, we digitized and rotated the NS and EW components to obtain the tangential (SH waves) and vertical-radial (P - SV waves) components. At these periods the motion appears to be well behaved, in that the P waves are not apparent on the tangential component. Particle motion studies of the type discussed by Vidale (1986) conducted on these recordings indicate that the first 10 sec of record is consistent with P waves and diffracted SV waves followed by Rayleigh motion. Similar analysis of filtered rotated torsion records indicates that separation of the P - SV and SH system occurs down to periods of about 1 sec (Fig. 3). Thus, it appears that two-dimensional models may prove effective in removing the propagational distortions so that source retrieval is possible.

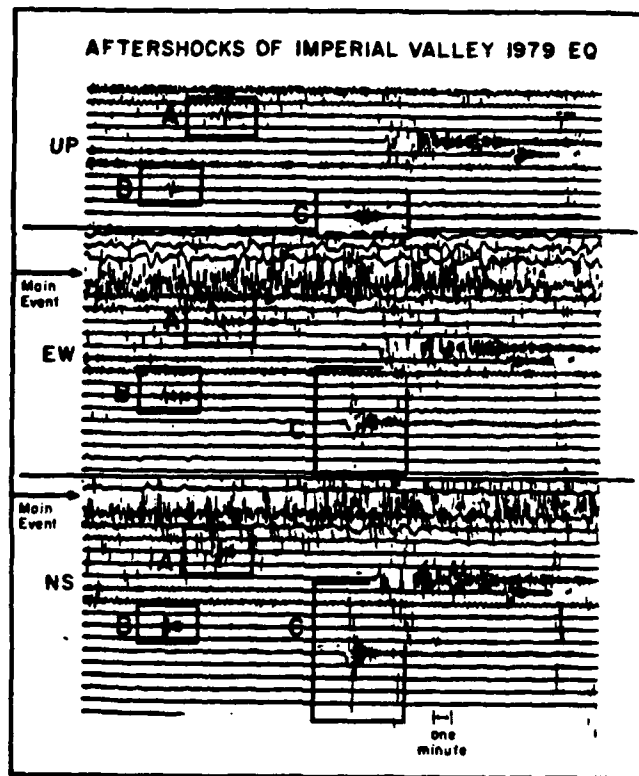


FIG. 2. Three-components seismograms of the aftershock sequence recorded on the long-period Press-Ewing 30-90 instrument at Pasadena. Note the difference in waveforms and relative amplitudes of the three boxed aftershocks A, B, and C between components. The event locations are given in Table 1.

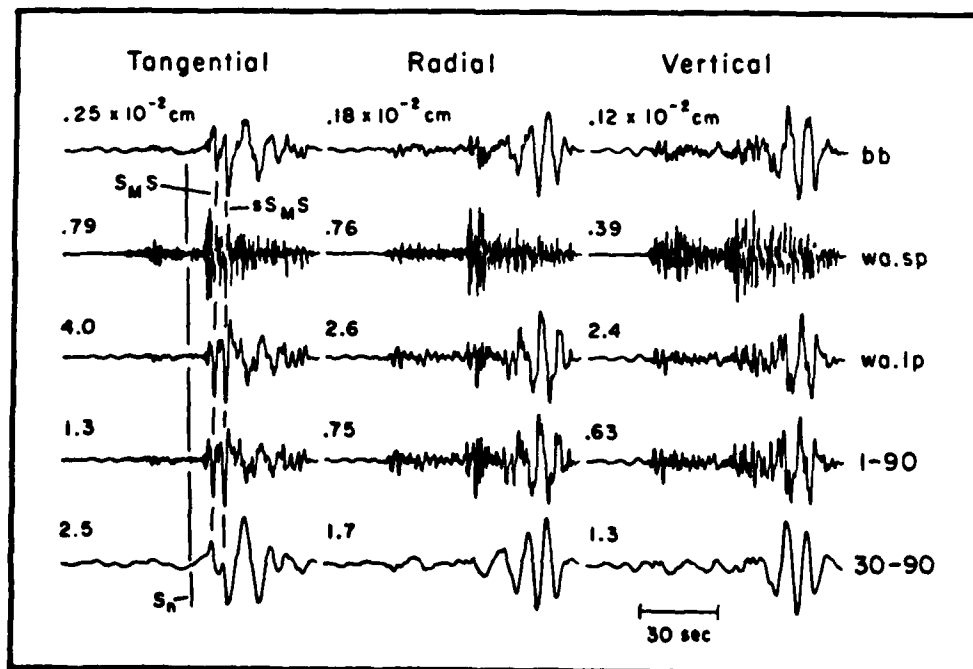


FIG. 3. Recording of a $M_L = 4.9$ aftershock of the Supersition Hills earthquake of 24 November 1987 along with the various simulations. This event occurred near the southern end of the fault breakage.

In this study, we will derive a 2-D model appropriate for a cross section from Imperial Valley to Pasadena using a master event and the forward modeling approach. The resulting Green's functions will then be used to examine some of the more important events located in the map displayed in Figure 4. Events occurring to the northwest of the Imperial Valley are relatively simple, while events in the basin are always complex, especially the shallow ones. Considering the obvious 3-D geometry indicated in Figure 4, it is rather surprising that these records do not show more evidence of multi-pathing and Love-Rayleigh mixing. This subject will be addressed later. We consider primarily the long-period tangential motions in this pilot study because less computational effort is involved compared to modeling the P-SV system recorded on the radial and vertical components.

CRUSTAL CROSS SECTION AND GREEN'S FUNCTIONS

Searching for suitable Green's functions by trial-and-error testing can be a time-consuming endeavor but the basic approach has proven effective in previous studies (Vidale *et al.*, 1985; Helmberger and Vidale, 1987). Two types of codes were employed, namely the generalized ray method (GRT) for laterally varying layers (Helmberger *et al.*, 1985) and a modified finite-difference (FD) technique (Vidale *et al.*, 1985). The first method is analytical and can be used effectively to adjust deeper smoothly varying structures for proper timing and critical angle positions. The truncation of basins, however, requires the more powerful numerical approach.

As in all forward modeling attempts, one starts with the best geophysical data available for constraining the initial model. Fortunately, considerable studies have been conducted in this region. For the Imperial Valley velocity profile, we used the model proposed by McMechan and Mooney (1980) and Fuis *et al.* (1982). Just outside the basin we used the results from Hamilton (1970), who investigated the Borrego Mountain aftershocks with controlled calibration shots. Hamilton's results suggest a thick crust-mantle transition zone. At Pasadena we adopted the model

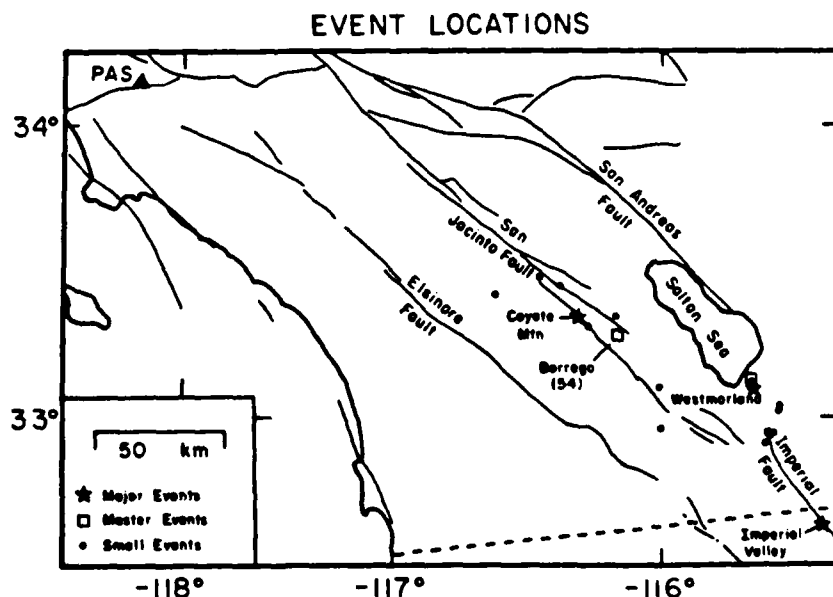


FIG. 4. Map showing locations of Pasadena, PAS, and events used in this study.

proposed by Hadley and Kanamori (1977, 1979) with a thick crust and relatively sharp Moho transition. These vertical profiles were assembled by allowing for a gentle dipping connecting structure and produced an initial cross-section from Imperial Valley to Pasadena.

An example calculation for a deep event near Anza is given in Figure 5, which shows the simplicity of the propagational path to Pasadena for hard-rock sections. All six events north of Borrego look similar to the upper plot (Fig. 6) and can be explained by a multitude of models. However, note the complexity of the bottom trace in Figure 5, $\Delta = 85$ km (synthetic), appropriate for a basin site. Features produced by this geometry are discussed at length by Vidale *et al.* (1985). Thus, the biggest difficulty is modeling the edge of the basin properly to explain the PAS records of the basin events.

Synthetic for a basin event are displayed in Figure 7 along with the master event (Brawley) observations, $\Delta = 256$ km. The source parameters for this event were determined earlier by Heaton and Helmberger (1978) and are treated as known.

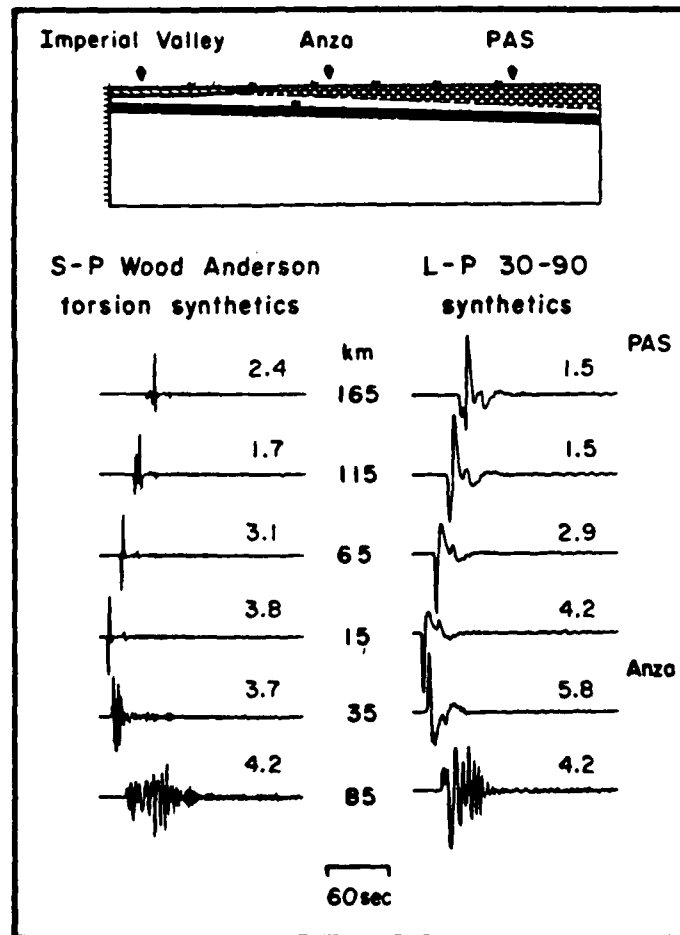


FIG. 5. Profile of Green's functions with the source outside the basin, small solid box beneath Anza. Little waveform distortion is observed along the path towards Pasadena (upper four traces) while very complicated waveforms develop rapidly in the basin (lower two traces), indicating the important effect of the basin edge on wave propagation along this profile.

MODELING REGIONAL LOVE WAVES

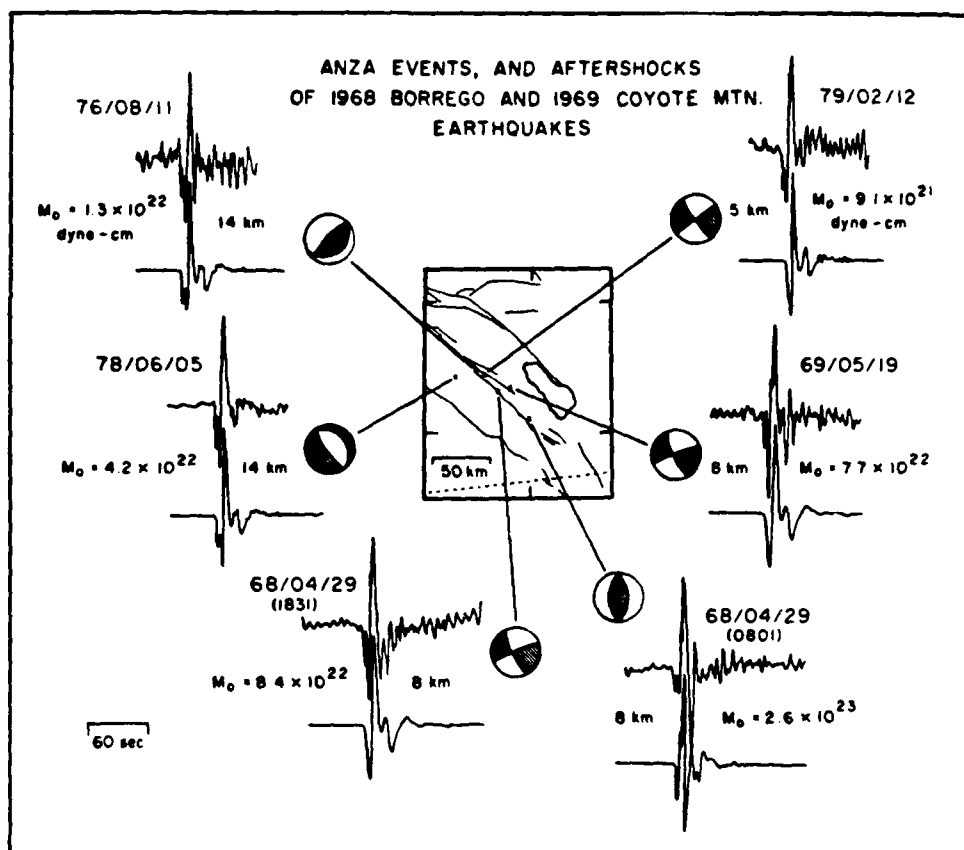


FIG. 6. Long-period modeling of three Anza events and two aftershocks of the 1968 Borrego Mountain event and one of the 1969 Coyote Mountain aftershocks. The corresponding focal mechanism is also shown.

This assumption allows us to perturb the various model parameters to improve agreement in waveform and absolute timing. Goodness-of-fit is determined simply by overlaying the synthetic and observed waveforms. This procedure goes relatively fast for long-period modeling but becomes increasingly tedious at higher frequencies.

The best-fitting model to date has a slow mantle velocity of 4.28 km/sec, a northwest-thinning Moho-crustal transition layer of 4.18 km/sec, a dipping crustal-Moho transition layer of 4.05 km/sec, a dipping lower crust of 3.78 km/sec that thins out to the northwest, and an upper crust of 3.38 km/sec that also dips northwest. The idealized Imperial Valley basin surface has two layers of very slow shear velocities of 1.0 km/sec and 2.34 km/sec, corresponding to what Fuis *et al.* (1982) described in their *P*-wave refraction profiles. A thin layer of 3.24 km/sec that thins out at the edge of the basin lies underneath the slow sediments. This model is displayed at the top of Figure 8 with strike-slip and dip-slip synthetics given below. Note the rapid development of dispersion and waveform complexity caused by the slow Valley structure which is evident at $\Delta = 62$ km. Not much more complexity develops along the remaining hard-rock path suggesting the applicability of numerical-analytical interfacing codes (Stead and Helmberger, 1988).

Depth sensitivity is displayed in Figure 9 at the range of 262 km, which is appropriate for the Imperial Valley aftershocks. For both strike-slip and dip-slip

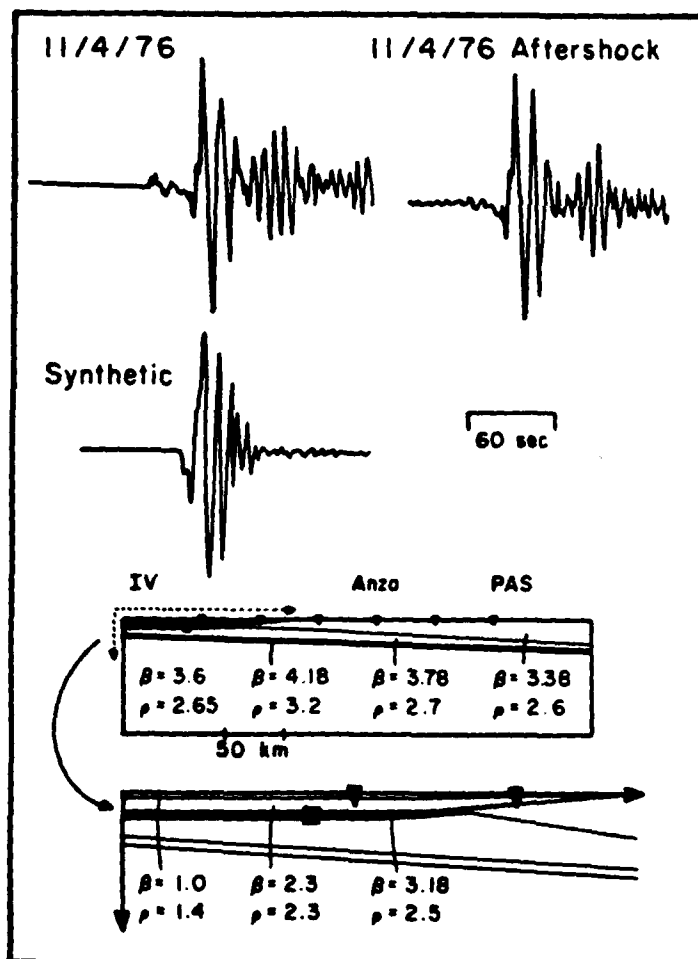


FIG. 7. Tangential component of the Brawley earthquake and its aftershock as recorded on LP 30-90 of the Pasadena station and the corresponding synthetics. The mechanism used to generate the synthetic is obtained from Heaton and Helmberger (1978).

mechanisms, absolute amplitude decreases with depth for a given moment. In addition, a pure strike-slip mechanism results in almost twice the amplitude of a pure dip-slip mechanism at all four depths. In general, we also expect to see a shallow source excite more surface waves for both mechanisms, and deeper source to show less complexity. These results are similar to those found in flat layered models.

For small events, we expect source durations to be short compared to the 30-90 instrumental response and, therefore, we should be able to fit any seismogram by a linear combination of the Green's functions displayed in Figure 9. A total of nine events with unknown source parameters, including the three aftershocks described earlier and the Brawley aftershock, were collected as a data set to which the Green's functions were applied. These events are listed in Table 1, where the locations and depths are from the Caltech catalog. After reviewing focal mechanisms for published mechanisms for events in this region (Johnson and Hadley, 1976; Heaton and Helmberger, 1978; Fuis *et al.*, 1982; Johnson and Hutton, 1982; Liu and Helmberger,

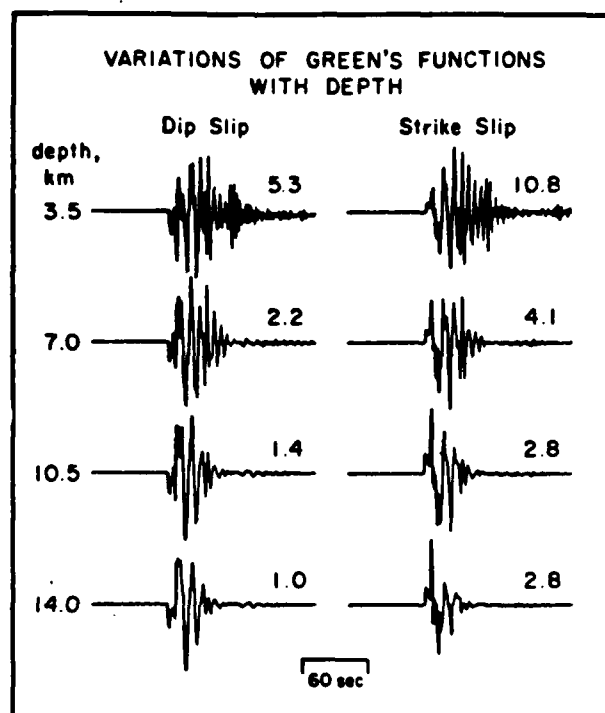


FIG. 9. Sensitivity of Green's functions to depth. Sources are put in four different depths at the same epicentral location as the 1976 Brawley event: 3.5, 7.0, 10.5, and 14.0 km. In general, when the source is still in the basin, more surface waves are generated and when the source is below the soft and slow sediments in the basin, the waveforms are simpler and energy drops off rapidly with time.

TABLE 1
SUMMARY OF EARTHQUAKES USED IN THE IMPERIAL VALLEY LONG-PERIOD STUDY

Event	Date (mm/dd/yy)	Time (GMT)	Latitude (N)	Longitude (W)	Depth (km)	Dip	Strike	Strike
1(A)	10-16-79	03:39:35.04	32° 56.92'	115° 33.01'	5.14	10°	90°	99°
2(B)	10-16-79	09:36:41.89	32° 56.98'	115° 31.41'	4.27	10°	90°	99°
3(C)	10-16-79	11:47:56.06	32° 54.81'	115° 33.61'	5.09	90°	180°	119°
4	11-4-76	14:12:50.28	33° 07.41'	115° 37.19'	2.71	90°	180°	328°
5*	11-4-76	10:41:37.54	33° 07.89'	115° 37.40'	0.55	90°	180°	328°
6	10-16-79	23:16:32.18	33° 01.33'	115° 30.37'	3.32	20°	180°	300°
7	10-17-79	22:45:33.82	33° 02.40'	115° 30.02'	1.87	70°	180°	334°
8	10-16-79	03:10:47.83	32° 57.06'	115° 32.10'	4.22	70°	180°	334°
9	10-16-79	06:49:10.97	32° 56.48'	115° 32.31'	4.66	10°	90°	99°
10	4-25-81	07:03:14.12	33° 06.24'	115° 37.69'	5.24	45°	-90°	0°

* Brawley Earthquake.

simple for both strike-slip and dip-slip mechanisms, and it changes only slightly with depth. It appears that the deeper the event, the simpler the waveform it created. This features proves useful in fixing the depths of events as did the amount of surface wave excitation for events in the Imperial Valley.

In order to check the derived crustal model for its accuracy outside the Imperial Valley sedimentary basin, we applied the same source-modeling process to three events at Anza, an aftershock of the Coyote Mountain 1969 event, and two aftershocks of the 1968 Borrego Mountain event (Fig. 6). The mechanisms used to

MODELING REGIONAL LOVE WAVES

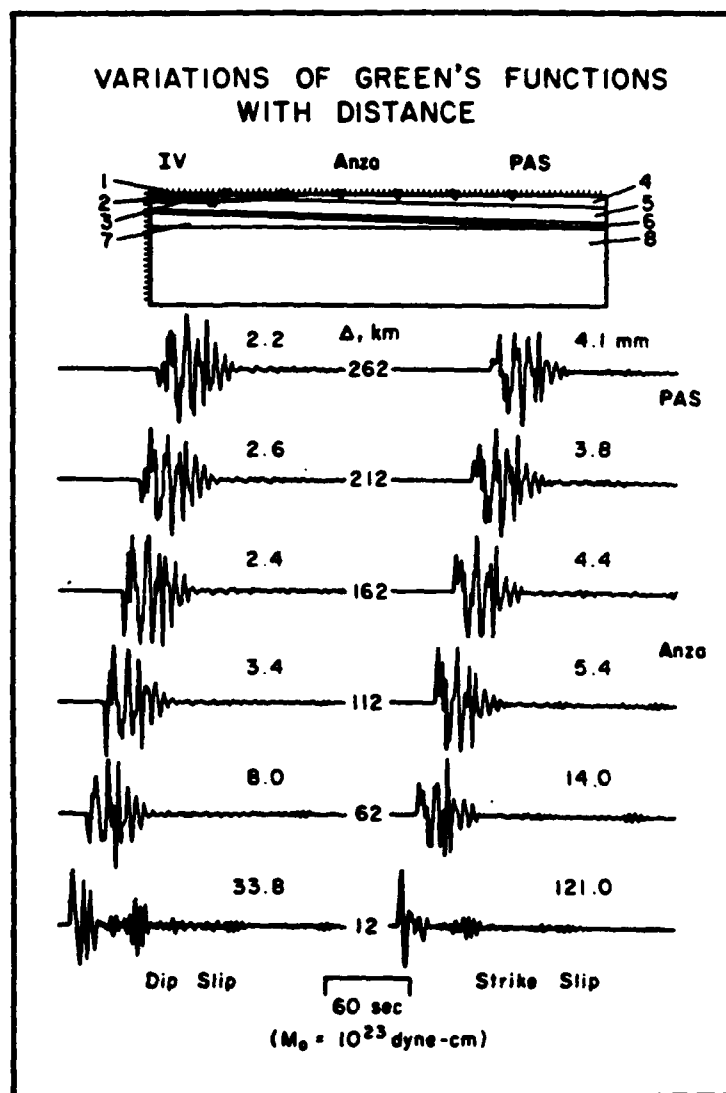


FIG. 8. Preferred velocity model and the corresponding Green's functions generated with a source depth of 7 km at the location of the 1976 Brawley earthquake ($\Delta = 262$ km). The stations are located at 50 km interval with the last station at Pasadena. Note the rapid development of surface waves in the basin portion of the path. Maximum amplitudes are given in $\text{mm} \times 10^{-2}$.

1985), a total of 21 possible orientations for each event was considered. The best-fitting combinations are displayed in Figure 10 with depths, magnitudes, and moment estimates given in Tables 1 and 2. Note that event C, as discussed earlier, is modeled as a deep strike-slip event, while event B appears to be a shallow dip-slip.

The moment required to match the Brawley data was 3.0×10^{23} dyne-cm, which can be compared with the 3.2 found by Heaton and Helmberger (1978) using local strong-motion data.

The sensitivity of Green's functions to depth for sources at Anza appears totally different from that in Imperial Valley (Fig. 11). In general, the waveform is very

MODELING REGIONAL LOVE WAVES

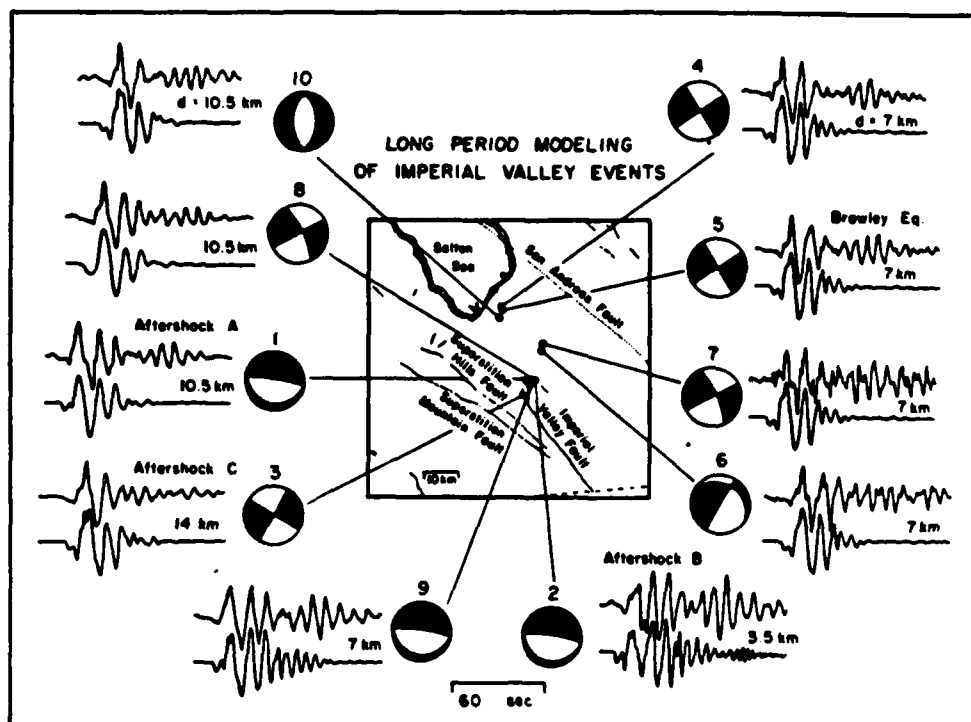


FIG. 10. Long-period modeling of nine unknown aftershocks and small events in the Imperial Valley, including the calibration event, the Brawley earthquake. Data shown are recorded on the LP \approx 30-90 instrument. The modeled mechanisms are also shown. Results indicate that event C is a deep strike-slip event, event B a shallow dip-slip event, and event A a mid-depth dip-slip event.

TABLE 2
IMPERIAL VALLEY MOMENTS OBTAINED BY FITTING LONG-PERIOD SH AND THE CORRESPONDING M_L AND DEPTHS COMPARED TO THE CATALOG VALUE

Event	M_s	M_L		Depth (km)	
		SH	catalog	Modeled	catalog
1	15.3	4.5	4.6	10.5	5.14
2	2.4	3.3	4.1	3.5	4.27
3	39.2	4.6	4.8	14.0	5.09
4	6.3	4.5	4.4	7.0	2.71
5	30.0	4.8	5.1	7.0	0.55
6	60.0	5.2	5.0	7.0	3.32
7	4.1	4.4	4.7	7.0	1.87
8	62.1	4.7	4.6	10.5	4.22
9	9.38	4.8	5.1	7.0	4.66
10	6.1	4.5	3.9	10.5	5.24

M_s are given in 10^{25} dyne-cm.

model the Anza events were again collected from various studies (Given, 1983; Sanders and Kanamori, 1984) and adjustments made to fit the data. The fits between synthetics and data are reasonably good with results given in Tables 3 and 4.

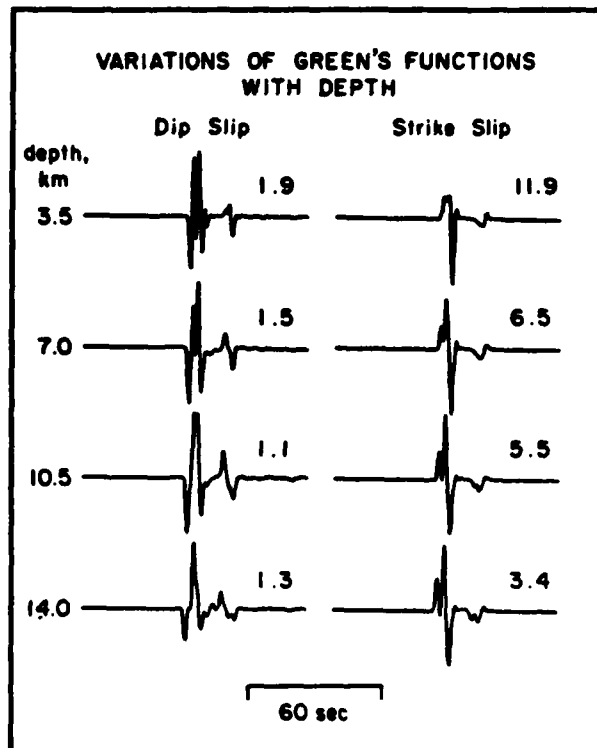


FIG. 11. Sensitivity of Green's functions to depth with the source at Anza distance. The waveforms are simple compared to those displayed in Figure 9. There is not as much difference in the complications of waveforms with depth as in the previous case.

TABLE 3
SUMMARY OF SOURCE MECHANISMS FIT TO THREE ANZA EVENTS IN THE LOCAL MAGNITUDE RANGE OF 4 TO 5

Event				Depth (km)	Dip	Rake	Strike
Date (mm/dd/yy)	Time (GMT)	Latitude (N)	Longitude (W)				
06-11-76	15:24:55.42	33° 28.9'	116° 30.62'	14.0	70°	-86°	45°
06-06-78	16:03:03.72	33° 25.21'	116° 41.61'	14.0	70°	-90°	152°
02-12-79	04:48:42.28	33° 27.21'	116° 25.44'	5.0	81°	0°	145°

Strike is measured clockwise from North.

TABLE 4
SUMMARY OF SOURCE MECHANISMS FIT TO AFTERSHOCKS OF THE 1968 BORREGO MOUNTAIN AND 1969 COYOTE MOUNTAIN EARTHQUAKES

Event					Dip	Rake	Strike
Date (mm/dd/yy)	Hr:min	Sec	Latitude (N)	Longitude (W)			
04-09-68	0800	38.5	33° 06.4'	116° 00.4'	45°	90°	0°
04-09-68	1831	38.5	33° 18.9'	116° 18.3'	80°	251°	163°
06-19-69	1440	33.0	33° 20.9'	116° 11.3'	80°	251°	163°

* Strike is measured clockwise from North.

MODELING REGIONAL LOVE WAVES

STRONG MOTIONS FROM IMPERIAL VALLEY EVENTS

One of the objectives of this study was to provide Green's functions appropriate for strong motions in the frequency domain of 10 to 0.1 Hz. Unfortunately, we do not have broadband data at these intensity levels so that we must rely on recordings from the low gain Wood-Anderson (100 \times).

At 10 Hz the problem becomes extremely complex and the motions no longer separate into the *P*-SV and *SH* systems. Also, we no longer expect events of this magnitude ($M_L > 5.5$) to be as simple as the small events discussed earlier. Thus, it is difficult to assess the adequacy of our results, since we can only compare predicted motions at Pasadena based on independently determined source studies from near-in data at Imperial Valley. Three-component data may help resolve the source properties by providing more data, and this subject will be addressed in a later effort. At this stage, we will examine only the 1979 Imperial Valley earthquake as an example. The secondary energy, arriving about 40 sec after the initial motion that accompanies many of the shallow events in the Valley, will be discussed later.

Several inversions were done on the 1979 Imperial Valley main shock. The general consensus of the rupture includes an initial 10 km deep epicenter that ruptured northwestward along the Imperial Fault at a rate of 75 per cent of the shear velocity; the rupture then continued on at a shallower depth (Hartzell and Helmberger, 1982; Olson and Apsel, 1982; Hartzell and Heaton, 1983) Archuleta (1984) holds a slightly different conclusion on the rupture process, with an initial strike-slip source at about 8 km depth rupturing northwestward. Subsequent rupture occurred at two

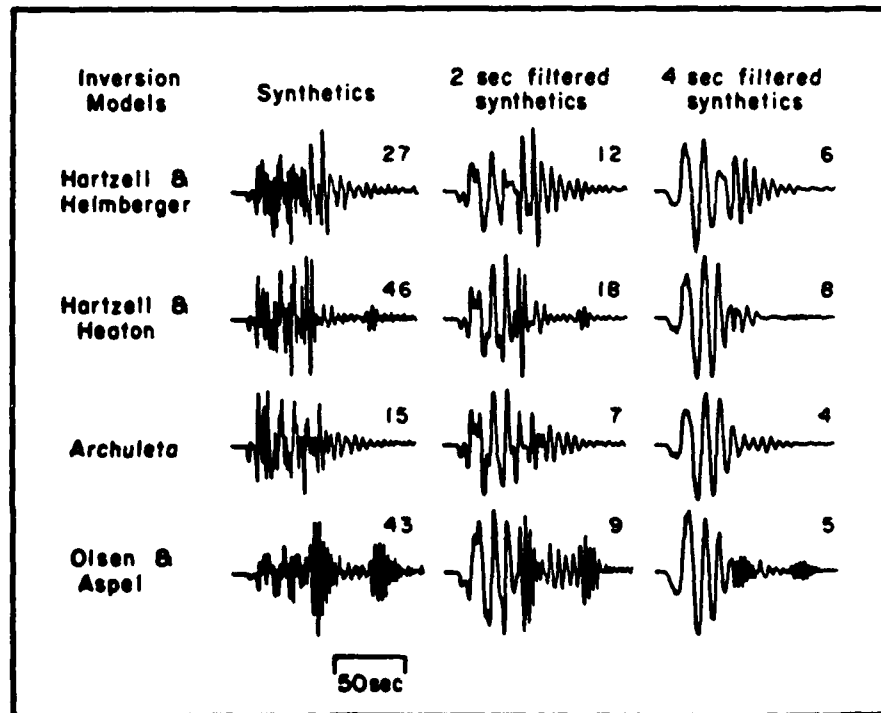


FIG. 12. Simulations of strong motion of the 1979 Imperial Valley event using four inversion models (Olson and Apsel, 1982; Hartzell and Helmberger, 1982; Hartzell and Heaton, 1983; Archuleta, 1984). Amplitudes are given in cm for a moment of 5.0×10^{25} dyne-cm.

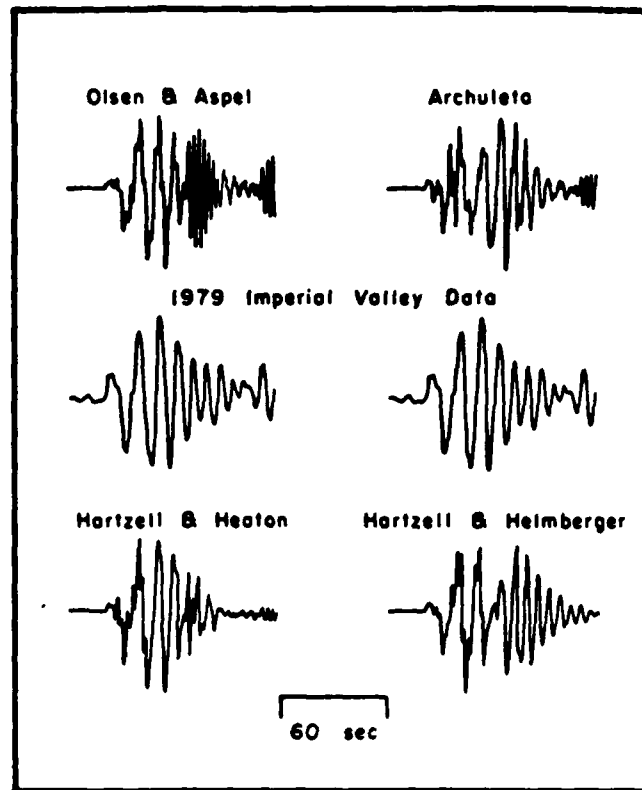


FIG. 13. Comparison of 4-sec filtered tangential motion against predicted synthetics.

main locations, both at about 10 km depth, with a minor dip-slip rupture at about 30 km from the epicenter along the strike of the fault. The Hartzell and Helmburger's model (model HH1) and the Hartzell and Heaton's model (model HH2) are very similar, while Olson and Aspel's model (model OA) is a more continuous model, which can be simulated using nine segments of rupture. We attempt to model this 1979 main shock by treating each rupture segment in each inversion model as an earthquake source. Using the same mechanism as inverted by the above workers, we combine our synthetics with the mechanisms and then add the segments up according to the corresponding delay time along the fault. Simulations of such strong motions appropriate for the Pasadena torsion are shown in Figure 12 with the corresponding inversion models.

A comparison of the filtered data with the synthetic predictions is displayed in Figure 13. The synthetic responses shown in Figure 12 require a time derivative to compare with the corresponding WA record in displacement which tends to emphasize the high frequency tails such as in the Olson-Aspel model. In general, all of these models display some merit, although it appears that the two models on the left fit the waveform data somewhat better. The important point in this comparison is not which model fits better but that complex earthquakes (multiple ruptures) can be probably distinguished from simple events when BB Green's functions are available. Thus, this type of regional data from historic events can be used to help delineate rupture patterns along important fault segments.

MODELING REGIONAL LOVE WAVES

DISCUSSION AND CONCLUSION

Many of the events in the Imperial Valley data set have a secondary arrival that is about 60 sec late (Fig. 10), which we have neglected. There are several possibilities for the secondary arrivals: (1) Source structural effects, which include three-dimensional scattering due to the Imperial Valley basin structure; (2) Source parameters effects, which suggest double events or complicated faulting mechanisms; (3) Receiver structural effects, which are local effects due to receiver being in or near a basin; and (4) Path complications, which suggest structural effects along the same path that are not in the present model.

Source structural effects would result in waves arriving at the receiver along different azimuths. We determined by complex polarization studies (Vidale, 1986) on the three components that the late arrival was traveling along approximately the same azimuth as the main arrival. So we believe that this late arrival comes mainly from the same ray azimuth as the main arrival, though there is a clockwise rotation after the first arrival at Pasadena. This effectively rules out possibility (1).

The three events we studied at Anza, the Borrego Mountain distance, and the Coyote Mountain events show no secondary arrival at all. The arrivals have relatively simple waveforms. The hypothesis that the secondary arrivals on the Imperial Valley events are effects of the local receiver structure is then ruled out because of the absence of such arrivals on the other records of events outside the basin.

We are now left with possibilities (2) and (4). It is fairly unreasonable to attribute double mechanisms to all events with secondary arrivals. However, shallow events have secondary arrivals, while deeper events do not. The secondary arrival also has lower frequency than the main arrival as recorded on the long-period instrument and are not found in high-frequency records. These features suggest that this

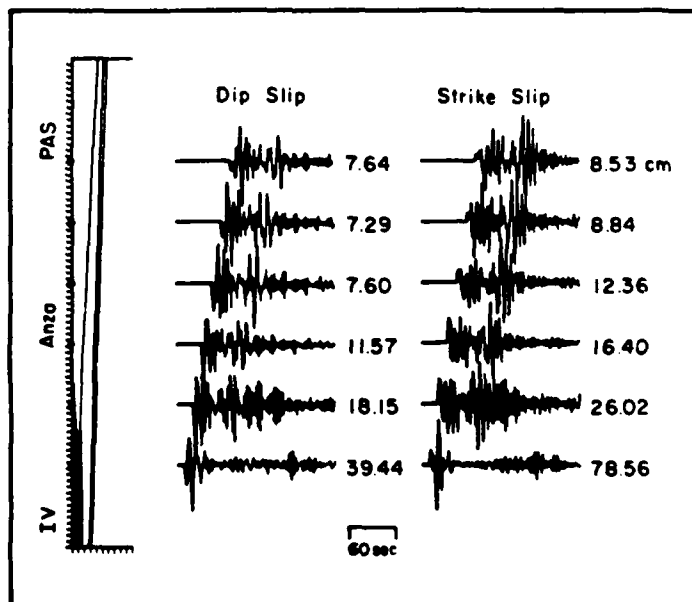


FIG. 14. Numerical responses along a profile from IV to PAS for an idealized basin model. Note the sharp edge of the basin typical of faulted structures at the western edge of this particular basin.

secondary pulse has traveled as a trapped surface wave in the surface sediments to the edge of the basin and regenerates into a normal Love wave.

A number of numerical profiles with sources placed at various depths in a variety of basin models were generated to test the above hypothesis. When the source is situated in the sediments and when the basin ends sharply, the secondary arrival becomes particularly strong, as displayed in Figure 14. Basin models with gentle dipping edges do not show the secondary arrival and apparently scatter the surface waves at lower ray parameters, probably teleseismically, as found in the study by Stead and Helmburger (1988).

The broadband responses displayed in Figure 14 do not contain the instrument and suggest that the secondary arrival is not depleted in high frequency as observed. Thus, the observed secondary arrival has lost its high frequency by attenuation in the soft sediments or, perhaps, the source excitation is very low stress drop. This subject is best pursued with broadband three-component array data and will be addressed in a subsequent paper.

In conclusion, we have demonstrated that many of the complexities of intermediate-period regional Love waves can be explained by 2-D models. The added modeling parameters allow the creation of complex dispersed wave trains to develop in basins and then travel relatively large distances with only slight modifications. The usefulness of Green's functions from such models will be explored in future efforts.

ACKNOWLEDGMENTS

We would like to thank Luciana Astiz, Gladys Engen, and Hiroo Kanamori for valuable comments on the manuscript, and Gladys Engen and Cindy Arvesen for helping with the data processing and drafting. This work was supported in part by the USGS 14-06-0001-G-1183 and by the Geophysical Sciences Division of the Air Force Geophysics Laboratory under contract F19628-87-K0028 and monitored by the Defense Advanced Research Projects Agency. Contribution no. 4571, from the Division of Geological and Planetary Sciences, California Institute of Technology, Pasadena, California.

REFERENCES

- Archuleta R. J. (1984). A faulting model for the 1979 Imperial Valley earthquake, *J. Geophys. Res.* **89**, 4559-4585.
- Bent, A. L., D. V. Helmburger, R. Stead, and P. Ho-Liu (1989). Waveform modeling of the November 1987 Superstition Hills earthquakes, *Bull. Seism. Soc. Am.* **79**, 500-514.
- Burdick, L. J. and G. K. Mellman (1976). Inversion of the body waves of the Borrego Mountain earthquake to the source mechanism, *Bull. Seism. Soc. Am.* **66**, 1485-1499.
- Ebel, J. E. and D. V. Helmburger (1982). P-wave complexity and fault asperities: the Borrego Mountain, California, earthquake of 1968, *Bull. Seism. Soc. Am.* **72**, 413-437.
- Fuis, G. S., W. D. Mooney, J. H. Healy, G. A. McMechan, and W. J. Lutter (1982). Crustal structure of the Imperial Valley region in the Imperial Valley, California earthquake of Oct. 15, 1979, *U. S. Geol. Survey Profess. Paper* **1254**, 25-49.
- Given, D. D. (1983). Seismicity and structure of the trifurcation in the San Jacinto fault zone, southern California, *M.S. Thesis*, California State University, Los Angeles.
- Hadley, D. and H. Kanamori (1977). Seismic structure of the Transverse Ranges, California, *Bull. Geol. Soc. Am.* **88**, 1469-1478.
- Hadley, D. and H. Kanamori (1979). Regional S-wave structure for southern California from the analysis of teleseismic Rayleigh waves, *Geophys. J. R. Astr. Soc.* **58**, 655-666.
- Hamilton, R. M. (1970). Time-term analysis of explosion data from the vicinity of the Borrego Mountain, California, earthquake of 9 April, 1968, *Bull. Seism. Soc. Am.* **60**, 367-381.
- Hartzell, S. T. (1978). Earthquake aftershocks as Green's functions, *Geophys. Res. Letts.* **5**, 1-4.
- Hartzell, S. T. and D. V. Helmburger (1982). Strong-motion modeling of the Imperial Valley earthquake of 1979, *Bull. Seism. Soc. Am.* **72**, 571-596.
- Hartzell, S. T. and T. H. Heaton (1983). Inversion of strong ground motion and teleseismic waveform

MODELING REGIONAL LOVE WAVES

- data for the fault rupture history of the 1979 Imperial Valley, California, earthquake, *Bull. Seism. Soc. Am.* **73**, 1553-1583.
- Heaton, T. H. and D. V. Helmberger (1978). Predictability of strong ground motion in the Imperial Valley: Modeling the M 4.9, November 4, 1976 Brawley earthquake, *Bull. Seism. Soc. Am.* **68**, 31-48.
- Helmberger, D. V. (1983). Theory and application of synthetic seismograms, earthquake: observations, theory and observations, in *Proceedings of the International School of Physics, Enrico Fermi Course LXXXV*, H. Kanamori and E. Boschi, Editors, North-Holland, Amsterdam, 174-217.
- Helmberger, D. V., G. Engen, and S. Grand (1985). Notes on wave propagation in laterally varying structure, *J. Geophys.* **58**, 82-91.
- Helmberger, D. V. and J. E. Vidale (1987). Modeling strong motions produced by earthquakes with 2-D numerical codes (submitted for publication).
- Johnson, C. E. and D. M. Hadley (1976). Tectonic implications of the Brawley earthquake swarm, Imperial Valley, California, January 1975, *Bull. Seism. Soc. Am.* **66**, 1133-1144.
- Johnson, C. E. and L. K. Hutton (1982). Aftershocks and preearthquake seismicity, California earthquake of Oct. 15, 1979, *U.S. Geol. Survey Profess. Paper* **1254**, 59-76.
- Kanamori, H. and J. Regan (1982). Long-period surface waves generated by the 1979 Imperial Valley earthquake, *U.S. Geol. Surv. Profess. Paper* **1254**, 55-58.
- Liu, H. L. and D. V. Helmberger (1985). The 23:19 aftershock of the 15 October 1979 Imperial Valley earthquake: more evidence for an asperity, *Bull. Seism. Soc. Am.* **75**, 689-708.
- McMechan, G. A. and W. D. Mooney (1980). Asymptotic ray theory and synthetic seismograms for laterally varying structure: theory and application to the Imperial Valley, California, *Bull. Seism. Soc. Am.* **70**, 2021-2036.
- Olson, A. H. and R. J. Apsel (1982). Finite faults and inverse theory with applications to the 1979 Imperial Valley earthquake, *Bull. Seism. Soc. Am.* **72**, 1969-2001.
- Sanders, C. O. and H. Kanamori (1984). A seismotectonic analysis of the Anza seismic gap, San Jacinto fault zone, southern California, *J. Geophys. Res.* **89**, 5873-5890.
- Sanders, C. O., H. Magistrale, and H. Kanamori (1986). Rupture patterns and preshocks of large earthquakes in the southern San Jacinto fault zone, *Bull. Seism. Soc. Am.* **76**, 1187-1206.
- Stead, R. J. and D. V. Helmberger (1988). Numerical-analytical interfacing in two dimensions with applications to modeling NTS seismograms, *Pure Appl. Geophys.* (in press).
- Thatcher, W. and R. M. Hamilton (1973). Aftershocks and source characteristics of the 1969 Coyote Mountain earthquake, San Jacinto fault zone, California, *Bull. Seism. Soc. Am.* **63**, 647-661.
- Thatcher, W. and T. C. Hanks (1973). Source parameters of southern California earthquakes, *J. Geophys. Res.* **78**, 8547-8576.
- Vidale, J., D. V. Helmberger, and R. W. Clayton (1985). Finite-difference seismograms for SH waves, *Bull. Seism. Soc. Am.* **75**, 1765-1782.
- Vidale, J. (1986). Complex polarization analysis of particle motion, *Bull. Seism. Soc. Am.* **76**, 1393-1405.

SEISMOLOGICAL LABORATORY 252-21
CALIFORNIA INSTITUTE OF TECHNOLOGY
PASADENA, CALIFORNIA 91125

Manuscript received 14 June 1988

SECTION 2

Numerical modelling of SH L_g waves in and near continental margins

Numerical modelling of SH L_g waves in and near continental margins

J. Regan

Geological Survey of Canada, 1 Observatory Crescent, Ottawa, Ontario, Canada K1A 0Y3

D. G. Harkrider

Seismological Laboratory 252-21, California Institute of Technology, Pasadena, CA 91125, USA

Accepted 1989 January 11. Received 1988 December 21; in original form 1988 June 27.

SUMMARY

The effect of transition regions between continental and oceanic structures on the propagation of L_g waves from continental sources is examined. In particular, the attenuation due to variations in layer thickness in such transition regions is calculated and explained for a suite of simple models. The measured attenuation, due to the geometry of the transition regions between the oceanic and continental structures within a partially oceanic path with source and receiver in a continental structure, is at most a factor of four for frequencies from 0.01 to 1 Hz. This is inadequate to explain the observed extinction of L_g along such paths. This extinction has previously been attributed to the effects of the transition region geometry. The method used to calculate the results presented in this study is developed and its validity and accuracy are demonstrated. Propagator matrix seismograms are coupled into a Finite Element calculation to produce hybrid teleseismic SH mode sum seismograms. These hybrid synthetics can be determined for paths including any regional transition zone or other heterogeneity that exists as part of a longer, mostly plane-layered, path. Numerical results presented for a suite of transition models show distinct trends in each of the regions through which the wavefield passes. The wavefield passes through a continent–ocean transition region, then a region of oceanic structure, and finally through an ocean–continent transition region. When an L_g wavefront passes through a continent–ocean transition, the amplitude and coda duration of the L_g wave at the surface both increase. At the same time, much of the modal L_g energy previously trapped in the continental crust is able to escape from the lower crust into the subcrustal layers as body waves. The magnitude of both these effects increases as the length of the transition region increases. When the wavefront passes through the region of oceanic structure further energy escapes from the crustal layer, and produces a decrease in L_g amplitude at the surface. The rate of amplitude decrease is maximum near the transition region and decreases with distance from it. When the wavefield passes through the ocean–continent transition region a rapid decrease in the L_g amplitude at the surface of the crust results. The energy previously trapped in the oceanic crustal layer spreads throughout the thickening crustal layer. Some of the body wave phases produced when the wavefield passes through the continent–ocean transition region are incident on the continental crust in the ocean–continent transition region. These waves are predominantly transmitted back into the crust. The other body wave phases reach depths below the depth of the base of the continental crust before reaching the ocean–continent transition and, thus, escape from the system.

Key words: synthetic seismograms, L_g waves, continental margins, finite element, attenuation

INTRODUCTION

This paper presents a study of the propagation of L_g waves across ocean–continent transition regions. The transition regions are represented by simplified models each consisting of a crustal layer with a smoothly varying thickness above a

half-space. The wavefields transmitted through the transition region models are calculated to model L_g . The modal interpretation of L_g on which the calculation of synthetic seismograms is based will be justified below. The importance of the method introduced in the next paragraph and its application to studies of L_g propagation in major

areas of study such as tectonic mapping and nuclear discrimination will be explained, and the new results this method will make possible will be discussed and related to previous work.

The changes to a L_g wavefield, as it travels across a transition region, are modelled using a hybrid method which combines the Finite Element method (FE) and the Propagator Matrix technique (PM) (Harkrider 1964, 1970, 1981). PM seismograms for L_g waves from a continental source are coupled into a FE calculation which propagates the L_g wavefield across the continent-ocean boundary. Results from the FE calculation are then coupled into a second FE calculation which propagates the L_g wavefield through an ocean to continent transition region. The results of either FE calculation may be propagated through a region of horizontally uniform waveguide by coupling them back into a PM calculation using the Seismic Representation theorem (RT) (de Hoop 1958). The FE to PM coupling can be used to economically investigate the effects of long ocean path lengths between regions and is the subject of later papers. Here we restrict ourselves to regions in and near transition zones separated by short (≤ 150 km) ocean paths.

One of the important types of observational studies of L_g has been to distinguish regions with oceanic crustal structures from those with continental crustal structures. Press & Ewing (1952) and Bath (1954) observed extinction of L_g when the propagation path included an oceanic portion of length greater than 200 km, and high attenuation or extinction when the oceanic path length was as short as 100 km. This led to the commonly used assumption that paths which pass under oceans but do not attenuate L_g are continental. The results of the present paper seriously challenge the interpretation that paths with short oceanic portions which show little or no L_g attenuation are necessarily continental. They may necessitate the reassessment of some of the results of studies of L_g in many regions of the world (Press, Ewing & Oliver 1956; Savarensky & Valdner 1960; Bolt 1957; Lehmann 1952, 1957; Oliver, Ewing & Press 1955; Herrin & Minton 1960; Wetmiller 1974; Gregersen 1984; Kennett & Mykkeltveit 1984).

Another major use of L_g waves is in the determination of magnitudes, m_{bL_g} , of explosions and earthquakes. Different types of magnitudes, including m_{bL_g} , are compared to discriminate between the two types of sources (Blandford 1982; Pomeroy, Best & McKeilly 1982). m_{bL_g} measurements are also used to derive γ , the coefficient of anelastic attenuation, which is important in many types of wave propagation and attenuation studies and can be employed to assess the possible destructiveness of earthquakes. It is important to understand if reflections, refractions, or diffractions from changes in crustal thickness, generally ignored in studies measuring m_{bL_g} or γ will produce significant effects not accounted for in the interpretations given (Nuttli 1973, 1978, 1981; Herrmann & Nuttli 1975, 1982; Street 1976, 1984; Street, Herrmann & Nuttli 1975; Street & Turcotte 1977; Jones, Long & McKee 1977; Bollinger 1979; Barker, Der & Mrazek 1981; Nicolas *et al.*, 1982; Dwyer, Herrmann & Nuttli 1983; Chung & Bernreuter 1981; Singh & Herrmann 1983; Campillo, Bouchon & Massinon 1984; Herrmann & Kijko 1983).

The preferred interpretation of L_g is in terms of a superposition of higher mode surface waves. This higher

mode surface wave interpretation of L_g was initially unpopular because, in its earliest forms, based on fundamental mode Love waves alone, it did not explain the vertical and longitudinal components and the long coda. However, it subsequently superseded the alternate explanation in terms of channel waves trapped in the crust above a low-velocity layer for the following reasons. Oliver & Ewing (1957, 1958), Oliver, Dorman & Sutton (1959) and Kovach & Anderson (1964) showed that all components of L_g could be interpreted by considering both higher mode Rayleigh and Love waves. Knopoff *et al.* (1975), Panza & Calcagnile (1974, 1975) and Bouchon (1981, 1982) used the higher mode interpretation of L_g to calculate synthetic seismograms, which demonstrate that a low-velocity channel below the crustal waveguide was unnecessary. Other phases previously defined in terms of the channel model have been successfully modelled using the higher mode surface wave model. Schwab, Kausel & Knopoff (1974) and Mantovani *et al.* (1977), considered S_n , Panza & Calcagnile (1975) considered R_g and L_n , and Stephens & Isacks (1977) considered the transverse component of S_n . Clearly, the multimode surface wave explanation of L_g is valid and useful. However, the long L_g coda observed is still not completely understood for phase velocities less than 2.8 km s^{-1} . The attribution of this long coda to diffraction and reflection from crustal structure is supported by the results presented in this study.

A simple parallel of the multimode surface wave interpretation, which is a very useful aid in the interpretation of the wavefields presented in this study, is the representation of the multimode L_g arrivals as superpositions of multiply reflected post-critical SH and SV rays trapped in the crustal layer. Bouchon (1982) used this type of interpretation for L_g arrivals for group velocities between 3.5 and 2.8 km s^{-1} . Pec (1967) and Kennett (1986) also used the ray approach to address properties of L_g . This type of interpretation can also be used to explain where structure causes conversions from L_g to distinct body waves or from one SH mode to another. Gregersen (1978) discusses conversion between different modes of Love waves and between Love and Rayleigh waves at ocean-continent boundaries. For near normal incidence conversion between Love and Rayleigh waves is shown to be a small effect. However, future 3-D modelling would be necessary to confirm these conclusions based on an approximate method. Understanding conversion between modes of L_g and between L_g and other phases is an important part of understanding the mechanisms of attenuation of L_g along mixed paths.

Many attempts to understand the propagation of seismic disturbances across regions of varying structure such as transition zones have been made. First, simple models were used and analytical solutions were derived for soluble special cases, then increasingly complicated models were considered as available computational power increased. The types of models that have been used to approximate transition regions can be separated into several types which are illustrated in Fig. 1. Sato (1961a) derived analytical results for models of type 1a (Fig. 1a) with $L = 0$ and $L > 0$. Kennett (1973) considered the problem of seismic waves interacting with a layer or layers in which properties change across a surface perpendicular to or at a specified angle from

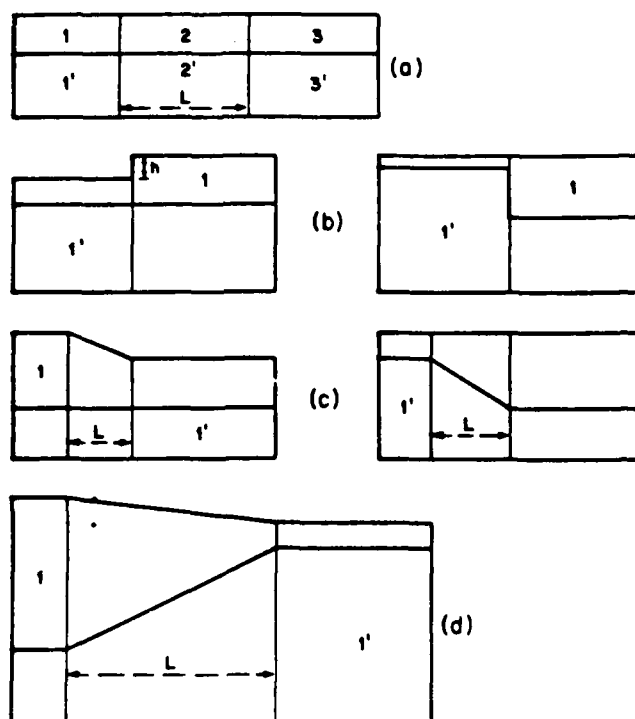


Figure 1. Types of models used in studies of propagation of Love waves across continent-ocean boundaries, in order of increasing complexity. (a) shows two homogeneous layered regions, 1 and 3, separated by an intermediate region, 2, in which elastic properties vary smoothly between their values in regions 1 and 2. (b) shows a layer over a half-space with a step change in the thickness of the layer. (c) shows a model with a smooth change in thickness, either at the surface or the Moho. (d) shows a model with a smooth change in thickness both at the surface and the Moho. The variations in (a), (c), and (d) occur in a transition region of length L .

the layering. Several types of solutions for models of type 1b (Fig. 1b) have been derived. Sato (1961b) obtained approximate analytical reflection and transmission coefficients, for $h \ll \lambda$, where h is the crustal thickness and λ is the incident wavelength. Hudson & Knopoff (1964), Knopoff & Hudson (1964), Hudson (1977) and Bose (1975) derived similar solutions without applying the $h \ll \lambda$ constraint. Alsop (1966) developed an approximate solution for these coefficients applicable when all energy remains in Love waves. Gregersen & Alsop (1974, 1976) extended this method to the case of non-normally incident Love waves. They found that for oblique incidence at angles less than 40° normal incidence is a good approximation. Kazi (1978a, b) derives solutions that account for and demonstrate the importance of the Love waves converted to scattered body waves at the surface step. Martel (1980) used a FE technique and spatial filtering to isolate the diffracted body wave component. Many workers have studied models of type 1c (Fig. 1c). Knopoff & Mal (1967), and Knopoff *et al.* (1970) derived an analytical solution usable when the slope of the surface (or Moho) in the transition region is small. Pec (1967) calculated the dispersion of Love waves propagating in a wedge-shaped layer and found that the largest changes in phase velocity and amplitudes occur at short periods. Boore (1970) studied the propagation of a

simple Love wave ($T > 20$ s), using the Finite Difference (FD) method. He noted that in the region of the transition mode conversions and conversion to other types of waves seemed to be important. Lymer & Drake (1971, 1972) and Drake (1972) use a FE method based on Zienkiewicz & Cheung (1967). This formulation requires that the incident modal energy is exactly equal to the sum of the reflected and transmitted modal energy. The body waves present in the system produce distortions to the elastic layer over a half-space eigenfunctions, which increase for higher modes. Drake & Bolt (1980) used the same method with a model of type 1d (Fig. 1d) to study a more realistic model fitting fundamental mode phase velocity data for events normally incident on the California continental margin at periods between 4.4 and 60 s.

All the studies discussed in the previous paragraph used periods much longer than those that will be considered in the following discussions. The shorter periods used in this study allow the examination of the effects of transition regions with L many times λ . The energy escaping from the crustal waveguide is shown in this study to be an important component of the explanation of the attenuation of the L_g phase travelling on partially oceanic paths. Previous studies considered mainly fundamental mode Love wave input sampled at a selection of discrete frequencies, while the forcing functions used in this study are a sum over a range of frequencies on the fundamental and first five higher branches. Of the previous studies, only Kennett & Mykkeltveit (1984) have generated realistic seismograms similar to those used in this study; instead other studies concentrated on measuring phase velocities and transmission and reflection coefficients.

PROPAGATOR TO FINITE ELEMENT COUPLING

The hybrid method used in the present study allows the determination of synthetic L_g seismograms for propagation paths which include a non-plane-layered transition region as a small portion of a longer mostly plane-layered path. A graphical representation of the hybrid method is shown in Fig. 2. No transition region is illustrated in the figure, but any type of structure may be inserted into the FE grid. Within a plane-layered medium, that is outside any transition region, the 'trapped' wavefield can be mathematically constructed at any point receiver using the PM technique and an appropriate form of a source representation. The resulting far-field seismogram will include not only a direct arrival but also the superposition of many multiple critical and post-critical reflections which produce the surface waves in the wavetrain. Each such PM seismogram is represented in Fig. 2 by a single solid line from the source to the receiver. A set of PM seismograms, for a specified source function, are generated at a group of intermediate receivers, equally spaced in x , located at the grid edge nodes of the FE grid, a horizontal distance X from the source. This type of set of seismograms will be referred to as a set of forcing functions. The depth spacing between the intermediate receivers, Δx , is also the node spacing in the FE grid of rectangular elements into which the wavefield is to be coupled. The PM forcing functions are applied as displacement time history constraints on the left-most

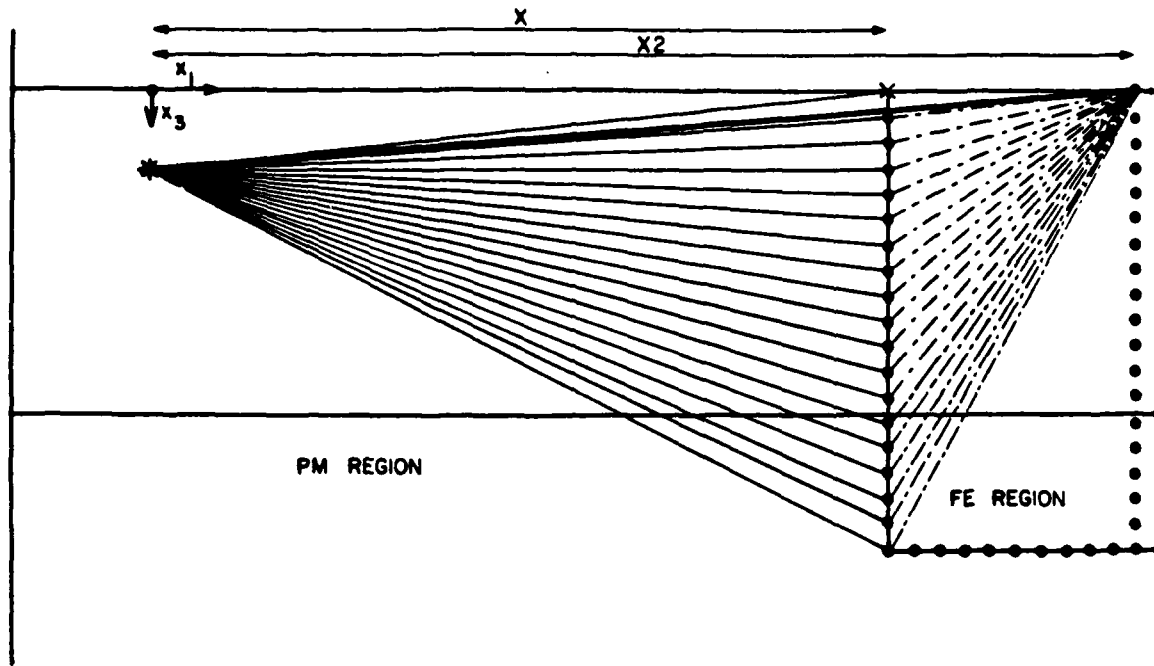


Figure 2. Geometry used to explain the coupling of PM seismograms from a source outside a FE grid into a FE grid. The two long horizontal lines show the free surface and the boundary between the layer and the half-space. The source is shown as an asterisk. Two columns of FE nodes are shown as dots. The vertical line connecting the dots and the short horizontal line perpendicular to it are grid edges. All receivers located at nodes on the left-most edge of the FE grid will be referred to as intermediate receivers. The heavy solid line from the source to the surface receiver in the grid denotes the direct analytical seismogram, the solid lines between the source and the grid edge nodes denote the direct forcing functions, and the dotted lines indicate the source to receiver paths, for the sources created by the application of the forcing functions at the grid edge. Integration over all dashed paths gives the hybrid seismogram.

column of nodes in the FE grid, thus, completely specifying the subsequent motion at all points in that FE grid. Each node to which a forcing function is applied becomes a source point in the FE calculation. Any point in the FE grid may be chosen as the receiver. The receiver is assumed to be a horizontal distance $X2$ from the source. The hybrid seismogram recorded at this receiver is a superposition of the seismograms produced by each source point along the FE grid edge. Each of these component seismograms are indicated by a dotted line in Fig. 2.

The seismograms used as forcing functions can be generated using more than one type of source. For a line source, in a homogeneous half-space or a layered half-space the applied forcing functions are $u_y(x, y, z)$. For a double couple point source the PM solutions can be expressed in cylindrical coordinates as

$$[\bar{u}(r, \phi, z)] = \bar{u}_v(\phi, z) \frac{\partial H_v^{(2)}(k_L r)}{\partial r},$$

where r is the source to receiver distance, k_L is the wavenumber of the Love wave mode being considered, $H_v^{(2)}(k_L r)$ is the Hankel function of the second kind, and $\bar{u}_v(\phi, z)$ is a factor containing all terms relating to the source and to propagation in z . 2-D and 3-D propagation show different rates of spreading with distance. The rectangular grid FE code used is based on the SWIS FE code (Frazier, Alexander & Petersen 1973), and is a 2-D Cartesian formulation. Thus, for consistency the forcing functions applied to the FE grid edge should be 2-D Cartesian results, u_y . It must be demonstrated that the

application of 3-D cylindrical forcing functions to a 2-D FE grid produces hybrid seismograms that approximate the 3-D cylindrical solution $[\bar{u}(r, \phi, z)]$ at the receiver. It is demonstrated below that the discrepancies in the 3-D cylindrical hybrid solution due to the 2-D propagation in the FE portion of the path are negligible or easily corrected for.

Consider a FE grid with its leftmost edge a distance $X = r_1$ from a source, and a receiver, where hybrid and analytical synthetic results are recorded, a distance $X2 = r_2$ from the source. Define the distance propagated within the FE grid as $\Delta r = r_2 - r_1$. Since we are considering the case of r large, $k_L \gg v/r$, $[\bar{u}(r_2, \phi, z)]$ can be expressed in terms of r_1 , ϕ , z , and Δr as

$$[\bar{u}(r_2, \phi, z)] = [\bar{u}(r_1, \phi, z)] \sqrt{\frac{r_1 + \Delta r}{r_1}} \exp(-ik_L \Delta r)$$

$$= [\bar{u}(r_1, \phi, z)] \exp(-ik_L \Delta r) \quad \Delta r \ll r_1 \quad k_L r_1 \gg 1.$$

Now, for a line source the analogous modal continuation relation is,

$$u_\phi(x_2, z) = u_\phi(x_1, z) \exp[-ik_L(x_2 - x_1)]$$

$$= u_\phi(x_1, z) \exp(-ik_L \Delta x).$$

Comparing, we see that both expressions have the same form. In each case the displacement at r_2 can be expressed as the displacement at r_1 multiplied by a propagation factor. A 2-D FE or RT calculation will give the same propagation factor for each mode as the analytical expression above. If the displacements at r_1 , $\bar{u}(r_1, \phi, z)$ or $u_y(x, z)$, and the propagation factors, $\exp(-ik_L \Delta r)$ or $\exp(-ik_L \Delta x)$, are

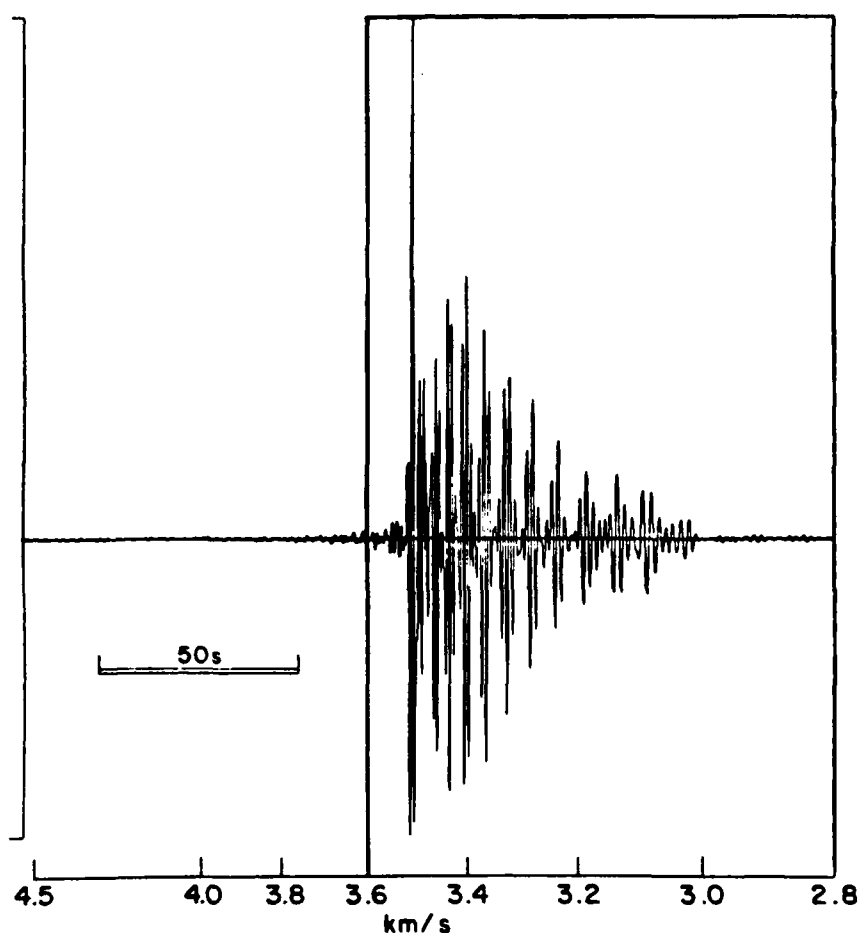


Figure 3. Sample PM mode sum synthetic seismogram for SH L_g 1500 km from the source. The seismogram includes modes with periods between 0.5 and 100 s. The fundamental and the first five higher modes are used. The seismogram has been bandpass filtered between 0.01 and 1 Hz, and has the WWSSN short period instrument response convolved with it. The box shows the time window used to select the forcing function. The numbers along the axis indicate the group velocities of the arrivals.

correlated by considering $x_1 = r_1$ and $\Delta x = \Delta r$, then $\bar{u}(r_2, \phi, z)$, the 3-D solution, will be given by $u_r(x_2, z)$, the result of the 2-D FE or RT calculation. The source must be many λ s from the boundary and r must be normal to the FE grid edge and in the plane of the FE grid.

The PM seismograms $\bar{u}(r, \phi, z)$ used as forcing functions in the tests discussed below show the overall character of the arrivals seen in data in the L_g group velocity range of between 2.8 and 3.5 km s⁻¹ (Fig. 3). The seismograms are complete to a period of 1.9 s and contain most of the energy for periods down to 0.5 s. A triangular time function with rise time 0.2 s, and decay time 0.2 s is used. The rectangle in Fig. 3 delimits the time window used to select the portions of the seismograms used as displacement time history forcing functions. No intrinsic attenuation is included in the seismograms, since the object of this study is to determine the attenuation caused by the geometry of the layers of the earth model. The forcing functions have been filtered between 0.01 and 1 Hz using a 3-coefficient two-way minimum phase time domain bandpass filter. This removes frequencies too high to be accurately transmitted in the FE grid. The forcing functions used in subsequent calculations differ from the seismogram shown in

Fig. 3 in that no instrument response has been applied. The instrument response is applied to the FE result.

DESIGNING FE GRIDS

The FE grids discussed in this section are designed to represent the two classes of transition models illustrated in Fig. 4. The difference between individual transition models within each class was L , the length of the transition region. Real ocean to continent type transitions occur over lengths of 50–300 km (Keen & Hyndman 1979; Hinz *et al.*, 1979; Eittrheim & Grantz 1979; Le Douaran, Burrus & Avedik 1984). However, for the present studies, an upper limit on L of 100 km was imposed by the computation limits discussed below. The lengths used for this investigation were a step transition ($L = 0$ km), $L = 25$, 50 and 100 km.

Results in this paper were generated using a Ridge computer at Caltech and a Convex C1 computer at the GSC. The largest FE calculation was allowed up to 48 cpu hours on the Ridge. Moving to a faster machine like the Convex or a supercomputer does not allow the increases in grid length that might be expected. As the path length in the grid increases, numerical dispersion becomes a more serious

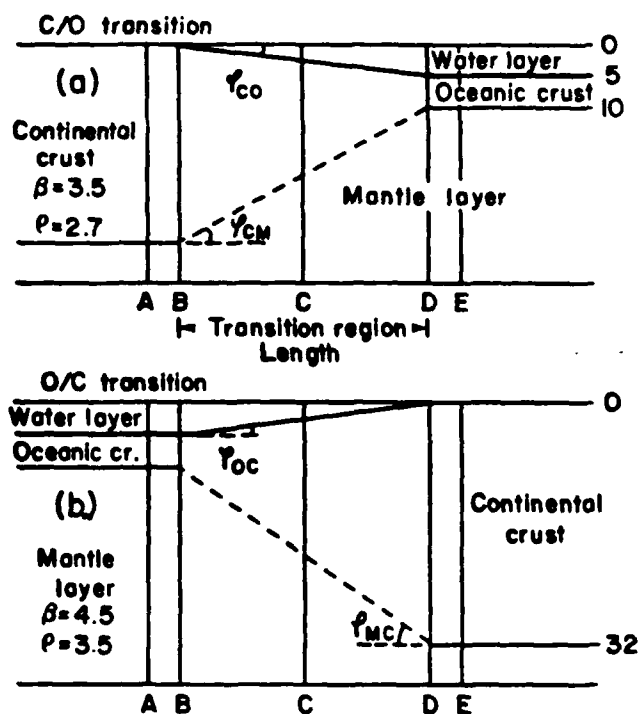


Figure 4. Explanation of terms and illustration of the model classes used to describe the behaviour on passage through a transition region. The heavy line between the water layer and the crustal layer is the surface. The sloping portion of this surface is the continent to ocean boundary (COB) for the C/O transition model and the ocean to continent boundary (OCB) for the O/C transition model. Similarly, the sloping dashed line between the crust and mantle layers is the crust to mantle boundary (CMB) for the C/O transition and the mantle to crust boundary (MCB) for the O/C case. The length of the transition, L , is the distance from B to D, B is referred to as the beginning of the transition, D as the end of the transition, C as the centre of the transition. A is 5 km from B, E is 5 km from D.

difficulty making decreases in grid spacing necessary. Also, the grid length grows 50 per cent faster than L . To obtain a significant increase in grid length a more accurate higher order FE or FD scheme would be advisable and double precision calculations might become necessary.

The first class of models used in this study describe continent to ocean transition regions. In further discussions these models will be referred to as C/O models, and the transitions they represent as C/O transitions. Similarly, the second class of models described ocean to continent transition regions, and will be referred to as O/C models. The transitions they represent will be referred to as O/C transitions. The continental reference model consists of a 32 km thick crustal layer over a half-space. The oceanic reference model consists of two 5 km layers, one water and one crust, over a half-space. Each C/O or O/C transition region is characterized by a continuous rate of thinning or thickening of the crustal layer. In all models the crustal layer has an SH wave velocity, of 3.5 km s^{-1} and a density of 2.7 g cc^{-1} , while the half-space has an SH wave velocity of 4.5 km s^{-1} and a density of 3.4 g cc^{-1} . Each class of transition models has the same boundary conditions (BCs) applied to each of its members. The forcing functions used to drive the C/O transition and continental reference FE

calculations are a vertical section of 60 mode sum seismograms, calculated at depth intervals of 0.5 km beginning at the surface, for a strike slip source at 8 km depth at a distance $X = 1500 \text{ km}$. The forcing functions for the O/C transition and oceanic reference tests are recorded during the 50 km C/O transition calculation. They consist of a depth section of hybrid seismograms recorded 25 km past the oceanic end of the 50 km C/O transition region, 1755 km from the source. The vertical spacing within the depth section is 0.5 km. All other BCs are identical for all models. The transmitting BC is applied to all edge nodes of the grid, excluding only the free surface and the nodes to which forcing functions are applied.

The first step in designing a grid for FE calculations is to determine grid spacing, dx , and the time step duration, dt . For computational efficiency it is important to maximize dx and dt . At least six nodes per wavelength (Frazier *et al.*, 1973) are needed to avoid numerical dispersion problems. To maintain numerical stability, the wavefront can travel no more than half the grid spacing per time step. Thus, dx and dt must be chosen to satisfy

$$dx \leq \frac{V_{\min}}{6f} \quad dt \leq \frac{dx}{2V_{\max}}$$

where f is the highest frequency in the waveform to be modelled and V_{\min} and V_{\max} are the minimum and maximum S velocities respectively in the dominant part of the model. In this study, we are considering L_s waves with a predominant period of approximately 1 s, in a medium with $V_{\min} = 3.5 \text{ km s}^{-1}$ and $V_{\max} = 4.5 \text{ km s}^{-1}$. Thus, we have chosen $dx = 0.5 \text{ km}$ and $dt = 0.05 \text{ s}$.

The next step in designing the grid is the determination of the dimensions of the grid, n_x and n_y , the duration of the input forcing functions, T_{in} , the duration of the calculated time series, T_{calc} , and the location of the transition region within the grid. The vertical column of nodes at which forcing functions are applied lie at the leftmost edge of the FE grid. This column of nodes at the grid edge appears as a rigid boundary to energy incident upon it from within the grid. The criteria below, used to choose the location of the transition region within the grid, are designed to avoid contamination from reflections from the leftmost grid edge. The location of the transition region within the grid is defined in terms of the distances from the leftmost grid edge to positions A, B, C, D, E, in Fig. 4. The values of these parameters were chosen to satisfy two criteria.

- A seismogram of duration D , seconds can be recorded at A (Fig. 4) before the multiple reflection of the input wave from the beginning of the transition, B, to the leftmost grid boundary and back again reaches A.
- A seismogram, uncontaminated by the multiple reflection, with duration D , seconds can be recorded at the receiver closest to the right-most edge of the grid. This receiver is defined to be at a distance x_r from the left-most grid edge.

Criteria A and B concern themselves only with reflections from the left-most edge of the grid. Non-physical reflections from the bottom and the right-most edge of the grid are removed using transparent BCs which will be discussed later. The BC cannot be applied at a node constrained by a

Table 1

model	nx # nodes	nz	nt # Δt	T_{max} s	A	B	C # nodes	D	E
0C/O	310	90	1921	96	230	240	240	240	250
25C/O	365	90	2101	105	240	250	275	300	310
50C/O	525	90	3101	155	350	360	410	460	470
100C/O	800	90	2441	122	250	260	260	460	470
00/C	350	90	2501	128	275	285	285	285	295
250/C	400	90	2501	125	275	285	310	335	345
500/C	450	90	2601	130	275	285	335	385	395
1000/C	525	90	2941	147	275	285	385	485	495
ref	330	90	3201	160					
ref	525	90	3201	160					

forcing function. The duration D , was chosen to be 55 s, the observed coda duration for a SH L_g mode sum seismogram at a distance of 1000 km from the source. For all the models used in this study the values of parameters defining the size of the grid and the location of the transition region within it are given in Table 1. Distances are given as the number of nodes in the horizontal direction from the left edge of the grid to the depth section or boundary indicated. The model names consist of a number that indicates L , then the model type. Reference layer over half-space models are indicated by ref.

SAMPLING FE SOLUTIONS

Analysis of the effects of various transitions on the waveforms and amplitudes of L_g waves using FE techniques requires that the motions of the nodes of the FE grid be sampled so that the progress of the L_g waves across the transition can be observed. Two methods of sampling are used in this study. Complete displacement time histories are recorded for selected nodes, and the displacements of all nodes in the grid are recorded at given time intervals. The first approach produces seismograms which can be used to illustrate variations of amplitude and waveform with distance or depth, the second approach produces time slices and is a clear way to illustrate the propagation and distortion of wavefronts caused by passage through the inhomogeneous structure. Time slices are self scaled so that successive time slices may show the same absolute amplitude as a different symbol size. Thus, the same region of the waveform will appear darker on a time slice with a given maximum amplitude than on another time slice with a larger maximum amplitude. This difference must be remembered when interpreting the time slices.

The amplitude of the first large positive and negative peaks in L_g mode sum seismograms (Fig. 3) are extremely sensitive to distance from the source and to the time spacing and starting time chosen when calculating the synthetics. It is not unusual for very small changes in these parameters to produce variations in amplitude of several per cent. An improved filtering technique would reduce the variation slightly by removing more of the sampling effects due to the non-zero spectral amplitude at the Nyquist frequency. However, a significant portion of the variation is apparently due to changes in the patterns of interference between multiple arrivals. In addition, the direct S pulse and the end of the S_n wavetrain arrive at the same time as the initial pulses in the L_g wavetrain. The longer period portions of the S and S_n arrivals have been removed by the bandpass filter. However, some non- L_g energy will be present in the

first few cycles of the trace. Unfortunately, the initial high frequency peaks, which are affected by the problems discussed above, yield the maximum peak to peak amplitude. This indicates that peak to peak amplitude will be a poor measure of the L_g amplitude. A more stable measure of amplitude correspondence between seismograms of this type is the rms amplitude calculated over some time window appropriate to the seismograms being compared:

$$\text{rms} = \sqrt{\frac{\sum_{n=1}^m [\text{amp}(n)^2]}{m}} \quad m = \frac{T_{\text{rms}}}{\Delta t}$$

where m is the number of points in a sampling window of duration T_{rms} seconds. Such an rms amplitude measure will reduce the effects of S or S_n contamination and of any other instabilities affecting the initial arrivals.

The evaluation of rms amplitudes is straightforward once the sampling window has been chosen. The location of the sampling window with respect to the arrivals of maximum amplitude, and the duration of the trace contained within the sampling window, have a significant effect on the value of the rms amplitude. Care must be taken to choose windows for two sets of results that produce meaningful comparisons. When results of two separate FE calculations are being compared, at corresponding nodes, both seismograms should begin at the same absolute time. When successive seismograms in a depth or distance section, from a single calculation, are being compared, the duration of the sampled portion of the trace with negligible amplitude that occurs before the first arrival must be constant. A general approach which does not require the use of theoretical travel times was chosen to determine windows in the latter case. The first and last point in the sampling window are selected by bracketing the portion of the seismogram with significant amplitude according to the following algorithm:

- (1) Set a cut-off value for the amplitude at some fraction of the maximum absolute value of amplitude in the seismogram (usually 0.01 or 0.05).
- (2) Let the sample at the location of the maximum absolute value be the first sample in each of two series. One series proceeds forward in time, the other backward. Scan each series until a subseries of samples n seconds in duration, all with amplitudes smaller than the cut-off amplitude, is found. The first point in each of these subseries defines an endpoint of the seismogram.

- (3) Calculate the rms amplitude for sampling windows with durations 15, 20, 25, ..., 85 s. If the duration of a sampling window exceeds the duration of the seismogram then no rms amplitude is determined.

This algorithm yields a series of rms amplitude values for the selected set of windows. If rms amplitudes of the data and the synthetics agree in all windows, and waveforms are similar the fit is considered to be excellent. When trends in rms amplitude are discussed, the longest window common to all seismograms being studied will be used. If rms amplitude trends change when window length is varied these changes will be discussed since examining the behaviour of the rms amplitude as a function of sample window length can give insight into the nature of and the underlying reasons for misfit between methods.

TESTS OF ACCURACY: SH L_g MODE SUM INPUT

The BCs are introduced to remove the non-physical reflections created by the artificial grid boundaries at the ends and bottom of the grid. Removing these reflections from the portions of the seismogram of interest by extending the grid requires an increase in execution time of between 30 and 500 per cent. As a comparison, the approximate BC used in this study increases execution time by 3–5 per cent. The BC used here was suggested by Frazier *et al.* (1973). The average of the rigid boundary and the free boundary displacements for each constrained node is calculated at each time step. For a normally incident plane wave this average exactly represents the transparent boundary. However in practice the incident wavefront is neither normally incident nor a plane wave. This means that the actual value at the transparent boundary is a linear combination of the rigid boundary and free boundary solutions whose coefficients depend upon the angle of incidence of the energy. The boundary condition used here assumes that the average of the two solutions will in most cases be the best approximation to the transparent boundary that can be simply implemented.

A series of tests were conducted to verify the accuracy of the coupling method and the efficiency of the transparent BCs. The tests used the continental reference model and a set of 90 forcing functions calculated for a strike slip point double couple source at a depth of 8 km and a distance $X = 1500$ km. Transparent BCs were applied to all grid boundaries except the free surface and the nodes to which forcing functions were applied.

The results of the accuracy and BC tests presented below are illustrated in Fig. 5. A continental reference structure is used for both the FE and PM portions of the path. This allows the direct comparison of the hybrid solutions and the

direct analytical synthetics calculated entirely with the PM technique. Four separate calculations were performed. First, L_g mode sum direct analytical seismograms for the same source used to generate the C/O transition forcing functions were calculated. Next, seismograms were generated using the hybrid method in a grid long enough (100×50 km) to prevent contamination from end reflections. Third, seismograms were generated using the hybrid method and a short (50×50 km) grid with the transparent BC applied at each node on its right-most edge. Finally, the previous FE calculation was repeated without the transparent BCs. The excellent agreement between the analytical and hybrid synthetics verifies the validity of the coupling method applied to a layered half-space. Small discrepancies are seen in the higher frequency component, particularly in the first 20 s of the trace. In the last trace of each group in Fig. 5 the single and multiple reflections from the grid edge are clear. Comparison of the long grid and the short grid with and without BCs shows that most of the reflected amplitude has been removed by the BCs. The misfit is lower for the longer period component of the traces. The significant misfit is coincident with reflections, and is largest for the multiple reflections. Despite visible differences in waveform the seismograms shown in Fig. 5 have rms amplitudes that agree to within less than 2 per cent for all rms window lengths. This indicates that small changes in waveform may be expected but the rms amplitudes of the seismograms should be stable and not significantly contaminated by incompletely removed reflections from the grid edges. The increased discrepancies in both waveform and amplitude introduced by the multiple reflections will be avoided in the transition FE grids described below. This reduces the discrepancies in rms amplitude to less than 1 per cent.

Reflections from the bottom edge of the grid should also be considered. The transparent BC can be very ineffective for the small angles of incidence seen at the grid bottom

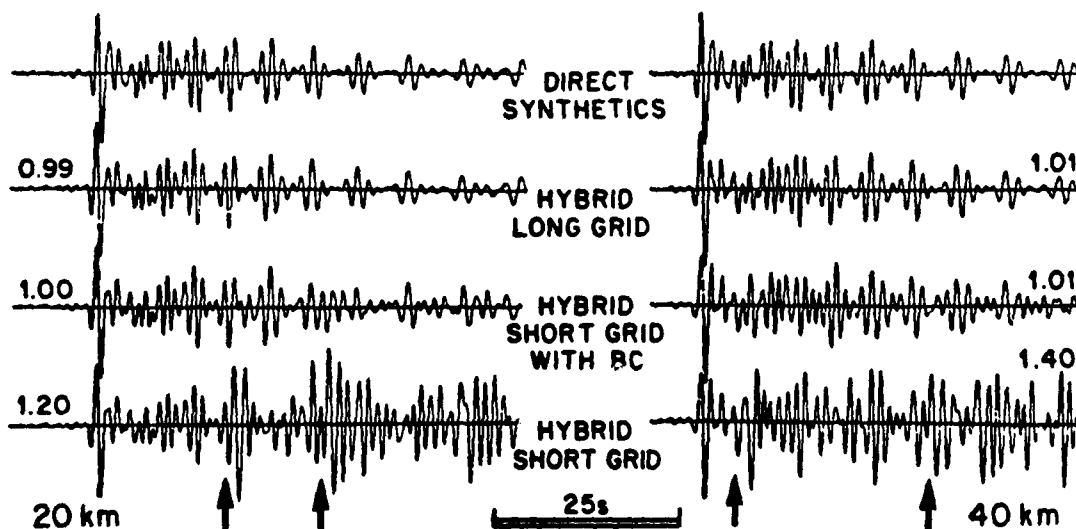


Figure 5. Seismograms recorded at the surface for $X2 = 1520$ and 1540 km. The first seismogram in each group is a direct synthetic, the second is a hybrid synthetic determined using the long grid (200×100), the third and fourth are hybrid synthetics determined using a short (100×100) grid with and without the transparent BC, respectively. When the boundary condition is applied it is applied only at the right-hand edge of the grid. The number beside each of the hybrid synthetics is the rms amplitude ratio between that hybrid seismogram and the direct synthetic. Seismograms have been bandpass filtered between 0.01 and 1 Hz and have been convolved with the short period WSSN instrument response. Arrival times of the single and multiple reflections are indicated by the arrows below each group of seismograms.

when a distant source is considered (Regan 1987). Fortunately, in a layered half-space, where L_g waves can be modelled as the superposition of multiply reflected post-critical SH waves in the crust, most of the energy in the SH type L_g waves should be trapped in the crustal layer. The time slices discussed later (Figs 6, 12) show that the SH type L_g waves propagating in a layer over a half-space are, in the most part, confined within the layer; rms amplitudes agree to within less than 0.1 per cent with and without the transparent BCs (Regan 1987). However, the purpose of the present study is to examine the effects of continental-oceanic boundaries on the transmission of L_g mode sum seismograms. When the crustal layer is thinned or thickened with distance, the modes are no longer completely trapped within the layer. Energy can be converted to modes compatible with the local layer thickness and to other forms including body waves that can propagate into the half-space. When the wavefield reaches the second layered structure, modes not trapped within the new crustal layer will leak out of the layer, rapidly at first, then at a steadily decreasing rate. This implies that wide angle reflections of energy escaping from the crustal layer towards the bottom boundary of the grid could possibly contaminate transition calculation results. However, the model grids do not extend far enough, in the x direction, beyond the transition for this to be a problem. The energy will encounter the rightmost end of the grid, either on the downgoing or the upgoing portion of its path, rather than reaching a receiver at or near the surface as a wide angle reflection. Since a wavefront which has a small angle of incidence with the bottom boundary has a large angle of incidence with respect to the end boundary, most of the amplitude of the wavefront incident on the right-most end boundary will be transmitted rather than reflected. Therefore, it is removed from the grid. Careful grid design will prevent significant contamination from wide angle bottom reflections.

CHANGES TO L_g WAVETRAINS ON PASSAGE THROUGH A C/O TRANSITION AND THEIR DEPENDENCE ON L

When a wavefield consisting of SH L_g mode sum energy passes through a C/O transition region such as that illustrated in Fig. 4(a) several important things happen. In order to clearly explain these effects and their variation with L one must think of the wavefield in terms of an incident wavefield, a reflected wavefield, and a transmitted wavefield. The transmitted wavefield is then subdivided into four subcomponents which will be useful in explaining the observed results. The entire wavefield, or any of its components or subcomponents can be interpreted as either a sum of modes or a sum of multiply reflected SH rays. To allow a clear definition of each of these components and subcomponents in terms of the ray interpretation the diagrams in Fig. 6 are critical.

Before each of the three components are defined the notation used in Fig. 6 must be explained. ϕ_{cm} is the angle between the base of the continental crust and the bottom boundary of the crustal layer in the transition region. ϕ_{oc} is the angle between the upper boundary of the crustal layer and the surface at $z=0$. The incident angle and the angle of reflection for the n th interaction of a ray with a

boundary (crust-mantle boundary, CMB, or crust-ocean boundary, COB) within the transition will be denoted j_n . Similarly, the transmission angle for the n th interaction of a ray with a boundary, will be denoted j'_n . As long as the ray remains in the transition region, $j_n = i - n(\phi_{c1} + \phi_{c2}) + \phi_{c2}$, where $\phi_{c1} = \phi_{oc}$ and $\phi_{c2} = \phi_{cm}$ if the first interaction is with the COB, and $\phi_{c1} = \phi_{cm}$ and $\phi_{c2} = \phi_{oc}$ if the first interaction is with the CMB. The angle of incidence is j_{oc} for rays transmitted into the oceanic crustal layer, and j_{oon} for rays reflected back into the continental crustal layer. When the first reflection of the ray exiting the transition region, from the upper or lower boundary of either the continental or oceanic crustal layer, is the n th reflection then $j_{oon} = j_{oc} = j_n + \phi_{oc}$, or $j_{oon} \times j_{oc} = j_n + \phi_{cm}$, respectively.

The incident wavefield is composed of the trapped modal SH L_g energy arriving from the source, and is complete and untransformed only in the region of continental structure. If the incident wavefield within the continental structure is viewed as a superposition of multiply reflected post-critical SH rays with a range of incident angles, its components can be followed into the transition region. As the wavefield passes through the transition region the rays of which it is composed may each interact with the COB or the CMB. Each time a ray interacts with a boundary its incident angle j_n is reduced. A ray remains a component of the incident wavefield until an interaction with a boundary causes j_n to become negative and the ray to be turned back towards the source. Thus, the incident wavefield within the transition region is defined to be the superposition of all rays travelling towards the region of oceanic structure. A few sample rays of an incident wavefield are shown in Fig. 6(a). All rays within the crustal layer of the transition region, shown as solid lines, are part of the incident wavefield.

The reflected wavefield is composed of all the SH rays which have been turned back towards the source by their interaction with the CMB and the COB. Thus the reflected wavefield is a superposition of rays for which j_n has become <0 for some previous interaction with a boundary. An example of such rays can be seen in Fig. 6(a). The rays which are part of the reflected wavefield are shown as dotted lines within the crustal layer of the transition region. The reflected wavefield travels sourcewards through the crustal layer of the transition region, and the region of continental structure. In the region of continental structure the reflected wavefield can also be conceived of as a superposition of trapped and leading modes reflected from the transition region.

The transmitted wavefield is composed of all the energy transmitted through the transition region into the crustal layer of the region of oceanic structure, and all the energy transmitted into the mantle layer. The transmitted wavefield is divided into four components, two in the mantle layer, one in the crustal layer, and one in both layers in the region of oceanic structure. These components are all easily explained in terms of the SH ray interpretation. The two components within the mantle layer are the forward transmitted wavefield and the reverse transmitted wavefield. Only energy crossing the CMB into the mantle layer is included in these components. The forward transmitted wavefield is the portion of the incident wavefield which is transmitted across the CMB into the mantle layer when the rays forming the incident wavefield (rays with $j_n > 0$)

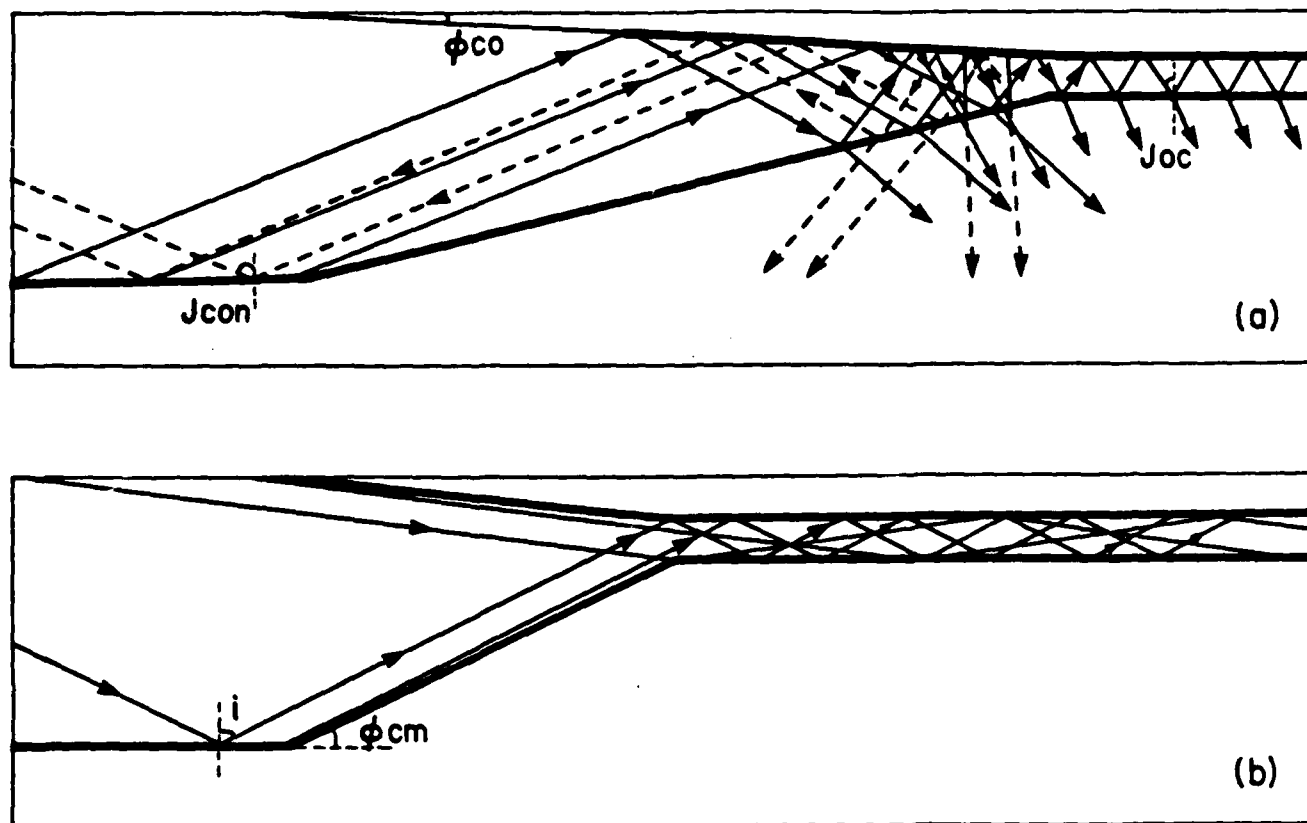


Figure 6. Definition of the components of the wavefield in terms of the ray interpretation. (a) shows examples of types of rays which constitute the incident wavefield (solid rays in the crustal layer), the reflected wavefield (dotted rays in the crustal layer), the forward transmitted wavefield (solid rays in the mantle layer), and the reverse transmitted wavefield (dotted rays in the mantle layer), within the transition region. (a) also shows an example of a type of ray which constitutes the transformed transmitted wavefield (solid ray transmitted through the transition into the crustal layer in the region of oceanic structure). Energy from the illustrated ray leaks into the mantle layer in the region of oceanic structure. Rays with post-critical angles of reflection in the crustal layer of the oceanic structure are produced similarly, and also constitute components of the transformed transmitted wavefield. (b) shows the types of rays which constitute the direct transmitted wavefield. All such rays travel through the transition region without interacting with the CMB or the COB.

interact with the CMB. All rays, shown as solid lines in the mantle layer of the transition region of Fig. 6(a), are components of a forward transmitted wavefield. The forward transmitted wavefield is present in the transition region and may propagate into the region of oceanic structure. The reverse transmitted wavefield is the portion of the reflected wavefield which crosses the CMB into the mantle layer when the rays which form the reflected wavefield (rays with $j_n < 0$) interact with the CMB. The reverse transmitted wavefield is present in the transition region and may propagate into the region of continental structure. Fig. 6(a) shows rays which form part of a reverse transmitted wavefield as dotted lines within the mantle layer of the transition region. The directly transmitted wavefield is a superposition of the SH rays in the incident wavefield that pass through the crustal layer of the transition region and into the crustal layer of the region of oceanic structure without interacting with the CMB or the COB. The rays are then trapped in the oceanic crustal layer. Some rays from a directly transmitted wavefield are illustrated in Fig. 6(b). The transformed transmitted wavefield is present only in the region of oceanic structure. It is composed of a superposition of rays which have interacted with the CMB

and/or COB one or more times as they propagated through the transition region into the oceanic crust. These rays have values of $j_n > 0$ for their last interaction with the CMB and/or the COB in the transition region. The values of j_{oc} for these rays are appropriate for both pre-critical and post-critical reflections. Pre-critical reflections are equivalent to leaking modes. Energy from these modes is visible as amplitudes in the crustal layer and in the mantle layer. As the transformed transmitted wavefield propagates through the oceanic structure energy from these modes escapes the oceanic crust and propagates in the mantle layer. Post-critical reflections correspond to trapped modes and continue to propagate through the oceanic crustal layer.

All models used in this portion of this study have crustal SH velocity of 3.5 km s^{-1} , crustal density of 2.7 g cm^{-3} , mantle SH velocity of 4.5 km s^{-1} and mantle density of 3.5 g cm^{-3} . All FE grids have the transmitting BC applied to all grid edges excepting the free surface and the surface on which the forcing functions are applied. All calculations use the same set of 60 forcing functions determined for a strike slip source at a depth of 8 km, a distance of 1500 km from the grid edge. Each of the components of the wavefield discussed above will be illustrated in the time slices or

seismograms for the 25 km C/O transition region. These time slices and seismograms are presented as an example of the general transmission properties of simple transition regions. The variation of such transmission properties with L will also be illustrated. The observed properties and their variations with L will then be explained.

A series of time slices for the 25 km C/O transition is shown in Fig. 7. In the first time slice the displacements entering the grid as dark, almost vertical bars are those which produce the largest peak to peak amplitudes in the seismograms. The second time slice shows the same high frequency arrivals after they have propagated about halfway through the transition region. The maximum amplitudes seen within the transition region of the third time slice are almost twice those seen in the unperturbed layer over a half-space wavefield seen in the first two time slices. So, the plotted amplitudes of all the displacements in the third time slice have been significantly reduced by scaling, making the same disturbances appear smaller. In the fourth time slice the highest amplitude regions of the wavefield have propagated past the right-most edge of the grid. The maximum amplitude is much smaller so the same disturbances appear to have much larger amplitudes. The fifth time slice shows a further amplification of the amplitude of the disturbances due to scaling. The amplification helps make the highest amplitude portion of the reflected wavefield (<5 per cent of incident amplitude) visible as a series of broken vertical bars near the left-most end of the grid. All sections of the incident wavefield show triangular regions of maximum amplitude. The extent of each triangular region, in the x direction, increases for regions of the wavefield incident on the left end of the grid at a later time. The end of the incident wavefield is seen, in the fifth time slice, about midway between the left grid edge and the arrow, to the right of the visible reflected component. The C/O transmitted wavefield is visible in the last three time slices as disturbances travelling through the half-space from the CMB towards the right-most edge of the grid. The reverse transmitted wavefield is clearly visible in the fifth time slice, and present in the last three time slices, as disturbances travelling through the half-space from the CMB towards the grid bottom and the source. For the earliest disturbances in the half-space the forward transmitted wavefield propagates along a path approximately parallel to the crust-mantle interface in the oceanic region, and the reverse transmitted wavefield propagates along paths nearly parallel to the CMB. As time progresses, the propagation paths of both the forward and reverse transmitted wavefields approach the normal to the CMB. Energy escaping from the through the oceanic crustal layer forms a forward bending arc of higher amplitudes in the mantle half-space. As the high amplitude regions of the forward transmitted wavefield propagate longer distances or propagate along paths with larger vertical components, the tails forming due to leakage from the oceanic crustal layer detach from the forward transmitted wavefield.

Figure 8 shows seismograms recorded at the receivers along a surface section. These seismograms illustrate the magnitude of the concentration of amplitude at the surface of the crust seen in the time slices, and the change in the waveforms as the wavefield passes through the transition. Fig. 9(a) shows the variation of 60 s rms amplitude with

distance, $X/2$, from the source for each of the C/O transition FE calculations. Amplitudes produced using the different C/O transition lengths are plotted at the same scale and are proportional to the source strength. The numerical values of amplitude shown on the amplitude axis are chosen so that the maximum value on the axis is one. To avoid blank spaces in the plots the minimum value was not chosen to be zero. The amplitudes recorded at nodes along the surface of the crustal layer within each transition region show a general increase as one moves from B towards D. The duration of the coda with amplitudes above one-third of the maximum peak to peak amplitude is also increasing. This increase in coda length supports the attribution of the later portions of the observed coda to diffraction and reflection from crustal structure. The size of the increase in rms amplitude is smallest for the step transition and increases as L increases. Superimposed on the general increase is an oscillatory term. The method of scaling the distance coordinate within the transition region, in Fig. 9, makes the coincidence of maxima and minima at approximately the same fraction of the transition length for all L 's considered very clear. Increases in amplitude before reaching distance B are due to energy reflected from the transition boundaries back towards the source. The amplitude increase near B is largest for a step transition and decreases as L increases. The fluctuations in amplitude following the transition region show that the wavefield has not completely adjusted to the oceanic structure in the few kilometres beyond the transition regions illustrated in this figure.

Figure 10 shows seismograms recorded on depth sections at distances B and D. Fig. 11 shows the variation of 55 s rms amplitude with depth at several distances. The seismograms shown in Fig. 10(b) are recorded at the depth of the surface of the oceanic crustal layer. They show a 50 per cent increase in amplitude as the energy travels from B to D. They also show that the amplitude of the coda becomes a larger portion of the maximum peak to peak amplitude, that is the envelope of the coda decays more slowly at D than at B. An increase in rms amplitude (20 per cent) and a slower coda decay is also seen if the free surface seismograms at B (Fig. 10a) and D (Fig. 10b) are compared. The seismograms recorded at the nodes at the depth of the bottom of the oceanic crustal layer (Fig. 10c) show a small decrease in rms amplitude across the transition. Comparing Fig. 11(b) and (d) the increase at the surface of the oceanic crust and the decrease at the base of the oceanic crust are clear for all transition lengths. Examination of seismograms at the nodes at distances B and D with depths between Fig. 10(b) and (c) shows that the amplitude increase between B and D is largest at the surface of the crust and decreases rapidly towards the base of the crust. This statement is supported by the amplitudes illustrated within the crust in Figs 11(b) and (d). These amplitudes in Fig. 11 form a summary subset of many measurements. Comparison of the seismograms at B and D in Figs 10(d) and (e) show that the amplitudes of the seismograms at depths below the base of the oceanic crust are decreased by passage through the transition region, from B to D. The transmitted waveforms are similar to the incident waveforms. The reduction in transmitted amplitude increases as depth increases. The latter observation is more obvious when the amplitude versus depth plots in Figs 11(b) and (d) are compared. Figs 11(a) and (b) shows that small

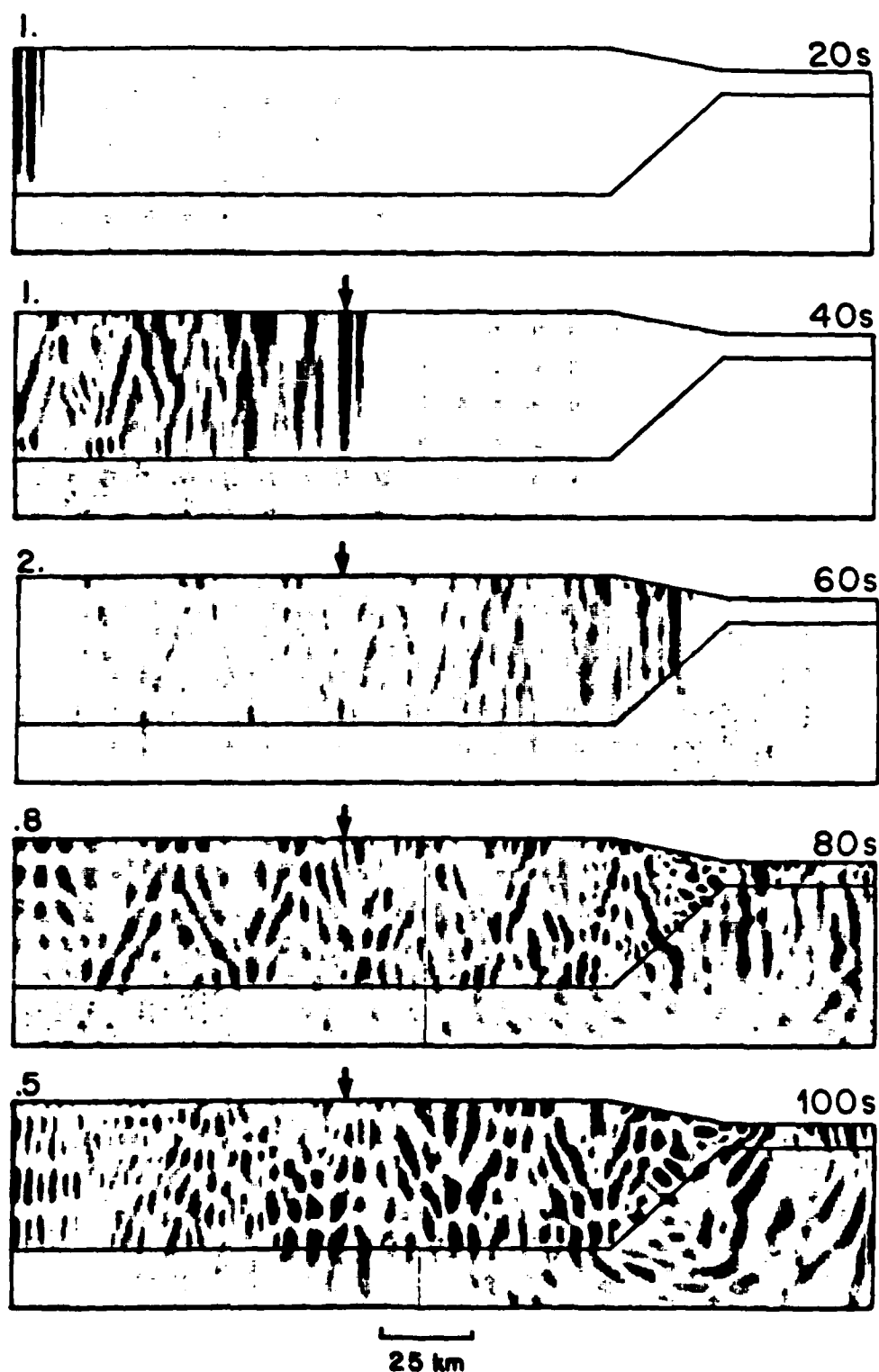


Figure 7. Time slices recorded during the 25 km C/O transition calculation. The crustal layer and the ends and bottom of the FE grid which contain it are outlined. Displacements are graphically represented by symbols plotted at an array of points depicting the nodes in the FE grid. The size of the symbol plotted at the node is increased as the absolute value of the displacement increases, producing darker areas where larger displacements are occurring. Each of the time slices is self scaled, that is the largest value of the absolute value of amplitude in the grid is set to the largest symbol size. A minimum amplitude cut-off of 2 per cent is defined below which no symbol is plotted. Sixty forcing functions were used. The time since the initiation of the FE calculation is shown above the right end of each grid. The arrow above a time slice shows the location to which the disturbances moving at 3.5 km s^{-1} , seen at the left end of the previous time slice, have moved in the intervening duration. The number above and to the left of each time slice is the scaling factor to bring that time slice to the same amplitude as the first time slice.

SH L_g waves in and near continental margins

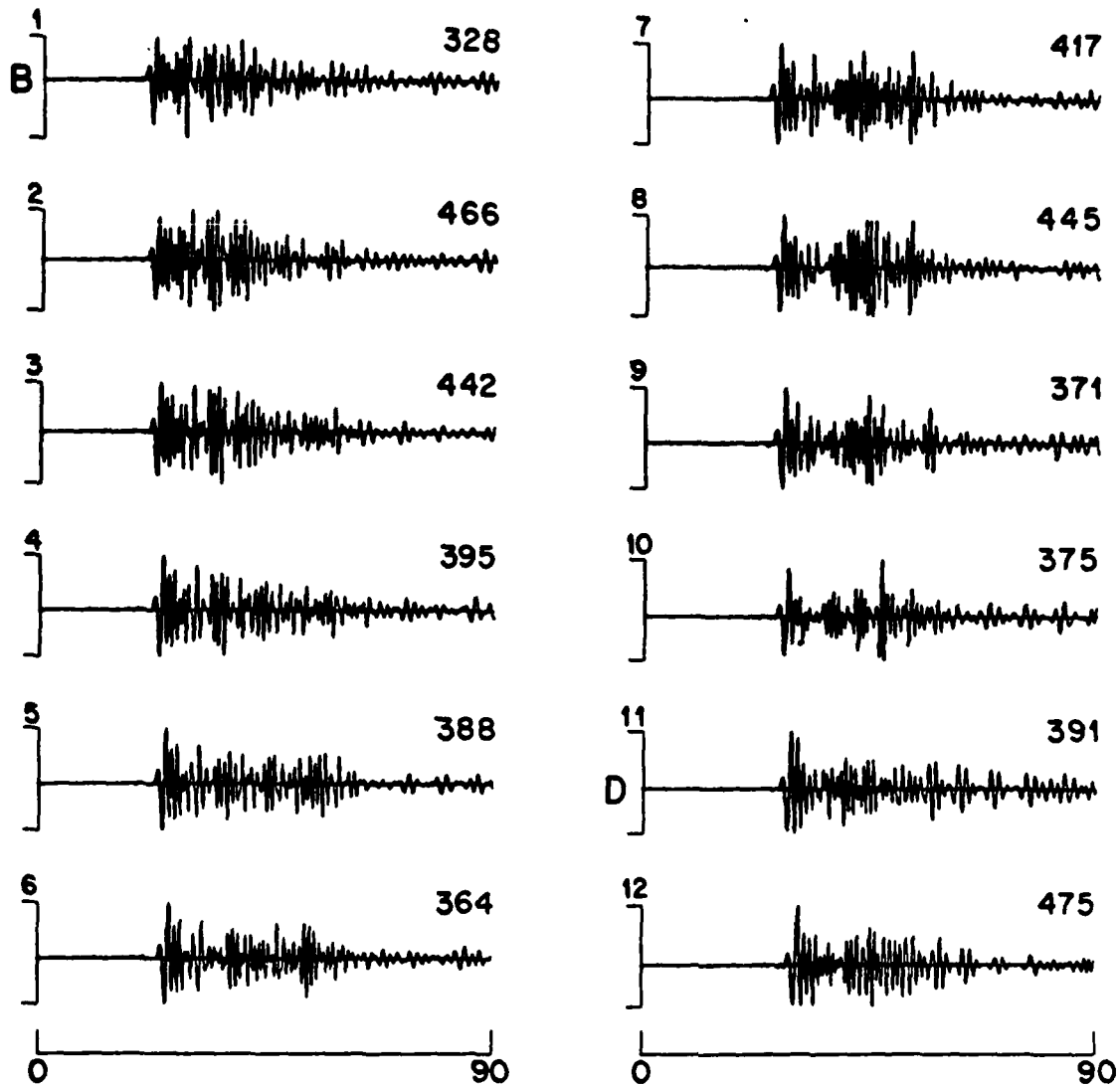


Figure 8. Surface section of seismograms recorded for a 25 km C/O transition calculation. The numbers to the left of each seismogram indicate the location of the node at which that seismogram is recorded. Seismogram 1 was recorded at B, seismogram 11 at D. The numbers increase as one moves farther from the source. The spacing between receivers in the transition zone is uniform. The numbers above the right end of each seismogram give the 60 s, rms amplitude of that seismogram.

amplitudes are seen at depths below the continental crustal layer. A large discontinuity in amplitude occurs at the base of the continental crust. Fig. 11(c) shows that this discontinuity remains at the depth of the base of the crustal layer within the transition region. Fig. 11(c) also shows that the amplitudes in the mantle layer within the transition region are maximum immediately below the CMB, and decay rapidly with depth below that boundary. Fig. 11(d) shows that the amplitude of the transmitted seismograms, in the mantle layer above the depth of the base of the continental crust, at D, decreases as L increases. Below the depth of the base of the continental crust amplitudes at D increase as L increases. At distances E and F (Figs 11e and f), further from the transition region, the magnitudes of these trends decrease. These observations are further support for the observation that as L increases larger energies are transmitted across the CMB and that these energies propagate downwards more rapidly.

The triangular pattern of maximum amplitudes in the wavefields (Fig. 7) can easily be explained. Consider the SH L_g energy in the crustal layer as a superposition of post-critically reflected multiple SH wave reflections. The critical angle is about 51° . Since the wavefront is perpendicular to the ray, the wavefronts that are visible as the triangular regions of maximum amplitudes should show angles of incidence with the bottom boundary of the crustal layer of between 0° and 39° . These are indeed the incident angles the wavefronts in the time slices (Fig. 7) are observed to exhibit. Near the front of the wavefield the dominant angles of incidence are near 0° , that is the regions of maximum amplitude are almost vertical. Later in the wavefield the dominant angles of incidence increase causing the widening triangular patterns of maximum amplitude. The increase in width of the triangular regions corresponds to a decrease in group velocity which can be translated to a decrease in period and/or a larger contribution from higher

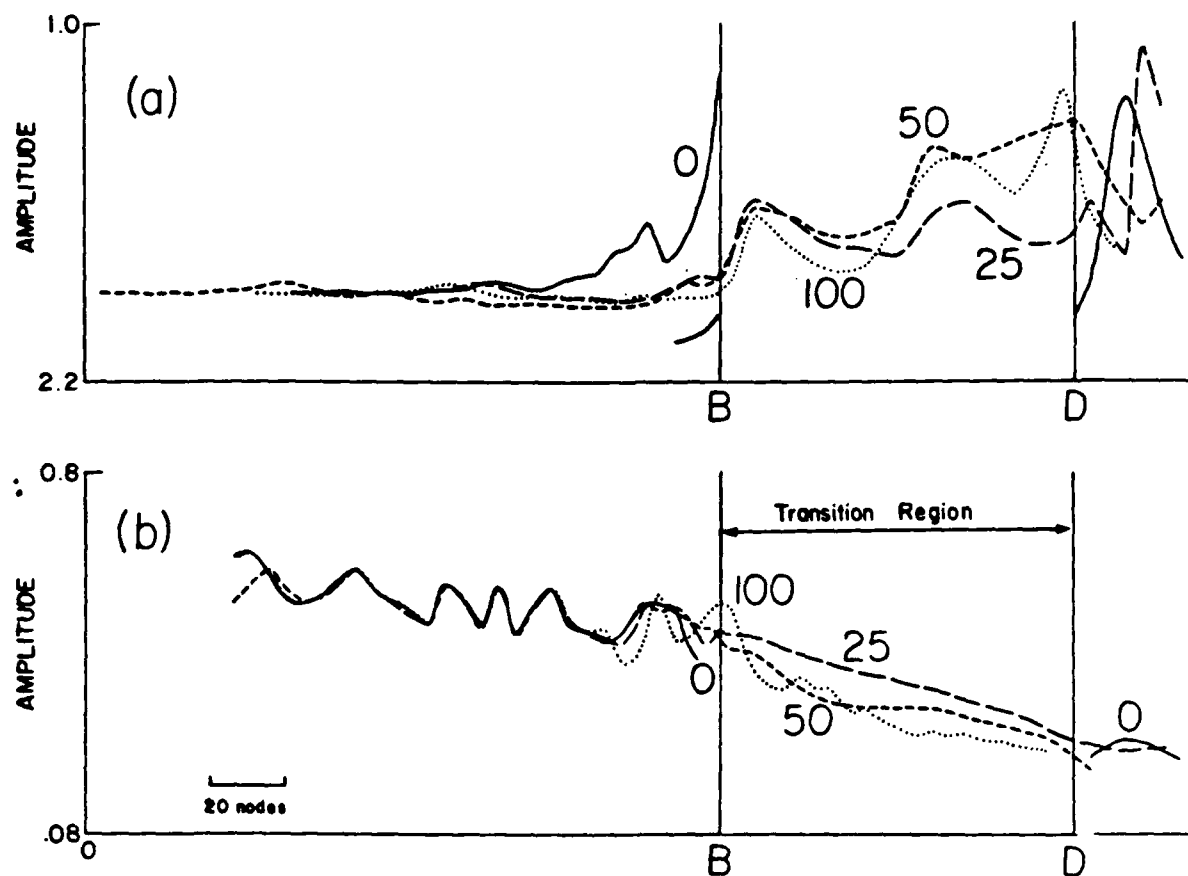


Figure 9. Variation in rms surface amplitude with distance, X_2 , from the source for (a) each C/O transition calculation (60 s rms), and for (b) each O/C transition calculation (50 s rms); rms amplitude is the y coordinate. The two vertical lines labelled B and D, indicate the limits of the transition region. Outside the transition region the scale is uniform. The distance scale (x coordinate) in the transition region is different for each L . Within the transition region all distances are plotted with respect to an origin at B, as fractions of L . Each line, labelled with the L it represents, was generated using rms measurements at intervals of 5 km along the crustal surface.

modes. The later parts of the seismogram are predominantly higher mode energy.

The growth in amplitude for seismograms at crustal surface nodes as distances range from B to D can be explained in terms of energy concentrated in the thinning crustal layer of the transition region. As j_n decreases toward zero for successive n 's, the reflection points at the boundaries in a transition region are separated by smaller horizontal distances (Fig. 6a). This implies that the density of rays will increase as the crustal layer thins, thereby producing higher amplitudes. An equal concentration would be expected at the CMB if no energy was transmitted across that boundary. In fact, for a model with the same geometry but with the mantle half-space replaced by water to disallow transmission across the CMB, an amplification of 75 per cent is observed at both boundaries. However for continent ocean boundary models, as j_n and thus, j'_n , decrease the displacement transmission coefficient,

$$T_n(j_n) = \frac{2 \cos(j_n)}{\cos(j_n) + 1.62 \cos(j'_n)},$$

increases. When more energy is concentrated at the CMB more energy is transmitted across it. The escape of energy from the crustal layer to form the transmitted wavefield also

explains the distribution of amplitude with depth within the crustal layer of the transition. The amount of concentration of amplitude increases as the distance from the CMB increases and the effects of the energy escaping across it become weaker.

Extending the above arguments explains the increase in the amount of concentrated energy, the increase in the magnitude of the transmitted wavefield, and the decrease in the amplitude of the reflected wavefield as L increases. Figs 12(a) and (b) show a pair of ray diagrams for a 25 km C/O transition region, Figs 12(c) and (d) shows a similar pair of ray diagrams for a 100 km C/O transition. These diagrams are useful when explaining the trends observed in the results presented above, and their dependence on L . Comparing Figs 12(a) and (c) or (b) and (d) shows that as L increases the angles ϕ_{m1} and ϕ_{m2} decrease causing j_n to decrease more slowly and allowing the number of reflections, m , within a transition to increase. When L increases, the increase in m causes an increase in ray density and explains the increase in concentrated amplitude at the COB. When L increases, by the same arguments, the amount of energy concentrated at the CMB also increases. The transmission of this energy across the CMB causes the amplitude of the transmitted wavefield to increase as L increases. It should be noted that increasing L reduces the rate at which the

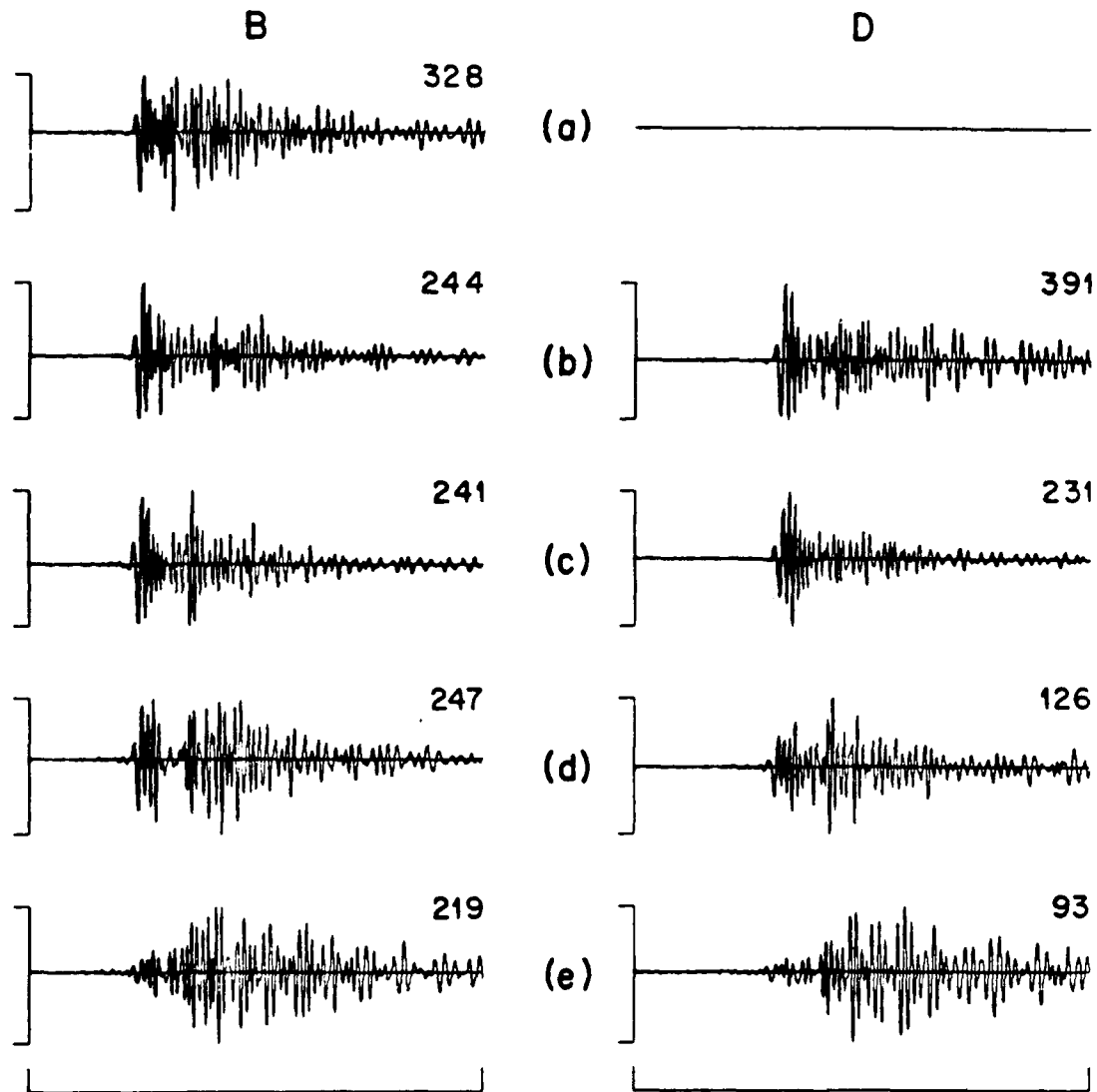


Figure 10. Depth sections of seismograms recorded at B and D for a 25 km C/O transition calculation. The numbers above the right end of each seismogram show the 60 s rms amplitude. Successive rows show pairs of receivers at increasing depths. (a) shows receivers at the depth of the surface of the continental crust, (b) shows receivers at the depth of the surface of the oceanic crust, (c) shows receivers at the depth of the base of the oceanic crust, (d) shows receivers midway between (c) and (e), (e) shows receivers at the depth of the base of the continental crust.

crustal thickness changes, so at a given distance from the beginning of a transition region the change in amplitude transmitted across the CMB per unit horizontal distance becomes smaller as L increases. However, integrated over the entire length of the transition region the amount of energy transmitted across the CMB increases. Since the amount of amplitude concentrated at the COB and thus transmitted into the oceanic crustal layer, and the amount of energy concentrated at the CMB and thus transmitted across the CMB both increase as L increases the amplitude of the reflected wavefield must decrease as L increases. Let seismogram A be a hybrid seismogram recorded on depth section A (Fig. 4) in a C/O transition calculation. Let seismogram B be the hybrid seismogram, recorded during the continental reference calculation, at the same depth and distance from the source as seismogram A. The reflected component is measured by analysing the component which remains when seismogram B is subtracted from seismogram

A. Reflected amplitudes measured in this manner show a clear decrease as L increases.

Figure 12 can be used to explain how and why the direction of propagation of the forward and reverse transmitted wavefields varies as time progresses. When the arrivals of the highest group velocity reach the CMB the resulting forward transmitted wavefield travels along a path approximately parallel to the crust half-space interface in the oceanic structure, and the resulting reverse transmitted wavefield travels along a path almost parallel to CMB. The incident angles j_n are maximum. As $|j_n|$ for a given n , and the group velocity, decrease the values of j'_n decrease. Thus, the propagation direction of both transmitted wavefields approach the normal to the CMB. As L increases larger values of n are possible within the transition region. For each value of n a transmitted wavefield is created at the CMB. Therefore, the range of propagation directions seen at a given time increases as L increases.

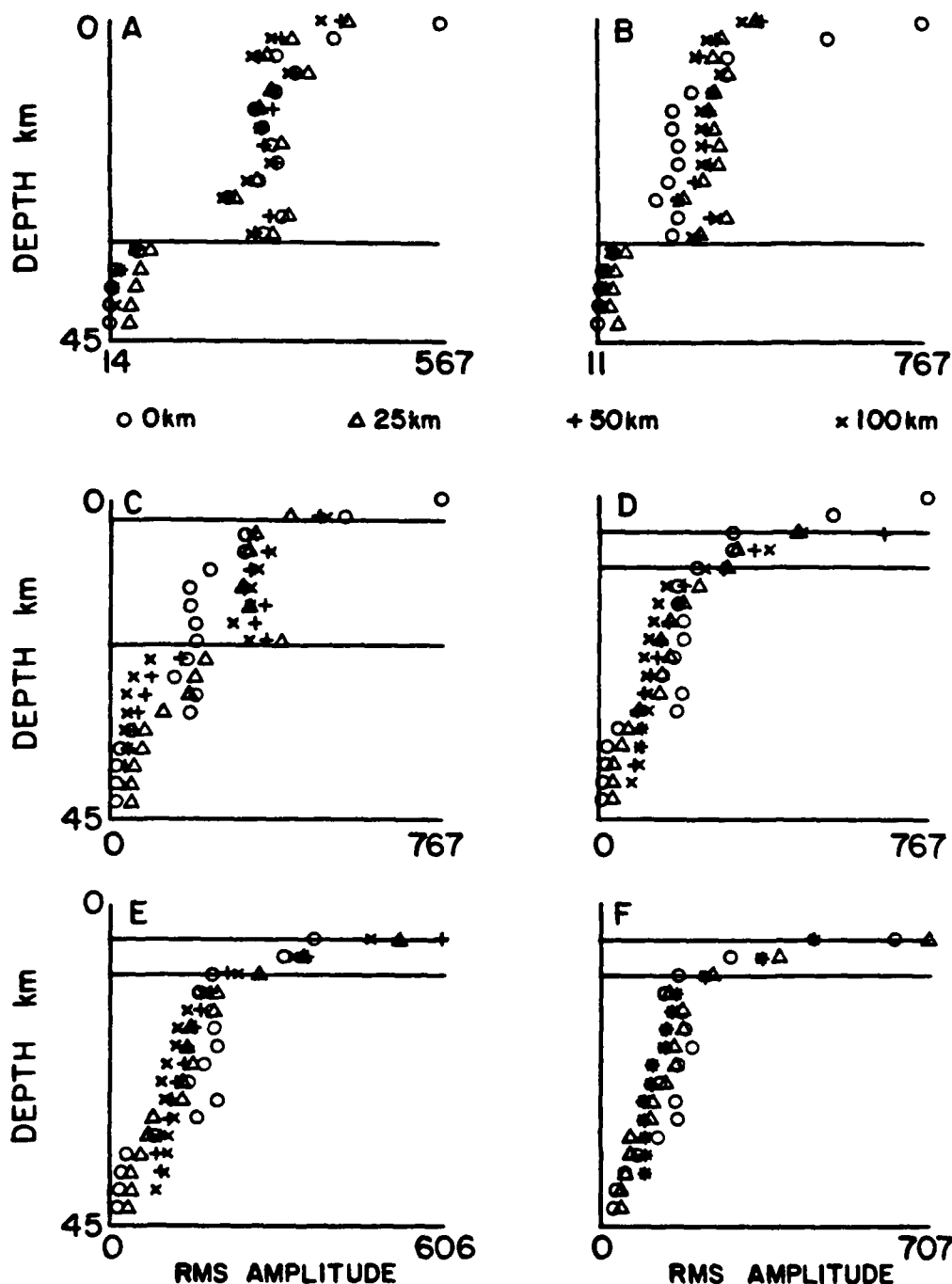


Figure 11. Variation of 55 s rms amplitude with depth on depth sections A, B, C, D, E, of Fig. 4, and F, located 10 km beyond E, for each C/O transition model. Each plot illustrates results for one depth section. The letter at the upper left of each plot identifies the location of the depth section. Amplitudes for the surface mode and nodes equally spaced down the depth section ($\Delta z = 2.5$ km) are shown. The two solid horizontal lines on each diagram show the base and top of the crustal layer at the location of the depth section. If only one solid line is present then it indicates the base of the crust. In this case the surface of the crust is at the top of the vertical axis.

The magnitude variations of the directly transmitted wavefield and the transformed transmitted wavefield can also be easily explained. Let the thickness of the oceanic crust be T_{oc} , and the thickness of the continental crust be T_{con} . For reflections immediately preceding the beginning of the transition region some rays ($i > 90 - \arctan[(T_{con} - T_{oc})/L]$) can propagate through the transition region without interacting with either the CMB or the COB. These

rays, which form the directly transmitted wavefield, continue to bounce with the same post-critical angles of incidence at the crust-mantle interface and the free surface as they did in the continental structure. They represent the energy transmitted through the transition directly, without changes in period or phase velocity. For these rays no mode conversion has occurred and no energy has been converted to other phases. These rays form the unchanged components

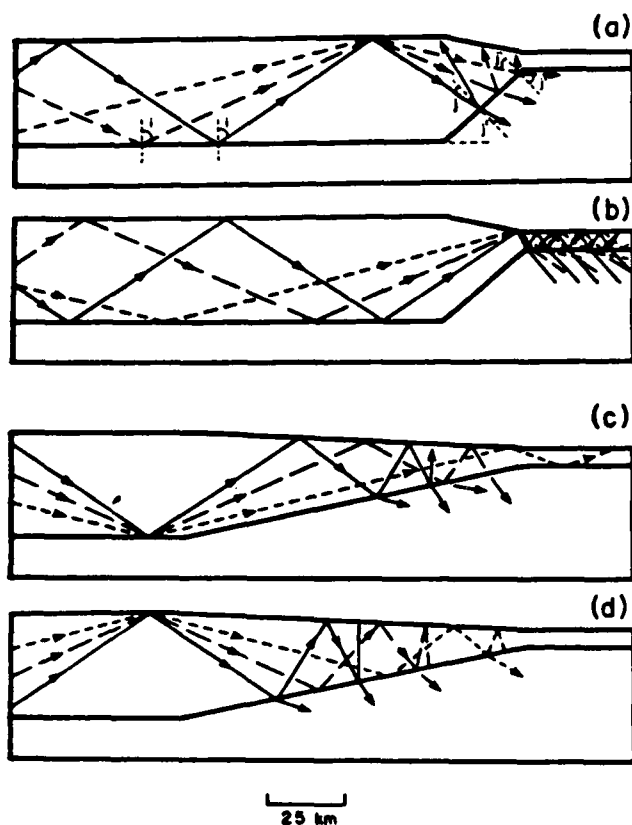


Figure 12. Illustration of ray paths within a 25 and a 100 km C/O transition structure. Diagrams are drawn to scale. Each diagram shows rays with angles of incidence, i , 55° , 65° , and 75° , at the free surface and crust-mantle interface in the continental portion of the model. These angles sample the possible range of post-critical incident angles ($>51^\circ$). The incident angle, j_n , and the transmission angle, j'_n , at the crustal boundaries in the transition regions are labelled. The upper diagram in each pair shows propagation paths for rays that encounter the CMB before the COB. The lower diagram shows propagation paths for rays that encounter the COB before the CMB. The arrows indicate the direction of propagation of the wavefront along the ray.

of the eigenfunctions defining each mode. The range of angles, i , over which the direct transmission occurs decreases as L increases. Thus, more unconverted energy is transmitted through shorter transitions. In contrast, the transformed transmitted wavefield is composed of rays which interact with the CMB or COB before being transmitted into the oceanic crustal layer. Such rays show changes in group velocity that indicate modal conversions are occurring. Energy is also converted into other phases as it escapes across the CMB to become part of the forward transmitted wavefield. As discussed above, the energies transmitted into the oceanic crustal layer and across the CMB both increase as L increases. As L increases, this increased transmitted energy is partially counteracted by the effects of decreased transmission of unconverted energy. This helps explain why the differences due to L are small.

The diagrams in Fig. 12 demonstrate why energy crosses the crust-mantle interface in the oceanic structure following the transition, why this transmitted energy is maximum near the transition and decreases as the distance from the

transition increases, and why this transmitted energy increases as L decreases. The paths illustrated in the second 25 km transition outline show one-way modes which are not of appropriate frequencies to be trapped within the oceanic crustal layer, enter that layer. Analogous paths for rays which interact first with the CMB or rays which interact multiple times with the crustal boundaries in the transition region also exist. All such rays produce rays at pre-critical, $j_{oc} < 51^\circ$, angles within the oceanic crust. For any such ray, the transmission coefficient at each successive reflection from the crust-mantle interface is $T(j_{oc})$. Thus, the proportion of reflected amplitude remaining in the crust after the n th bounce is $A_n = [1 - T(j_{oc})]^n A$, where A is the original amplitude. Clearly, the amount of escaping energy decreases with distance. For a shorter transition j_n , for a given i , is smaller. Thus, a larger range of angles $j_{oc} < 51^\circ$ are produced for each path through the shorter transition. This means a higher density of pre-critical rays and higher amplitudes in and escaping from the oceanic crustal layer of shorter transitions.

The use of the interpretation of L_g waves in terms of multiply reflected SH rays to explain the FE results has been instructive. However, the many interacting effects involved in determining the properties of the reflected, converted, and transmitted wavefields would be extremely difficult to predict using this approach. Thus, the FE method is necessary to determine which effects are important and which need not be considered.

CHANGES TO L_g WAVETRAINS PASSING THROUGH AN O/C TRANSITION REGION: THEIR DEPENDENCE ON L

Next we will consider the passage of a wavefield consisting of SH type L_g mode sum energy, which has already passed through a continental region followed by a C/O transition region of 50 km length, through an O/C transition. An example of an O/C transition is illustrated in Fig. 4(b). Propagation through such an O/C transition has several effects on the wavefield. Results of the calculations for propagation through a 50 km O/C transition will be presented in detail so as to illustrate these effects. The O/C transition tests using a variety of L 's will be summarized to illustrate how these effects depend on L . The noted effects and their variations with L will be explained. The set of forcing functions used to drive the O/C FE calculations were recorded during the FE calculation for the 50 km C/O model.

Before proceeding to these discussions the errors introduced due to the truncation inherent in coupling the C/O transition FE results into the O/C transition grid should be mentioned. The finite vertical extent of nodes driven by forcing functions at the left-most edge of the O/C transition grid will cause a vertical truncation of the incoming wavefield. Also, any reflections included in the seismograms recorded for use as forcing functions will be added to the forward propagating wavefield in the O/C calculation. These effects tend to increase the amplitudes at the surface of the oceanic layer near the left end of the grid. The uncertainties introduced by the coupling process appear to increase the amplitudes in the second grid by as much as 3 per cent. Therefore, they could possibly lead to a slight

underestimate of the magnitude of the attenuation effect, but should not lead to an overestimate.

A series of time slices, shown in Fig. 13, illustrates the FE calculation results for the 50 km long O/C transition. The highest amplitude concentrations visible in the first four slices correspond to the maximum amplitudes in the seismograms illustrated in Fig. 14. The first two time slices illustrate the wavefield travelling through the oceanic structure. The third time slice illustrates the passage of the highest amplitude portions of the wavefield through the transition region. In the fourth time slice these highest amplitude regions appear at the right-most end of the grid.

In the fifth time slice they have exited the grid. The maximum amplitude in a given time slice decreases with time in the third to fifth time slice. The maximum amplitudes in the transition region decrease as the wavefront proceeds through the transition region. Thus, normalizing by the largest amplitude in each slice causes identical disturbances to increase in extent and intensity in successive slices. Triangular regions of maxima can be seen in the oceanic crust but they are not nearly so clear as those seen in the continental crust of the C/O transition. The third and fourth time slices clearly show that the energy which was previously trapped in the oceanic crustal layer

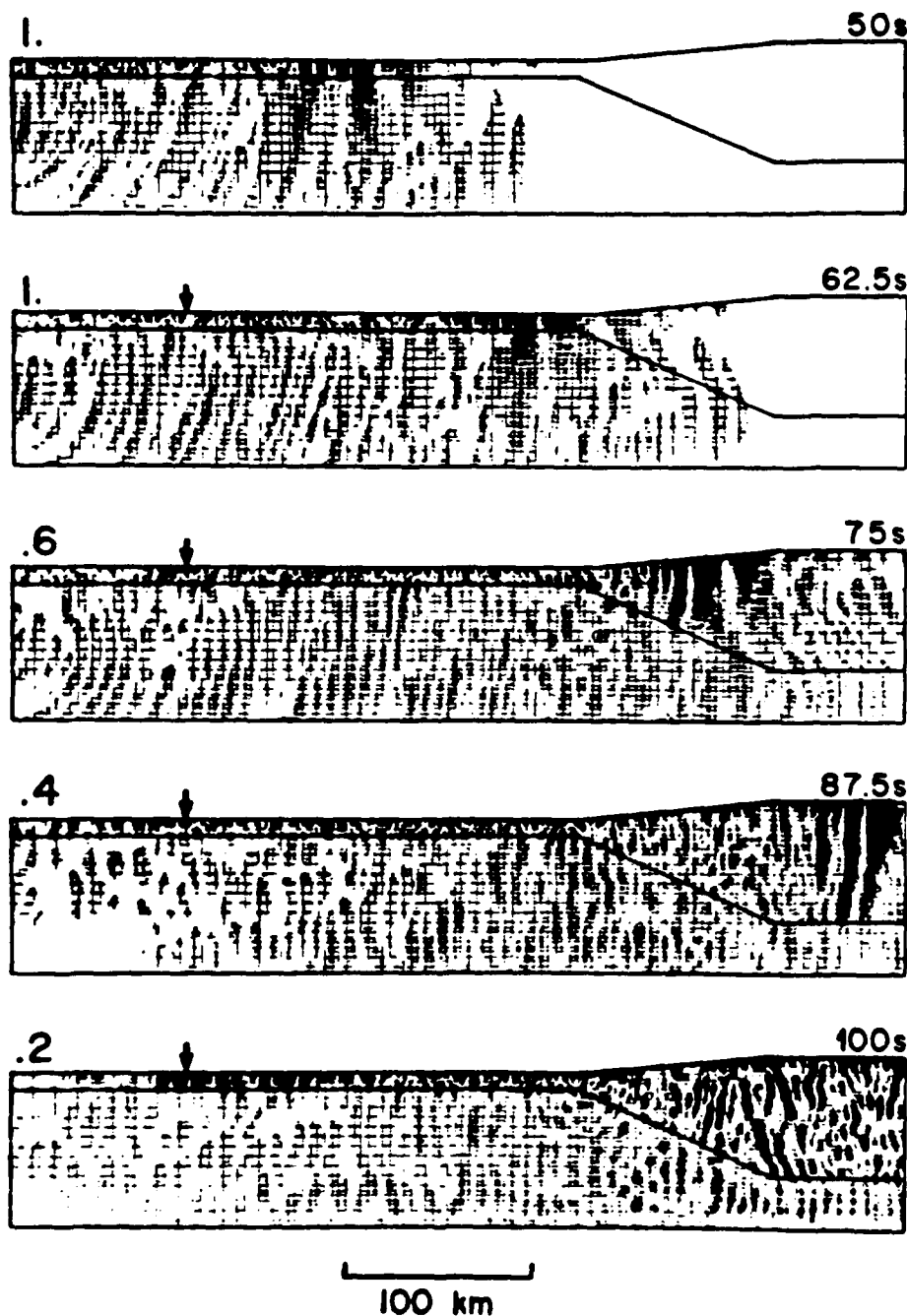


Figure 13. Time slices recorded during the 50 km O/C transition calculation. Details are identical to Fig. 7. 40 s rms amplitudes are shown.

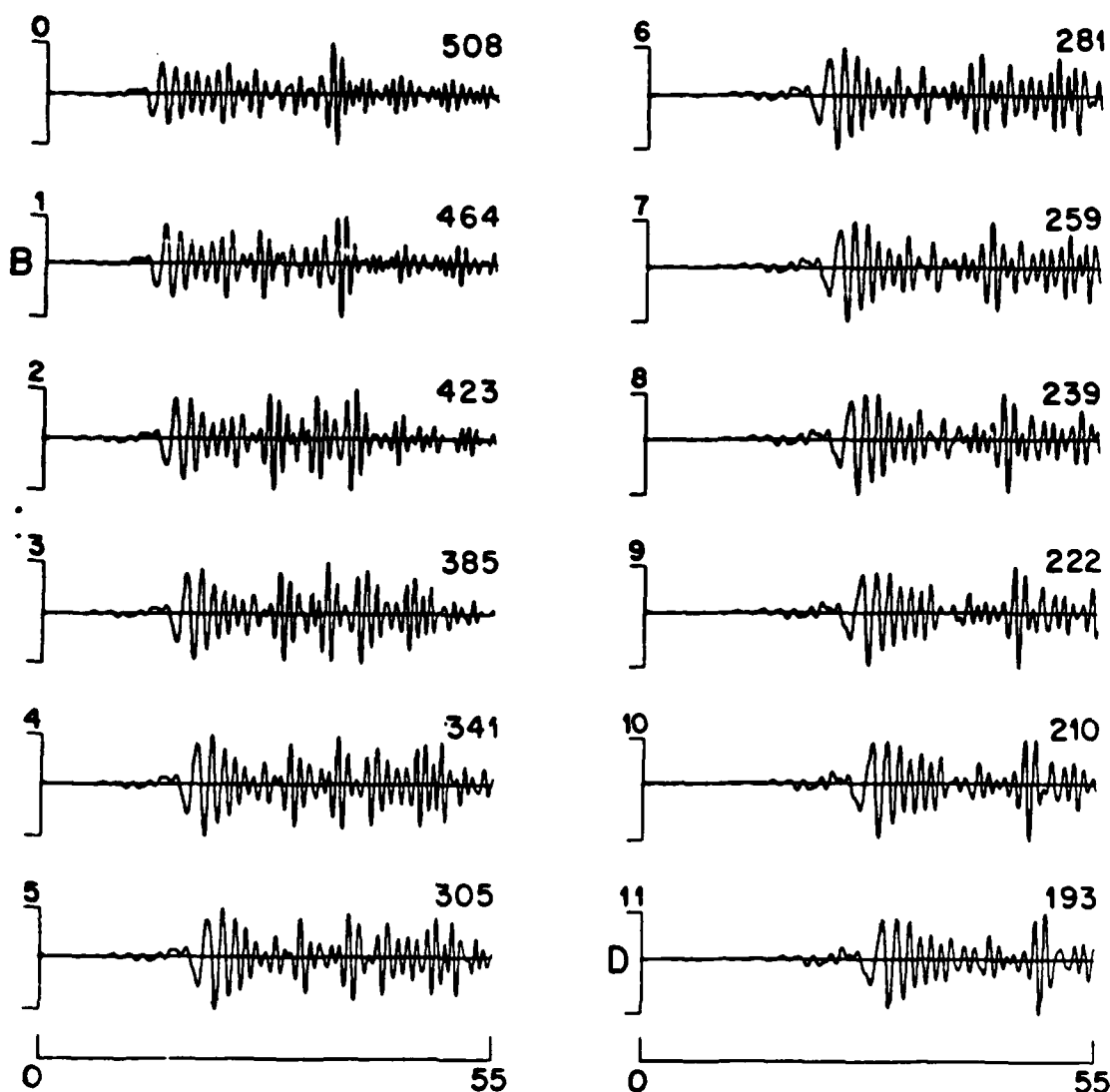


Figure 14. Surface section of seismograms recorded for a 50 km O/C transition calculation. Details explained in Fig. 8.

distributes itself throughout the crustal layer as it passes through the transition region and the region of continental structure. The amplitudes remain much larger near the surface, and decay rapidly with depth. The fifth time slice shows triangular regions maximum amplitude are beginning to appear in the continental structure. Further propagation in x is necessary before the wavefield becomes fully adjusted to the new layering in the region of continental structure.

The disturbances seen in the half-space of the oceanic region of the O/C transition grid contain significant energy. Examining the time slices shows that for a subset of these disturbances, equivalent to the forward transmitted wavefield discussed earlier, the z component of translation in the half-space is increasing for successive groups of disturbances. This is due to the interactions at the CMB in the C/O transition as explained earlier. It is more visible in these time slices than the C/O transition time slices due to the increased distance from the CMB. It is clear that these packets of amplitude are translated rapidly enough in z that some will pass into the half-space below the continental

crustal layer before they reach the O/C transition region. Thus, the energy contained within them escapes the system and is not reconverted to L_g energy when the wavefield passes through the O/C transition. The amount of energy escaping from the system in this manner increases as L , or the length of the intermediate oceanic path, increases.

Figure 14 shows a surface section of seismograms for a 50 km O/C transition. Fig. 9(b) shows the variation of 55 s rms amplitude with distance, $X/2$, from the source for each of the O/C transition FE calculations. A decrease in rms amplitudes is seen as one moves along the surface of the oceanic crustal layer approaching the transition region. This decrease is clear for short rms windows and almost vanishes for window length of 65 s or more. This indicates that the portion of the coda with amplitudes comparable to the maximum amplitude is decreasing in length, that is, that the rate of coda decay is increasing. Superimposed on this slow decrease in amplitude is an oscillatory term with amplitude approximately 15 per cent of the mean amplitude at the surface in the oceanic structure. The rms amplitudes

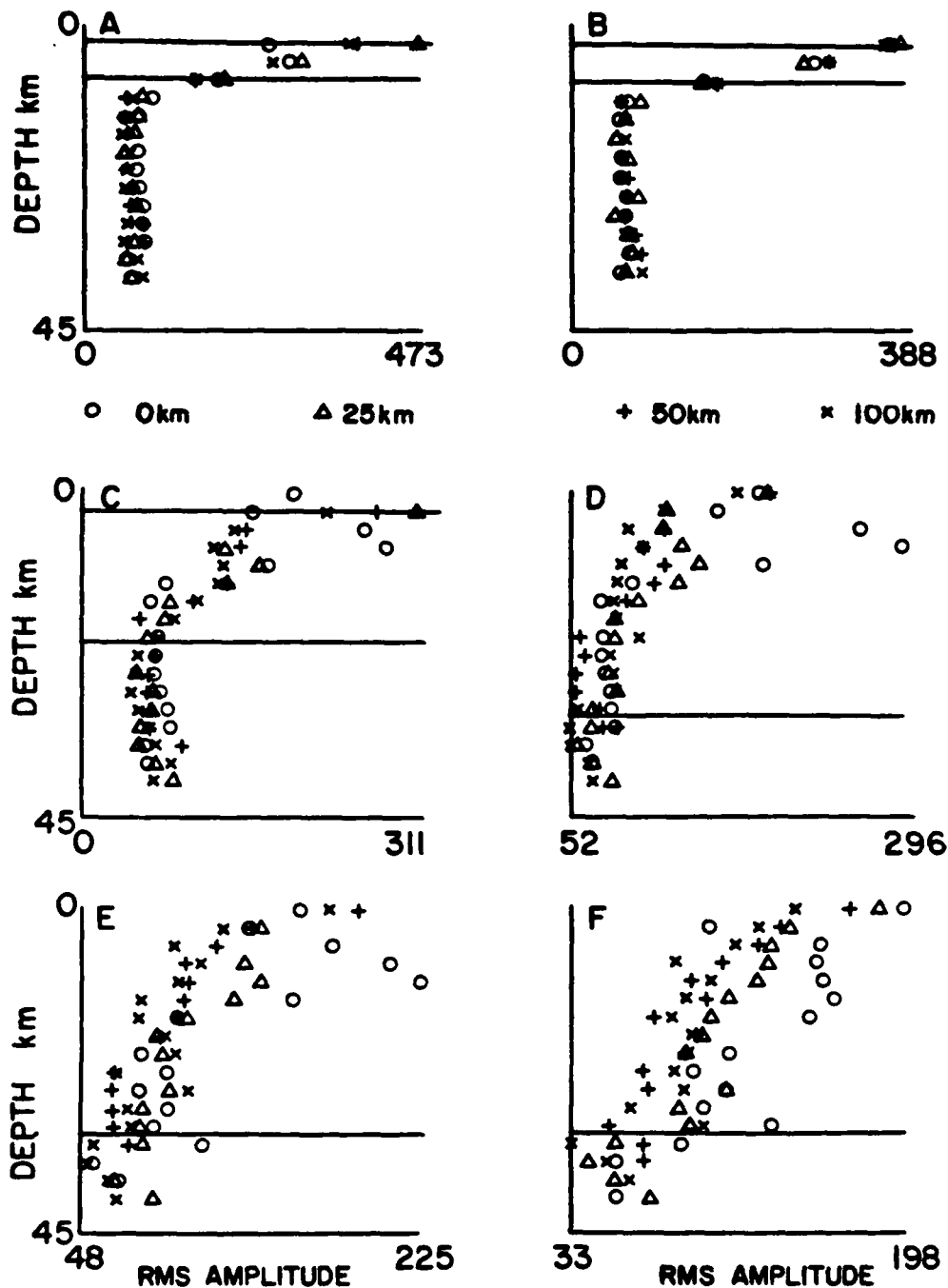


Figure 15. Variation of 55 s rms amplitude with depth. Details are as explained in Fig. 11.

recorded at nodes along the surface of the crustal layer within each O/C transition region decrease as one moves from B towards D. The size of this decrease is smallest for the step transition and increases as L increases. The rate of decay shows some tendency to become smaller towards the end of the transition. The superimposed oscillations seen in the O/C transition results are much smaller than those seen in the C/O transition results. They appear to be confined near the beginning of the transition region. The oscillation in amplitude following the transition region shows that the wavefield has not fully adjusted to the continental structure in the few kilometres beyond the transition regions

illustrated in Fig. 9(b). Additional results which are not illustrated show the rms amplitude continues to decrease slowly until the wavefield readjusts to the new continental structure.

Figure 15 shows the variation of 55 s rms amplitude with depth. At the depth of the surface of the oceanic crustal layer propagation through the transition reduces the rms amplitude by more than a factor of two, and the peak to peak amplitude by 25 per cent. This indicates that the duration and amplitude of the coda are decreasing more rapidly than the amplitude of the largest arrival. At depths between the surface of the continental crust and the surface

of the oceanic crust amplitude decreases with depth. Then energy incident on the MCB is largely transmitted across the MCB into the crustal layer. Some of this energy eventually escapes across the CMB in the region of continental structure. The amplitudes below the crustal layer of the transition region decrease slowly with depth or even increase with depth. An increase of amplitude with depth below the crustal layer indicates that energy is travelling down towards the grid bottom and out of the system being considered.

Most of the energy incident on the MCB is transmitted across it. Thus, in the last four time slices, the reflections from the MCB are not easily distinguished from the later portions of the incident wavefield. The pattern of displacements seen in the oceanic half-space is distorted when the energy producing it is transmitted across the MCB. The uppermost portion of a disturbance crosses the boundary first and begins to move more slowly. The remainder of the disturbance, still in the mantle layer continues to move with the mantle's faster velocity. As the disturbance moves through the length of the transition, an increasing proportion of it moves into the crustal layer. This results in a slope being superimposed on the portion of the disturbance which has propagated back into the crustal layer. The slope,

$$\text{Slope} = \frac{L(v_M - v_c)}{v_M},$$

is dependent on L , the velocity in the crustal layer, v_c , and the velocity in the mantle, v_M . The slope, in this case about $\tan 52^\circ$, is observed easily in both the second and third time slices. It is also seen in the fourth and fifth time slices. However, in these time slices the amplitude incident from the oceanic crustal layer dominates that transmitted from the oceanic mantle layer making observation of the slope more difficult. If a realistic Q model were included the energy travelling through the half-space would be attenuated faster than the energy travelling through the crustal layer. However, since the energy incident from the oceanic crustal layer dominates in the highest amplitude portions of the trace, the increased attenuation in the half-space should not be important in this study.

The effect of the O/C transition region on the energy previously travelling in the oceanic crustal layer will now be discussed. Concentrations of amplitude incident from the oceanic crustal layer travel up the surface of the OCB. As they propagate up the OCB the lower edge of the amplitude concentrations are no longer constrained by the lower edge of the oceanic crustal layer. Consequently the energy can migrate downwards towards the depth of the base of the continental crustal layer. This diffusion of energy can be explained using a mechanism which is the converse of that used to explain the concentration of energy in the C/O transition. The incident angle for the ray perpendicular to each wavefront, j_n , increases as n increases. Subsequent reflection points are separated by larger horizontal distances producing a dilution in ray density and thus a decrease in amplitude. However, there is an important difference that simplifies the analysis of the O/C transition. Incident angles, j_1 , for all rays trapped in and travelling through the oceanic crustal layer are greater than 51° . For $n > 1$ these angles

increase. Therefore, no energy originally trapped in the oceanic crust is transmitted across the MCB, or reflected back towards the source.

Observations indicate that the length of the intermediate oceanic path between the C/O and O/C transitions is important. The results of this study suggest some reasons why this is so. For short paths energy transmitted into the mantle layer has little time to travel towards the bottom of the grid and thus out of the region of consideration before much of it passes back into the crustal layer in the O/C transition region. This implies that there may be a critical length of intermediate oceanic path beyond which enough of the energy has escaped from the region of interest that amplitudes of the attenuated L_g recorded after the O/C transition would be reduced sufficiently to explain the observed data. To completely analyse this assertion requires the use of the RT coupling method for continuing FE calculations through a plane-layered structure using RT integration and PM Green's functions. The accuracy of the numerical implementation of this method must be established before such calculations can be presented. Therefore, the discussion of the numerical implementation of this method and of the results examining the effects of the intermediate path length in the oceanic structure will be left for other papers.

CONCLUSIONS

This paper presents a discussion of the propagation of L_g along partially oceanic paths and the attenuation of L_g due to propagation through the transition regions between the continental and oceanic portions of these paths. The transition regions are modelled by a crustal layer with smoothly varying thickness which connects the continental and oceanic structures. The results will be discussed in three parts. First, propagation through the transition from continental to oceanic structure. Then, propagation through the oceanic structure and, finally, propagation through the transition from oceanic to continental structure.

The effects produced when a SH L_g mode sum wavefield is propagated through a continent to ocean (C/O) transition region, and their dependence on the horizontal extent of that transition region, L , will now be summarized. Amplitudes at the surface of the crust and in the crust are amplified by as much as 50 per cent as the wavefield passes through the transition region from the continental structure to the oceanic structure. These amplitude increases in the crustal layer have been explained by the increased ray density in the thinning crustal layer. The amount of amplification increases as L increases. Increased numbers of reflections within a longer transition region, cause an increase in ray density, explaining the increase in energy as L increases. Amplification is maximum at the surface and decreases with depth until the base of the oceanic crust is reached. In the transition region energy is transmitted across the boundary between the crustal layer and the mantle layer (the CMB) but not across the boundary between the crustal layer and the ocean layer (the COB). Thus, the amplification is maximum at the COB and decays as the CMB is approached and the effects of energy transmitted across the CMB increase. The amount of energy transmitted across the CMB increases as L increases. The translation

direction of the forward transmitted wavefield has a larger vertical component later in the seismogram when it approaches the normal to the CMB. Thus, for a longer transition, with a smaller ϕ_{cm} and thus a more horizontal CMB, the path length in the oceanic structure will have a larger vertical component. This will allow the transmitted energy to escape the system more readily as L increases.

After the wavefield has travelled through the transition region it travels through a region of oceanic structure. While travelling in this oceanic region additional energy escapes from the crustal layer. This leakage is largest near the end of the transition region and decreases with distance away from it. The size of the decrease in amplitude is controlled by the energy in wavefronts propagating through the oceanic crustal layer with pre-critical angles of incidence. At each successive reflection of such a wavefront at the crust half-space interface in the oceanic structure, a fraction of the total amplitude remaining, $T(j_{oc})$ is transmitted across the interface. Thus, the total amplitude of this component decays most rapidly in the first kilometres of the oceanic structure while the incident wave still has significant amplitudes.

After propagating through the oceanic region, the wavefield propagates through an ocean to continent (O/C) transition region. As the wavefield travels through the O/C transition region the surface amplitude decreases rapidly. The energy forming the concentrations of amplitude previously trapped in the oceanic crustal layer travels up the boundary between the oceanic and crustal layers (OCB) in the transition region while spreading throughout the depth extent of the crustal layer. The maxima in these regions remain at the surface. The amplitude decreases rapidly with depth down to the crust-mantle interface. The amplitude incident upon the boundary between the mantle layer and the crustal layer (MCB) in the O/C transition region from the oceanic half-space is transmitted across it with a resulting distortion in the wavefield. The form of this distortion is the superposition of a slope,

$$\text{Slope} = \tan^{-1} \left[\frac{l(v_N - v_C)}{v_M} \right],$$

on to the disturbance incident at the MCB after it has passed into the continental crustal layer.

Finally, attenuation of L_g propagating along a mixed path with simple transition regions and an oceanic path length of 147 km, is not sufficient to explain the observed values. The highest attenuations observed produced a reduction of a factor of two to three in amplitude. Observations of the trends due to varying L indicate that a longer C/O transition could increase the attenuation. But, even using the optimal L attenuation of more than a factor of four would not be expected. Thus, other factors and/or more complex structures must be considered to explain the observed attenuation of L_g along mixed paths.

ACKNOWLEDGMENTS

J. Regan conducted part of this research while a Canadian Government Laboratory Visiting Fellow at Geophysics Division, Geological Survey of Canada, Ottawa. This research was supported in part by the Advanced Research

Projects Agency of the US Department of Defense and was monitored by the US Air Force Geophysics Laboratory under contract F19628-87-K-0028; Division of Geological Sciences Contribution No. 4623; Geological Survey of Canada Contribution No. 20988.

REFERENCES

- Alsop, L. E., 1966. Transmission and reflection of Love waves at a vertical discontinuity, *J. geophys. Res.*, **71**, 3969-3984.
- Barker, B., W., Der, Z. A., Mracek, C. P., 1981. The effect of crustal structure on the regional phases P_g and L_g at the Nevada test site, *J. geophys. Res.*, **86**, 1686-1700.
- Bath, M., 1954. The elastic waves L_g and R_g along Euroasiatic paths, *Arkiv Geofysik*, **2**, 295-342.
- Blandford, R., 1982. Seismic event discrimination, *Bull. seism. Soc. Am.*, **72**, s69-s87.
- Bolt, B. A., 1957. Velocity of the seismic waves L_g and R_g across Australia, *Nature*, **180**, 495.
- Bollinger, G. A., 1979. Attenuation of the L_g phases and determination of m_b in the southeastern United States, *Bull. seism. Soc. Am.*, **69**, 45-63.
- Boore, D., 1970. Love waves in nonuniform wave guides: finite difference calculations, *J. geophys. Res.*, **75**, 1512-1527.
- Bose, S. K., 1975. Transmission of SH waves across a rectangular step, *Bull. seism. Soc. Am.*, **65**, 1779-1786.
- Bouchon, M., 1981. A simple method to calculate Green's functions for elastic layered media, *Bull. seism. Soc. Am.*, **71**, 959-971.
- Bouchon, M., 1982. The complete synthesis of seismic crustal phases at regional distances, *J. geophys. Res.*, **87**, 1735-1741.
- Campillo, M., Bouchon, M. & Massinon, B., 1984. Theoretical study of the excitation, spectral characteristics, and geometrical attenuation of regional seismic phases, *Bull. seism. Soc. Am.*, **74**, 79-90.
- Chung, D. H. & Bernreuter, D. L., 1981. Regional relationships among earthquake magnitude scales, *Rev. geophys. Space Phys.*, **19**, 649-663.
- Drake, L. A., 1972. Love and Rayleigh waves in nonhorizontally layered media, *Bull. Seism. Soc. Am.*, **62**, 1241-1258.
- Drake, L. A. & Bolt, B. A., 1980. Love waves normally incident at a continental boundary, *Bull. seism. Soc. Am.*, **70**, 1103-1123.
- Dwyer, J. J., Herrmann, R. B. & Nuttli, O. W. 1983. Spatial attenuation of the L_g wave in the central United States, *Bull. seism. Soc. Am.*, **73**, 781-796.
- Eitrem, S. & Grantz, A., 1979. CDP seismic sections of the western Beaufort continental margin, *Tectonophysics*, **59**, 251-262.
- Frazier, G. A., Alexander, J. H. & Petersen, C. M., 1973. 3-D seismic code for the ILLIAC IV. Systems, Science and Software Report Report SSS-R-73-1506.
- Gregersen, S., 1978. Possible mode conversion between Love and Rayleigh waves at a continental margin, *Geophys. J. R. astr. Soc.*, **54**, 121-127.
- Gregersen, S., 1984. L_g wave propagation and crustal structure differences near Denmark and North Sea, *Geophys. J. R. astr. Soc.*, **79**, 217-234.
- Gregersen, S. & Alsop, L. E., 1974. Amplitudes of horizontally refracted Love waves, *Bull. seism. Soc. Am.*, **64**, 535-553.
- Gregersen, S. & Alsop, L. E., 1976. Mode conversion of Love waves at a continental margin, *Bull. seism. Soc. Am.*, **66**, 1855-1872.
- Harkrider, D. G., 1964. Surface waves in multilayered media, Part I. Rayleigh and Love waves from buried sources in a multilayered elastic half-space *Bull. seism. Soc. Am.*, **54**, 627-679.
- Harkrider, D. G., 1970. Surface waves in multilayered elastic media, Part II. Higher mode spectra and spectra ratios from point sources in plane layered earth models, *Bull. seism. Soc. Am.*, **60**, 1937-1987.
- Harkrider, D. G., 1981. Coupling near source phenomena into surface wave generation, in *Identification of Seismic Sources—Earthquake or Underground Explosion*, pp. 277-326, eds Husebye, E. S. & Mykkeltveit, S., Reidel, Dordrecht.

- Herrin, E. E. & Minton, P. D., 1960. The velocity of L_g in the southwestern United States and Mexico, *Bull. seism. Soc. Am.*, **50**, 35–44.
- Herrmann, R. B. & Kijko, A., 1983. Short period L_g magnitudes: instrument, attenuation, and source effects, *Bull. seism. Soc. Am.*, **73**, 1835–1850.
- Herrmann, R. B. & Nuttli, O. W., 1975. Ground motion modelling at regional distances for earthquakes in a continental interior, II. Effect of focal depth, azimuth, and attenuation, *Int. J. Earthq. Eng. Struct. Dyn.*, **4**, 59–77.
- Herrmann, R. B. & Nuttli, O. W., 1982. Magnitude: the relation of M_L to m_{bL} , *Bull. seism. Soc. Am.*, **72**, 389–397.
- Hinz, K., Schluter, H.-U., Grant, A. C., Srivastava, S. P., Unpleby, D. & Woodside, J., 1979. Geophysical transects of the Labrador Sea: Labrador to southwest Greenland, *Tectonophysics*, **59**, 151–183.
- de Hoop, A. T., 1958. Representation theorems for the displacement in an elastic solid and their application to elastodynamic diffraction theory, *ScD Thesis*, Technische Hogeschool, Delft.
- Hudson, J. A., 1977. The passage of elastic waves through an anomalous region—IV. Transmission of Love waves through a laterally varying structure, *Geophys. J. R. astr. Soc.*, **49**, 645–654.
- Hudson, J. A. & Knopoff, L., 1964. Transmission and reflection of surface waves at a corner: I. Love waves, *J. geophys. Res.*, **69**, 275–280.
- Jones, F. B., Long, L. T. & McKee, J. H., 1977. Study of the attenuation and azimuthal dependence of seismic wave propagation in the southeastern United States, *Bull. seism. Soc. Am.*, **67**, 1503–1513.
- Kazi, M. H., 1978a. The Love wave scattering matrix for a continental margin (theoretical), *Geophys. J. R. astr. Soc.*, **52**, 25–44.
- Kazi, M. H., 1978b. The Love wave scattering matrix for a continental margin (numerical), *Geophys. J. R. astr. Soc.*, **53**, 227–243.
- Keen, C. E. & Hyndman, R. D., 1979. Geophysical review of the continental margins of eastern and western Canada, *Can. J. Earth Sci.*, **16**, 712–747.
- Kennett, B. L. N., 1973. The interaction of seismic waves with horizontal velocity contrasts, *Geophys. J. R. astr. Soc.*, **33**, 431–450.
- Kennett, B. L. N. & Mykkeltveit, S., 1984. Guided wave propagation in laterally varying media—II. L_g -waves in north-western Europe, *Geophys. J. R. astr. Soc.*, **79**, 257–267.
- Kennett, B. L. N., 1986. L_g waves and structural boundaries, *Bull. seism. Soc. Am.*, **76**, 1133–1142.
- Knopoff, L. & Hudson, J. A., 1964. Transmission of Love waves past a continental margin, *J. geophys. Res.*, **69**, 1649–1653.
- Knopoff, L. & Mal, A. K., 1967. Phase velocities of surface waves in the transition zone of continental margins—I. Love waves, *J. geophys. Res.*, **72**, 1769–1776.
- Knopoff, L., Mal, A. K., Alsop, L. E. & Phinney, R. A., 1970. A property of long-period Love waves, *J. geophys. Res.*, **75**, 4084–4086.
- Knopoff, L., Schwab, F., Nakanishi, K. & Chang, F., 1975. Evaluation of L_g as a discriminant among different continental crustal structures, *Geophys. J. R. astr. Soc.*, **39**, 41–70.
- Knopoff, L., Schwab, F. & Kausel, E., 1973. Interpretation of L_g , *Geophys. J. R. astr. Soc.*, **33**, 389–404.
- Kovach, R. L. & Anderson, D. L., 1964. Higher mode surface waves and their bearing on the structure of the Earth's mantle, *Bull. seism. Soc. Am.*, **54**, 161–182.
- Le Douaran, S., Burnus, J. & Avedik, F., 1984. Deep structure of the north-western Mediterranean basin: results of a two-ship survey, *Mar. Geol.*, **55**, 325–345.
- Lehmann, I., 1952. On short period surface wave L_g and crustal structures, *Bull. D'information L'UGGI 2^e Année*, 248–251.
- Lehmann, I., 1957. On L_g as read in North American records, *Ann. Geofis.*, **10**, 1–28.
- Lysmer, J. & Drake, L. A., 1971. The propagation of Love waves across nonhorizontally layered structures, *Bull. seism. Soc. Am.*, **61**, 1233–1251.
- Lysmer, J. & Drake, L. A., 1972. A finite element method for seismology, in *Methods in Computational Physics 11, Seismology*, Alder, B., Fernbach, S. & Bolt, B. A., Academic Press, New York.
- Martel, L., 1980. Love wave propagation across a step by finite elements and spatial filtering, *Geophys. J. R. astr. Soc.*, **61**, 639–677.
- Mantovani, E., Schwab, F., Liao, H. & Knopoff, L., 1977. Generation of complete theoretical seismograms for SH-II, *Geophys. J. R. astr. Soc.*, **48**, 531–535.
- Nicolas, M., Massinon, B., Mechler, P. & Bouchon, M., 1982. Attenuation of regional phases in western Europe, *Bull. seism. Soc. Am.*, **72**, 2089–2106.
- Nuttli, O. W., 1973. Seismic wave attenuation and magnitude relations for eastern North America, *J. geophys. Res.*, **78**, 876–885.
- Nuttli, O. W., 1978. A time domain study of the attenuation of 10-Hz waves in the new Madrid seismic zone, *Bull. seism. Soc. Am.*, **68**, 343–355.
- Nuttli, O. W., 1981. On the attenuation of L_g waves in western and central Asia and their use as a discriminant between earthquakes and explosions, *Bull. seism. Soc. Am.*, **71**, 249–261.
- Oliver, J., Dorman, J. & Sutton, G., 1959. The second shear mode of continental Rayleigh waves, *Bull. seism. Soc. Am.*, **49**, 379–389.
- Oliver, J., Ewing, M. & Press, F., 1955. Crustal structure of the Arctic regions from the L_g phase, *Bull. seism. Soc. Am.*, **66**, 1063–1074.
- Oliver, J. & Ewing, M., 1957. Higher modes of continental Rayleigh waves, *Bull. seism. Soc. Am.*, **47**, 187–204.
- Oliver, J. & Ewing, M., 1958. Normal modes of continental surface waves, *Bull. seism. Soc. Am.*, **48**, 33–49.
- Panza, G. F. & Calcagnile, G., 1974. Comparison of multimode surface wave response in structures with and without a low velocity channel (Part I: Dip slip sources on a vertical fault plane), *Pure appl. Geophys.*, **112**, 583–596.
- Panza, G. F. & Calcagnile, G., 1975. L_g , L , and R_g from Rayleigh modes, *Geophys. J. R. astr. Soc.*, **48**, 475–487.
- Pec, K., 1967. Theoretical dispersion tables for Love waves propagating in a wedge and in a single nonhomogeneous layer with a linear velocity gradient, *Pub. Dominion Obs. Ottawa*, **35**.
- Pomeroy, P. W., Best, W. J. & McKevelly, T. V., 1982. Test ban treaty verification with regional data: a review, *Bull. seism. Soc. Am.*, **72**, s89–s129.
- Press, F., 1956. Velocity of L_g waves in California, *Trans. Am. geophys. Un.*, **37**, 615–618.
- Press, F. & Ewing, M., 1952. Two slow surface waves across North America, *Bull. seism. Soc. Am.*, **42**, 219–228.
- Press, F., Ewing, M. & Oliver, J., 1956. Crustal structure and surface-wave dispersion in Africa, *Bull. seism. Soc. Am.*, **46**, 97–103.
- Regan, J., 1987. Numerical studies of propagation of L_g waves across ocean continent boundaries using the representation theorem, *PhD thesis*, California Institute of Technology, Pasadena, Ca.
- Sato, R., 1961a. Love waves propagated across transitional zone, *Japan. J. Geophys.*, **2**, 117–134.
- Sato, R., 1961b. Love waves in case the surface layer is variable in thickness, *J. Phys. Earth.*, **9**, 19–36.
- Savarensky, E. & Valdener, N., 1960. Observations of L_g and R_g waves from the Black Sea basin earthquakes, *Ann. Geofis.*, **13**, 129–134.
- Schwab, F., Kausel, E. & Knopoff, L., 1974. Interpretation of S_g for a shield structure, *Geophys. J. R. astr. Soc.*, **36**, 737–742.
- Singh, S. & Herrmann, R. B., 1983. Regionalization of crustal coda Q in the continental United States, *J. geophys. Res.*, **88**, 527–538.
- Stephens, C. & Isaacs, B. L., 1977. Toward an understanding of S_g : normal modes of Love waves in an oceanic structure, *Bull. seism. Soc. Am.*, **67**, 69–76.
- Street, R., 1976. Scaling northeastern United States/southeastern Canadian earthquakes by their L_g waves, *Bull. seism. Soc. Am.*, **66**, 1525–1537.
- Street, R., 1984. Some recent L_g phase displacement spectral

- densities and their implications with respect to the prediction of ground motions in eastern North America, *Bull. seism. Soc. Am.*, **74**, 757-762.
- Street, R., Herrmann, R. B. & Nuttli, O. W., 1975. Spectral characteristics of the L_g wave generated by central United States earthquakes *Geophys. J. R. astr. Soc.*, **41**, 51-63.
- Street, R. & Turcotte, F. T., 1977. A study of northeastern North American spectral moments, magnitudes, and intensities, *Bull. seism. Soc. Am.*, **67**, 599-614.
- Wetmiller, R. J., 1974. Crustal structure of Baffin Bay from earthquake generated L_g phases, *Can. J. Earth Sci.*, **11**, 123-130.
- Zienkiewicz, O. C. & Cheung, Y., 1967. *The Finite Element Method in Structural and Continuum Mechanics*, McGraw-Hill.

SECTION 3

Seismic representation theorem coupling: synthetic SH mode sum
seismograms for non-homogeneous paths

Seismic representation theorem coupling: synthetic SH mode sum seismograms for non-homogeneous paths

J. Regan

Geological Survey of Canada, 1 Observatory Crescent, Ottawa, Ontario, Canada K1A 0Y3

D. G. Harkrider

Seismological Laboratory 252-21, California Institute of Technology, Pasadena, CA 91125, USA

Accepted 1989 February 7. Received 1989 February 7; in original form 1988 October 3

SUMMARY

In this paper the methods for representation theorem coupling of finite-element or finite difference calculations and propagator matrix method calculations (Harkrider) are developed. The validity and accuracy of the resulting hybrid method are demonstrated. The resulting hybrid technique can be used to study the propagation of any phase that can be represented in terms of an SH mode sum seismogram, across regional transition zones or other heterogeneities. These heterogeneities may exist in regions which form subsegments of a longer, mostly plane-layered, path. Examples of structures of interest through which such waves can be propagated using these techniques include, regions of crustal thickening or thinning such as continent-ocean transitions or basins, anomalous bodies of any shape located in the path, and sudden transitions from one layered structure to another. Examples of the types of phases that may be propagated through these structures include Love waves, L_g , S_n , and S_g .

Key words: coupling, non-homogeneous paths, representation theorem, seismograms

1 INTRODUCTION

The hybrid method is simple in concept. The propagation path is divided into plane-layered segments, and non-plane-layered segments. The non-plane-layered segments may contain arbitrary structures. The propagator matrix (PM) technique is used to propagate the disturbance through the plane-layered segments and the finite element (FE) or finite difference (FD) method is used to propagate it through the non-plane-layered segments. The source is assumed to lie within a plane-layered region. Since neither coupling technique (PM to FE or FE to PM) provides a complete solution if it is applied at the physical boundary between plane-layered and non-plane-layered regions, the FE or FD grid must contain not only the complex region but also segments of each of the plane-layered structures which adjoin the ends of the complex region. Reflections from the complex structure within the grid must be carefully considered when designing the grid (Regan 1987) to ensure that their effects are included in the final solution. The wavefield is propagated from the source to the boundary of the FE or FD grid containing the first complex region using the PM method. The method used to transmit the wavefield across the boundary into the FD or FE grid containing the non-plane-layered region is straightforward (Regan & Harkrider 1989; Regan 1987). The wavefield is then

propagated through the non-plane-layered region using the FE or FD method. Next, the wavefield can be transmitted across the boundary between the FD or FE grid containing the non-plane-layered region and the remainder of the second plane-layered region using the representation theorem (RT) integration coupling method developed in this paper. This sequence of procedures can be repeated any number of times so that any number of non-plane-layered regions can be included in the source to receiver path. The RT integration coupling method uses a 2-D Cartesian finite element formulation. Analogous methods for the 3-D case follow directly.

Many methods have been used to model the propagation of seismic disturbances across regions of varying structure such as transition zones. The types of models that have been used to approximate transition regions can be separated into several types which are illustrated in Fig. 1.

The simplest type of model (Fig. 1a) consists of two homogeneous layered regions, 11', and 33' separated by a vertical boundary or a region 22' in which elastic properties vary smoothly. Sato (1961a) derives analytical expressions for the transmitted and reflected waves, the phase and group velocities, and evaluates the approximate reflection and transmission coefficients (R and T) in each case. More recently, Kennett (1973) has developed a numerical technique for solving the problem of seismic waves

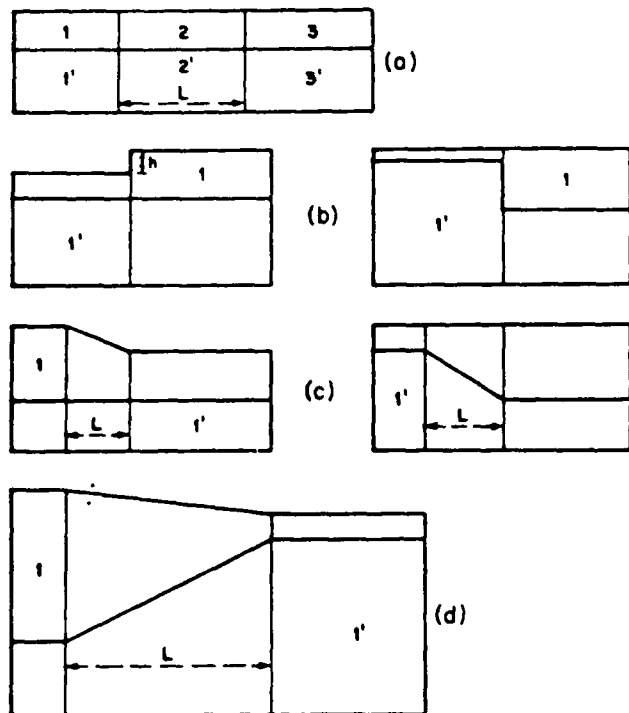


Figure 1. Types of models used in studies of propagation of Love waves across continent-ocean boundaries, in order of increasing complexity; (a) shows two homogeneous layered regions, 1 and 3, separated by an intermediate region, 2, in which elastic properties vary smoothly between their values in regions 1 and 2; (b) shows a layer over a half-space with a step change in the thickness of the layer; (c) shows a model with a smooth change in thickness, either at the surface or the Moho; (d) shows a model with a smooth change in thickness both at the surface and the Moho. The variations in (a), (c), and (d) occur in a transition region of length L .

interacting with a layer or layers in which properties change across a surface perpendicular to or at a specified angle from the layering.

The next level of model complexity is the inclusion of a change in the thickness of the surface layer at the discontinuity between the two structures (Fig. 1b). Sato (1961b) obtained analytical solutions and thus approximate expressions for R and T for the special case of a surface step with height h much less than the wavelength of the incident wavefield. Hudson & Knopoff (1964) obtained expressions for more general surface step models. Alsop (1966) developed an approximate method for determining R and T which assumes that all energy remains in Love waves. Gregersen & Alsop (1974, 1976) used an extended form of the method of Alsop (1966, 1968) to show that normal incidence is a good approximation for oblique incidence at angles of incidence of less than 40° . Bose (1975) used an integral equation formulation to yield asymptotic solutions at large distances from the step consistent with results derived for the step models by Regan & Harkrider (1989) using the PM to FE coupling technique that forms part of the overall hybrid technique. Kazi (1978a, b) uses a variational method to show that T increases after the cut-off frequency when the conversion of Love waves to body waves at the surface step is considered. Earlier studies by

Alsop (1966) and Knopoff & Hudson (1964) showed that T decreased when the body waves were neglected. Martel (1980) used a FE technique to evaluate propagation of Love waves across a Moho step. Spatial filtering of the transmitted and reflected modes to determine transmission and reflection coefficients allowed the isolation of the diffracted body wave component. The modal filtering technique discussed in this paper would provide a simple way to do such decompositions on FE or FD results determined for any complex structures. Also these structures would not need to be near the end of the propagation path as is the case with a pure FE or FD type calculation.

Studies using the surface step model and the Moho step model have been generalized in several ways. We will discuss only one, replacing the step by a transition region (Fig. 1c). Knopoff & Mal (1967), and Knopoff *et al.* (1970) explained an analytical solution for models of type (1c) when the slope of the surface (or Moho) in the transition region is small. Pec (1967) calculated the dispersion of Love waves propagating in a wedge-shaped layer. Boore (1970) used FD to study the propagation of a simple low frequency Love wave across a transition region (Fig. 1c). He noted that in the region of the transition mode conversions and conversion to other types of waves were important. Lysmer & Drake (1971, 1972) and Drake (1972), use a FE method based on Zienkiewicz & Cheung (1967) which includes a rigid grid bottom and thus allows no energy to escape the grid. The formulation also requires that the incident modal energy is exactly equal to the sum of the reflected and transmitted modal energy. Conversion to body waves is seen as a distortion of the modal eigenfunctions. Lysmer & Drake (1971) use this method to study the effect of a transition of type 1c, or 1d, on the incident fundamental mode Love wave energy. They attribute the differences between their results and those of Boore (1970) to body wave interference in Boore's results. However, conversion to body waves and escape of those body waves from the system defined by the finite element grid play an important role in understanding the propagation of waves across regional variations in structure (Regan & Harkrider 1989). So, in fact, the method of Lysmer & Drake (1972) with its distorted eigenfunctions might be interpreted to be the method containing body wave interference. Thus, the approach used by Boore (1970) and the approach used in the present study will provide more physical insight into the processes of attenuation along complex paths. The method of Lysmer & Drake (1971) also includes a method for calculating 'mode participation factors'. These measure the ratio of the energy of a single mode seismogram incident on the complex region and the resulting energy of each single mode exiting the complex region. Similar ratios can be determined using the Green's function filtering technique presented in the present study. Both methods are based on the Love wave orthogonality relations. Drake & Bolt (1980) used the method of Lysmer & Drake (1972) to study fundamental mode Love waves normally incident on the California continental margin. They conclude that the ocean continent boundary strongly increases the attenuation of fundamental mode Love waves, as Regan & Harkrider (1989) suggest.

All the studies discussed in the previous paragraph used

periods much longer than those that will be considered in the following discussions. Most previous studies considered transition regions with lengths comparable the wavelength of the incident energy. The shorter periods used in this study allow the examination of the effects of transition regions with lengths many times the wavelength of the incident energy. Of all previous studies mentioned above only Kennett & Mykkeltveit (1984) and Bouchon (1981, 1982) have generated realistic seismograms, the latter at regional distances only. Instead, most studies concentrated on measuring phase velocities and transmission and reflection coefficients for individual modes. In this study the input energy is in the form of seismograms containing a sum over a range of modes for fundamental and overtone Love waves. This approach produces a realistic output seismogram which can be filtered and decomposed to yield the transmission and reflection coefficients if they are needed. In light of these facts it is clear that the results derived using the method developed in the present paper can provide a significant improvement in the understanding of the propagation of L_g waves and other phases that can be expressed in terms of mode sum seismograms.

2 THE RT INTEGRATION METHOD FOR FE TO PM COUPLING

To clearly explain the method used to couple finite element and propagator matrix methods, it is useful to first discuss some of the foundations on which each method is based, and to explain the basic concepts inherent in the use of the representation theorem. In Section 2.1 the representation theorem will be discussed, and the assumptions that lead to the form of the representation theorem used in this study will be presented. The theory used to derive the version of the PM technique used in the present study is explained in detail by Harkrider (1964). The notation and the basic concepts of the PM technique needed to explain the representation theorem integration coupling technique developed in the present paper are summarized in Section 2.2. The FE method used in this study is an extensively modified version of the stress waves in solids code (Frazier, Alexander & Petersen 1973). The result is an explicit time domain FE method using a rectangular grid, and the hourglass correction terms which the rectangular grid necessitates (Kosloff & Frazier 1978; Regan 1987). The FE method can be driven by a source distant from the finite element grid, as outlined by Regan & Harkrider (1989). Displacement or stress time histories can be recorded at any node or element centre in the grid. Given these time histories further details of the particular implementation of the FE method are not important to the understanding of the coupling technique. The implementation of the RT coupling technique will be discussed in Section 2.3. A method for determining the accuracy of the RT coupling results will be presented in Section 2.4. A method for modal Green's function filtering of finite element or hybrid results is developed in Section 2.4. Finally, in Section 3, all aspects of the method are tested using a simple model which enables the calculation of PM synthetics for direct comparison to the hybrid results.

2.1 The representation theorem and Green's functions

The basis of the method used to couple the results of a finite element calculation into the PM calculation is the application of the representation theorem on the boundary between the regions in which each method is used. The representation theorem relates the displacement at any point, ξ , in a volume V to the body forces f_i acting within V and to the displacements u_i and the tractions T_i acting on the surface S of V . There are many equivalent ways of expressing the representation theorem, for example (Aki & Richards 1980, eq. 2.41)

$$u_p(\mathbf{x}, t) = \int_{-\infty}^{+\infty} d\tau \int_V f_i(\xi, \tau) G_{ip}(\mathbf{x}, t - \tau; \xi, 0) dV(\xi) + \int_{-\infty}^{+\infty} d\tau \int_S \left(G_{ip}(\mathbf{x}, t - \tau; \xi, 0) T_i[\mathbf{u}(\xi, \tau), n_j] - c_{ijk} \frac{\partial}{\partial x_j} G_{kp}(\mathbf{x}, t - \tau; \xi, 0) u_j(\xi, \tau) n_j \right) dS(\xi) \quad (1)$$

where ξ is the location of a point on S , \mathbf{x} the location of a receiver in V , $u_p(\mathbf{x}, t)$ is the p component of the displacement at time t at \mathbf{x} , t is the observation time, τ is the source time, n_j is the j th component of the outward unit normal to S , $T_i[\mathbf{u}(\xi, \tau), n_j] = \tau_{ij} n_j = (u_{i,j} + u_{j,i}) n_j$ and $u_i(\xi, \tau)$ are the boundary conditions specifying stress and displacement as a function of source time τ for all points ξ on S , and G_{ip} is the Green's function which represents the displacement in the i th direction at \mathbf{x} at time t due to a unit impulse applied in the p th direction at position ξ at time τ .

The general form of the representation theorem given above is not suitable for demonstrating how the coupling of the FE and PM methods is accomplished. To transform it to a more manageable form it is assumed that no body forces are present within volume V , and that the medium is isotropic. Applying both conditions allows the representation theorem to be written as follows.

$$u_p(\mathbf{x}, t) = \int_{-\infty}^{+\infty} d\tau \int_S \{ G_{pi} \tau_{ij} + \lambda G_{pi,i} u_i + \mu (G_{pi,j} + G_{pj,i}) u_j \} n_j dS(\xi) \quad (2)$$

where all derivatives are with respect to ξ .

For the case of SH waves only, eq. (2) can be further simplified to

$$u_2(\mathbf{x}, t) = \int_{-\infty}^{+\infty} d\tau \int_S \mu(\xi_3) \{ G_{22} u_{2,k} + G_{22,k} u_2 \} n_k dS(\xi), \quad (3)$$

For the 2-D SH solutions at \mathbf{x} in V , eq. (3) is integrated from $-\infty$ to $+\infty$ over the variable ξ_2 . The representation theorem becomes (de Hoop 1958)

$$u_2(\mathbf{x}, t) = \int_0^t d\tau \oint_C \mu(\xi_3) \{ \Gamma_{22} u_{2,k} + \Gamma_{22,k} u_2 \} n_k dC(\xi_1, \xi_3) \quad (4)$$

where C is the curve defined by the intersection of the surface S with the x_1 - x_3 plane, $\mu(\xi_3)$ is the rigidity at the depth ξ_3 , and the half-space Green's functions Γ_{22} and the forcing functions $u_2(\xi_1, \xi_3, t)$ satisfy the initial conditions

$$u_2 = u_{2,k} = \Gamma_{22} = \Gamma_{22,k} = 0 \quad t \leq \tau \quad (5a)$$

the radiation conditions,

$$u_2 \rightarrow 0 \quad u_{2,z} \rightarrow 0 \quad \text{as } \xi \rightarrow \infty \quad (5b)$$

and the boundary conditions,

$$u_{2,z} = \bar{\Gamma}_{22,z} = 0 \quad \text{at } z = 0. \quad (5c)$$

Following the notation of de Hoop (1958) the half-space Green's function is

$$\begin{aligned} \bar{\Gamma}_{22}(x, s; \xi) &= \int_{-\infty}^{+\infty} \bar{G}_{22}(x, s; \xi) d\xi_3 \\ &= \frac{1}{2\pi\rho\beta^2} [K_0(sa^-/\beta) + K_0(sa^+/\beta)] \end{aligned} \quad (6)$$

where $a^\pm = \sqrt{(x_1 - \xi_1)^2 + (z \pm \xi_3)^2}$. To compare this form for the Green's functions with the forms of the displacements used in the rest of this discussion it is first necessary to transform equation (6) from the Laplace transform domain to the Fourier transform domain. Applying the change of variables, $s = i\omega$, and transforming the modified Bessel functions, K_0 , into Hankel functions gives

$$\bar{\Gamma}_{22}(x, \omega; \xi) = \frac{-i}{4\mu} [H_0^{(2)}(k_\beta a^+) + H_0^{(2)}(k_\beta a^-)]. \quad (7)$$

This form is analogous with the displacement solution for the line source in a half-space:

$$\bar{u}_y(x, \omega) = \bar{u}_y(r, \phi, z) = \frac{i\pi}{2} [H_0^{(2)}(k_\beta a^+) + H_0^{(2)}(k_\beta a^-)]. \quad (8)$$

Thus,

$$\bar{u}_y(r, \phi, z) = -2\pi\mu \bar{\Gamma}_{22}(x, \xi) \quad (9)$$

and the displacement Green's function can be calculated in a manner similar to the displacement solution. The line source displacements and the line source Green's functions differ only by a multiplicative factor of $-2\pi\mu$.

2.2 The propagator matrix technique

To implement the representation theorem integration coupling algorithm for coupling finite element results into propagator matrix calculations it is first necessary to obtain and evaluate expressions for the displacement and stress seismograms and the stress and displacement Green's functions used in the representation theorem integral (equation 4). Evaluation of displacement and/or stress Green's functions ($\bar{\Gamma}_{22}$, $\bar{\Gamma}_{22,1}$, $\bar{\Gamma}_{22,3}$) is necessary in all applications of the RT integration coupling method regardless of whether the forcing functions are FE results, analytical stress and displacement seismograms evaluated using PM or other techniques, or stresses and displacements from other sources. However, the PM stress seismograms are used in the following discussions only as an example of a well-defined and easily evaluated form of forcing functions. Using a single plane-layered model for all segments of the path and stress and displacement PM seismograms (\bar{u}_2 ,

$\bar{u}_{2,1}$, $\bar{u}_{2,3}$) as forcing functions produces RT integration results (hybrid seismograms) which may be directly compared with synthetics generated using only a single PM calculation. Synthetics generated for comparison to hybrid results by using a single PM calculation will be referred to as pure propagator matrix seismograms (PPM).

For the SH problem in Cartesian coordinates the expressions that need to be considered are for $\bar{\Gamma}_{22}$, $\bar{\Gamma}_{22,1}$, $\bar{\Gamma}_{22,3}$, \bar{u}_2 , $\bar{\sigma}_{xy}$, and $\bar{\sigma}_{zy}$. For the geometry (Fig. 2) used to couple surface waves from a finite element grid into a layered medium, through which the waves will be transmitted by convolution with propagator matrix generated Green's functions only the $\bar{\Gamma}_{22}$, $\bar{\Gamma}_{22,1}$, \bar{u}_2 , and $\bar{\sigma}_{xy}$ are used. However, $\bar{\Gamma}_{22,3}$ and $\bar{\sigma}_{zy}$ will also be derived for completeness. Should the geometry change so that it would be necessary to integrate over a horizontal surface such as the bottom of the grid then $\bar{\Gamma}_{22,3}$ and $\bar{\sigma}_{zy}$ would also be used.

The stresses $\bar{\Gamma}_{22,1}$, $\bar{\Gamma}_{22,3}$, $\bar{\sigma}_{xy}$, and $\bar{\sigma}_{zy}$ can be expressed in terms of spatial derivatives of displacements. Evaluating the numerical derivative gives a reasonable approximation to the desired stress values. However, a more direct, and more efficient, method for determining the values of the stresses is to evaluate the analytical expression for each stress derived from the corresponding analytical displacement expressions. The displacement and stress expressions for double-couple sources, line sources, and line source Green's functions are

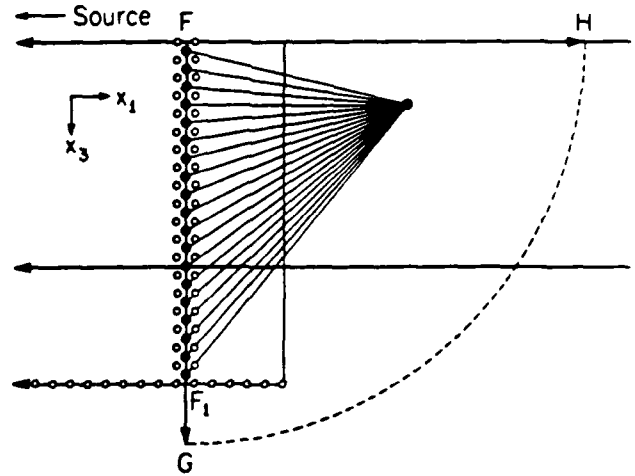


Figure 2. Geometry of FE to PM coupling. The two long horizontal lines show the free surface and the boundary between a layer and a half-space. The short vertical and horizontal lines show the boundaries of the finite element grid. The FE grid continues off the figure to the left. The open circles within the grid and along its bottom boundary represent nodes in the finite element grid. The solid circles represent element centres where the forcing functions $u_2(t)$ and $\sigma_{12}(t)$ are recorded during the FE calculations. The integration path of the representation theorem integral, C , is illustrated as the closed curve $FGHF$. The arrows at G and H indicate that the $x_1 = x$ coordinate at H and the $x_3 = z$ component at G both tend to infinity. The large dot within contour G denotes a receiver. The lines connecting the element centres (filled dots) and this receiver denote the line source Green's functions which propagate the forcing functions to the receiver. The line FG denotes the boundary between the 'complex' region to its left, and the 'simple' region to its right. The finite element grid extends into the 'simple' region to provide numerical stability.

presented in terms of propagator matrix notation in the Appendix. The evaluation of these expressions is accomplished using a generalized version of Harkrider's (1964) PM codes. The general form of the expressions and the propagator matrix notation used in the remainder of the present paper are summarized below.

The basic idea behind the propagator matrix method as implemented by Harkrider (1964, 1970) is to transmit the disturbance produced by a source within a layered half-space structure through that structure by combining terms that describe the source, the medium response, and the propagation effects. The terms that apply the effects of the propagation path in the z direction are in the form of propagator matrices. For source and receiver both at depth, they are separated into two parts, the propagation in z from the source to the surface, and the propagation in z from the surface to the receiver. An additional propagation term adds the effect of the propagation in the r coordinate. In most cases the general form of a modal displacement at a receiver at depth is

$$v(r, \phi, z) = S \Delta_L \left[\frac{v_s(h)}{v_0} \right]_H \left[\frac{v_R(z)}{v_0} \right]_H P \quad (10)$$

where S is a function of the source strength and geometry, Δ_L represents the medium response for a surface source and a surface receiver, P expresses the propagation effects in direction r ,

$$\left[\frac{v_s(h)}{v_0} \right]_H$$

is the term for transmitting the disturbance from the source depth to the surface which because of reciprocity can be expressed as a modal propagator from the surface to the source depth h , and

$$\left[\frac{v_R(z)}{v_0} \right]_H$$

is the propagator from the surface to the receiver depth. The subscript H denotes homogeneous, that is independent of and not containing a source. The terms within the square brackets represent matrix quantities, not simple ratios. If the source is a stress source rather than a displacement source then

$$\left[\frac{v_s(h)}{v_0} \right]_H$$

is replaced by

$$\frac{k_L}{\mu(h)} \left[\frac{\tau^s(h)}{v_0/c_L} \right]_H$$

where $\mu(h)$ is the rigidity at the depth of the source. If stress rather than displacement is to be recorded at the receiver, then

$$\left[\frac{v_R(z)}{v_0} \right]_H$$

is replaced by

$$\frac{k_L}{\mu(z)} \left[\frac{\tau^s(z)}{v_0/c_L} \right]_H$$

where z is the depth of the receiver.

2.3 FE to PM coupling

In the present study, a simple geometry, consisting of the same layer over a half-space for all segments of the path, is used as a test case to illustrate the method and assess its accuracy. The geometry of the simple problem is illustrated in Fig. 2. The coupling of FE seismograms into a layered media through which they are transmitted by the PM technique and the application of the representation theorem is accomplished by direct evaluation of the representation theorem integral as given in equation (4). The evaluation of the representation theorem integral on the contour, FGH (Fig. 2), will be discussed in three parts. First, the quantities used in the evaluation of the representation theorem integral on the subsegment FG of the contour, FGH, will be discussed. Then, the procedure used to estimate the value of this integral along FG will be explained. Finally, it will be shown that the contributions to the representation theorem integral from integration along segments GH and HF of the contour, FGH, are zero.

Before the particulars of the integration procedure can be discussed, each of the quantities in equation (4) must be defined. The integration surface for the segment FG is a line with the x -coordinate held constant, only the terms generated by setting $k=1$ in equation (4) need to be considered. Thus, the quantities of interest are, μ , u_y , σ_{xy} , Γ_{22} , and $\Gamma_{22,1}$. The displacement and stress seismograms at the element centres, illustrated as dots in Fig. 2, are recorded during the FE calculation. The element centre displacement u_y , and the element centre stress, σ_{xy} , are used as the u_2 and $\mu u_{2,1}$ terms, respectively. Line source Green's functions are calculated for the transmission of a unit line displacement, applied at each of the element centres illustrated as dots in Fig. 2, to the receiver point. These displacement and stress Green's functions, calculated using the PM method, are the Γ_{22} , and $\mu \Gamma_{22,1}$ terms in equation (4).

The representation theorem integral is evaluated using trapezoidal rule numerical integration of equation (4) along segment FG of contour FGH. The displacement and stress seismograms, and the displacement and stress Green's functions are time series. The time spacing between successive points in each time series is the time step duration, Δt , used in the FE calculation. Similarly, the distance between integration points along the integration surface is Δz , the grid spacing within the finite element grid. It should be remembered that the terms $\Gamma_{22} u_{2,k}$ and $\Gamma_{22,k} u_2$, in the representation theorem integral, equation (4), are convolutions. Thus, the products of the Green's functions and FE results, $\Gamma_{22} u_{2,k}$ and $\Gamma_{22,k} u_2$, are calculated in the Fourier transform domain, then, inverse Fourier transformed into the time domain and summed. Integration along the segment FG of the contour, FGH, is approximated by numerically integrating along the subsegment FF₁ of the segment FG, and assuming that the

contributions to the integral from the remainder of segment FG are negligible. The assumption that no significant contribution is made by integration along segment F₁G can be justified for the case where F₁ is chosen so that the earliest possible arrival of energy from a source at depth F₁ is later than the last arrival in the seismogram being considered. The uncertainties introduced when this criterion is not satisfied will be assessed in the next section. For the remainder of this discussion we will assume that the depth F₁ illustrated in Fig. 2 satisfies this criterion.

Next, the integration over the remaining two segments of the contour, C, will be shown to give no contribution to the representation theorem integral. The segment of the contour FH, along the free surface will be considered first. The integration surface for the segment FH of the contour, C, is a line with the z -coordinate held constant. Thus, only terms generated by setting $k = 3$ in equation (4) need to be considered. The free surface boundary condition applied on this surface states that at $z = 0$ the stress, $\mu u_{2,3}$, is zero. Since the Green's function, Γ_{22} , used in all the calculations also satisfies the free surface BC, the Green's function stress, $\mu \Gamma_{22,3}$, is also zero at $z = 0$. Therefore, one term in each product in the integrand of equation (4) is zero, causing the value of the integral along this portion of the contour, C, to be zero. Next, the segment GH of the contour, C, will be considered. As $\xi \rightarrow \infty$ the displacements u_2 and $u_{2,k}$ must approach zero since the radiation condition is satisfied. Again, one component of each product in the integrand of equation (4) is zero. Clearly, this makes the integrand zero and verifies that the section GH of contour, C, makes no contribution to the representation theorem integral.

Before summarizing the method one further simplification in the evaluation of the representation theorem integral will be presented. The integration of equation (4) along a vertical surface equivalent to contour FG can be expressed as

$$u_2(x, z) = \int_0^\infty \mu(\xi_3) [\Gamma_{22}(x, z; \xi_1, \xi_3) u_{2,1}(\xi_1, \xi_3) + \Gamma_{22,1}(x, z; \xi_1, \xi_3) u_2(\xi_1, \xi_3)] n_k d\xi_3. \quad (11)$$

The forcing functions, $u_2(\xi_1, \xi_3)$ and $\mu(\xi_3) u_{2,1}(\xi_1, \xi_3) = \sigma_{xy}$, can be expressed in terms of the variables used in the PM method. For the line source this is done by substituting expressions from the Appendix, eqs (A10) and (A11b), respectively, for $u_2(\xi_1, \xi_3)$ and σ_{xy} . The line source Green's functions, Γ_{22} and $\mu(\xi_3) \Gamma_{22,1}$ can be expanded in terms of PM variables by substituting equations (A12) and (A13b) for Γ_{22} and $\Gamma_{22,1}$, respectively. Performing these substitutions, and bringing all terms not dependent on ξ_3 out of the integral, yields equation (12a). For a point double-couple source the substitutions for the Green functions are unchanged. For the strike-slip point double-couple source, equations (A4) and (A8b) are substituted for u_2 and σ_{xy} to yield equation (12b). For the dip-slip point double-couple source equations (A5) and (A9b) are substituted for u_2 and σ_{xy} to yield equation (12c).

$$u_2(x, z) = \frac{-4\pi i \mu(h) e^{-ik_L z}}{k_L} \left[\frac{v_S(h)}{v_0} \right]_H \left[\frac{v_R(z)}{v_0} \right]_H \Delta_L^2 \times \int_0^\infty \mu(\xi_3) \left[\frac{v_R(\xi_3)}{v_0} \right]_H \left[\frac{v_S(\xi_3)}{v_0} \right]_H d\xi_3 \quad (12a)$$

$$u_2(x, z) = \frac{2M_0}{\omega} H_2 \left[\frac{v_S(h)}{v_0} \right]_H \left[\frac{v_R(z)}{v_0} \right]_H \Delta_L^2 \times \int_0^\infty \mu(\xi_3) \left[\frac{v_R(\xi_3)}{v_0} \right]_H \left[\frac{v_S(\xi_3)}{v_0} \right]_H d\xi_3 \quad (12b)$$

$$u_2(x, z) = \frac{2M_0}{\omega \mu(h)} H_1 \left[\frac{v_S(h)}{v_0} \right]_H \left[\frac{v_R(z)}{v_0} \right]_H \Delta_L^2 \times \int_0^\infty \mu(\xi_3) \left[\frac{v_R(\xi_3)}{v_0} \right]_H \left[\frac{v_S(\xi_3)}{v_0} \right]_H d\xi_3 \quad (12c)$$

where

$$H_k = e^{-ik_L(x-\xi_1)} \frac{\partial H_v^{(2)}(k_L r)}{\partial r} \Big|_{r=\xi_1} = \sqrt{\frac{\xi_1}{r}} \frac{\partial H_v^{(2)}(k_L r)}{\partial r} \Big|_{r=x}.$$

For all the types of sources discussed in the present paper both convolutions in the integrand of equation (11) produce identical expressions. Thus, it should be possible to accelerate the numerical evaluation of equation (11) by doubling the result of the integration of either convolution. This approach makes it unnecessary to record both displacement and stress seismograms in the FE calculations. Either one of these should be sufficient to calculate a 2-D SH representation theorem integral. This approach also allows the value of the representation theorem integral to be determined using half the number of the Green's functions. The representation theorem integral will be evaluated by doubling the value of the first term in equation (11).

In summary, the procedure used to propagate move sum seismograms along a path that may include one or more segments of non-plane-layered structure within a longer plane-layered path will be described below, and, for clarity, illustrated in the flow diagram in Fig. 3. The details of the FE to PM coupling technique discussed in this section will be emphasized in this description (see points (2)–(6) below), and its relation to the complete hybrid propagation technique will be demonstrated. The method can be broken down into eight steps.

(1) Choose a source type, a source depth, h , and a horizontal propagation distance, Δ_s , from the source to the finite element grid edge. This distance Δ_s is slightly less than the horizontal distance, Δ_{c1} , from the source to the edge of the first complex region. Also choose Δ_z , the vertical spacing between nodes in the finite element grid, and n , the number of nodes in a column in the finite element grid. The quantities n , Δ_z , and Δ_s , are chosen when designing the finite element grid containing the complex region (Regan & Harkrider 1989, Regan 1987). Use the parameter source type, h , n , Δ_s , and Δ_z , to generate a vertical section of PM seismograms containing one seismogram at the location of each node in the first column of the finite element grid. This set of seismograms will be called the FE forcing functions.

(2) The FE forcing functions are used as displacement time history constraints on the first column of finite element nodes. This passes the wavefield into the finite element grid providing a complete solution at every node within the finite element grid. A vertical section of displacement seismograms is recorded at a column of finite element centres a horizontal distance, Δ_{FE} , from the beginning of the finite element grid. This set of seismograms will be called the RT forcing functions. $\Delta_s + \Delta_{FE}$ is slightly larger than the

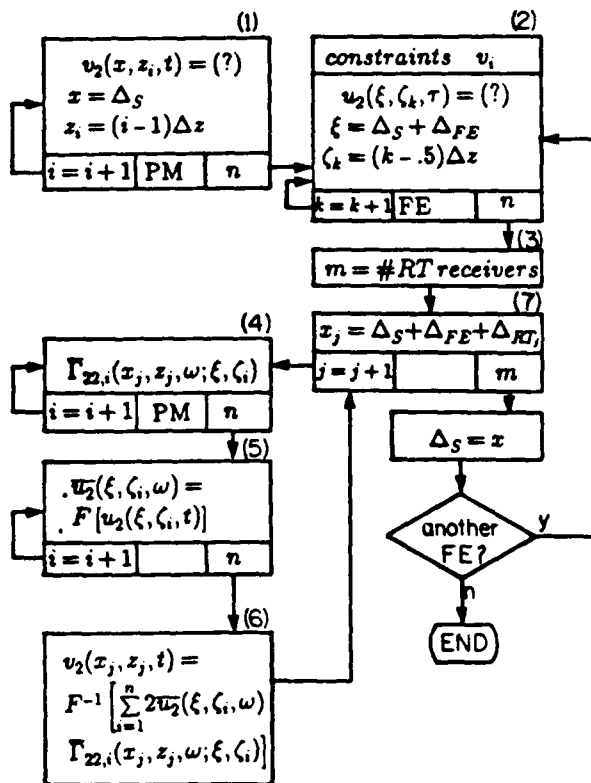


Figure 3. A flow diagram of the generation of a hybrid synthetic mode sum seismogram. The numbers in parentheses above some boxes relate the procedure within that box to a step number in the summary of the method in the text. To avoid double subscripts in the figure $\xi = (\xi, \zeta)$, and $x = (x, z)$. As in the text, a bar over a quantity indicates the Fourier transform of that quantity. The three small boxes along the bottom of boxes (1), (2), (4), and (5) indicate a loop. The variable in the left-most box indicates the incremented variable in the loop. The centre box is used to indicate the technique used to calculate the quantity. The right-most box shows the largest possible value of the increment variable.

horizontal distance from the source to the end of the region of complex structure and Δ_{FE} is chosen when designing the finite element grid.

(3) Choose the number, j , and locations, (x, z) , of desired receivers. The horizontal distance between a receiver and $\Delta_s + \Delta_{FE}$ is Δ_{RT} . If the path from $\Delta_s + \Delta_{FE}$ to the final receiver locations contains another complex region a complete depth section of hybrid seismograms is needed and $j = n$, and $\Delta_{RT} \leq \Delta_{c_0} - (\Delta_s + \Delta_{FE})$. The horizontal distance from the source to the edge of the next finite element grid is Δ_{c_0} .

(4) Calculate line source stress Green's functions. One Green's function is calculated to transmit the disturbance at each element centre to a receiver.

(5) Fourier transform the displacement seismograms in the set of RT forcing functions.

(6) For each element centre, multiply the displacement seismogram from the set of RT forcing functions with the stress Green's function which transmits that displacement seismogram to the receiver. Then, add the resulting product seismograms for all element centres on the depth section and multiply the resulting sum by $2\Delta z$. Inverse Fourier

transform the result to give the time domain displacement seismogram at a receiver.

(7) Repeat steps (4)–(6) for each of the j receivers chosen in (3). If another complex region lies in the path from the locations of j to the final receivers this repetition will produce a new set of FE forcing functions. Otherwise the final solution has been reached.

(8) Repeat steps (2)–(7) to propagate across the next complex region.

2.4 Uncertainty estimates and modal filtering for RT coupling

As stated in Section 2.3, the evaluation of the representation theorem along path FG (Fig. 2) is in practice, carried out only along subsegment FF₁. The contributions to the representation theorem integral from integration along subsegment F₁G are assumed to be zero. To insure that the contribution from F₁G is zero, the earliest possible arrival from a source at depth F_1 must be later than the end of the hybrid seismogram being calculated. To rigorously apply this condition, when a seismogram duration of 55 s, a reasonable duration for L_s at $\Delta_s = 1000$ km, is used requires that F_1 lie at a depth in excess of 250 km. FE calculations extending to such depths would be prohibitive. At larger distances the L_s seismogram has even longer durations requiring the integration surface to extend yet deeper. Thus, it is desirable to assess the size of the contributions along subsegment F₁G when the depth of F_1 is considerably smaller than would ideally be the case, and to determine the minimum values of the depth F_1 that will result in acceptable solutions. Fortunately, it is straightforward to derive a simple relation expressing the mode by mode accuracy for a given F_1 , and grid spacing (Δz). This relation can be simply and rapidly evaluated before RT integration coupling is attempted. The mode by mode uncertainty estimates can then be used to assess the effect of a particular choice of F_1 , Δz , and the time spacing on the accuracy of the hybrid synthetics and to choose optimal values for F_1 and Δz .

To derive the expression for mode by mode integration accuracy we return to the expression of the representation theorem integral along FG in terms of propagator matrix notation (equation 12). Comparing the quantities outside the integral, in each equation in (12), with the expression for displacement due to the corresponding source in a layered medium, equation (A10) to equation (12a), equation (A4) to equation (12b), and equation (A5) to equation (12c), allows equation (12) to be rewritten as

$$u_2(x, t) = u_2(x, t) * 2\Delta_L \int_0^{\infty} \mu(\xi_3) \left[\frac{v_R(\xi_3)}{v_0} \right]_H \left[\frac{v_S(\xi_3)}{v_0} \right]_H d\xi_3. \quad (13)$$

Define I_1 to be the relation

$$I_1 = \int_0^{\infty} \mu(\xi_3) \left[\frac{v_R(\xi_3)}{v_0} \right]_H \left[\frac{v_S(\xi_3)}{v_0} \right]_H d\xi_3. \quad (14)$$

This immediately leads to the relation

$$2\Delta_L I_1 = 1. \quad (15)$$

Evaluation of this simple equation provides a direct estimate of the accuracy of the integration on a mode by mode basis.

The estimate of the accuracy is obtained by evaluating the I_1 integrand at each integration point used in the RT integration, for each frequency on each branch of the dispersion curve used. For each single frequency mode the quantity on the left hand side of equation (15) is determined at each integration point and summed over the integration surface. If the solution were perfect with no error present, then the sum would be exactly one. In practice the sum departs from one by some amount which gives an estimate of the size of the minimum error that could be expected in that mode in the RT integration results. The estimate is a minimum since it does not account for the phase of the arrivals nor for possible errors in that phase. The evaluation of the error using this relation is much faster than comparing results from multiple applications of RT integration coupling.

An additional result obtained from equation (14) allows a simple method of modal filtering to be defined. It is well known that if i and j represent two different modes for a given period, ($k_i \neq k_j$ for $\omega_i = \omega_j$), then the orthogonality relation for Love waves states that

$$\int_0^\infty \mu(z) v_i(z) v_j(z) dz = 0 \quad i \neq j. \quad (16)$$

Comparing equations (16) and (14), and equating

$$v_i = \left[\frac{v_R(\xi_3)}{v_0} \right]_H,$$

and

$$v_j = \left[\frac{v_S(\xi_3)}{v_0} \right]_H$$

shows that equation (13) is a form of the orthogonality relation. At this point it is useful to notice that the two

$$\left[\frac{v_R(\xi_3)}{v_0} \right]_H$$

terms in the equation (13) each have separate origins. One originates with the forcing functions and the other with the Green's functions. Thus, any single modes not common to both the

$$\left[\frac{v_R(\xi_3)}{v_0} \right]_H$$

term from the forcing function and the

$$\left[\frac{v_S(\xi_3)}{v_0} \right]_H$$

term from the Green's function will produce zero contribution to the resulting hybrid result. This implies that the only modes present in both the Green's functions and the forcing functions will be present in the RT integration results. Thus, choosing Green's functions with a subset of the modes present in the forcing function will produce a filter that gives RT integration results that contain only that subset of modes.

3 RT COUPLING OF ANALYTIC SEISMOGRAMS AND GREEN'S FUNCTIONS

In this section the validity and accuracy of the numerical implementation of the representation theorem integration

coupling technique will be discussed in detail. In the following discussions a seismogram resulting from a RT integration will be referred to as a hybrid seismogram. However, since the representation theorem integral can be evaluated regardless of the method used to generate the forcing functions, easily generated PM forcing functions are used in most tests of the accuracy of the coupling technique, rather than more computationally intensive FE forcing functions. A single test using FE forcing functions is presented for completeness. All the numerical experiments discussed below use the same layer over a half-space model for all portions of the path allowing hybrid results to be directly compared with PPM results. In all cases the layer has a thickness of 32 km, an SH wave velocity 3.5 km s^{-1} , and a density 2.7 g cm^{-3} . The half-space has SH wave velocity 4.5 km s^{-1} and density 3.4 g cm^{-3} .

In the following sections the results of tests of several aspects of the representation theorem integration coupling technique and Green's function filtering will be presented. First, the estimation of uncertainties is discussed, and the values of Δz , Δt and F_1 are chosen. Then, results of the RT integration for the fundamental mode and for each of the first five overtones are presented to illustrate where the discrepancies between the RT results and the analytical results originate. Mode sum results for a line source and for a point source are then presented. Modal filtering of FE or hybrid results is then discussed, and examples of its efficiency are presented. Before these results can be discussed the sets of forcing functions and Green's functions used in the tests need to be explained.

The forcing functions used are the displacement and stress seismograms for a source depth of 8 km. They are evaluated at positions corresponding to the element centres of the right-most column of elements in a FE grid with horizontal and vertical spacing of 0.5 km, whose right-hand edge lies $\Delta_r = 1500.25 \text{ km}$ from the source. Thus, the seismograms are evaluated at points along a vertical surface 1500 km from the source, at depth intervals of 0.5 km, beginning at a depth of 0.25 km below the surface. Separate sets of forcing functions were generated for the fundamental mode and for each of the first five higher modes. Also, an additional set of forcing functions was calculated by summing over the fundamental and the first five higher modes. Single mode and mode sum forcing functions were determined for both a line source and a strike-slip point source. Similarly mode sum and single mode Green's functions were evaluated for a line source at each of the locations where displacement and stress forcing functions were evaluated for a line source at each of the locations where displacement and stress forcing functions were determined and a receiver at the surface. Single mode and mode sum Green functions for a propagation distance of $\Delta_{RT} = 100$, and mode sum Green functions for propagation distances of $\Delta_{RT} = 50, 100, 150, 250, 500$, and 1000 km are used. The representation theorem integration surface for all RT integration examples extended to a depth of 50 km.

3.1 Analysis of uncertainties

Before representation theorem integration calculations are performed it is useful to consider the choices of Δt , the time step in the displacement and stress seismograms, Δ_r , the spacing between integration points, and F_1 , the vertical

extent of the integration surface. Once a desired level of accuracy has been defined and the highest frequency to be modelled has been chosen a reasonable set of values for these parameters can be determined. The values of Δz and F_1 are selected using the mode by mode estimator of accuracy discussed in Section 2.4. The tolerated level of uncertainty, $U = 1 - 2\Delta z I_1$, in the representation theorem integrations described in the present paper is 2 per cent. The translation of this tolerance level to values of Δz and F_1 is discussed below. The integral I_1 , equation (14), used to estimate the accuracy of the representation theorem integration is independent of Δt . The value of Δt is chosen so that $1/2\Delta t$ exceeds the highest frequency used in the time series. In practice it is inadvisable to use a value of Δt which is larger than half the minimum travel time for travelling the distance Δz , since this may cause increased errors at the shortest periods.

The effects of varying Δz were studied. Estimations of accuracy were determined for several values of F_1 and Δz . The resulting values of U were examined to determine the effect of changing Δz on the value of U . The results of this examination indicate that $U = U_0 \Delta z$, where U_0 is the uncertainty using $\Delta z = 1$ km. The choice of an acceptable value of Δz requires examination of the actual values of U . Table 1 shows the values of U for a small selection of periods on each branch of the dispersion curve. The uncertainty estimation which produced Table 1 used $\Delta z = 0.5$ km, and $F_1 = 50$ km, the values used in the RT integration tests below. These values of Δz and F_1 produce errors below $U = 0.02$ for most modes. The pattern of the variation of U with period seen in this table is typical of all the sample combinations of Δz and F_1 examined. The mode by mode values of U for each separate overtone, and for the fundamental show that U is small and approximately constant until the value of F_1 is reduced to a value comparable to λ , the wavelength for the mode being

considered. Further reduction of F_1 causes rapid increases in the value of U .

The effects of varying F_1 were also investigated. The values of U for several values of F_1 at each value of Δz were reexamined to determine the effect of changing the value of F_1 on the value of U . The period below which no uncertainty estimates exceeded 2 per cent was determined for each F_1 . The resulting minimum values of T for each F_1 , and for $U_0 = 0.4$, and $\Delta z = 0.5$, are plotted in Fig. 4. The curves in Fig. 4 are model-dependent and must be determined for each model used. All values of F_1 below the fundamental

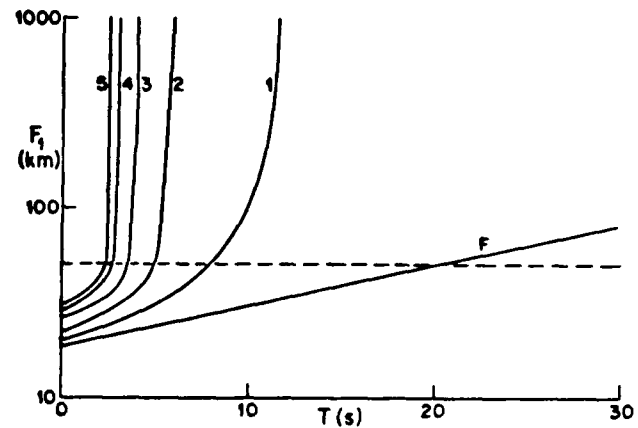


Figure 4. RT integration uncertainty estimates for $\Delta z = 0.5$ km. F_1 is the depth of the deepest integration point on the RT integration surface in kilometres. T is the period of the mode. Each curve is labelled to indicate which overtone it refers to. F refers to the fundamental mode, 1 to the first overtone, etc. Each curve is the locus of points (T, F_1) , where T is the maximum period for which a mode can be accurately reconstructed ($U \leq 0.02$) using RT integration to a depth F_1 . The horizontal dotted line indicates the 50 km value of F_1 used in the tests of the RT integration technique.

Table 1. RT integration uncertainty estimates

Period (s)	$U = 1 - 2\Delta z I_1$					
	Fund.	1st	2nd	3rd	4th	5th
500.0000	0.9948					
90.0000	0.8456					
60.0000	0.6726					
30.0000	0.1732					
20.0000	0.0234					
14.0000	0.0069					
11.4000		0.4701				
10.0000	0.0124	0.3129				
8.0000	0.0135	0.0212				
6.0000	0.0142	0.0098				
5.7000			0.3940			
4.0000	0.0148	0.0135	0.0091			
3.8000			0.0102	0.3003		
2.8000				0.0093	0.0526	
2.5000		0.0147	0.0136	0.0112	0.0046	
2.2000				0.0125	0.0091	0.0047
2.0000	0.0152	0.0149	0.0143	0.0132	0.0109	0.0056
1.6000	0.0154	0.0151	0.0148	0.0142	0.0131	0.0112
1.2001	0.0154	0.0153	0.0151	0.0148	0.0143	0.0136
0.8001	0.0154	0.0154	0.0154	0.0152	0.0151	0.0148
0.4000	0.0158	0.0155	0.0155	0.0158	0.0155	0.0154
0.2000	0.0190	0.0159	0.0161	0.0147	0.0156	0.0161
0.1000	0.0130	1.7330	0.0096	0.0085	0.0080	0.0078

mode curve produce uncertainty estimates in excess of $U = 0.02$, the specified cut-off level. The values of F_1 which fall below the part of a given overtone curve that is not near vertical produce uncertainty estimates in excess of $U = 0.02$ for that overtone. The almost vertical portions of the overtone curves, which have periods near the cut-off frequency of the overtone, indicate the values of F_1 that produce acceptable values of U for all periods. Fig. 4 provides a good way to estimate the minimum acceptable value of F_1 . Examining Fig. 4 for a given choice of F_1 on a overtone by overtone basis helps to predict and explain the causes of the inaccuracies noted below in the actual RT integration results. The value of F_1 chosen for use in the tests of the RT integration is 50 km, and is indicated by a dotted line in Fig. 4. This value is the minimum value of F_1 that produces acceptable values of U for the longer period modes on the overtone curves. The intersections of the $F_1 = 50$ km line and the curve for each mode indicates the expected uncertainties. The second through fifth overtones should be accurately represented at all periods. The first overtone will introduce somewhat higher uncertainties, although still acceptable, particularly between 8 and 11 s period. The fundamental mode will be accurate for periods less than about 21 s.

3.2 Demonstrating RT integration coupling

The first group of tests using the sets of forcing functions and Green's functions discussed above produced mode by mode hybrid results directly comparable to PPM synthetic single mode seismograms. PPM synthetic seismograms were calculated at $\Delta_s = 1600$ km for each of the fundamental mode and the first five overtones. For the fundamental mode and each of the first five overtones a set of single mode PM forcing functions, at $\Delta_s = 1500$ km, was combined with the corresponding single mode set of Green's functions, for a propagation distance of $\Delta_{RT} = 100$ km, according to the representation theorem integral. This produced a hybrid seismogram for that mode at $\Delta = 1600$ km to compare with the corresponding PPM single mode synthetic. Comparisons of the RT integration sums and the PPM synthetics for each individual mode are shown in Fig. 5. All the seismograms are bandpass filtered for periods between 1 and 25 s. The short period limit on the bandpass filter was chosen to improve the correspondence between the waveform of the PPM synthetic and the RT integration result for the same mode. The short period limit corresponds to the shortest period energy that can be transmitted through a finite element grid with grid spacing equal to the spacing of the

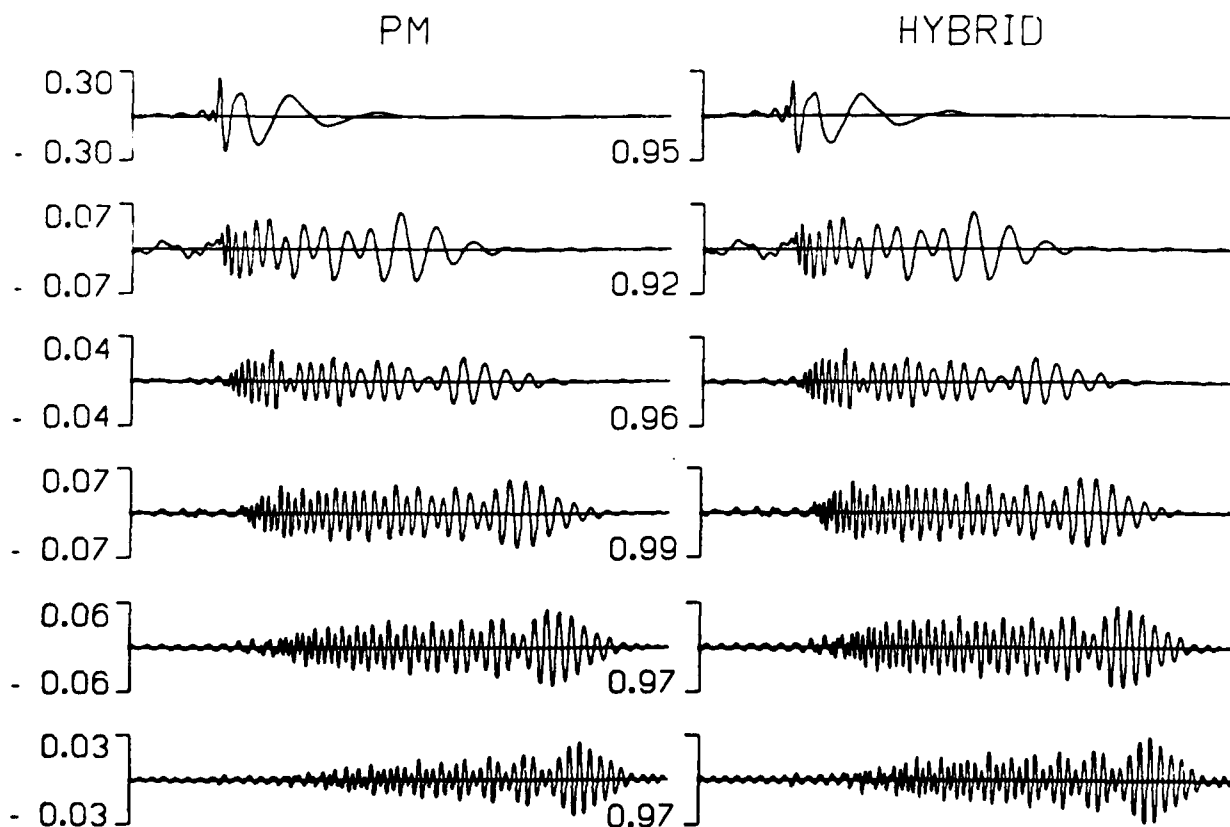


Figure 5. Mode by mode RT integration results bandpass filtered between 0.04 and 1 Hz. Two columns of seismograms are illustrated. The first column, labelled PM, shows PPM synthetics for each overtone and for the fundamental mode. The PPM synthetics are calculated for a line source at a depth of 8 km, at a distance $\Delta_s = 1600$ km from the source, using a single PM calculation. The second column, labelled hybrid, shows the hybrid synthetics for a PM path length of $\Delta_s = 1500$ km (line source) and a RT integration path length of $\Delta_{RT} = 100$ km. Each row of seismograms represent results for a different overtone. The first row shows the fundamental mode, the second row the first overtone, the third row the second overtone, the fourth row the third overtone, the fifth row the fourth overtone, and the sixth row the fifth overtone. Each row of seismograms is plotted using the same scaling. The numbers at the left hand edge of each row indicate the amplitude. The numbers between each pair of seismograms indicate the rms amplitude ratio of the hybrid seismogram to the PPM seismogram.

integration points in the RT integration. The long period cut-off of the filter is chosen to remove the long period component of the fundamental mode which cannot be accurately reconstituted without increasing F_1 . When the integration surface is truncated at progressively shallower depths the long period cut-off of the filter must be progressively reduced to maintain the fit between hybrid and PPM fundamental mode seismograms. As F_1 is reduced below 50 km the correspondence between the hybrid and PPM overtone seismograms for each overtone degenerates. As predicted in the error analysis the largest discrepancies between the PPM and hybrid results, for $F_1 = 50$ km, occur in the first overtone seismograms. Some discrepancies are seen in the fundamental mode due to the longer periods between 21 and 25 s which are not removed by the filter. The higher overtones fit well and approach the accuracy predicted by the minimum error estimates above.

In practice a full mode sum seismogram is the desired result of representation theorem integration coupling. The mode by mode tests discussed above illustrate the validity of the method and illustrate our understanding of the sources of possible uncertainty. To illustrate the accuracy obtained using mode sum forcing functions and Green's functions the hybrid synthetic resulting from RT integration using mode

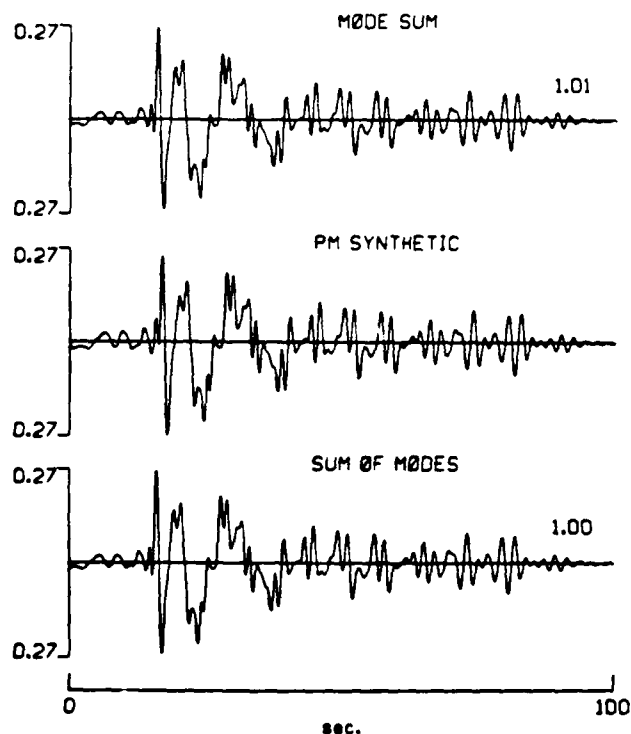


Figure 6. Mode sum RT integration results bandpass filtered between 0.04 and 1 Hz. The centre seismogram is a PPM seismogram for a line source at a depth of 8 km at a distance $\Delta_s = 1600$ km from the source. The upper-most and lower-most seismograms are hybrid seismograms for a PM (line source) path length of $\Delta_s = 1500$ km and a RT integration coupling path length of $\Delta_{RT} = 100$ km. The seismogram labelled mode sum was calculated using a single RT integration of mode sum, line source, forcing functions and mode sum Green's functions. The seismogram labelled sum of modes is a sum of the single mode RT integration results shown in Fig. 4.

Seismic representation theorem coupling

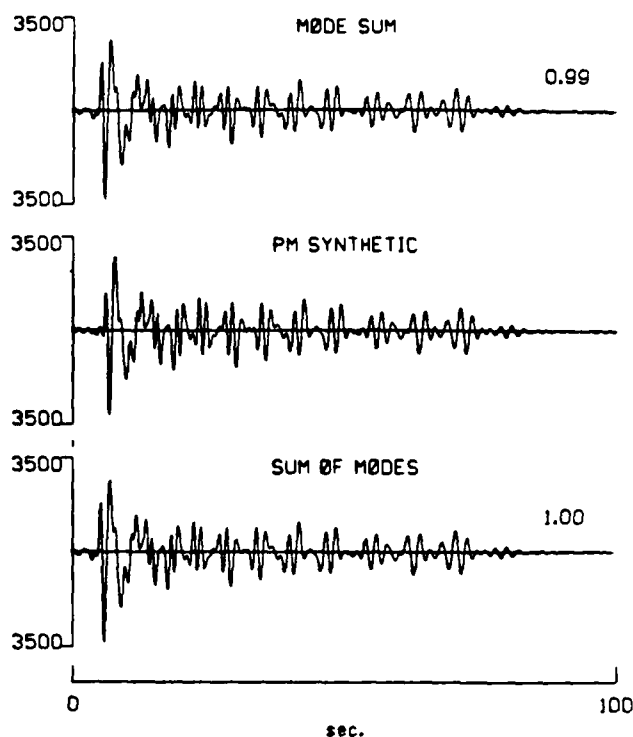


Figure 7. Mode sum RT integration results. PM seismograms are calculated for a strike-slip point double-couple source. Other details as in Fig. 6.

sum forcing functions and Green's functions is compared with the corresponding PPM mode sum synthetic. Fig. 6 shows results using a line source, and Fig. 7 shows results using a point source. The agreement in amplitude and waveform between the PPM and hybrid mode sum results is excellent. The sum of modes synthetic calculated as a sum over the single mode hybrid results shown in Fig. 5 gives a similar result. The agreement between the mode sum hybrid seismogram and the sum of single modes hybrid seismogram provides an independent check and the validity of the filtering technique, since any cross-terms that did not cancel due to orthogonality would appear as deviations between the two sets of resulting seismograms. That is, cross-terms present in the mode sum result would not be present in the sum of modes result.

3.3 Demonstration of Green's function filtering

Next, a series of calculations investigating the accuracy and efficiency of the Green's function filtering technique will be discussed. The Green's function filtering method uses Green's functions, containing only a subset of the modes present in the forcing functions, as a filter to extract only those modes from the forcing functions. In particular, the single mode sets of Green's functions are used in the representation theorem integral along with the mode sum set of forcing functions. The resulting hybrid seismograms contain energy only in the single mode present in the Green's function. A representation theorem integration was performed using each single mode set of Green's functions and the set of mode sum forcing functions. As an example results using the third higher mode Green's functions and a

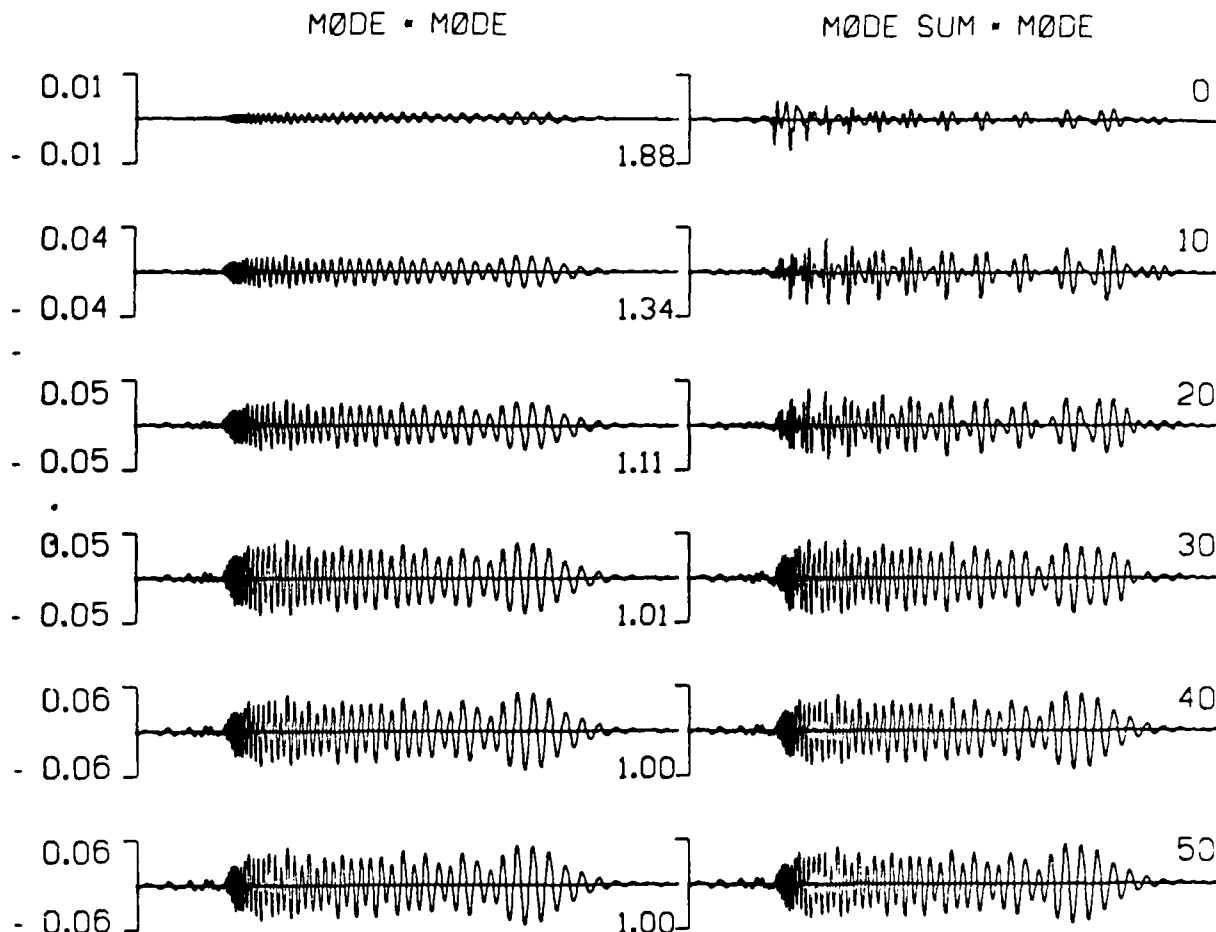


Figure 8. Green's function filtering using the third overtone as an example. All illustrated seismograms are bandpass filtered between 0.04 and 1 Hz. The results of a different RT integration are presented in each column. Both columns show hybrid seismograms for a line source at a depth of 8 km and a distance $\Delta_s + \Delta_{RT} = 1600$ km from the source. In both cases the PM path length is $\Delta_s = 1500$ km, and the RT integration path length is $\Delta_{RT} = 100$ km. In the first column, labelled mode * mode, the hybrid seismograms are derived using the third overtone forcing functions and the third overtone Green's functions. In the second column, labelled mode sum * mode, the hybrid seismograms are derived using the mode sum forcing functions and the third overtone Green's functions. Each pair of seismograms is plotted using the same scale, but the scale changes from pair to pair. The amplitude is indicated at the left end of each pair of seismograms. The RT integration begins at the surface and proceeds down FF_1 (Fig. 2) to F_1 . The first row of seismograms is a single convolution, the sum down to a depth of 0.25 km. The second row is the sum of 21 convolutions, and includes all integration points to a depth of 10 km. This pattern continues with the depth of the deepest point included in the integration indicated to the right of each pair of seismograms. The numbers between the pairs of seismograms indicate the rms amplitude ratios of the mode sum * mode seismograms to the mode * mode seismograms.

line source are shown in Fig. 8. When a depth of $F_1 = 50$ km is reached the waveforms are indistinguishable and the amplitudes agree to within less than 1 per cent. Studying similar plots for each overtone and for the fundamental mode shows several trends that hold for both point sources and line sources. In general the integration must proceed to a depth F_1 of about 30 km before the waveforms of the filtered mode sum seismograms closely resemble those of the single mode hybrid results. For the third to fifth overtones the filtered results at $F_1 = 50$ km and the analytical results agree in amplitude (rms amplitude differ by <1 per cent) and are not visibly different in waveform. Integration over the full 50 km is necessary to stabilize the results. Integration to depths greater than 50 km does not improve the correspondence between hybrid and filtered results. For the first and second overtones integration to

depths greater than 50 km improves the results slightly due to better fits at longer periods. For the fundamental mode increasing F_1 allows longer period energy to be modelled.

Fig. 9 illustrates the mode by mode results of the RT integrations discussed above for $F_1 = 50$ km. For the fundamental mode and all illustrated overtones the waveforms of the mode * mode hybrid results and the mode sum * mode results are essentially identical. The rms amplitude ratio of the two different types of hybrid result is one for each pair of seismograms shown. In fact even the peak-to-peak amplitudes agree to within less than 1 per cent for all modes. Clearly the Green's function filtering technique is accurate and promises to be very useful in the interpretation of hybrid seismograms for paths including complex structures. In summary, the effect of using a set of Green's functions containing a subset of the modes present

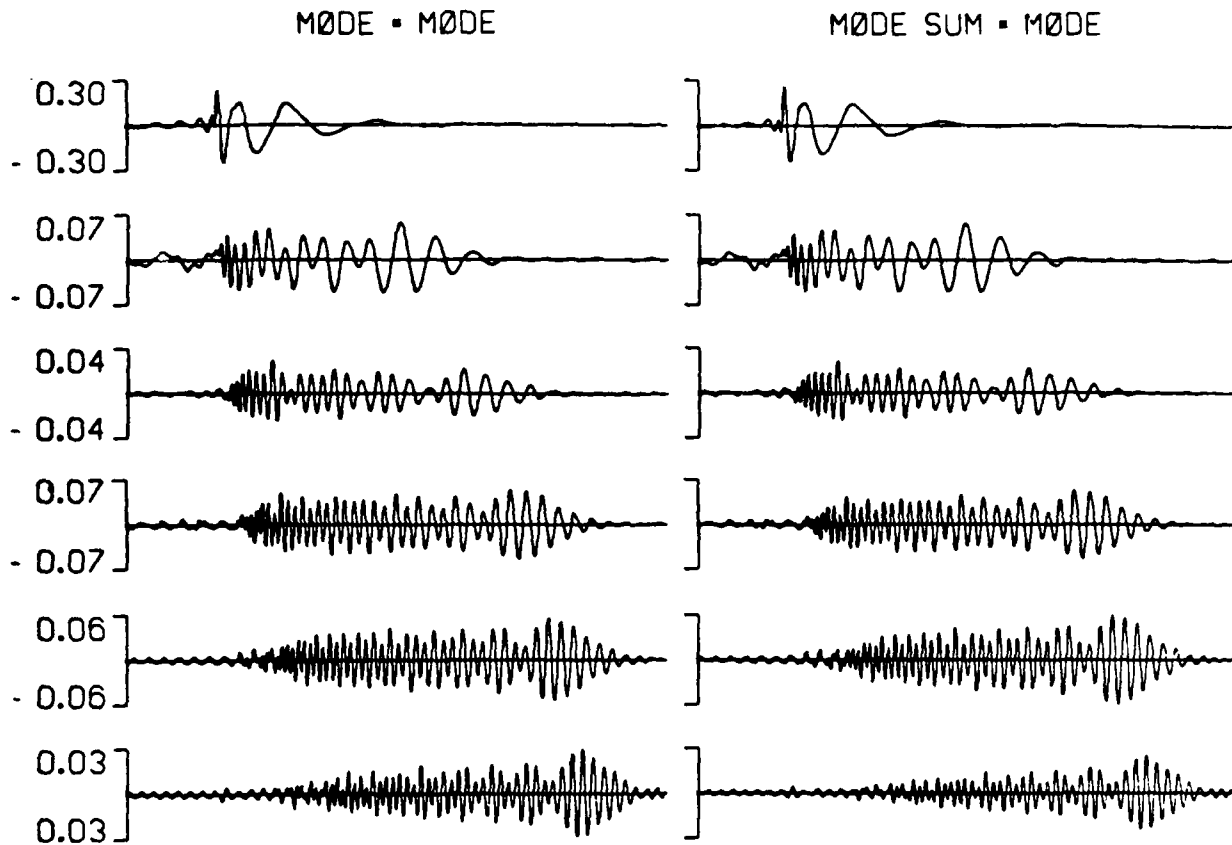


Figure 9. Mode by mode results of Green's function filtering. All seismograms are bandpass filtered between 0.04 and 1 Hz. The first row shows results for the fundamental mode, each successive row shows results for the next higher overtone. The results of a different RT integration are presented in each column. Both columns show hybrid seismograms for a line source at a depth of 8 km and a distance $\Delta_s + \Delta_{RT} = 1600$ km from the source. In both cases the PM path length is $\Delta_s = 1500$ km, and the RT integration path length is $\Delta_{RT} = 100$ km. In the first column, labelled mode = mode, the hybrid seismograms are derived using the single mode forcing functions and the single mode Green's functions for that same mode. In the second column, labelled mode sum = mode, the hybrid seismograms are derived using the mode sum forcing functions and the single mode Green's functions. The extent of the integration surface, F_1 , is 50 km for all illustrated seismograms. The amplitude scale is given to the left of each pair of seismograms. The rms amplitude ratios of the mode sum = mode seismograms to the mode = mode seismograms is one in all cases and is thus not illustrated on the diagram.

in the set of forcing functions is to produce an efficient filter that allows only the modes common to both sets to appear in the hybrid result.

3.4 RT integration coupling and Green's function filtering using FE forcing functions

The examples of representation theorem integration coupling discussed to this point demonstrate the validity of coupling a wavefield expressed in terms of displacement seismograms, generated using the PM method, recorded at equal intervals along a vertical boundary, across that boundary. The wavefield is coupled across the boundary by RT integration, evaluation of equation (4) along that vertical surface, of the displacement seismograms and the appropriate line source Green's functions. It remains to be shown that RT integration coupling and Green's function filtering are valid when FE or FD displacement seismograms are used, and that the entire sequence of operations used to include a complex subsegment of a propagation path in that path is valid. The final example of RT coupling, presented in this section, addresses these questions.

The final example of RT coupling produces hybrid seismograms due to the propagation of energy from a source, through the first section of its path using the PM method, through the second section of its path using the FE method, and finally, through the last section of the path using RT integration coupling. Again, for this example, the entire path consists of a single simple plane-layered structure to allow direct comparison of the hybrid results to FPM results. A strike-slip double-couple point source at a depth of 8 km was used to generate a set of PM displacement seismograms along a vertical surface $\Delta_s = 1500$ km from the source. The spacing between the points at which these seismograms were recorded was 0.5 km. Each of these seismograms was used as a displacement time history constraint on a grid point along the left-hand edge of a finite element grid with grid spacing 0.5 km. The application of this set of displacement time history constraints to the end of the finite element grid completely specified the motion of all nodes within the finite element grid for the duration of the FE calculation. At a column of nodes within the finite element grid displacement seismograms were recorded during the FE calculation. The

displacement seismograms were recorded at column 101, a distance Δ , $\Delta_{FE} = 1550$ km from the source. These displacement seismograms were then used as forcing functions in a representation theorem integration. The distance propagated using representation theorem integration varied from 50 to 1000 km.

The results of the example described in the previous paragraph are illustrated in Fig. 10. The correspondence between the hybrid seismograms and the PPM seismograms is excellent. As the distance propagated using RT integration coupling increases the PPM seismograms appear to decay in amplitude faster than the hybrid seismograms despite the fact that the rms amplitude ratios remain relatively constant. This is an artefact of the fact that the rms amplitude ratio has the decay correction $\sqrt{\xi_1/x}$ from equation (12) included in it but the plotted seismograms are not scaled by the correction factor. This allows one to see the increasing importance of the 2-D to 3-D propagation correction as the portion of the path traversed using the 2-D finite element and representation theorem integration

coupling techniques increases with respect to the portion of the path traversed using the 3-D propagator matrix propagation. The origin time of each seismogram in Fig. 10 is slightly different. When absolute times are considered the first peaks in each pair of seismograms align exactly.

Next, this example will be extended to present the results of a Green's function modal filtering of one of the hybrid seismograms in Fig. 10. The hybrid seismogram propagated $\Delta_{RT} = 100$ km using representation theorem integration is chosen for this analysis so that the single mode Green's functions already calculated can be used in the modal filtering analysis. The location at which this seismogram is recorded will be referred to as A. Since a single layer over a half-space structure is used for the entire path it is simple to predict that the transmission coefficients across the 'complex' region within the finite element grid should all be one and that the reflection coefficients should all be zero. Thus, the hybrid single mode seismograms recorded at A should be identical to the single mode PPM seismograms for a propagation path length of Δ , $\Delta = 1650$ km. Fig. 11 shows

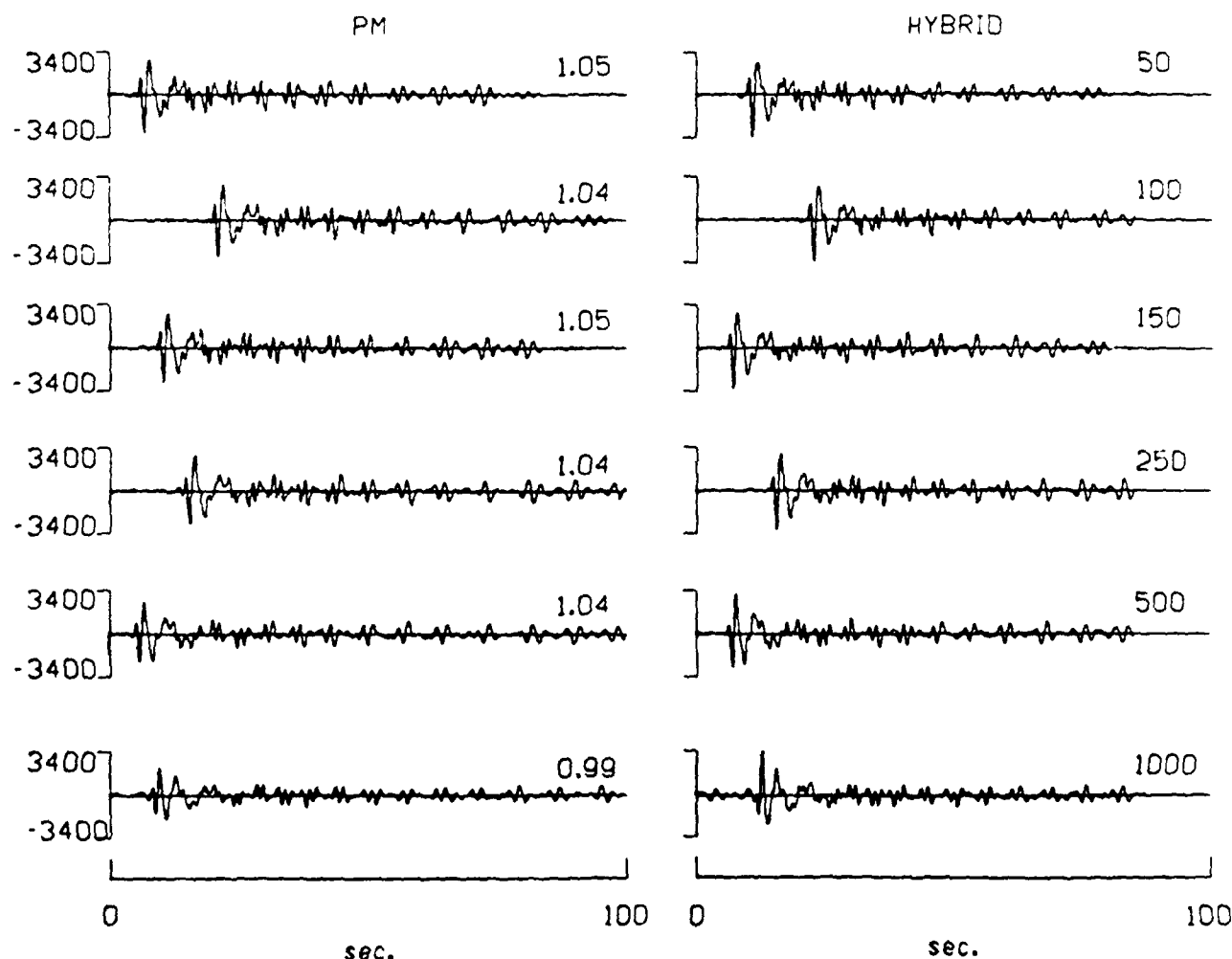


Figure 10. Mode sum RT results using FE forcing functions. All seismograms are bandpass filtered between 0.04 and 1 Hz. The first column show PPM results for each case, the second column shows the corresponding hybrid results. Each row illustrates results for a different propagation distance. For all hybrid seismograms the initial PM propagation distance from the source to the finite element grid edge is $\Delta_s = 1500$ km, and the propagation distance within the grid is $\Delta_{FE} = 50$ km. The distance, in kilometres, propagated using RT integration coupling, Δ_{RT} , is indicated to the right of each pair. The rms amplitude ratios of the hybrid results to the PPM results are shown between each pair of seismograms. Origin times of the plotted seismograms are arbitrary. Arrows below each seismogram indicate the arrival times.

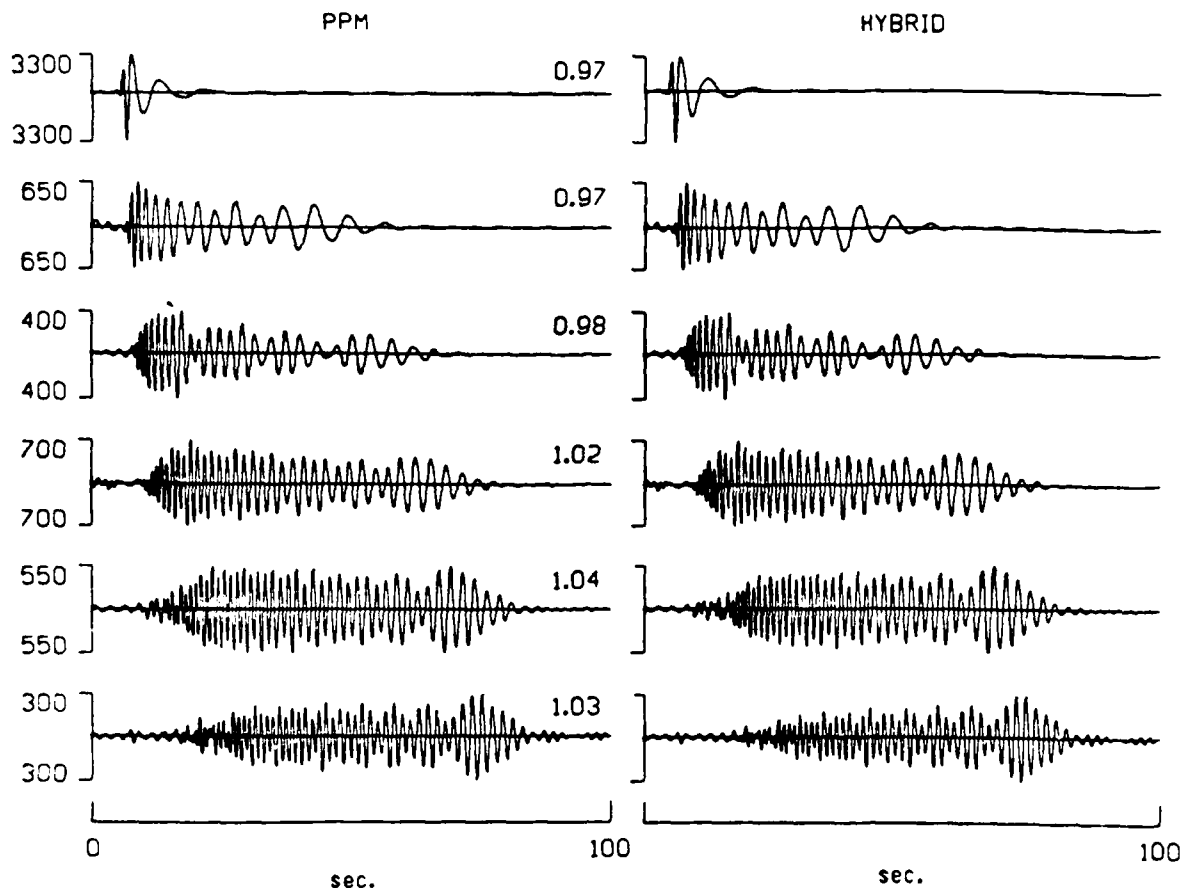


Figure 11. Example of Green's function filtering of hybrid synthetics. The hybrid seismogram for receiver A, with $\Delta_s = 1500$ km source to FE distance, $\Delta_{FE} = 50$ km FE propagation distance, and $\Delta_{RT} = 100$ km RT integration coupling propagation distance, shown in row 2 of Fig. 10 is analysed using mode by mode filtering. In the left-most column PPM seismograms for each single mode at receiver A are illustrated. In the right-most column hybrid filtered seismograms calculated using RT integration with the time series $u(A, t)$ recorded during the FE calculations as forcing functions and the single mode Green's functions for $\Delta_{FE} = 100$ km propagation are illustrated. The hybrid to PPM seismogram rms amplitude ratios are illustrated between each pair of seismograms. Amplitudes are shown to the left of each pair of seismograms.

mode by mode results which verify this. The hybrid single mode seismograms illustrated in Fig. 11 are calculated using the FE displacements, which contain modes on the fundamental and first five overtone branches, as forcing functions and single mode Green's functions.

For a real case the complex region within the finite element grid would produce mode to mode conversions and conversions to body waves which would cause non-unitary transmission coefficients and non-zero reflection coefficients. A modal analysis of a hybrid mode sum seismogram would require the calculation of the reflection and transmission coefficients for each mode. To determine the transmission coefficient the ratio of the hybrid seismogram to the PPM seismogram would be taken at a point which the wavefront reaches after propagating through the complex region. To determine the reflection coefficient the ratio of the energy in the seismogram resulting when the hybrid and PPM seismograms are differenced and the energy in the PPM seismogram would be taken at a point which the incident wavefront reaches before propagating through the complex region.

4 CONCLUSIONS

In this paper a method for propagating a mode sum wavefield through a long path containing short segments which include complex regions is presented. The wavefield is produced by a point double-couple or line source and is propagated from that source through a plane-layered medium to the edge of a mixed region using the propagator matrix method (PM). The mixed region must contain the complex region and small sections of the layered structures adjoining each end of the complex region. The wavefield is passed across the boundary between the plane-layered region and the mixed region using the technique discussed by Regan & Harkrider (1989). The wavefield is then propagated through the mixed region using the finite element (FE) method. After propagation through the mixed region, the FE wavefield is sampled at each node along a vertical surface. This surface must lie in the plane-layered region which the wavefield reaches after it has propagated through the complex region. The resulting seismograms are used as forcing functions in the representation theorem

integral which propagates the wavefield from the edge of the mixed region through the remainder of the second plane layered region.

In this paper the mathematical implementation of the representation theorem integration coupling method is developed and tested. A method of estimating the accuracy of the technique, based on the orthogonality of Love waves, is presented. Finally, the Green's function filtering technique for modal analysis of FE or hybrid results is derived and illustrated. A simple model which consists of a layer over a half-space is used for all sections of the propagation path in all tests described in this paper. This simple model allows the hybrid seismograms to be directly compared with seismograms generated using a single application of the propagator matrix method for the entire path (PPM). The agreement between hybrid seismograms and PPM seismograms for examples illustrated in this paper demonstrates the validity of the representation theorem integration coupling method. It shows that the method can produce hybrid synthetic seismograms of high accuracy. Evaluation of a simple expression derived from the expressions for the hybrid seismograms in propagator matrix notation and the corresponding expression of the orthogonality relation for Love waves allows one to evaluate the expected uncertainty for any single mode contribution to the hybrid seismogram. Evaluation of the uncertainty for each single frequency mode included in a mode sum seismogram has been demonstrated to be a good indicator of the sources of uncertainties in hybrid seismograms. The modal uncertainties have also been shown to provide an easily evaluated predictor of the vertical extent of the integration surface, and the minimum spacing between evaluation points on that surface, needed to provide a given level of accuracy. Results presented in this paper indicate that the Green's function filtering method provides accurate hybrid seismograms containing only those modes present in both the representation theorem integration forcing functions and the Green's functions used as a filter. Thus, single mode Green's functions yield hybrid results containing only a single mode.

ACKNOWLEDGMENTS

J. Regan conducted part of this research while a Canadian Government Laboratory Visiting Fellow at Geophysics Division, Geological Survey of Canada, Ottawa. This research was supported in part by the Advanced Research Projects Agency of the US Department of Defense and was monitored by the US Air Force Geophysics Laboratory under Contract F19628-87-K-0028. Division of Geological Sciences Contribution No. 4668. Geological Survey of Canada Contribution No. 30788.

REFERENCES

- Ali, K. & Richards, P. G., 1980. *Quantitative Seismology*, W. H. Freeman, San Francisco.
- Alsop, L. E., 1966. Transmission and reflection of Love waves at a vertical discontinuity, *J. geophys. Res.*, **71**, 3969-3984.
- Alsop, L. E., 1968. An orthonormality relation for elastic body waves, *Bull. seism. Soc. Am.*, **58**, 1949-1954.
- Boore, D., 1970. Love waves in nonuniform wave guides: finite difference calculations, *J. geophys. Res.*, **75**, 1512-1527.
- Bose, S. K., 1975. Transmission of SH waves across a rectangular step, *Bull. seism. Soc. Am.*, **65**, 1779-1786.
- Bouchon, M., 1981. A simple method to calculate Green's functions for elastic layered media, *Bull. seism. Soc. Am.*, **71**, 959-971.
- Bouchon, M., 1982. The complete synthesis of seismic crustal phases at regional distances, *J. geophys. Res.*, **87**, 1735-1741.
- de Hoop, A. T., 1958. Representation theorems for the displacement in an elastic solid and their application to elastodynamic diffraction theory, DSc thesis, Technische Hogeschool, Delft.
- Drake, L. A., 1972. Love and Rayleigh waves in nonhorizontally layered media, *Bull. seism. Soc. Am.*, **62**, 1241-1258.
- Drake, L. A. & Bolt, B. A., 1980. Love waves normally incident at a continental boundary, *Bull. seism. Soc. Am.*, **70**, 1103-1123.
- Frazier, G. A., Alexander, J. H. & Petersen, C. M., 1973. 3-D seismic code for the ILLIAC IV. *Systems, Science and Software Report SSS-R-73-1506*.
- Gregersen, S. & Alsop, L. E., 1974. Amplitudes of horizontally refracted Love waves, *Bull. seism. Soc. Am.*, **64**, 535-553.
- Gregersen, S. & Alsop, L. E., 1976. Mode conversion of Love waves at a continental margin, *Bull. seism. Soc. Am.*, **66**, 1855-1872.
- Harkrider, D. G., 1964. Surface waves in multilayered media. Part I. Rayleigh and Love waves from buried sources in a multilayered elastic half-space, *Bull. seism. Soc. Am.*, **54**, 627-679.
- Harkrider, D. G., 1970. Surface waves in multilayered elastic media, Part II. Higher mode spectra and spectral ratios from point sources in plane layered earth models, *Bull. seism. Soc. Am.*, **60**, 1937-1987.
- Hudson, J. A. & Knopoff, L., 1964. Transmission and reflection of surface waves at a corner: I. Love waves, *J. geophys. Res.*, **69**, 275-280.
- Kazi, M. H., 1978a. The Love wave scattering matrix for a continental margin (theoretical), *Geophys. J. R. astr. Soc.*, **52**, 25-44.
- Kazi, M. H., 1978b. The Love wave scattering matrix for a continental margin (numerical), *Geophys. J. R. astr. Soc.*, **53**, 227-243.
- Kennett, B. L. N., 1973. The interaction of seismic waves with horizontal velocity contrasts, *Geophys. J. R. astr. Soc.*, **33**, 431-450.
- Kennett, B. L. N. & Mykkeltveit, S., 1984. Guided wave propagation in laterally varying media - II. L_g -waves in north-western Europe, *Geophys. J. R. astr. Soc.*, **79**, 257-267.
- Knopoff, L. & Hudson, J. A., 1964. Transmission of Love waves past a continental margin, *J. geophys. Res.*, **69**, 1649-1653.
- Knopoff, L. & Mal, A. K., 1967. Phase velocities of surface waves in the transition zone of continental margins - I. Love waves, *J. Geophys. Res.*, **72**, 1769-1776.
- Knopoff, L., Mal, A. K., Alsop, L. E. & Phinney, R. A., 1970. A property of long-period Love waves, *J. geophys. Res.*, **75**, 4084-4086.
- Kosloff, D. & Frazier, G. A., 1978. Treatment of hourglass patterns in lower order finite element codes, *Int. J. Numeric. Analyt. Method.*, **2**, 57-72.
- Lysmer, J. & Drake, L. A., 1971. The propagation of Love waves across nonhorizontally layered structures, *Bull. seism. Soc. Am.*, **61**, 1233-1251.
- Lysmer, J. & Drake, L. A., 1972. A finite element method for seismology, in *Methods in Computational Physics*, **11**, *Seismology*, ch. 6, eds Alder, B., Fernbach, S. & Bolt, B. A., Academic Press.
- Martel, L., 1980. Love wave propagation across a step by finite elements and spatial filtering, *Geophys. J. R. astr. Soc.*, **61**, 639-677.
- Pec, K., 1967. Theoretical dispersion tables for Love waves propagating in a wedge and in a single nonhomogeneous layer with a linear velocity gradient, *Pub. Dominion Obs. Ottawa*, **35**.
- Regan, J. & Harkrider, D. G., 1989. Numerical modelling of SH L_g waves in and near continental margins, *Geophys. J.*, in press.
- Regan, J., 1987. Numerical studies of propagation of L_g waves across ocean continent boundaries using the representation theorem, *Ph D thesis*, California Institute of Technology, Pasadena, Ca.

- Sato, R., 1961a. Love waves propagated across transitional zone. *Japan. J. Geophys.*, 2, 117-134.
- Sato, R., 1961b. Love waves in case the surface layer is variable in thickness. *J. Phys. Earth.*, 9, 19-36.
- Zienkiewicz, O. C. & Cheung, H., 1967. *The Finite Element Method in Structural and Continuum Mechanics*, McGraw-Hill, New York.

APPENDIX A

In this appendix the expression for SH displacement and stress at a receiver at depth z due to a source at depth h are presented in terms of Harkrider's (1964) propagator matrix notation. First strike-slip and dip-slip double-couple sources are considered, then line source results are given. Finally, line source Green function displacements and stresses are developed.

The displacement for an arbitrary double-couple source follows directly from the expression for the SH displacement at depth z produced by a double-couple source of arbitrary orientation at depth h (Harkrider 1964, 1970).

$$[v(r, \phi, z, \omega)] = 2\pi i K_\alpha k_\beta^2 \mu \Delta_L \left\{ \left(\cos \lambda \sin \delta \cos 2\phi - \sin \frac{2\delta}{2} \sin 2\phi \right) \left[\frac{v_s(h)}{v_0} \right]_H \frac{\partial H_2^{(2)}(k_L r)}{\partial r} - (\sin \lambda \cos 2\delta \cos \phi + \cos \lambda \cos \delta \sin \phi) \times \left(\frac{1}{\mu(h)} \left[\frac{\tau^*(h)}{\dot{v}_0/c_L} \right]_H \right) \frac{\partial H_1^{(2)}(k_L r)}{\partial r} \right\} \left[\frac{v_R(z)}{v_0} \right]_H \quad (A1)$$

where

$$K_\alpha = \frac{-\tilde{M}(\omega)}{4\pi\rho\omega^2} = \frac{iM_0}{4\pi\rho\omega^3} \quad \dot{v}_0 = i\omega v_0 \quad (A2)$$

$$k_\beta^2 = \frac{\omega^2}{\beta^2} = \frac{\rho_s \omega^2}{\mu(h)} \quad k_L = \frac{\omega}{c_L} \quad \tau = i\tau^* \quad (A3)$$

In equations (A1)–(A3), λ is the strike of the double-couple source, δ is the dip, ϕ is the azimuth to the station, β is the SH wave velocity, ρ_s is the density at the depth of the source, h is the source depth, ω is the frequency, r is the distance from the source to the receiver, c_L is the Love wave velocity, $\mu(h)$ and $\mu(z)$ are respectively the rigidity at the source depth and at the receiver depth,

$$\left[\frac{v_s(h)}{v_0} \right]_H \quad \text{and} \quad \left[\frac{\tau^*(h)}{\dot{v}_0/c_L} \right]_H$$

are the terms that transmit the source disturbance in the z direction from the source to the surface,

$$\left[\frac{v_R(z)}{v_0} \right]_H$$

is the term that transmits the disruption in z from the surface to the receiver, and the term containing the Hankel function is the propagation term in the r direction. The source term is defined to contain all the angular dependence on δ , λ , and ϕ , as well as the term $2\pi i k_\beta^2 \mu K_\alpha$. The second equality in the first expression of equation (A2) assumes a step moment, that is $\tilde{M}(\omega) = M_0/i\omega$.

It is well known that a double-couple of arbitrary orientation can be expressed in terms of a linear

combination of double-couple sources of three types, vertical strike-slip ($\delta = 90^\circ$, and $\lambda = 0^\circ$), vertical dip-slip ($\delta = 90^\circ$ and $\lambda = 90^\circ$), and 45° dip-slip ($\delta = 45^\circ$ and $\lambda = 90^\circ$). Thus, results for these three fault types can be added to produce results for an arbitrary orientation, removing the necessity to repeat the entire procedure for each orientation to be studied. In fact, for SH waves, any fault geometry can be modelled using a linear combination of only the vertical dip-slip and the vertical strike-slip faults. Evaluating equation (A1) for each of these two fault types, yields the expressions used to determine displacement seismograms at a receiver at depth z due to a vertical strike-slip fault at depth h

$$[v(r, z)] = -\frac{M_0}{2\omega} \Delta_L \frac{\partial H_2^{(2)}(k_L r)}{\partial r} \left[\frac{v_s(h)}{v_0} \right]_H \left[\frac{v_R(z)}{v_0} \right]_H \quad (A4)$$

and due to a vertical dip-slip fault at depth h .

$$[v(r, z)] = -\frac{M_0}{2\omega} \Delta_L \frac{1}{\mu(h)} \frac{\partial H_1^{(2)}(k_L r)}{\partial r} \left[\frac{\tau^*(h)}{\dot{v}_0/c_L} \right]_H \left[\frac{v_R(z)}{v_0} \right]_H \quad (A5)$$

The analytical expressions for the stress components for SH waves from a point double-couple source follow directly from these expressions. Only the final term in equations (A4) and (A5) depend directly on z . From Harkrider (1964)

$$\frac{\partial}{\partial z} \left[\frac{v_R(z)}{v_0} \right]_H = -\frac{k_L}{\mu(z)} \left[\frac{\tau^*(z)}{\dot{v}_0/c_L} \right]_H \quad (A6)$$

All terms in equations (A4) and (A5) except the Hankel function are constant with respect to z . By expanding the Hankel function term in an asymptotic series for large r , and ignoring terms of order $1/r$, it can be shown that

$$\frac{\partial}{\partial r} \left(\frac{\partial H_2^{(2)}(k_L r)}{\partial r} \right) = -ik_L \frac{\partial H_2^{(2)}(k_L r)}{\partial r} \quad (A7)$$

Thus, taking the appropriate derivatives of the displacement expressions yields the expressions used to determine stress time histories at a receiver at depth z due to a vertical strike-slip fault at depth h

$$[\sigma_{xy}(r, z)] = k_L \frac{M_0}{2\omega} \Delta_L \frac{\partial H_2^{(2)}(k_L r)}{\partial r} \left[\frac{v_s(h)}{v_0} \right]_H \left[\frac{\tau^*(z)}{\dot{v}_0/c_L} \right]_H \quad (A8a)$$

$$[\sigma_{xy}(r, z)] = ik_L \mu(z) \frac{M_0}{2\omega} \Delta_L \frac{\partial H_2^{(2)}(k_L r)}{\partial r} \left[\frac{v_s(h)}{v_0} \right]_H \left[\frac{v_R(z)}{v_0} \right]_H \quad (A8b)$$

and due to a vertical dip-slip fault at depth h .

$$[\sigma_{xy}(r, z)] = k_L \frac{M_0}{2\omega} \Delta_L \frac{1}{\mu(h)} \frac{\partial H_1^{(2)}(k_L r)}{\partial r} \left[\frac{\tau^*(h)}{\dot{v}_0/c_L} \right]_H \left[\frac{\tau^*(z)}{\dot{v}_0/c_L} \right]_H \quad (A9a)$$

$$[\sigma_{xy}(r, z)] = \frac{ik_L \mu(z)}{\mu(h)} \frac{M_0}{2\omega} \Delta_L \frac{\partial H_1^{(2)}(k_L r)}{\partial r} \left[\frac{\tau^*(h)}{\dot{v}_0/c_L} \right]_H \left[\frac{v_R(z)}{v_0} \right]_H \quad (A9b)$$

The analytical expressions for stress due to a line source in a layered medium are found by a procedure similar to

that used above to obtain the stress expressions for the point double-couple source. The displacement at depth z due to a line source at depth h is

$$\{u_y(x, z)\} = 2\pi i \Delta_L \frac{\mu(h)}{k_L} \left[\frac{v_S(h)}{v_0} \right]_H \left[\frac{v_R(z)}{v_0} \right]_H e^{-\mu_L x}. \quad (\text{A10})$$

Therefore, the stresses for the 2-D line source are

$$[\sigma_{xy}(x, z)] = -2\pi i \mu(h) \Delta_L \left[\frac{v_S(h)}{v_0} \right]_H \left[\frac{\tau^*(z)}{v_0/c_L} \right]_H e^{-\mu_L x} \quad (\text{A11a})$$

$$[\sigma_{xx}(x, z)] = 2\pi \mu(h) \mu(z) \Delta_L \left[\frac{v_S(h)}{v_0} \right]_H \left[\frac{v_R(z)}{v_0} \right]_H e^{-\mu_L x}. \quad (\text{A11b})$$

Applying the same treatment to the expression for the displacement Green's function for a line source in a layered

half-space,

$$[\overline{F}_{22}(x, z; \xi_1, \xi_3)] = \frac{-i}{k_L} \Delta_L \left[\frac{v_S(\xi_3)}{v_0} \right]_H \left[\frac{v_R(z)}{v_0} \right]_H e^{-\mu_L(x-\xi_1)}, \quad (\text{A12})$$

gives expressions for $\overline{F}_{22,3}$, and $\overline{F}_{22,1}$. In this case a stress source term rather than a stress receiver term is needed. Thus, the depth derivative is taken with respect to the source term. The form of the depth derivative is identical to that in equation (A6) except that z is replaced by h . Therefore the derivatives of the Green's function are

$$[\overline{F}_{22,3}(x, z; \xi_1, \xi_3)] = \frac{i}{\mu(\xi_3)} \Delta_L \left[\frac{\tau^*(\xi_3)}{v_0/c_L} \right]_H \left[\frac{v_R(z)}{v_0} \right]_H e^{-\mu_L(x-\xi_1)} \quad (\text{A13a})$$

$$[\overline{F}_{22,1}(x, z; \xi_1, \xi_3)] = -\Delta_L \left[\frac{v_S(\xi_3)}{v_0} \right]_H \left[\frac{v_R(z)}{v_0} \right]_H e^{-\mu_L(x-\xi_1)}. \quad (\text{A13b})$$

SECTION 4

On Modeling Explosions using 2-D Numerical Methods

On Modeling Explosions using 2-D Numerical Methods

Richard J. Stead, John E. Vidale and Donald V. Helmberger

Seismological Laboratory

California Institute of Technology

Pasadena, CA 91125

ABSTRACT

Although seismic structures are generally three-dimensional (3-D), numerical simulation of wave propagation through laterally heterogeneous media is conceptually simpler and less computationally intensive in two dimensions (2-D). Source expressions for 2-D that have the same radiation patterns as their 3-D counterparts have been derived which can also correct for the differences between 2-D and 3-D wave propagation (Vidale and Helmberger, 1986; Stead and Helmberger, 1988; Helmberger and Vidale, 1988). Because that technique approximately transforms waves from a cartesian 2-D grid to a cylindrically symmetric 3-D world, slightly anisotropic geometrical spreading in 2-D better approximates isotropic spreading in 3-D than simple isotropic spreading in 2-D does. This paper describes a correction to the explosive source expression which reduces energy traveling vertically out of the source region, but leaves unchanged the energy traveling laterally out of the source region. We show that this correction will significantly improve the results of using a 2-D grid to simulate elastic wave propagation from an explosive point source.

The effect of shallow station structure and lateral velocity variation are investigated for records of the Amchitka blasts MILROW and CANNIKIN. The differences between the Mueller-Murphy, Helmberger-Hadley, and von Seggern-Blandford reduced displacement potential (RDP) source representations are smaller than the differences produced by various possible velocity structures. Using a model based on known structure, a better fit is obtained for the records of MILROW, primarily for the surface waves. In addition, a technique is developed to include possible source asphericity. Using this technique, the Amchitka blasts, especially CANNIKIN, show evidence of significant aspherical cavity formation.

INTRODUCTION

Ideally, one would like to simulate wave propagation in the earth with 3-D numerical grids. Such experiments are, in fact, now being attempted (Stevens and Day, 1985, Reshef, et al., 1988a, Reshef, et al., 1988b). They require, however, very large amounts of computer time and allow energy to propagate only a limited number of wavelengths, so that they do not apply to many problems of geophysical interest (see, for example, Figure 13.11 of Aki and Richards, 1977, for the range of application of various methods). Numerical grids in 2-D have been used for many years to provide insight into 3-D wave propagation problems (see Boore, 1972, for example). Recently, we have developed source expressions which allow the simulation of point slip dislocations and explosions with 2-D numerical grids (Vidale et al., 1985; Vidale and Helmberger, 1986; Stead and Helmberger, 1988; Helmberger and Vidale, 1988). These expressions are applied to a fourth-order explicit FD method. We find this method to be accurate, flexible and more efficient numerically than implicit FD or pseudo-spectral methods (pseudo-spectral methods are discussed by Reshef, et al., 1988a and Reshef, et al., 1988b, among others). The source formulations are most accurate for energy that propagates horizontally away from the source, partly because the asymptotic solution is most accurate for large range, high frequency, and non-vertical take-off angle (Vidale and Helmberger, 1986), but also because a 2-D grid does not properly simulate 3-D geometrical spreading. We describe herein a source term that corrects for the improper geometrical spreading at most take-off angles.

We then demonstrate the use of this refinement by calculating finite difference synthetics for the Amchitka Island, Alaska blasts MILROW and CANIKIN. The LONGSHOT blast is not considered due to the lack of near-field data. These blasts have been studied extensively by other researchers (Lay, Burdick and Helmberger, 1984, Lay, Helmberger and Harkrider, 1984, Burdick, et al., 1984, King, et al., 1974, Perret, 1972 and Toksoz and Kehrner, 1972, among many others). In this research, because the structure and the source time functions have been investigated, these blasts are a good demonstration case.

The blasts are described in detail by Perret (1972). MILROW was detonated October 2, 1969 at a depth of 1219 m. Its yield was approximately 1 Mt. CANNIKIN was detonated November 6, 1971 at a depth of 1791 m with a yield not more than 5 Mt. Both shot points were in pillow lavas beneath a varied sequence of volcanic breccias, basalts and sediments.

These events, because of their size, location and the wealth of data that was released at the time, provided seismologists a unique opportunity to study a broad range of seismological properties of nuclear explosions (Willis, et al., 1972 and Engdahl, 1972, among others). In this paper, we will be concerned with the near-field seismic records of these blasts. The modeling of these records has been the subject of several other studies, most notably Burdick, et al. (1984) and Lay, Burdick and Helmberger (1984), where the researchers simultaneously model the near-field and teleseismic data. Here, we will take the source parameters and seismic structure from these studies as known, to demonstrate the effects of some modeling procedures made possible using finite difference (FD) wave propagation. We will not address the close-in records of the Sandia Laboratories experiments (Perret, 1973; Perret and Breiding, 1972) because our FD algorithm does not account for the spall observed in those records. We use FD in this research to demonstrate the limitations of one-dimensional (1-D) modeling and to explore the effects that realistic 2-D structures can have when superimposed on a good 1-D model.

DIFFERENCE BETWEEN 2-D AND 3-D WAVE PROPAGATION

The equations for 2-D and 3-D wave propagation are similar, but there are important differences. We will examine the acoustic case, although the same arguments hold for the elastic case. In the acoustic case, the 2-D wave equation for homogeneous media is

$$P_{\alpha\alpha} = c^2 (P_{xx} + P_{zz}), \quad (1)$$

where P is pressure, c is the wave velocity, x and z are cartesian coordinates,

and subscripts indicate derivatives. The 3-D acoustic wave equation for homogeneous media is

$$P_{tt} = c^2 (P_{xx} + P_{yy} + P_{zz}), \quad (2)$$

where y is the third cartesian coordinate. Cylindrical co-ordinates are also appropriate for wave propagation near a horizontal free surface. In cylindrical coordinates

$$P_{tt} = c^2 (P_{rr} + P_{zz} + \frac{P_r}{r}), \quad (3)$$

where r and z are the radial and vertical coordinates, and azimuthal symmetry in the wavefield is assumed. The term that is multiplied by $1/r$ becomes negligible as r becomes large, and in this case the Equations (1) and (3) are nearly equivalent.

There are several differences between waves propagating according to Equations (1) and (3). In 2-D, wave amplitude decays with geometrical spreading by $1/\sqrt{R}$, where $R = \sqrt{x^2 + z^2}$, but in 3-D, wave amplitude decays by $1/R$, where $R = \sqrt{r^2 + z^2}$. This difference can be corrected by multiplying the amplitude of seismograms produced with Equation (1) by $1/\sqrt{R}$, but this correction is exact only for a homogeneous media. If the true raypath is strongly bent by velocity gradients, the appropriate R may be difficult to find. If there are several raypaths between the source and receiver, the appropriate R is ambiguous and impossible to find.

In 2-D, an impulsive burst of energy at the source results in an impulsive burst of energy at the receiver followed by a line source tail which decays as $1/\sqrt{t}$, where t is the time after the first arrival of energy at the receiver. In 3-D, an impulsive burst of energy at the source results solely in an impulsive burst of energy at the receiver. The arrivals with a line source tail that result from the use of a 2-D numerical grid can be restored to point-source-like impulsiveness by convolution with the time series $H(t)/\sqrt{t}$, followed by differentiation with respect to time. Here $H(t)$ is the Heaviside step function. The seismograms

produced are approximately those that would result from a source on the axis of symmetry in a cylindrically symmetric medium.

The corrections above have been suggested in Vidale et al. (1985) and Vidale and Helmberger (1986), but a further correction has been derived in Stead and Helmberger (1988) to approximate the anisotropy in geometrical spreading necessary to exactly simulate 3-D wave propagation in a 2-D numerical grid. Below, we provide physical insight into this correction.

CORRECTION FACTOR FOR EXPLOSIONS IN 2-D

We will show that the amount of energy leaving the source region at an angle i with the vertical in the 2-D grid may be approximated by the amount of energy in the point source case multiplied by $\sqrt{\sin i}$. The additional $\sqrt{\sin i}$ in the point source or 3-D solution can be explained in terms of geometrical spreading, as is shown in Figure 1. The energy between takeoff angles i_0 and $i_0 + di_0$ for the point source becomes

$$E_P = \frac{(2\pi \sin i_0 r) r di_0}{2\pi r^2} = \sin i_0 di_0 \quad (4)$$

while for the line-source

$$E_L = \frac{2\pi r di_0}{2\pi r} = di_0 \quad (5)$$

Since energy is proportional to the square of the amplitude we obtain the $\sqrt{\sin i}$ dependence.

If we use an isotropic explosion as the source in the 2-D model, each arrival in a record may have a different take-off angle i , but we can only correct for a constant $\sqrt{\sin i}$. The result is that the vertically traveling energy is emphasized over horizontally traveling energy in the line source compared to the point source case. One might ask why not simply multiply the isotropic source by $\sqrt{\sin i}$. Unfortunately, such a source does not satisfy the 2-D elastic wave equation and will not maintain the $\sqrt{\sin i}$ radiation pattern once the energy leaves the source

region, primarily because the cusp in the $\sqrt{\sin i}$ at $i = 0^\circ$ does not satisfy the 2-D elastic wave equation.

The source functions found to be solutions to the 2-D elastic wave equation have radiation patterns of $\sin^n i \cos^m i$, where n and m are free parameters. An isotropic line source explosion, for example, is the solution with $n = m = 0$, and the dislocation sources have $n + m = 2$ (Vidale and Helmberger, 1986; Helmberger and Vidale, 1988). Also, because of the asymptotic nature of our solutions, the compressional and shear parts of the source separate. The 2-D to 3-D correction we adopt is to add the compressional component of the horizontally-directed force term ($n = 1$ and $m = 0$) to the isotropic explosive source. This term is added so that it decreases the amplitude of energy leaving the source vertically, but leaves unchanged the amplitude of energy leaving the source horizontally.

These two terms can be thought of as the first two terms of a Taylor series expansion of $\sqrt{\sin i}$ about the point $i = 90^\circ$. Higher order corrections could be added, but we choose not to, for the following reasons. The first two terms alone provide a sufficiently accurate solution, but when n or m is increased by 1 the pseudo-near-field terms in the solution grow more prominent by a factor of t , that is, the asymptotic solution diverges by another factor of t . An isotropic line-source explosion has a constant pseudo-near-field term, which is analogous to an explosion in a 3-D medium, where there may be some permanent deformation near the source. The compressional component of force described below grows with time as t , and slip dislocation sources grow with time as t^2 (see Vidale and Helmberger, 1986). Therefore, while the addition of higher-order terms in the Taylor series would make the source radiation pattern more closely resemble $\sqrt{\sin i}$, it would also add more severe pseudo-near-field terms to the displacement field in the finite difference grid.

The following solutions for a delta function source in a whole-space (see Stead and Helmberger, 1988). Define

$$T_a = \frac{R^2}{t^2 \alpha^2} \quad (6)$$

and

$$\Phi_a = \frac{\sqrt{2}}{\sqrt{\alpha}} \frac{H(t-R/\alpha)}{\sqrt{1-T_a}} \frac{1}{\pi R^2}, \quad (7)$$

where α is compressional wave velocity, R is the absolute distance between the source and receiver, and t is time. The analytic whole-space expressions for an isotropic explosion, that may be used as internal boundary conditions surrounding a source in a 2-D numerical grid, are

$$\begin{aligned} Q_E &= r \Phi_a \text{ and} \\ W_E &= -z \Phi_a, \end{aligned} \quad (8)$$

where r is the horizontal component of R , and is positive in the direction of the receiver, and z is the vertical component of R , and is positive downward. Q_E and W_E are the radial and vertical components of displacement.

The expressions for Q_F and W_F for a line-force, which has a $\sin i$ radiation pattern are

$$\begin{aligned} Q_F &= \frac{\alpha t}{R^2} \Phi_a (r^2 - z^2 + T_a z^2) \text{ and} \\ W_F &= \frac{\alpha t}{R^2} \Phi_a (-2rz + T_a rz). \end{aligned} \quad (9)$$

Taken together, allowing for arbitrary combination of the terms using the parameter k_f (force ratio), the result is

$$\begin{bmatrix} Q \\ W \end{bmatrix} = \Phi_a \left[(1 - k_f) \begin{bmatrix} r \\ -z \end{bmatrix} + k_f \frac{\alpha t}{R^2} \begin{bmatrix} r^2 - z^2 + z^2 T_a \\ (T_a - 2) rz \end{bmatrix} \right]. \quad (10)$$

The time function appropriate for an explosion, the RDP, is included by convolution after propagating the source, Q and W , through the FD grid and extracting the response, \tilde{Q} and \tilde{W} , at the desired receiver. Thus, the complete expression for the line source synthetic is

$$\begin{pmatrix} Q_1 \\ W_1 \end{pmatrix} = - \frac{\partial \Psi(t)}{\partial t} * \begin{pmatrix} \tilde{Q} \\ \tilde{W} \end{pmatrix} * I * A, \quad (11)$$

where $\Psi(t) = \Psi_\infty(1 - e^{-Kt})(1 + Kt + \dots)$, and Ψ_∞ has units of volume. The function I is the instrument response, and the function A is the attenuation operator. This is similar to the moment release expression in Vidale and Helmberger (1986)

$$\begin{pmatrix} Q_1 \\ W_1 \end{pmatrix} = \frac{10^{-10}}{4\pi\rho\alpha^2} \frac{\partial M_0(t)}{\partial t} * \begin{pmatrix} \tilde{Q} \\ \tilde{W} \end{pmatrix} * I * A, \quad (12)$$

where M_0 is the earthquake moment and ρ is the density.

By judiciously mixing the explosive and force terms (varying k_f), we can modify the vertical radiation pattern of the explosion to better mimic $\sqrt{\sin i}$ in the range we desire. Figure 2 shows the radiation patterns that result from using $k_f = 0$, $k_f = 0.5$ and $k_f = 0.6$. These cases are compared with $\sqrt{\sin i}$ and isotropic line source radiation patterns. Energy that leaves the source at angles near $i = 90^\circ$ is not affected by the correction, but energy at angles near $i = 0^\circ$ is markedly affected. The mix of explosion and line-force expressions determines where in the radiation pattern the source is most accurate. As seen in Figure 2, $k_f = 0.5$ is most accurate near $i = 90^\circ$ while $k_f = 0.6$ is less accurate near $i = 90^\circ$, but more accurate near $i = 30^\circ$. It is clear from Figure 2 that only energy leaving the source at positive angles may be modeled with this corrected source.

As described in Stead and Helmberger (1988), the line source seismograms are transformed into point source seismograms by:

$$\begin{pmatrix} Q_p \\ W_p \end{pmatrix} = \frac{2}{\sqrt{R} + \sqrt{r}} \frac{d}{dt} \left(\frac{1}{\sqrt{t}} * \begin{pmatrix} Q_1 \\ W_1 \end{pmatrix} \right) \quad (13)$$

where Q_p and W_p are horizontal and vertical displacements in cm.

This correction factor will change the relative amplitude of arrivals by the $\sqrt{\sin i}$ factor shown in Figure 2. The effect of a $k_f = 0.5$ correction for an explosion in a half-space is shown in Figure 3. The corrected FD seismograms

have Rayleigh waves of larger amplitude relative to the direct compressional waves than do the uncorrected seismograms, and they agree better with the seismograms generated by the Cagnaird method, which is known to be accurate (see Apsel and Luco, 1983, for example). The $\sqrt{\sin i}$ corresponds to \sqrt{p} , where the real part of the horizontal slowness p is $p = rt / R^2$. The correction increases the size of the Rayleigh waves because they have a greater horizontal slowness than the direct compressional waves. The correction becomes more important the more nearly vertically the energy is traveling. In modeling short-period P waves from the Nevada test site, Stead and Helmberger (1988) have found this correction to be crucial.

APPLICATION TO AN EXPLOSION ON AMCHITKA

We now use the corrected source to investigate the records of explosions on Amchitka Island, which is among the Rat Islands group of the Aleutian Islands in the Pacific ocean. As discussed above, the models in Burdick, et al. (1984), Lay, Burdick and Helmberger (1984) and Lay, Helmberger and Harkrider (1984) are taken here as the best 1-D approximations. Burdick, et al. (1984) show that the records from the explosion MILROW for the stations shown in Figure 4 can be modeled fairly well with a layered structure. The P-wave crustal model in Table 2 consists of 8 of the 9 layers derived by Burdick, et al. (1984) by fine-tuning the model proposed by Engdahl (1972). This model predicted the observed P-wave travel times well, and the S-wave velocity structure was added in that investigation to model the Rayleigh wave arrivals. A comparison of synthetics generated by various methods including FD and assuming the flat-layered Burdick model is discussed in Vidale and Helmberger (1988). We will be interested primarily in perturbations of this flat-layered structure and the corresponding effects on the resulting waveforms.

Geologic constraints on the structure are obtained from a report by Orphal et al. (1970) which displays geologic cross-sections from the blast to the various stations. Density, shear wave velocity and compressional wave velocity for the

Amchitka sites can be obtained from well-log information, Perret (1973) and Perret and Breeding (1972). Figures 5a through 5c show the S-velocity, P-velocity and density profiles chosen as models of the Amchitka structure. These models are tested below to evaluate the relative importance of various features in the available information about Amchitka structure.

The first experiment tests the effect of smoothing the layer boundaries. This is accomplished by specifying a gradient region which straddles the original sharp layer boundary (see Table 3). The results of these trials are shown in Figure 6. In this figure, the synthetics for both the sharp layer boundaries and gradient boundaries are compared at two ranges for the events CANNIKIN and MILROW. The RDP source time function used is that of Helmberger and Hadley (1981)

$$\Psi(t) = \Psi_{\infty} \left[1 - e^{-Kt} (1 + Kt + 0.5(Kt)^2 - B(Kt)^3) \right] \quad (14)$$

The source for MILROW has $K=6$, $B=1$ and $\Psi_{\infty}=10^{11}$, and the source for CANNIKIN has $K=9$, $B=0.625$ and $\Psi_{\infty}=5.69 \times 10^{11}$, both as determined by Lay, Helmberger and Harkrider (1984). The most obvious effect is a change in frequency content. This is to be expected; a gradient zone appears 'sharper' to low-frequency energy than to higher-frequency energy. In fact, the gradients used in this case are more effective in turning long period energy than sharp boundaries, as shown by the larger Rayleigh waves for the CANNIKIN synthetics. Another effect is that individual reflected phases, and multiples in particular, are not large and impulsive in the gradient case. This effect is particularly evident for a phase about 7 seconds after the first arrival on the radial component of the CANNIKIN synthetics at 20 km. The large arrival for the sharp boundary case is completely unresolved in the gradient synthetic. The apparent slowness, phase behavior and timing are consistent with a wide-angle multiple. One would expect wide-angle reflections and multiples to be affected most strongly by gradational layer boundaries. Several other similar phases exist for both MILROW and CANNIKIN synthetics at various ranges, although normally they are reduced in

amplitude by about one-half and resolved for both models. Thus, late multiples can be greatly reduced in amplitude by gradients, while the direct arrivals and refractions near the first arrival are virtually unchanged. This is important to consider since observed seismic boundaries typically have some gradational character even at sharp geologic boundaries.

A second case we examine is the effect of 'random' media. Observed seismic structure usually is not constant or smoothly varying with depth on scales as small as 100 meters. The media parameters are observed to fluctuate about some smoother large-scale structure. This is evident in the velocity and density logs taken from the instrument holes on Amchitka Island (Figures 7a and 7b, adapted from Perret and Breiding, 1972 and Perret, 1973). These structures correlate with the geology and are likely to be larger horizontally than vertically. To investigate the effect of such variations we add randomness to the upper layers of the gradient model discussed above (see Table 4). The gradient model is used as a base to avoid large, perhaps unrealistic variations in the synthetics resulting from caustics in the sharp-boundary case. The variances are larger (in percent) for the shallowest layers to allow for some effect of pressure in reducing the amplitude of variations. The randomness in the model is not as strongly varying as the observed well-log data, but is a filtered version to demonstrate the effect without requiring too fine a grid spacing for the FD model. We also permit the horizontal and vertical aspects to differ, for the reasons stated above. The aspects are essentially the mean anomaly radii in each dimension. The results are shown in Figure 8, compared to the gradient case. As expected, the random media scatter high-frequency energy far back into the coda; it is even seen following the arrival of the Rayleigh wave. The scattering completely obscures later multiples in the record. This has interesting implications for one-dimensional (1-D) models. Fundamentally, it means that crustal multiples from sources less than 2 km deep may not be well-behaved and should not be used to constrain 1-D velocity models. Perhaps late pulses in the near field should not be modeled; this would be additional justification for the approach of Burdick, et al. (1984), where just

the first few arrivals and the surface wave are modeled. The information contained in such coda could determine statistical properties of the medium, but little more.

The effect of site material is investigated in Figure 9. Site properties often vary among stations due to the erosion of fault or fold geometries or the existence of basins, ridges and other structures. Here, we surround one station with a fast (hard) material lens 1 km in diameter, and the next station out with a slow (soft) lens, also 1 km in diameter. Both lenses are tapered somewhat with depth to mimic the generic forms for the corresponding geologic structures. That is, the fast lens is wider at its base, and the slow lens is wider at top. The slow material has compressional wave velocity $\alpha = 2.0 \text{ km s}^{-1}$, shear wave velocity $\beta = 1.13 \text{ km s}^{-1}$, and density $\rho = 2.3 \text{ g cm}^{-3}$, the fast material has $\alpha = 4.5 \text{ km s}^{-1}$, $\beta = 2.55 \text{ km s}^{-1}$, and $\rho = 2.7 \text{ g cm}^{-3}$, and the top of the rest of the layer, which is 200 meters thick, has $\alpha = 3.0 \text{ km s}^{-1}$, $\beta = 1.7 \text{ km s}^{-1}$, and $\rho = 2.5 \text{ g cm}^{-3}$. The remaining layers are the same as those listed in Table 3.

For both CANNIKIN and MILROW the amplitude at the receiver on the slow site is a factor of 1.5 larger than at the receiver in the same position in the plane-layered model. A simple conservation of energy argument, ignoring the transmission coefficient into the slow layer, would predict an amplification of $(v_2 \sqrt{\rho_2}) / (v_1 \sqrt{\rho_1}) = 1.6$, where v is velocity and ρ is density, subscript 1 refers to the slow medium and subscript 2 refers to the top layer of the plane-layered model. When the transmission loss on entering the slow material is considered, the observed amplification factor agrees with the simple prediction. Another effect is that the particle motion for MILROW at the slow site (receiver at 7 km) is more vertical than that for the laterally homogeneous case. This is due to the greater refraction of the ray due in turn to the greater velocity contrast. Small reverberations and conversions in the slow media may be seen 1 to 2 seconds after the initial pulse. At 15 km for CANNIKIN, the Rayleigh wave is not amplified as much as the initial P-wave. This is most likely due to the relative frequency content of the waves; the Rayleigh wave (2 second period) samples a

range of depths much greater than 200 meters and is therefore less affected by the contrast. At the station on the faster material, the amplitude is smaller by a factor of 1.2 versus the simple prediction of 1.5, not corrected for transmission. Thus, the simple prediction does not work well. Other factors, such as focusing, diffraction, and the free-surface interaction may be important. The direct waves and longer-period surface waves are unchanged at the ranges of 10 and 12 km (which are beyond the local station structures), although small scattered shorter-period phases do enter the records.

The structure between the blast and station M05 (Figure 10) is approximated from Orphal et al. (1970). The velocity model below the source is the same as in the sharp boundary model, and the synthetics are compared to those of the sharp boundary case in Figure 11. This result is similar to the result of the previous case in that the waveforms are quite sensitive to the structure where the rays bottom. The amplitudes differ by up to 50%. About 30% more amplitude, which translates to 70% more energy, is converted into the surface wave by the structures which dip down away from the source. This tendency of dipping layers to convert body waves to surface waves is examined in more detail in Vidale, et al. (1985). Conversely, we note here that layers dipping the opposite direction convert surface waves to body waves (Stead and Helmberger, 1988).

Shallow structure is seen to affect the amplitude of body waves as well as surface waves. These effects are difficult to model deterministically because the structures are poorly known. Derivation of a relatively detailed flat-layered model with sharp boundaries using ray techniques may help to understand the wave propagation involved, but should not be taken to represent the detailed structure of the earth. Unknown shallow structure may contribute to the misfit between the synthetic seismograms and the data to be examined below.

COMPARISON OF VARIOUS STRUCTURE MODELS AND DATA

Now we compare the synthetics for the various cases described above to the available near-field data. The purpose is to show which of the various structures result in the best fit to the data. We choose four stations, two for each event, as representative of the available data. For MILROW these stations are M01 and M06, at 8.0 and 11.5 km, respectively. For CANNIKIN, we choose M05 and M06 at 15.8 and 18.7 km, respectively.

Figure 12 shows a comparison of the radial and vertical records from station M01 for MILROW. These data are compared to the synthetic response at 8 km for four of the above models: the gradient boundaries, the sharp boundaries, the faulted geometry and the random media. The first arrival is well-modeled by both the sharp and gradient boundary cases. This is not surprising, since Burdick, et al. (1984) fine-tuned the sharp boundary model to the data. But, the longer-period part of the signal, which includes the Rayleigh wave, is best modeled by the faulted geometry. This station is not far from the faults represented in Figure 10, so the effects of the faults and tilted layers are resolved in this case. In Figure 13, the station M06 for MILROW shows the same result, the faulted model most accurately models the data.

The CANNIKIN station M05 is compared to the synthetics in Figure 14. Here, the gradient model is the best fitting. From this we infer that the effect of the faults on the larger, longer period and more distant source CANNIKIN is not as strong as that for MILROW. In addition, the effects of sharp boundaries are clearly not present in the data. Some filtering appears necessary for the other three cases, perhaps crustal Q is important and would reduce some of the higher frequencies in the coda. Station M06 for CANNIKIN shows the same result (Figure 15).

COMPARISON OF VARIOUS BOMB SOURCES AND DATA

In this section we will show that for the data we are using, structure has more effect in determining the amplitudes and shaping the waveforms than the type of RDP used. Several RDP functions have been proposed, but in this section we will show that no one source model significantly outperforms the others for the near-field body and surface waves for the explosion MILROW and CAN-NIKIN. The source of Helmberger and Hadley (1981) (H-H) was described above, but the sources of von Seggern and Blandford (1972) (vS-B) and Mueller and Murphy (1971) (M-M) are also frequently used in the study of explosions.

Von Seggern and Blandford (1972) postulate a source given by

$$\Psi(t) = \Psi_{\infty} \left[1 - e^{-K' t} (1 + K' t - B' (K' t)^2) \right] \quad (15)$$

where Ψ_{∞} is the source strength, and K' and B' are corner frequency and overshoot parameters similar to K and B in the H-H source.

Meuller and Murphy (1971) postulate a source most easily expressed as a convolution (Barker et al., 1985):

$$\Psi(t) = \frac{r_{el} V_p^2}{4 \mu} P(t) * F(t) \quad (16)$$

where the $*$ indicates convolution and $P(t)$ and $F(t)$ are as follows:

$$P(t) = (P_{0S} - P_{0C}) e^{-\alpha t} + P_{0C} H(t) \quad (17)$$

and

$$F(t) = \frac{\sin(bt) e^{at}}{\beta b} \quad (18)$$

Furthermore,

$$\text{dynamic cavity pressure } P_{0C} = \frac{4}{3} C_s \mu \left(\frac{r_c}{r_{el}} \right)^3 \quad (19)$$

$$\text{static cavity pressure } P_{0S} = 1.5 \rho g h \quad (20)$$

$$\text{elastic radius } r_{el} = C_1 \frac{Y^{0.33}}{(h/100)^{0.42}} \quad (21)$$

$$\text{cavity radius } r_c = C_2 \frac{Y^{0.29}}{(h/100)^{0.11}} \quad (22)$$

and

$$\alpha = C_4 \omega_0 = \frac{C_4 r_{el}}{V_p} \quad (23)$$

$$\beta = \frac{\lambda + 2\mu}{4\mu} \quad (24)$$

$$a = \frac{-\omega_0}{2\beta} \quad (25)$$

$$b = \frac{\omega_0}{\beta} (\beta - 0.25)^{0.5} \quad (26)$$

The constants C_1 through C_4 are calibration constants dependent on the source medium and defined as follows

$$C_1 = 200,000 \left(\frac{A}{\rho A_{cal}} \right)^{\frac{1}{2.4}} \quad (27)$$

$$C_2 = 1630 E^{0.62} \mu^{-0.24} \rho^{-0.67} \quad (28)$$

$$C_3 = \text{compaction factor (hard rock 1.0, tuff 0.6)} \quad (29)$$

$$C_4 = \text{proportionality factor (tuff 1.5, rhyolite 2.0)} \quad (30)$$

The amplitude calibration, A/A_{cal} , is determined using calibration events (eg: 2.8 for salt, 2.0 for shale and 0.25 for tuff). For the other values in the equations, Y is the yield in kilotons, h is the source depth, ρ is the density, V_p is the compressional wave velocity, E is Young's modulus, and λ and μ are Lamé's constants. All parameters except the yield are in cgs units. The convolution in Equation 16 is analytic, resulting in the following expression for the source

$$\begin{aligned} \Psi(t) = \frac{r_{el}}{\rho b} \left\{ \frac{P_0}{(a+\alpha)^2 + b^2} \left[(a+\alpha)e^{\alpha t} \sin(bt) - be^{\alpha t} \cos(bt) + be^{-\alpha t} \right] \right. \\ \left. + \frac{P_0 c}{a^2 + b^2} \left[ae^{\alpha t} \sin(bt) - be^{\alpha t} \cos(bt) + b \right] \right\} \quad (31) \end{aligned}$$

Although the expression of Equation 16 is simpler, this expression is often more convenient in practice.

The parameters used for the three sources are given in Table 5. Those for the M-M source are determined by local structure, source depth and source size. The parameters for the other two sources are determined from teleseismic body and surface waves by Lay, Helmberger and Harkrider (1984).

The three RDP representations are compared in Figure 16. The far-field displacement time functions for the three sources are shown at the top. There is little difference between the three traces. The RDP functions are plotted next, and the level of the permanent offset, Ψ_{∞} , is 1.4×10^{11} for the H-H and vS-B sources and 2.4×10^{11} for the M-M source. At the bottom are the spectra of the displacement time histories. The spectra are similar except that the M-M source has a higher long-period level.

The data are compared to FD seismograms computed for the M-M, vS-B, and H-H sources in Figures 17 and 18. The various source time functions are convolved with the FD impulse responses to form the seismograms in these figures.

Figure 17 shows the comparison for MILROW at station M01. Here, the vertical amplitudes are all within 5% of those for the data, but the fit to the radial component is not as good. There is little difference between the three RDP sources. This observation agrees with the spectra in Figure 16, where there is little difference between the different sources. Figure 18 shows the comparison for CANNIKIN at station M05. The amplitudes of the RDP seismograms are within 35% of the those of the data in all cases, and within 20% in every case but one. Here, there appears to be a slight preference for the M-M formulation.

The fit to the data is good, but the differences between the synthetics for the various sources are less than the difference between the data and any of the synthetics. The differences between the data and the synthetics are of the same order as the differences between the synthetics for different plausible structures.

In this case, tilting layers which can trap more energy and local receiver effects which amplify or diminish body-wave arrivals are at least as important as differences in the type of RDP. Details of the structure must be better determined before details of the source time function can be resolved in the near-field.

A final variation on the bomb source is the inclusion of possible source asymmetry. The motivation for investigating this effect is large variations in the ratio of first arrival amplitude to Rayleigh wave amplitude seen in the data, but not accurately modeled by the various approaches discussed above. Physical conditions which would lead to the formation of asymmetrical cavities are readily postulated; for example, bedding plane control or rapid vertical changes in material strength. The inclusion of asymmetry is accomplished through modification of the radiation pattern, similar to the implementation of the correction discussed above. The correction for an ellipsoidal cavity requires the introduction of S-wave radiation at the source. Figure 19 is the basis for the development of the correction: the correction is quadrupole-like, and for ellipsoidal cavities with a principle axis oriented vertically, this quadrupole should be well-approximated by a 45° dip-slip double-couple. We say quadrupole-like because in 3-D the pattern is radially symmetric, yet this is ideal for 2-D simulations. Double-couple sources are derived and discussed in Helmberger and Vidale (1988). When scaled for RDP instead of moment, the double-couple may be added linearly to the explosion result to produce the response from any ellipsoidal cavity in a radially-symmetric medium, cavities ranging from pancakes to pencils. The explosion result should already include its correction, with k_f set for the appropriate take-off angles.

The linear combination of the two sources to provide a range of cavities from pancake to pencil may be expressed as Explosion + $e \times$ Double-Couple, where $-1 < e < 1$. Note that for the pencil case (prolate), we expect a smaller teleseismic P-wave, whereas the pancake shape (oblate) enhances the P-wave. At near-regional distances the P-waves are affected less, but the surface waves are strongly affected as displayed in Figures 20 and 21. The e factor is set at 0.4 in

these two figures for demonstration. Rayleigh waves are relatively enhanced for the prolate case. MILROW observations favor the spherical explosion with perhaps a small prolate correction for some of the stations (eg. M04). The CANNIKIN observations strongly support a prolate correction with respect to the surface-wave development. However, the estimates are crude, taking into account the fact that the correction postulated here for ellipsoidal cavities is completely ad-hoc; it has not been rigorously derived with attention to frequency dependence, coupling, anelastic material behavior, etc. Nevertheless, we believe this correction is a good first-order approach to the asphericity problem and note that due to its quadrupole nature, it may be necessary to consider when estimating tectonic release.

CONCLUSIONS

The use of two-dimensional finite difference algorithms to understand acoustic and elastic wave propagation is a powerful tool. The additional term described in this paper to correct for the difference between two- and three-dimensional geometrical spreading significantly improves the accuracy of these numerical solutions.

Shallow station structure and lateral velocity variations have considerable effect on the synthetic records computed for the Amchitka blast MILROW. The velocity structure is shown to be at least as important as the choice of explosion time function in computing synthetic ground motion for the near-field velocity data we examine in this paper. The medium immediately surrounding a station can greatly affect the amplitude of the observed waves, but estimating media properties at the stations from amplitude variations alone is unreliable. When possible, station structure should be determined in the field, to a depth and radius from the station consistent with the periods to be observed. Gradational boundaries are shown to fit the data better than sharp boundaries. When coupled with the effects of random media, we find that impulsive, large-amplitude arrivals in the coda are not deterministic, and can not be fit to multiples in a medium

with sharp boundaries. Deterministic 2-D local structure is shown to be important for MILROW, where faults near the stations are shown to affect the surface waves.

Source asymmetry strongly affects the near-field surface waves. Such asymmetry can be modeled as the addition of a quadrupole response to the explosion response. The pancake (oblate cavity) case tends to reduce surface waves while the prolate contribution tends to enhance surface waves. CANNIKIN favors a substantial prolate contribution, and thus, smaller teleseismic m_b and larger local surface waves. A characteristic change in cavity shape from spherical to prolate (elongated vertically) for larger events could explain the change of slope in the m_b yield curves.

ACKNOWLEDGEMENTS

J. E. V. was supported by an NSF fellowship. Cindy Arvesen drafted the figures. This research was supported in part by the Advanced Research Projects Agency of the U. S. Department of Defense and was monitored by the U. S. Air Force Geophysics Laboratory under Contract F19628-87-K-0028. Contribution number 4311 from the Division of Geological and Planetary Sciences, California Institute of Technology, Pasadena, California, 91125. and contribution number 67 of the Richter Laboratory at the University of California, Santa Cruz.

REFERENCES

- Aki, K., and P. G. Richards (1980). *Quantitative Seismology, theory and methods*, W. H. Freeman and Co., San Francisco, 749.
- Apsel, R. J. and J. E. Luco (1983). On the Green's functions for a layered half-space, Part II, *Bull. Seism. Soc. Amer.*, **73**, 931-952.
- Barker, J. S., L. J. Burdick, and T. C. Wallace (1985). Analysis of near-field seismic waveforms from underground nuclear explosions, Scientific Report No.

- 1, AFGL-TR-85-0321, Woodward-Clyde Consultants, Pasadena, California, 39 pp.
- Boore (1972). Finite difference methods for wave propagation in heterogeneous materials, in *Methods of Computational Physics*, vol. 2, B. Alder, S. Fernbach, and M. Rotenberg, Editors, Academic Press, New York, 1-37.
- Burdick, L., T. Wallace and T. Lay (1984). Modeling near-field and teleseismic observations from the Amchitka test site, *J. Geophys. Res.*, **89**, 4373-4388.
- Engdahl, E. (1972). Seismic effects of the MILROW and CANNIKIN nuclear explosions, *Bull. Seism. Soc. Am.*, **62**, 1411-1423.
- Helmberger, D. V., and D. Hadley (1981). Seismic source functions and attenuation from local and teleseismic observations of the NTS events JORUM and HANDLEY, *Bull. Seism. Soc. Am.*, **71**, 51-67.
- Helmberger, D. V., and J. E. Vidale (1988). Modeling strong motions produced by earthquakes with two-dimensional numerical codes, *Bull. Seism. Soc. Am.*, **78**, 109-121.
- King, C., A. Abo-Zena and J. Murdock (1974). Teleseismic source parameters of the LONGSHOT, MILROW and CANNIKIN nuclear explosions, *J. Geophys. Res.* **79**, 712-718.
- Lay, T., L. Burdick, and D. V. Helmberger (1984). Estimating the yields of the Amchitka tests by waveform intercorrelation, *Geophys. J. R. Astr. Soc.*, **78**, 181-208.
- Lay, T., D. V. Helmberger, and D. Harkrider (1984). Source models and yield-scaling relations for underground nuclear explosions at Amchitka Island, *Bull. Seism. Soc. Am.*, **74**, 843-862.
- Meuller, R. A. and J. R. Murphy (1971). Seismic characteristics of underground nuclear detonations, Part I, Seismic spectrum scaling, *Bull. Seism. Soc. Am.*, **61**, 1675-1694.
- Orphal, D. L., C. T. Spiker, L. R. West, M. D. Wronski (1970). Analysis of seismic data, MILROW Event, Rept. NVO-1163-209, Environmental Research Corporation, Alexandria, Virginia, 81pp.

- Perret, W. (1973). Ground motion in the vicinity of the CANNIKIN nuclear explosion, Rept. SLA-73 0043, Sandia Laboratories, Albuquerque, New Mexico, 79 pp.
- Perret, W. and D. Breiding (1973). Ground motion in the vicinity of an underground nuclear explosion in the Aleutian Islands: MILROW event, Rept. SL-RR-72 0668, Sandia Laboratories, Albuquerque, New Mexico, 84 pp.
- Reshef, M., D. Kosloff, M. Edwards and C. Hsiung (1988a). Three-dimensional acoustic modeling by the Fourier method, *Geophysics.*, **53**, 1175-1183.
- Reshef, M., D. Kosloff, M. Edwards and C. Hsiung (1988b). Three-dimensional elastic modeling by the Fourier method, *Geophysics.*, **53**, 1184-1193.
- Stead, R. J., and D. V. Helmberger (1988). Numerical-analytical interfacing in two dimensions with applications to modeling NTS seismograms. *J. Pure and Appl. Geophys.*, **128**, 101-193.
- Stevens, J. L. and S. M. Day (1985). The physical basis of m_b , M_S and variable frequency magnitude methods for earthquake/explosion discrimination. *J. Geophys. Res.*, **90**, 3009-3020.
- Toksoz, M. and H. Kehler (1972). Tectonic strain release characteristics of CANNIKIN, *Bull. Seism. Soc. Am.*, **62**, 1425-1438.
- Vidale, J. E., D. V. Helmberger, and R. W. Clayton (1985). Finite-difference seismograms for SH waves, *Bull. Seism. Soc. Am.*, **75**, 1765-1782.
- Vidale, J. E., and D. V. Helmberger (1987). Path effects in strong motion seismology, in *Methods of Computational Physics*, Bruce Bolt, Editor, Academic Press, New York, 267-319.
- von Seggern, D. and R. Blandford (1972). Source time functions and spectra for underground nuclear explosions, *Geophys. J.*, **31**, 83-97

Table 1. Layer over halfspace model

V_p km s ⁻¹	V_s km s ⁻¹	ρ g cm ⁻³	layer thickness km
6.2	3.5	2.7	32.0
8.2	4.5	3.4	∞

Model identical to that of Apsel and Luco (1983).

Table 2. Properties of sharp boundary model

Key	V_p km s⁻¹	V_s km s⁻¹	ρ g cm⁻³	layer thickness m
A	3.0	1.7	2.5	200
B	3.7	1.9	2.5	650
C	4.2	2.0	2.5	575
D	4.7	2.0	2.5	525
E	4.9	2.1	2.55	600
F	5.35	3.1	2.55	500
G	5.5	3.2	2.8	6950
H	6.9	4.0	2.8	∞

The letters in the Key column are used in Figure 12.

Table 3. Properties of gradient boundary model

V_p km s ⁻¹	V_s km s ⁻¹	ρ g cm ⁻³	layer thickness m
3.0	1.7	2.5	100
g*	g	2.5	200
3.7	1.9	2.5	350
g	g	2.5	375
4.2	2.0	2.5	225
g	2.0	2.5	375
4.7	2.0	2.5	125
g	g	g	375
4.9	2.1	2.55	250
g	g	2.55	375
5.35	3.1	2.55	125
g	g	g	375
5.5	3.2	2.6	4250
g	g	g	5000
6.9	4.0	2.8	∞

*g = linear gradient across layer

Table 4. Properties of random media model

V_p	V_s	ρ	V_p	horizontal	vertical	layer
			variance	aspect	aspect	thickness
km s^{-1}	km s^{-1}	g cm^{-3}	km s^{-1}	m	m	km
3.0	1.7	2.5	0.4	125	20	100
3.3	1.8	2.5	0.35	188	30	200
3.7	1.9	2.5	0.3	250	50	350
3.9	1.95	2.5	0.25	250	50	375
4.2	2.0	2.5	0.25	375	50	225
4.4	2.0	2.5	0.25	375	50	375
4.7	2.0	2.5	0.25	500	50	125
4.8	2.05	2.5	0.25	500	50	375
4.9	2.1	2.55				250
g*	g	2.55				375
5.35	3.1	2.55				125
g	g	g				375
5.5	3.2	2.6				4250
g	g	g				5000
6.9	4.0	2.8				∞

*g = linear gradient across layer

Table 5. RDP parameters

Helmberger and Hadley (1981) source

$$K = 8.0 \text{ s}^{-1}$$

$$B = 1.0$$

$$\Psi_{\infty} = 1.4 \times 10^{11}$$

Von Seggern and Blandford (1972) source

$$K' = 5.2 \text{ s}^{-1}$$

$$B' = 2.5$$

$$\Psi_{\infty} = 1.4 \times 10^{11}$$

Meuller and Murphy (1971) source

$$\text{Yield} = 1000 \text{ Kt}$$

$$h = 1200 \text{ m}$$

$$V_p = 3.4 \text{ km/sec}$$

$$V_s = 1.7 \text{ km/sec}$$

$$\rho = 2.1 \text{ g/cm}^3$$

Table 6. RDP parameters

Factor	MILROW	CANNIKIN
Helmberger and Hadley (1981) source		
K (s⁻¹)	9.0	6.0
B	1.0	0.625
Ψ_{∞} (cm³)	1.0 x 10¹¹	5.69 x 10¹¹
Von Seggern and Blandford (1972) source		
K' (s⁻¹)	9.0	6.0
B'	1.0	0.625
Ψ_{∞} (cm³)	1.0 x 10¹¹	5.69 x 10¹¹
Meuller and Murphy (1971) source		
Yield (Kt)	1000	5000
h (m)	1125	1725
V_p (km s⁻¹)	4.2	4.7
V_s (km s⁻¹)	2.0	2.0
ρ (g cm⁻³)	2.5	2.5
A/A_{cal}	2.0	2.0
Comp. factor	0.8	0.8
Prop. factor	2.0	2.0

See text for detailed explanation of factors.

FIGURE CAPTIONS

Figure 1 Diagrams showing energy with takeoff angle i in the range $i_0 < i < i_0 + \Delta i$ for a point source and for a line source. The energy varies as $\sin i_0$ for the point source case but does not vary as a function of i for the line source case.

Figure 2 Comparison of radiation pattern for corrected and uncorrected line sources. The horizontal line shows the isotropic radiation pattern which results from an uncorrected explosive line source. The $\sqrt{\sin i}$ curve shows the best radiation pattern to simulate an explosive point source. The two sinusoidal curves show the result of mixing a line source force with a line source explosion with $k_{\text{subf}}=0.5$ and $k_{\text{subf}}=0.6$ (50/50 mix and 60/40 mix, respectively). The mixed sources are meant to be accurate in the range $i = +20^\circ$ to $+160^\circ$.

Figure 3 Comparison between uncorrected and corrected FD seismograms and analytic Cagnaird seismograms for an explosive point source in a half-space. The receiver is at a range 30 times the source depth to allow for the development of a Rayleigh wave that is large compared to the direct P-wave. The amplitude scale is the same for all the radial and all the vertical traces, but different between the radial and vertical components.

Figure 4 Location of the Amchitka nuclear tests and the near-field strong motion instruments deployed to record them.

Figure 5 a) S-velocity profiles used for finite difference simulations. Three cases are shown: flat layers with sharp boundaries (sharp), gradient boundaries (gradient) and random media (random). The profile for sharp boundaries is located correctly along the velocity axis, all other profiles have been shifted 1.0 and 2.0 km/s for clarity. These models are also described in Tables 2, 3 and 4. Two profiles, A and B are shown for the random media to show the variation horizontally as well as vertically; the two profiles are 12 km apart horizontally. b) P-velocity profiles used. The gradient and random media curves have been shifted 2.0 km/s relative to the sharp boundary profile. c) Density profiles used. The curves have been shifted 0.2 g/cm³ relative to the sharp boundary profile.

Figure 6 Comparison of finite difference simulations for sharp and gradient boundaries. Models are described in Figure 5 and Tables 2 and 3. Depths and RDP sources (H-H) are appropriate for MILROW and CANNIKIN, respectively. Ranges (given in center) are consistent with available data. Amplitudes are in cm/s.

Figure 7 a) P-velocity profiles showing well-log data from Perret and Breiding (1972), and Perret (1973). The heavy solid line is the sharp boundary model and is correctly located in velocity. The dashed line is the random model used for the simulation, shifted 2.0 km/s. The light lines are the observed profiles for CANNIKIN and MILROW, shifted 2.0 and 5.0 km/s, respectively. b) Corresponding density profiles. Dashed line and light line are shifted 0.4 and 0.75 g/cm³, respectively. Only CANNIKIN density log is available.

Figure 8 Comparison of finite difference simulations for random and gradient models. Models are described in Figure 5 and Tables 3 and 4. Depths and RDP sources (H-H) are appropriate for MILROW and CANNIKIN, respectively. Ranges (given in center) are consistent with available data. Amplitudes are in cm/s.

Figure 9 Comparison of finite difference simulations for fast and slow sites on the gradient model, and the original gradient model. See text for description of fast and slow sites. Depths and RDP sources (H-H) are appropriate for MILROW and CANNIKIN, respectively. Ranges (given in center) are consistent with available data. Amplitudes are in cm/s.

Figure 10 Diagram of the faulted model. The distances are in km. The fault locations and offsets are taken from Orphal, et al. (1971), for the MILROW - M05 cross-section. The base model is the sharp boundary model described in Figure 5 and Table 2, and the letters are keyed to Table 2. The vertical fault offsets are added to the sharp boundary model. The dip of the layers in the region of the sources incorporates the finding of Burdick, et al. (1984) that the structure above the sources is slightly different for CANNIKIN and MILROW.

Figure 11 Comparison of finite difference simulations for faulted and sharp boundary models. The sharp boundary model is described in Figure 5 and Tables 2. The faulted model is described in Figure 10. Depths and RDP sources (H-H) are appropriate for MILROW and CANNIKIN, respectively. Ranges (given in center) are consistent with available data. Amplitudes are in cm/s.

Figure 12 Comparison of data to four of the models previously described (Figures 6, 8, 9 and 11). Data is for station M01 for MILROW, at a range of 8.0 km. The synthetics are all at a range of 8.0 km. Amplitudes are in cm/s.

Figure 13 Comparison of data to four of the models previously described (Figures 6, 8, 9 and 11). Data is for station M06 for MILROW, at a range of 11.5 km. The synthetics are all at a range of 12.0 km. Amplitudes are in cm/s.

Figure 14 Comparison of data to four of the models previously described (Figures 6, 8, 9 and 11). Data is for station M05 for CANNIKIN, at a range of 15.8 km. The synthetics are all at a range of 16.0 km. Amplitudes are in cm/s.

Figure 15 Comparison of data to four of the models previously described (Figures 6, 8, 9 and 11). Data is for station M06 for CANNIKIN, at a range of 18.7 km. The synthetics are all at a range of 19.0 km. Amplitudes are in cm/s.

Figure 16 Comparisons of the Helmberger-Hadley, Mueller-Murphy, and von Seggern-Blandford RDP functions. The top graph shows the time derivative of the RDP, which is the far-field displacement time function for the 3 sources. The next graph shows the RDP's of the 3 sources. The long-period asymptote of the RDP is the ψ_{∞} of the source. The bottom graph shows the amplitude spectra of the far-field displacement time functions for the 3 sources. The parameters used for these RDP functions are listed in Table 5.

Figure 17 Comparison of the Mueller-Murphy, von Seggern-Blandford and Helmberger-Hadley RDP functions used with the gradient boundary model (Table 3). Amplitudes are in cm/s. The parameters used in the RDP functions are listed in Table 6.

Figure 18 Comparison of the Mueller-Murphy, von Seggern-Blandford and Helmberger-Hadley RDP functions used with the gradient boundary model (Table 3). Amplitudes are in cm/s. The parameters used in the RDP functions are listed in Table 6.

Figure 19 Development of a quadrupole correction for cavity asphericity. Cavity on left is ellipsoidal, with the long axis vertical. The arrow on the inside of the cavity represents the pressure acting on the cavity wall. This pressure will radiate both P- and S-wave energy, as partitioned along and normal to the propagation direction. The resultant radiation patterns are shown immediately to the right of the cavity. The P-wave pattern is elongate horizontally, because the increased radius of cavity curvature will amplify the P-wave energy, while decreased radius of curvature will diminish it. This result is further partitioned into an explosion and a quadrupole. The size of the explosion should be that for a spherical cavity of the same net volume as the ellipsoidal cavity. The quadrupole is added to this in varying amounts, dependent on the amount of asphericity.

Figure 20 Comparison of synthetics for a spherical and aspherical cavity explosions (labeled Explosion, Prolate and Oblate) to data from MILROW. The prolate and oblate cavity synthetics are made with a quadrupole correction for asphericity, both fixed at a 40% contribution. Synthetics for all sources are scaled equivalently. Amplitudes are in cm/s. Both radial (R) and vertical (V) components are shown. The synthetics have been filtered with a $T^* = 0.05$ operator and detrended to remove an exponential with time artifact of the higher-order terms of the asymptotic source expansion.

Figure 21 Comparison of synthetics for a spherical and aspherical cavity explosions (labeled Explosion, Prolate and Oblate) to data from CANNIKIN. Only radial components are shown. Compare Figure 20 (MILROW). Scaling and filtering of these synthetics are the same as in Figure 20.

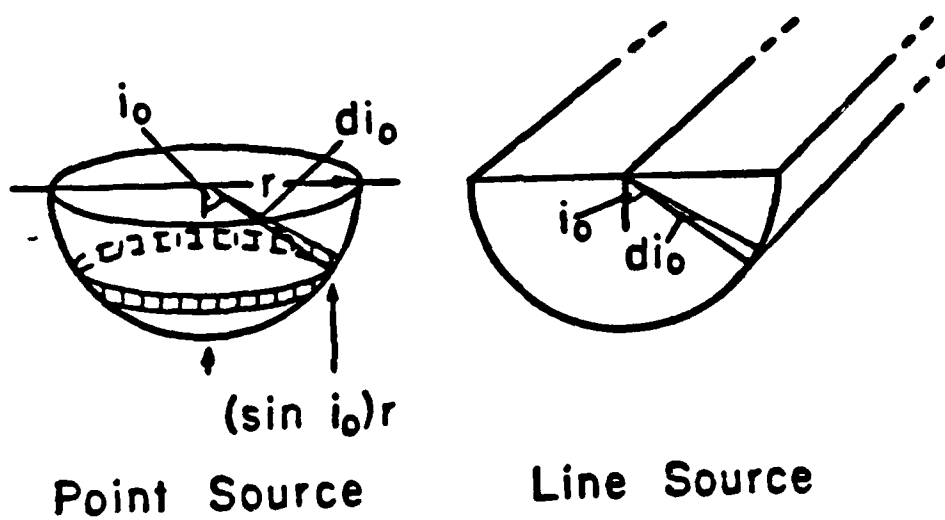


FIGURE 1

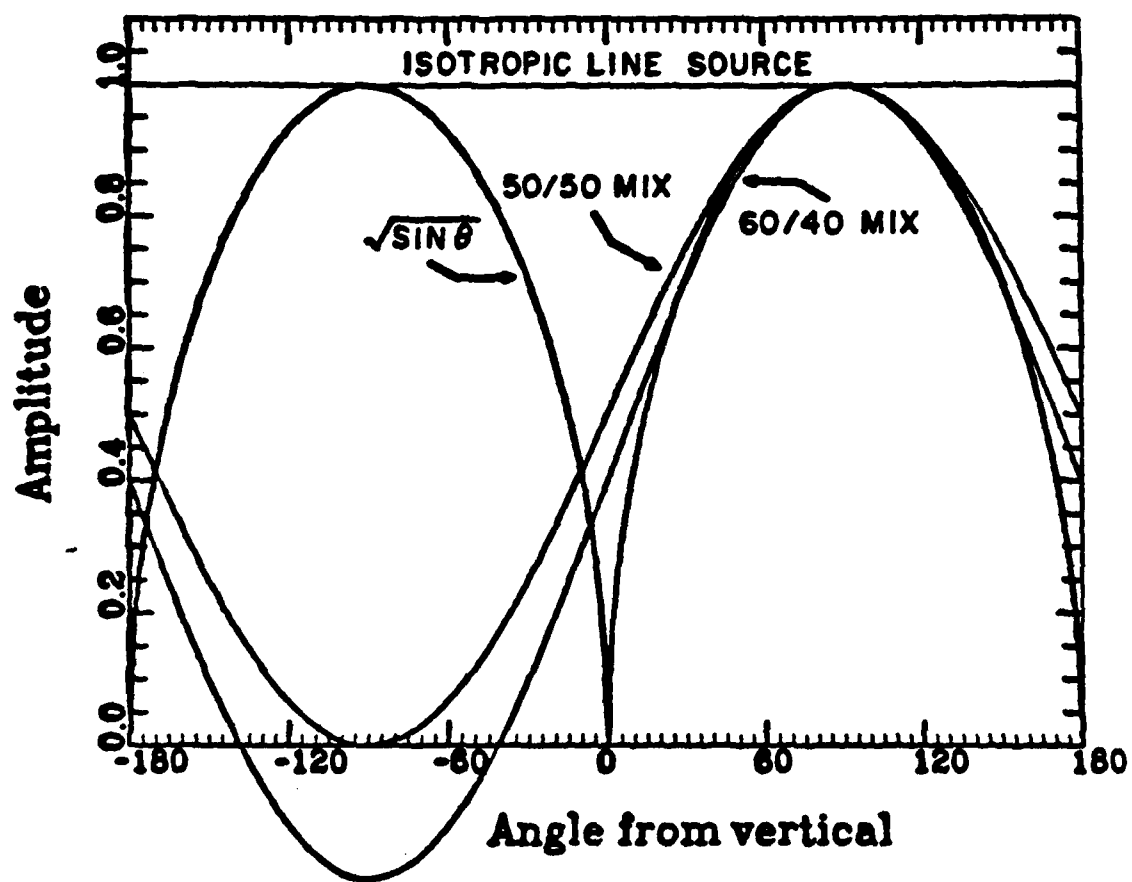


FIGURE 2

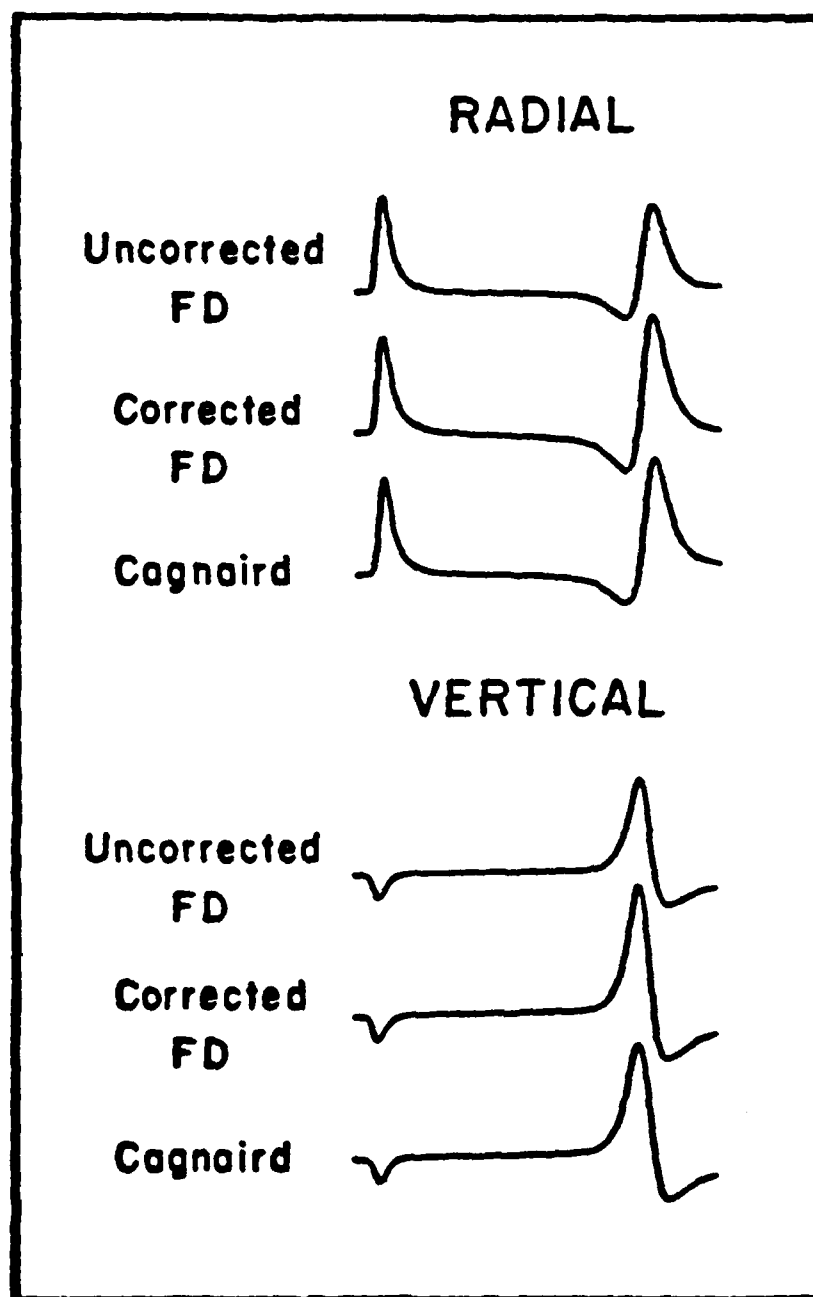


FIGURE 3

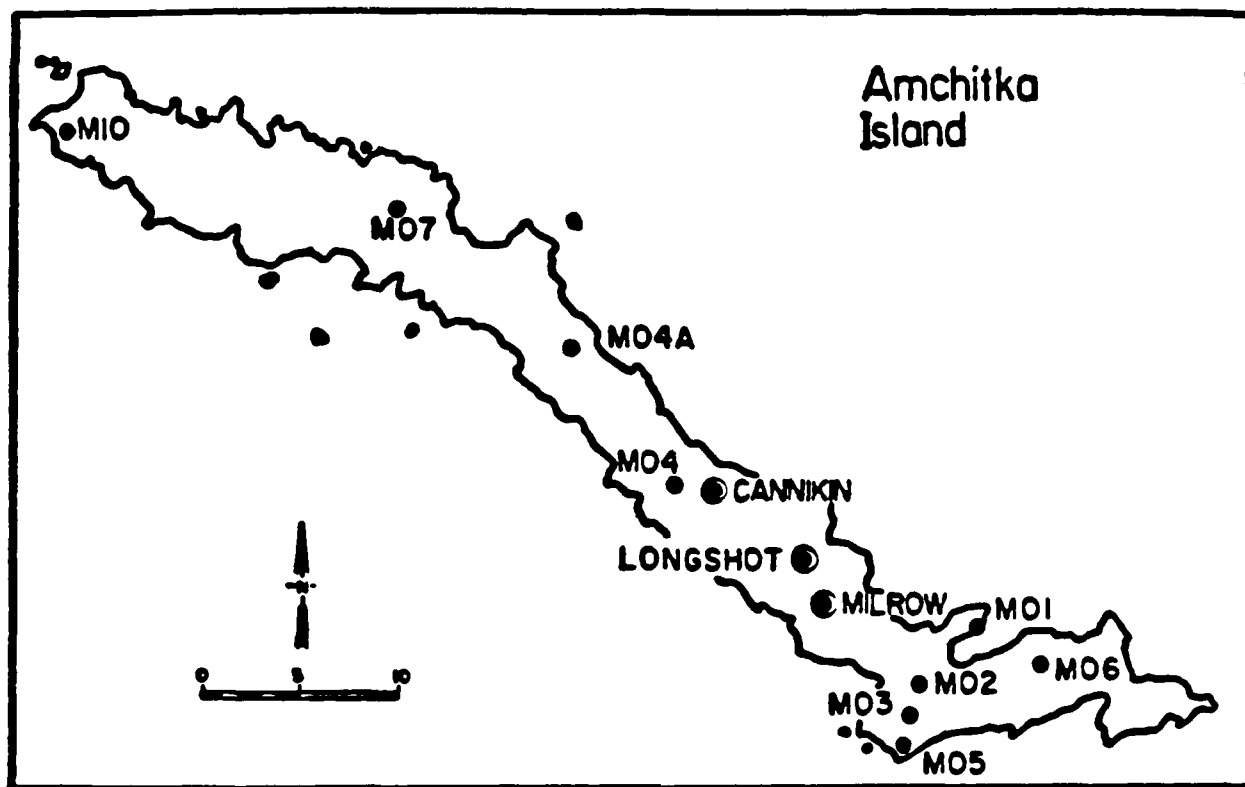


FIGURE 4

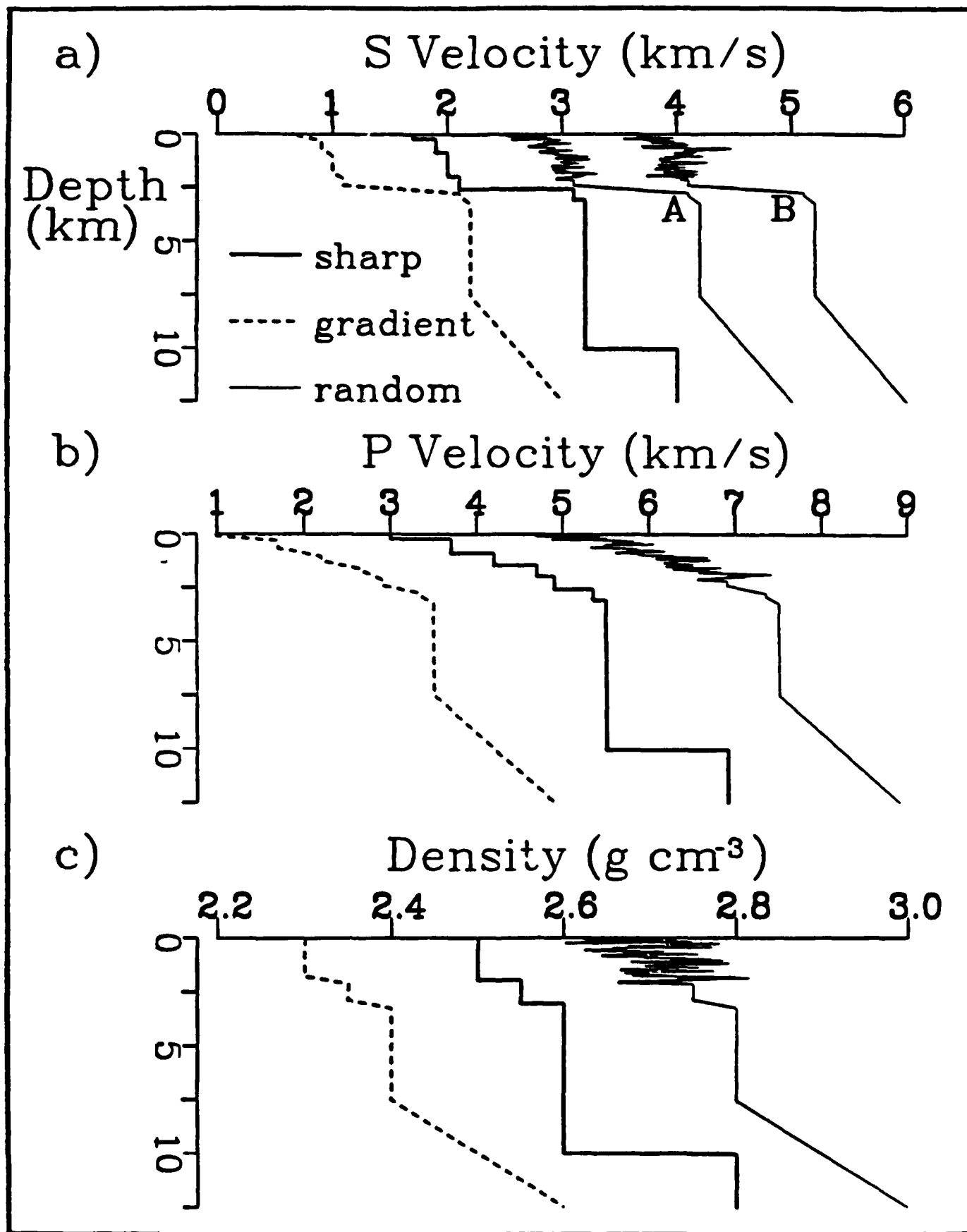
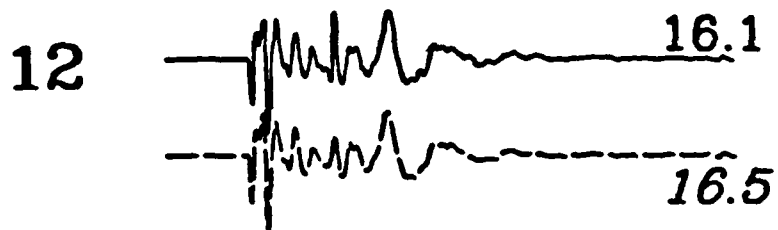
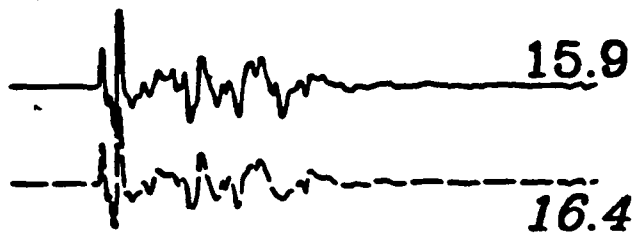
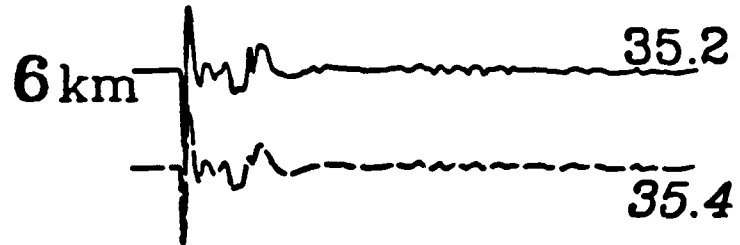
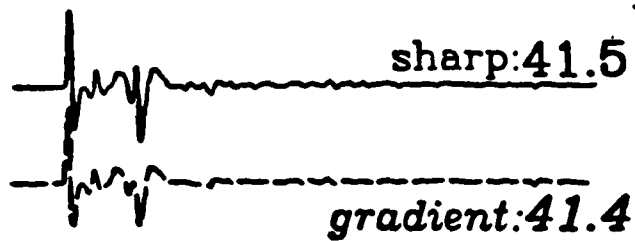
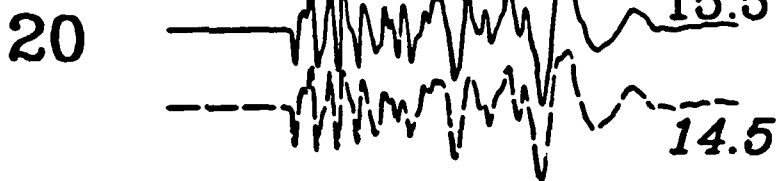
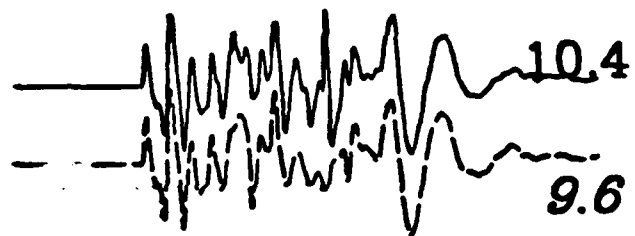
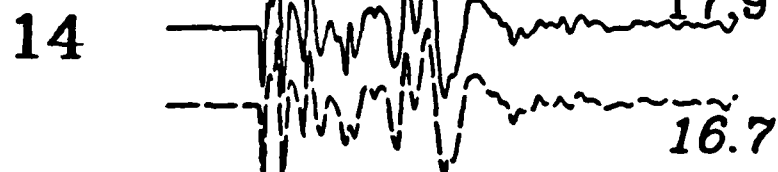
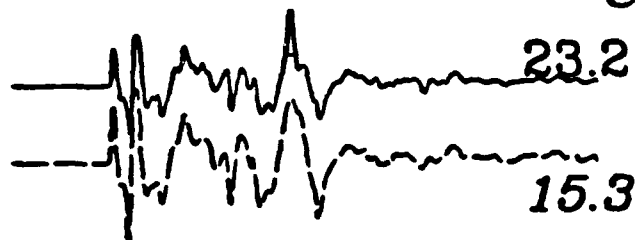


FIGURE 5

MILROW



CANNIKIN



Radial

5 sec

Vertical

FIGURE 6

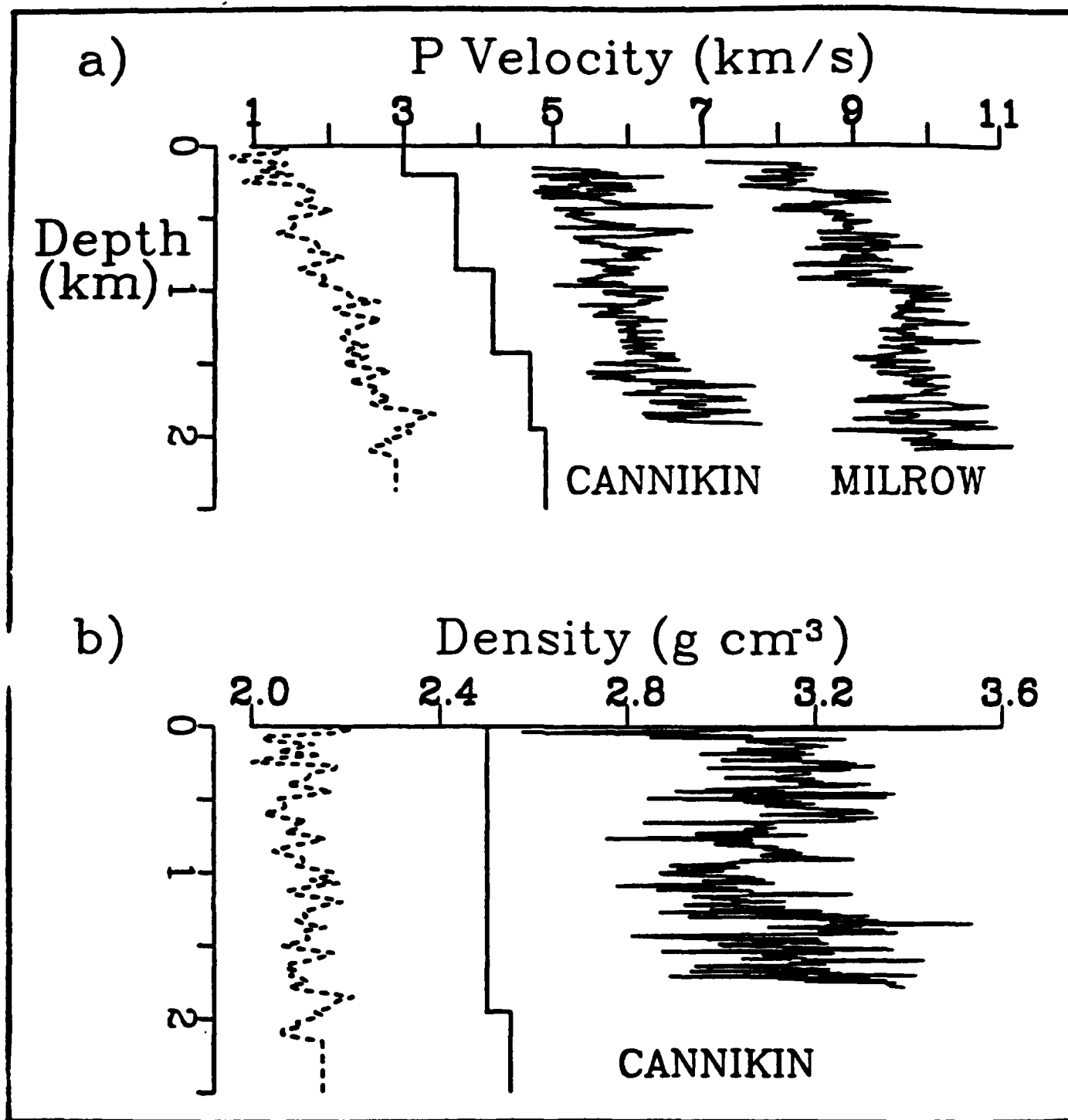


FIGURE 7

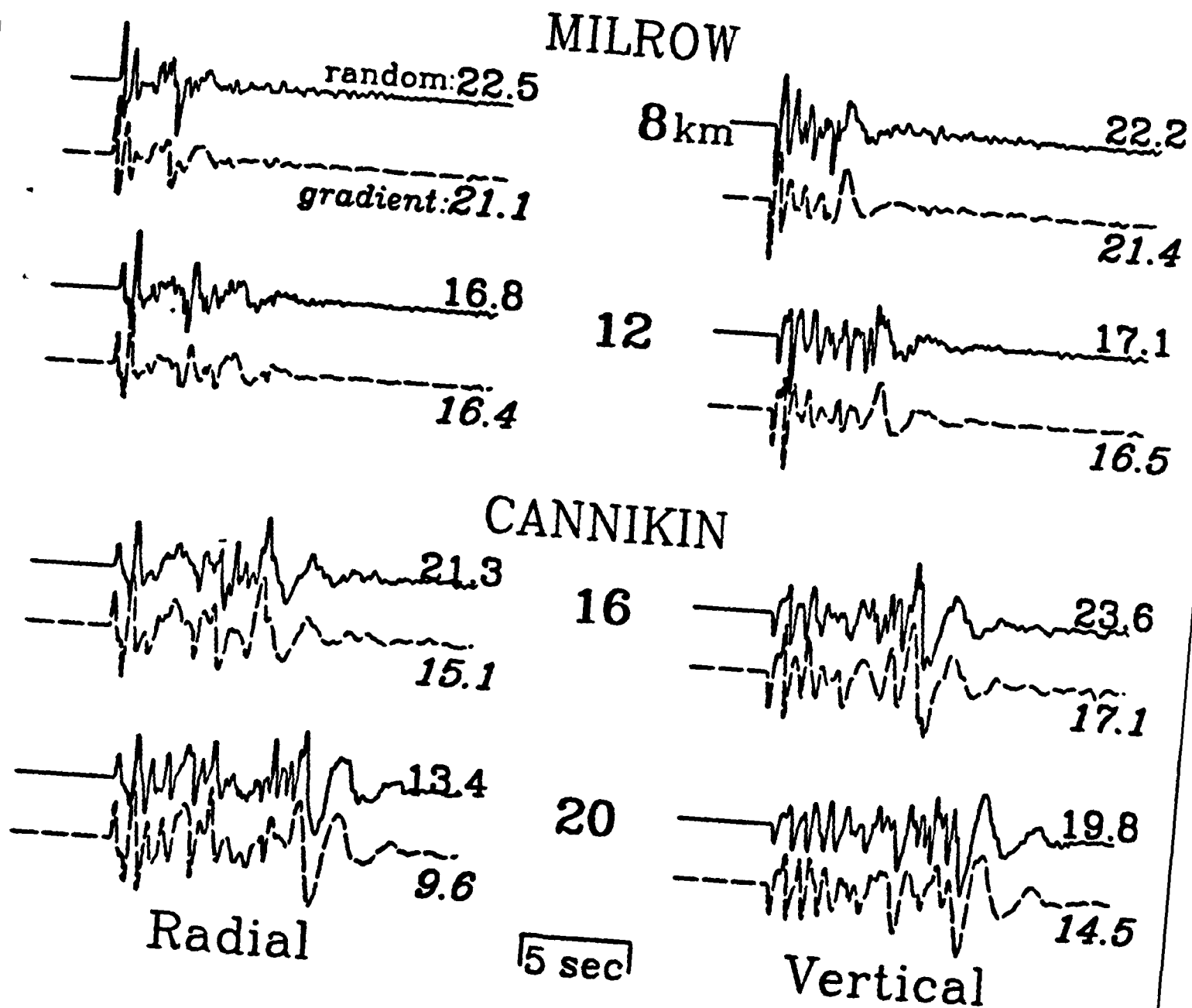
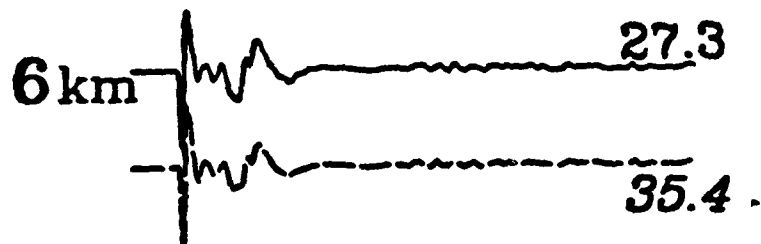
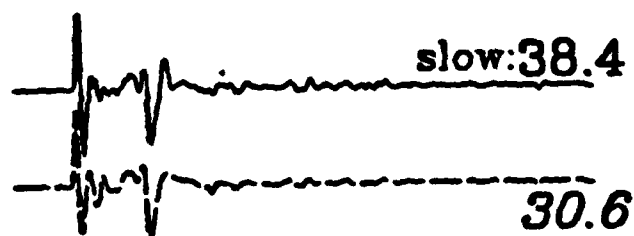
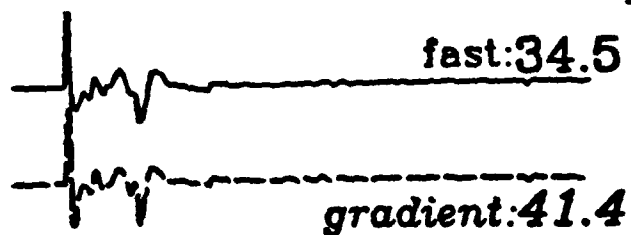
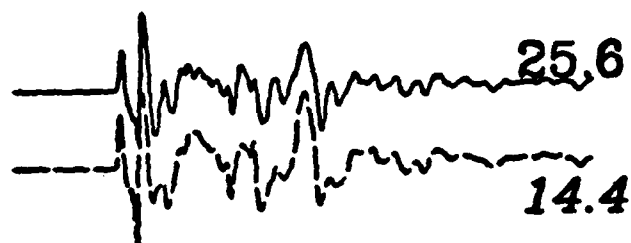
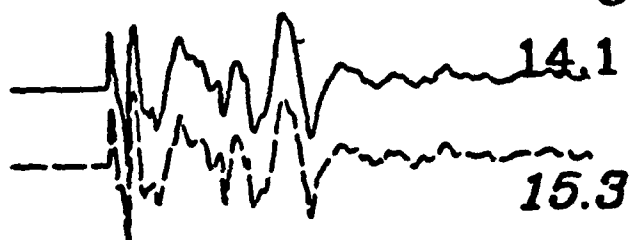


FIGURE 8

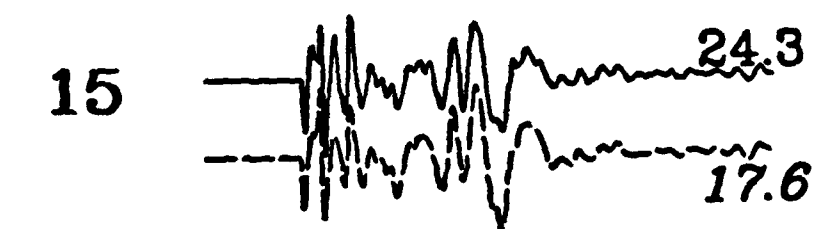
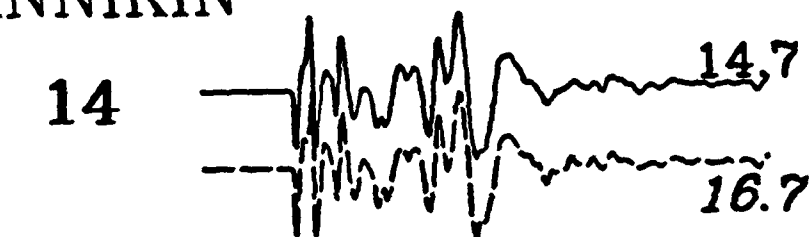
MILROW



CANNIKIN



Radial



Vertical

5 sec

FIGURE 9

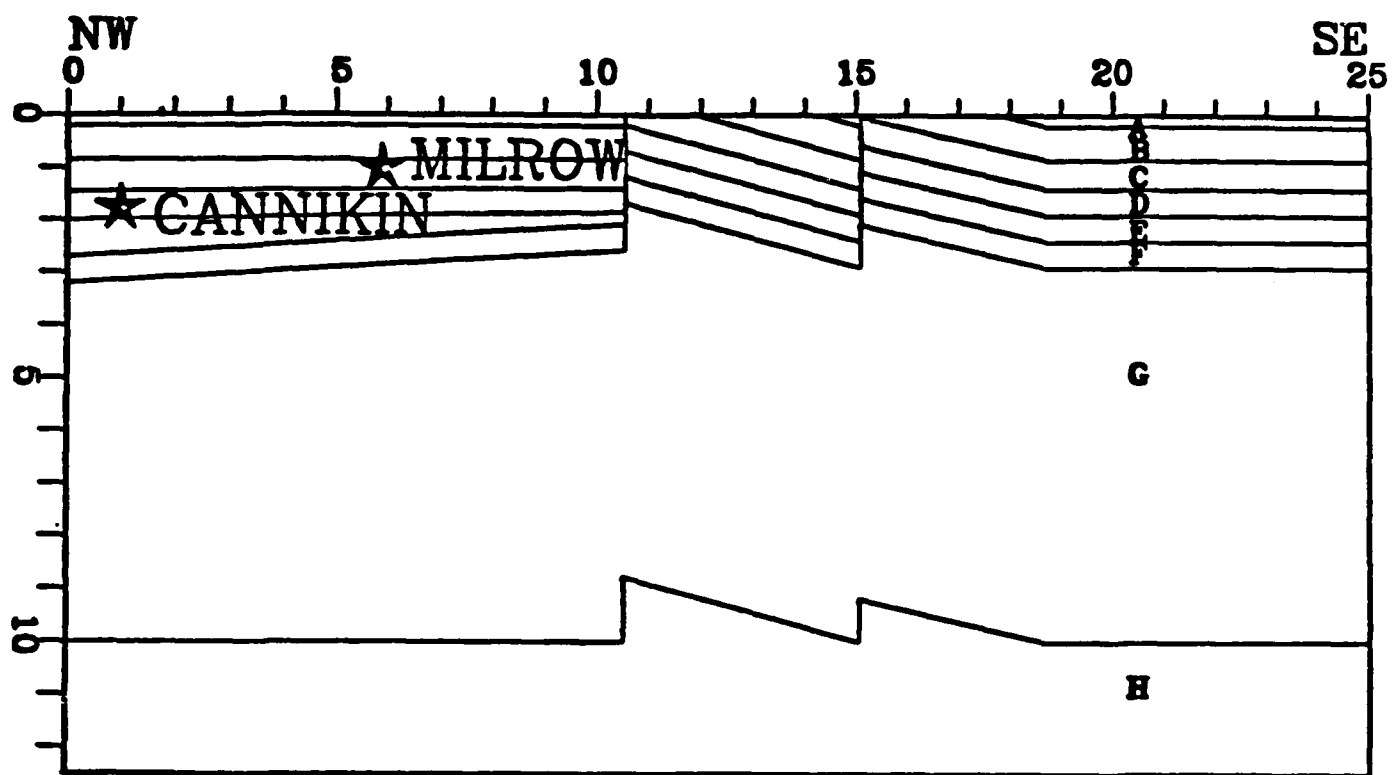


FIGURE 10

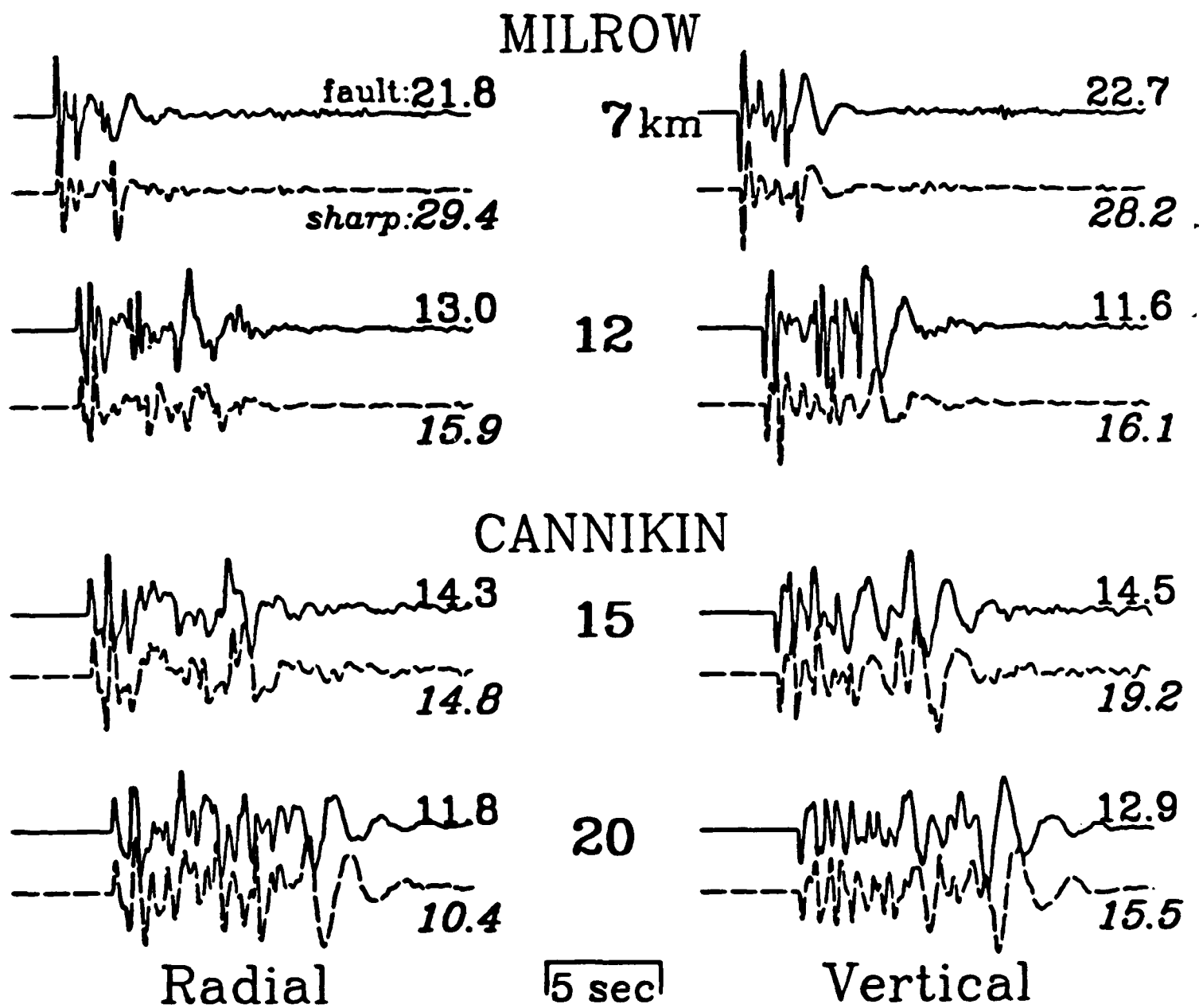


FIGURE 11

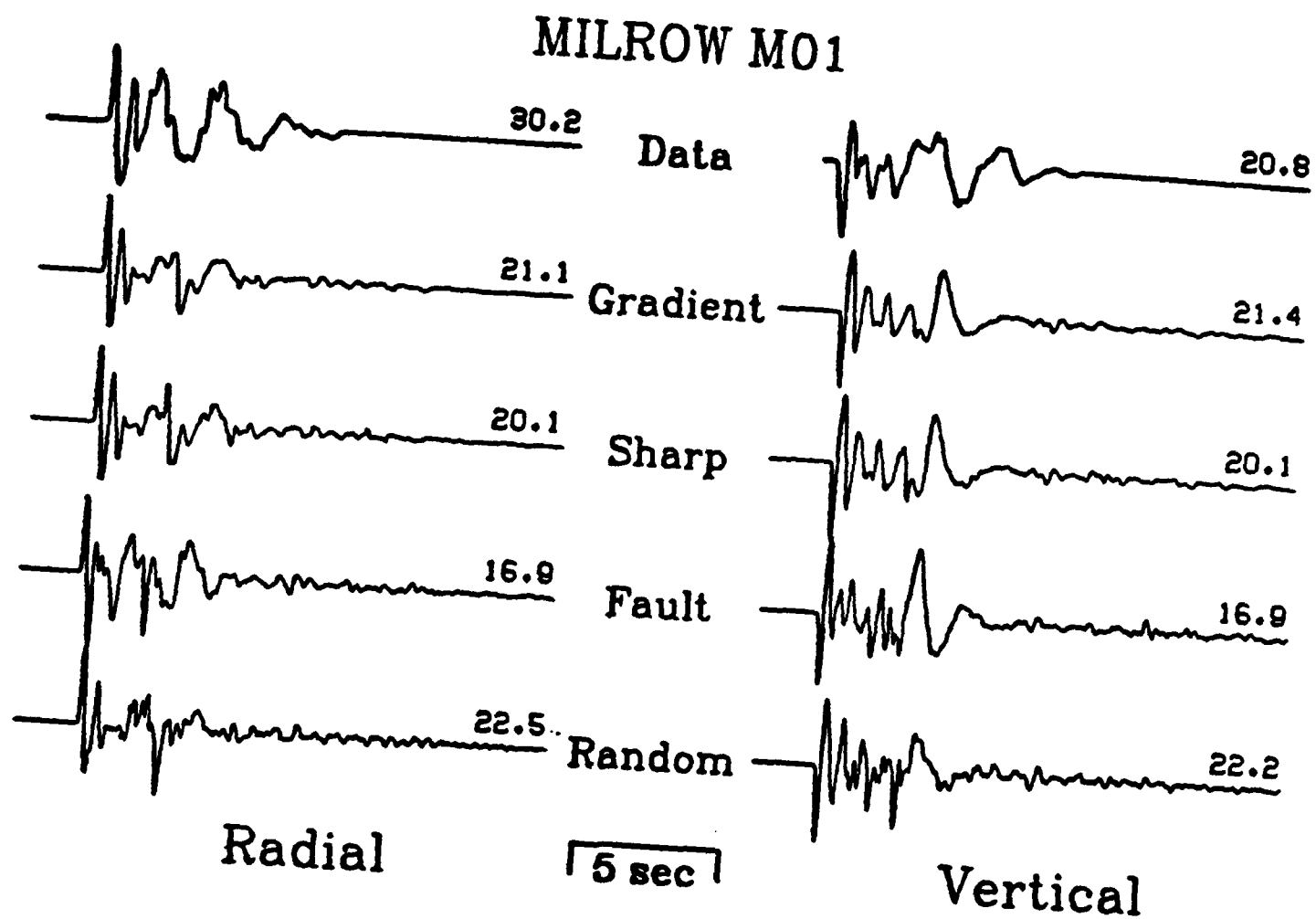


FIGURE 12

MILROW M06

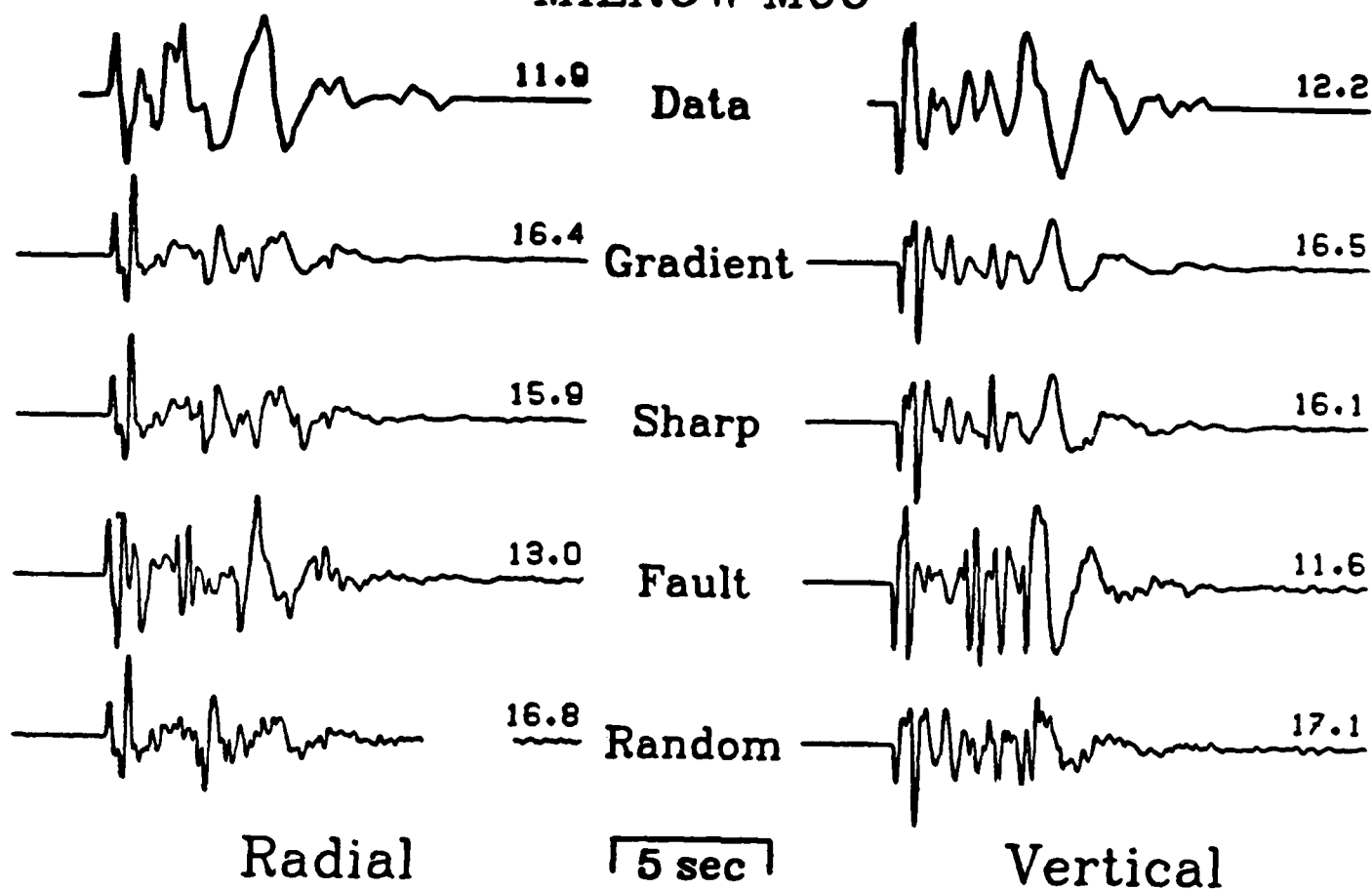


FIGURE 13

CANNIKIN M05

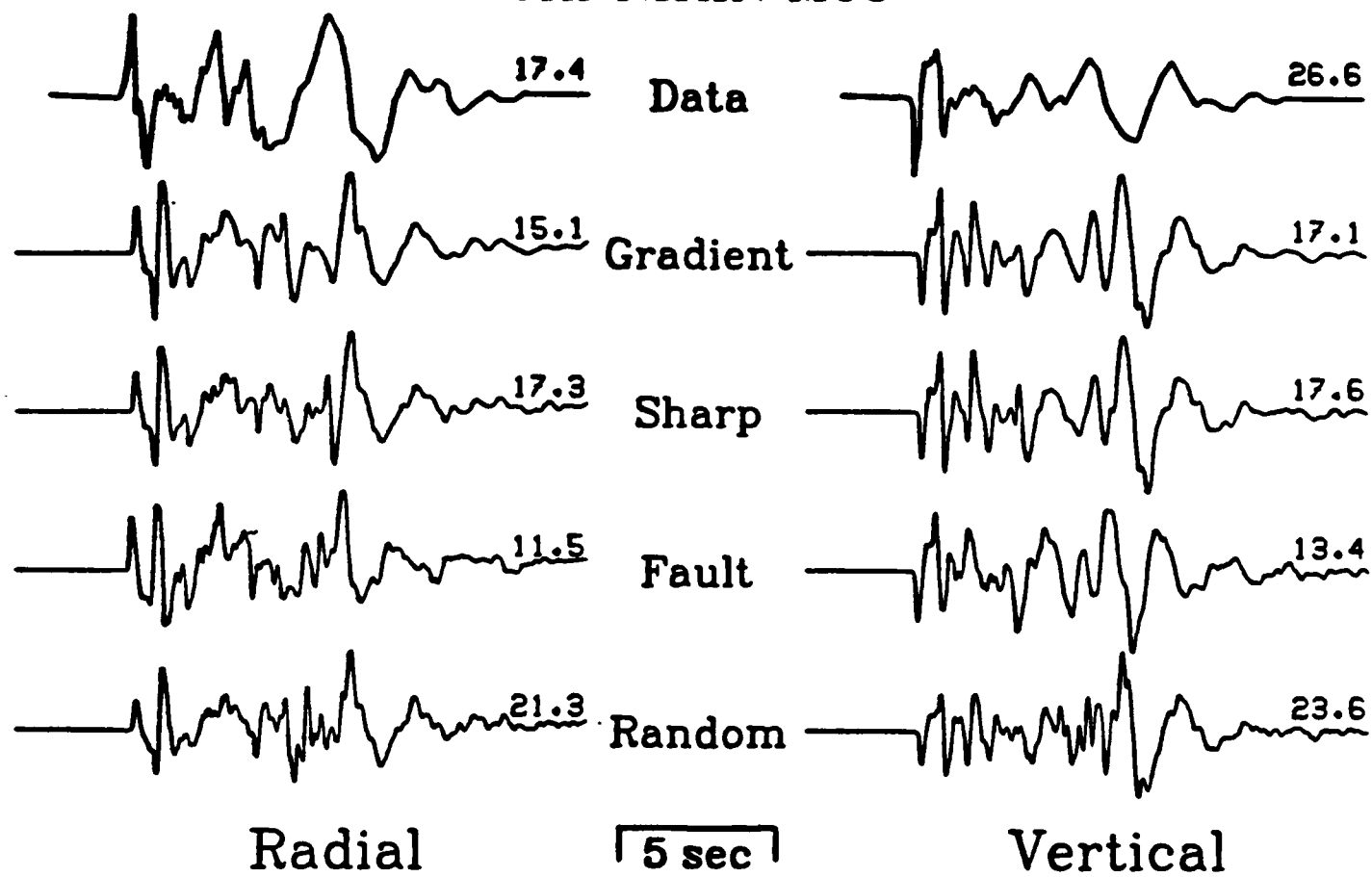


FIGURE 14

CANNIKIN M06

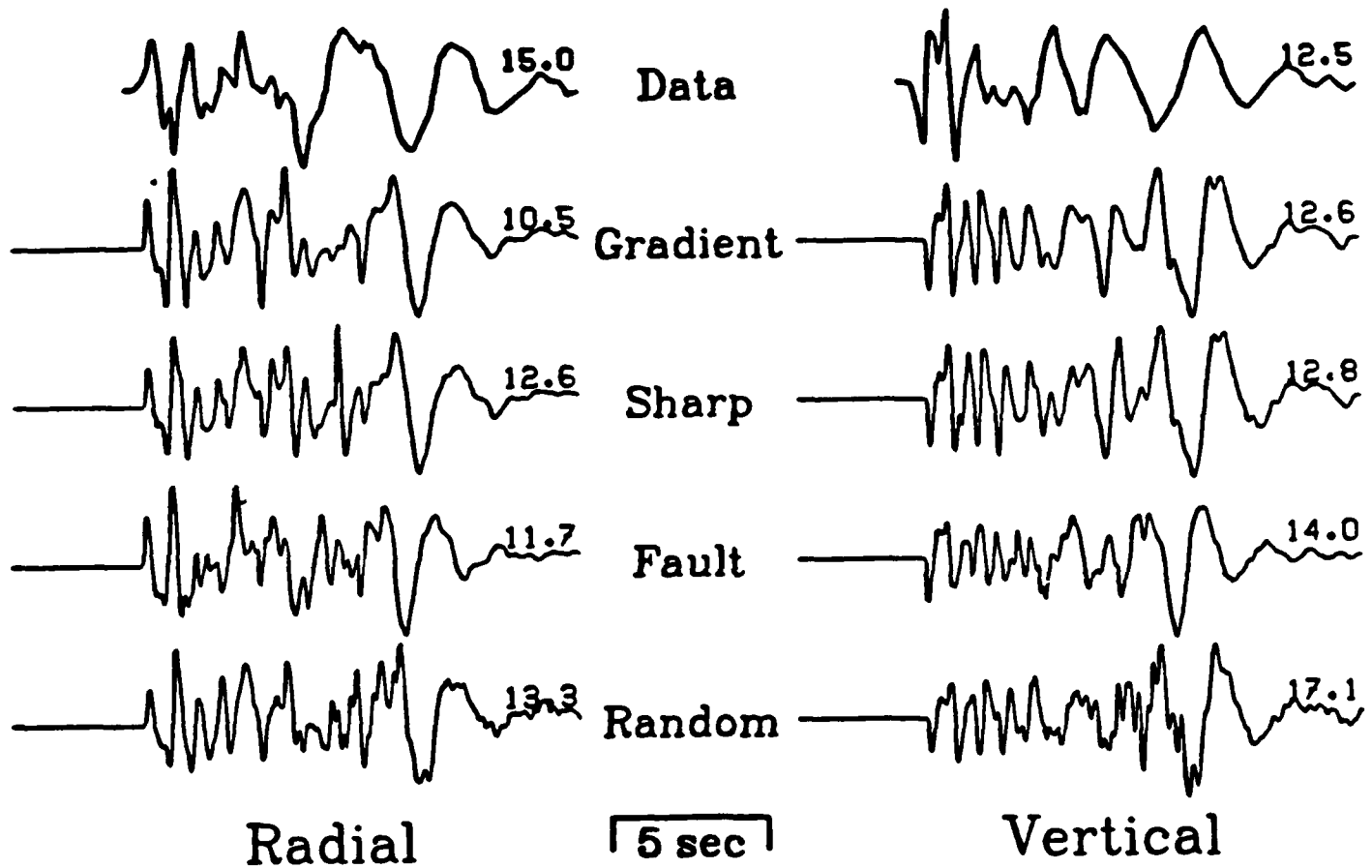


FIGURE 15

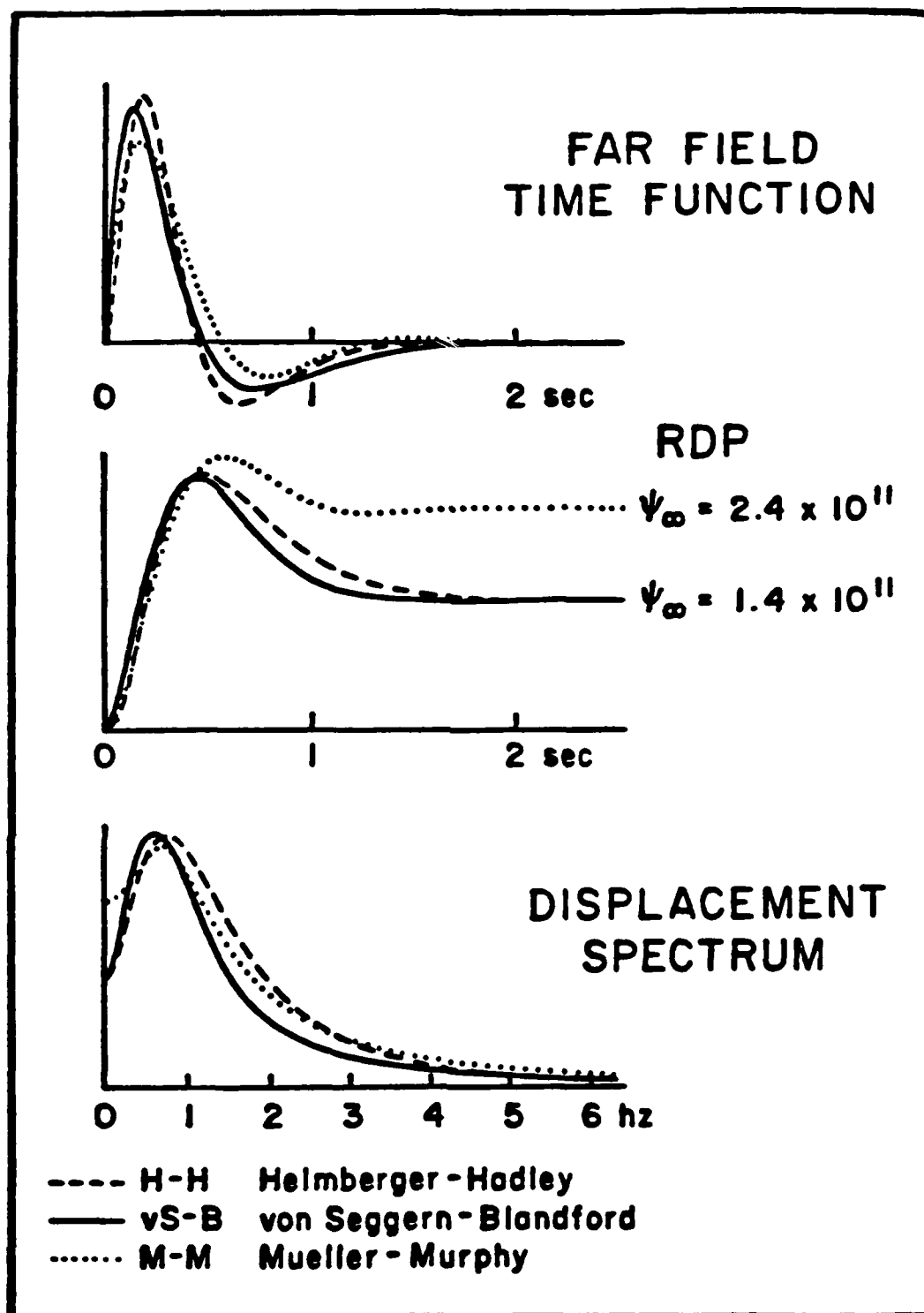


FIGURE 16

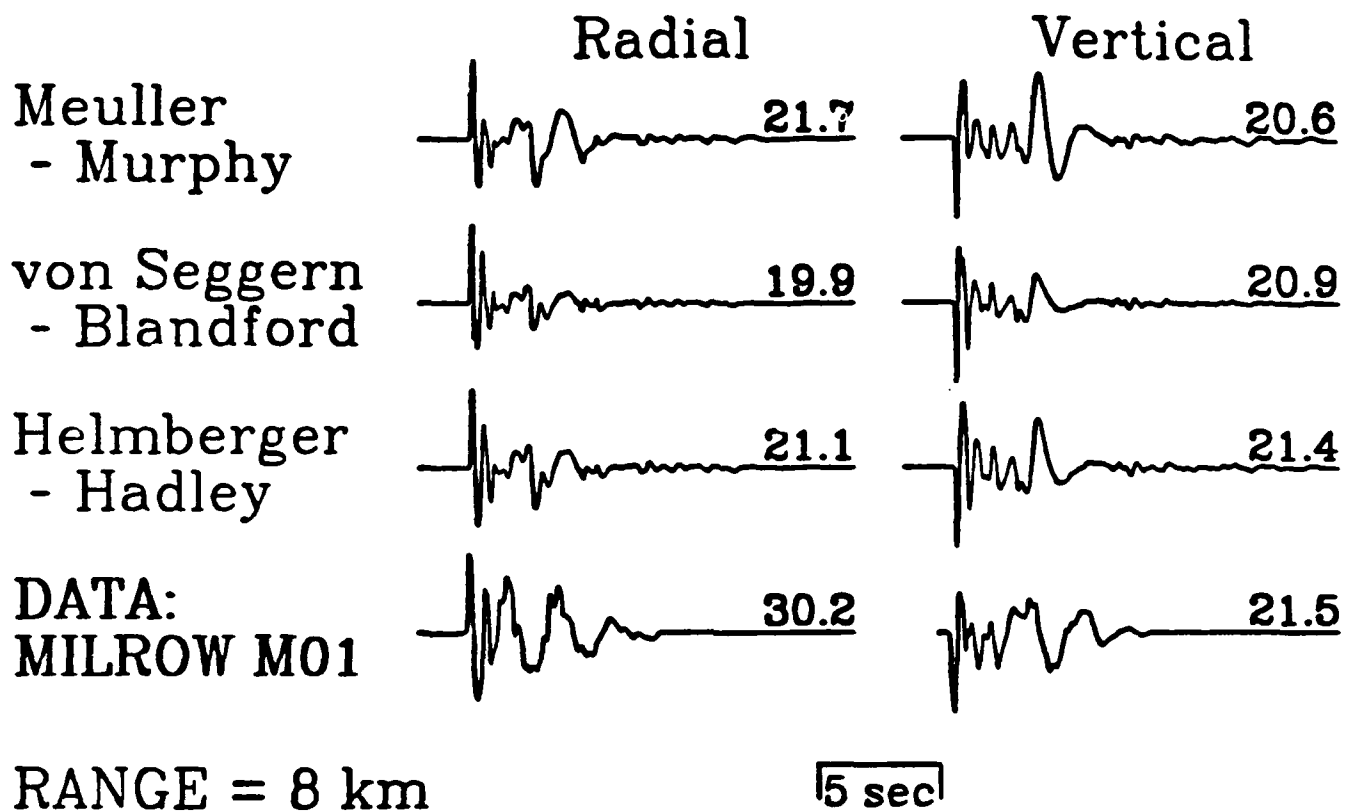


FIGURE 17

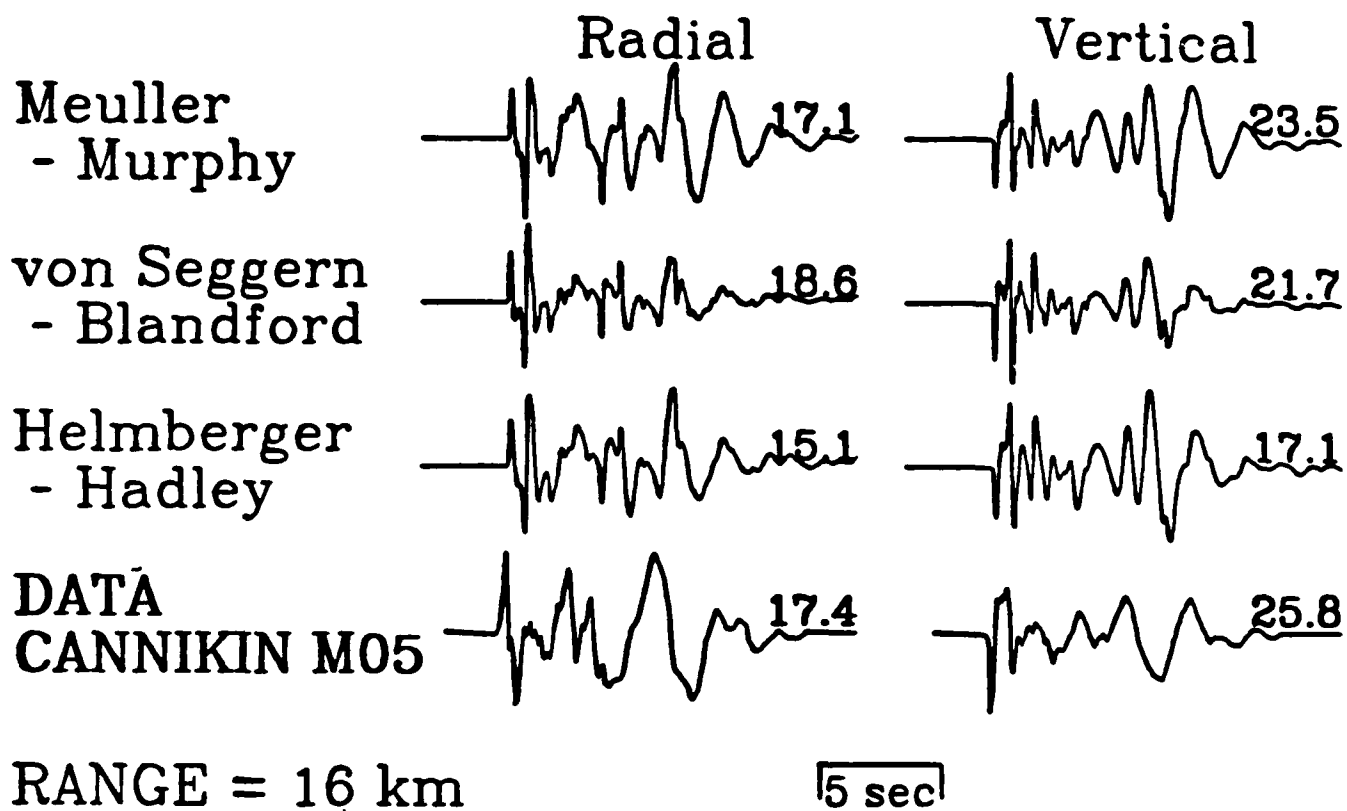


FIGURE 18

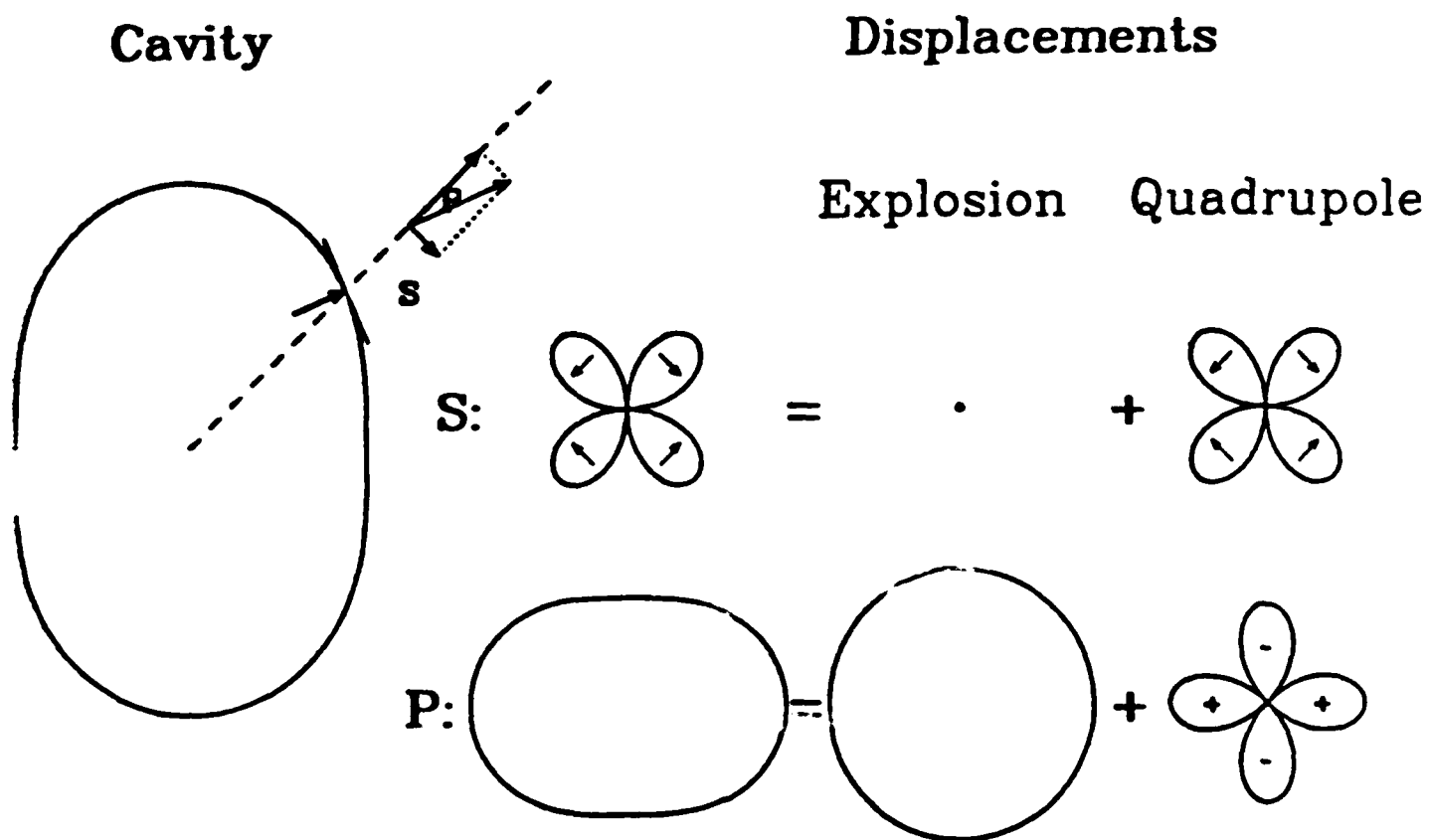


FIGURE 19

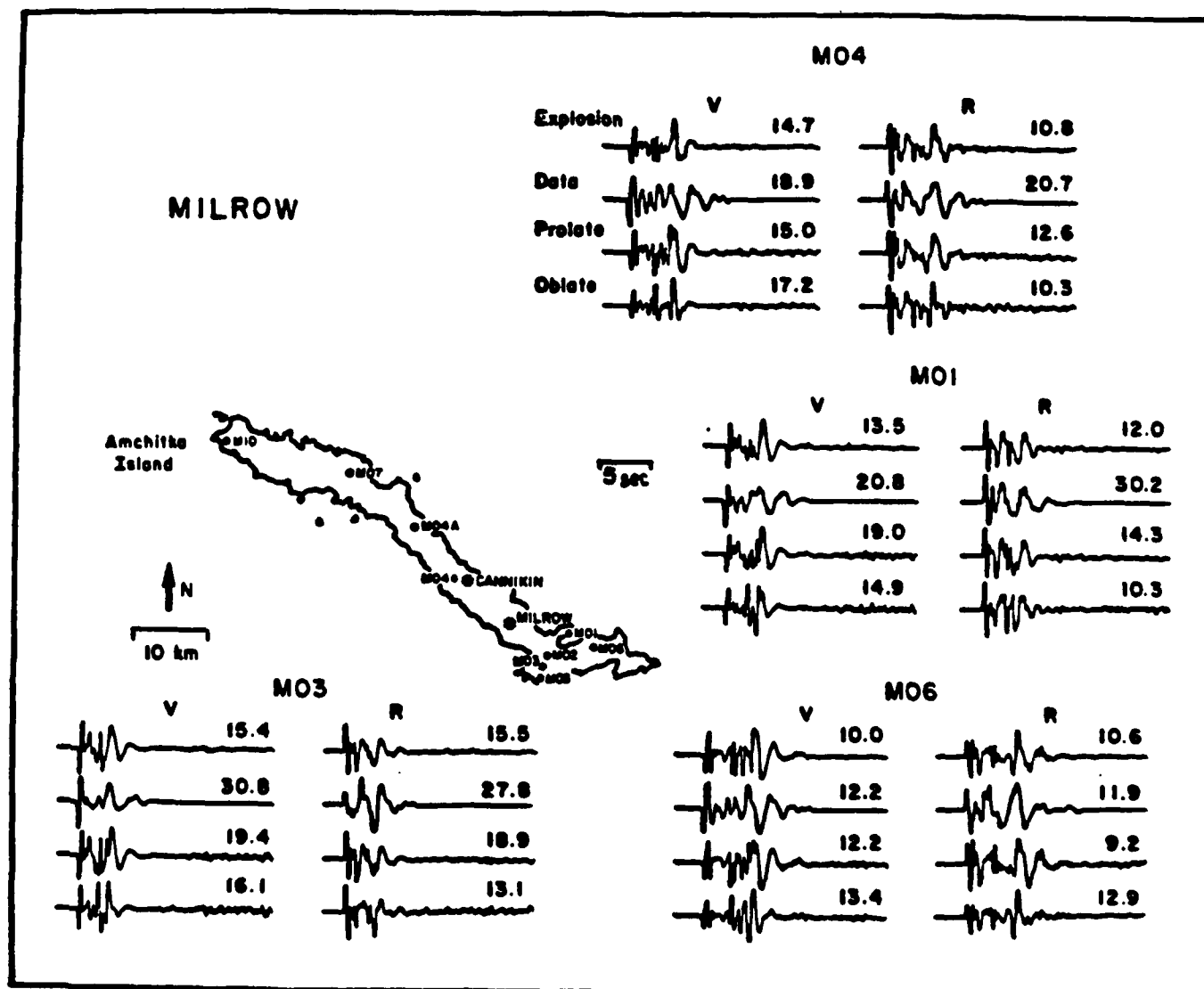


FIGURE 20

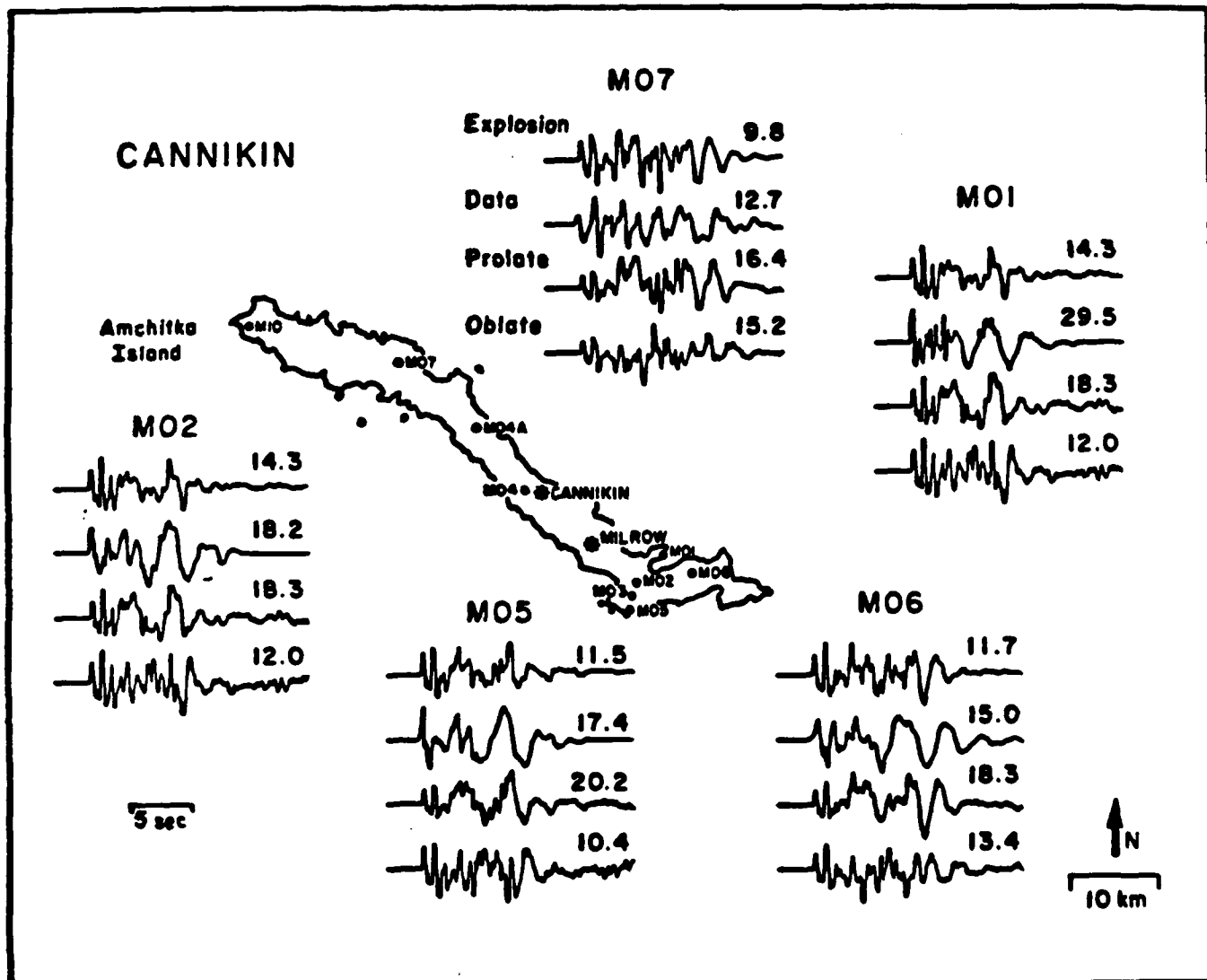


FIGURE 21

SECTION 5

THEORETICAL RAYLEIGH AND LOVE WAVES FROM AN EXPLOSION IN PRESTRESSED SOURCE REGIONS

THEORETICAL RAYLEIGH AND LOVE WAVES FROM AN EXPLOSION IN PRESTRESSED SOURCE REGIONS

BY D. G. HARKRIDER, J. L. STEVENS, AND C. B. ARCHAMBEAU

ABSTRACT

Expressions and synthetics for Rayleigh and Love waves generated by various tectonic release models are presented. The multipole formulas are given in terms of the strengths and time functions of the source potentials. This form of the Rayleigh and Love wave expressions is convenient for separating the contribution to the Rayleigh wave due to the compressional and shear wave source radiation and the contribution of the upgoing and downgoing source radiation for both Rayleigh and Love waves. Because of the ease of using different compression and shear wave source time functions, these formula are especially suited for sources for which second and higher degree moment tensors are needed to describe the source, such as the initial value cavity release problem.

A frequently used model of tectonic release is a double couple superimposed on an explosion. Eventually we will compare synthetics of this and more realistic models in order to determine for what dimensions of the tectonic release model this assumption is valid and whether the Rayleigh wave is most sensitive to the compressional or shear wave source history. The pure shear cavity release model is a double couple with separate P wave and S wave source histories. The time scales are proportional to the source region's dimension and differ by their respective body wave velocities. Thus, a convenient way to model the effect of differing shot point velocities and source dimensions is to run a suite of double couple time history calculations for the P wave and SV wave sources separately and then sum the different combinations.

One of the more interesting results from this analysis is that the well known effect of vanishing Rayleigh wave amplitude as a vertical or horizontal dip slip double couple model approaches the free surface is due to the destructive interference between the P wave and SV wave generated Rayleigh waves. The individual Rayleigh wave amplitudes, unlike the SH generated Love waves, are comparable in size to those from other double couple orientations. This has important implications to the modeling of Rayleigh waves from shallow dip slip fault models. Also, the P wave radiation from double couple sources is a more efficient generator of Rayleigh waves than the associated SV wave or the P wave from explosions. The latter is probably due to the vertical radiation pattern or amplitude variation over the wave front. This effect should be similar to that of the interaction of wave front curvature with the free surface.

INTRODUCTION

A frequently used model of tectonic release from underground nuclear explosions is a double couple superimposed on an explosion. For a point double couple, the time histories for the source compressional (P) and shear (S) waves are identical. For more realistic models of tectonic release such as the formation of a cavity in a pure shear field, the source radiation pattern is identical to a double couple but the P- and S- wave source histories differ. We restrict tectonic release to explosion induced volume relaxation sources in a prestressed medium and do not consider earthquake triggering by an explosion. For a spherical cavity, the P- and S- wave time scales are roughly proportional to the cavity dimensions and differ by their respective body wave velocities. We will show that Rayleigh waves excited by the source P-waves are almost completely out of phase with the S-wave generated Rayleigh waves and thus this difference in source time histories may in some cases be important.

We present expressions and synthetics for Rayleigh and Love waves generated by various tectonic release models. The multipole formulas are given in terms of the strengths and time functions of the source potentials. This form of the Rayleigh and Love wave expressions is convenient for separating the contribution to the Rayleigh wave due to the P- and S-wave source radiation and the contribution of the upgoing and downgoing source radiation for both Rayleigh and Love waves. Because of the ease of using different compression and shear wave source time functions, these formula are especially suited for sources for which second and higher degree moment tensors are needed to describe the source, such as the initial value cavity release problem.

In 1964 Haskell and Harkrider presented formulations for sources and receivers in multilayered isotropic halfspaces. The formulations were for general point sources which were simplified for particular sources. Haskell gave the results for point forces, dipoles, couples, double couples and explosions. Harkrider gave expressions for the surface waves from explosions and Green's functions, i.e. point forces. Both formulations used propagator

matrices for homogeneous isotropic layers. Ben-Menahem and Harkrider (1984) extended the far field results of Harkrider (1984) to couples and double couples of arbitrary orientation.

Other than the sources investigated the basic difference between the results was that Haskell propagated from the source up to the free surface, while Harkrider obtained the source and receiver depth effects in terms of layer propagators from the surface down to the source as well as the receiver in order to demonstrate reciprocity. To obtain the latter result Harkrider used inverses for the homogeneous layer propagators which formed a group, ie. the inverse of the product of two layer propagator matrices was related in the same way to the elements of the product as the inverse of each layer matrix was to the elements of the homogeneous matrix. This is not true for the homogeneous layer inverse which is produced by replacing the layer thickness with the negative layer thickness. Each formulation has advantages. Harkrider (1970) reduced the numerical problems of his formulation by evaluating his expressions using the compound matrix relations of Dunkin(1965) and Gilbert and Backus (1966). Further numerical improvements to layer matrix methods can be found in Kind and Odom (1983).

Hudson(1969) extended the formulation of Haskell(1964) to propagators for isotropic vertically inhomogeneous velocity and density structures. Since Haskell's formulation did not use inverse propagators this was relatively straightforward. Douglas, etal(1971) used reciprocity relations with Hudson's formulation to obtain the vertically inhomogeneous results for explosions equivalent to Harkrider's multilayer result. It was not until the middle 1970's that Woodhouse (1974) showed that this inverse was true for the more general isotropic inhomogeneous halfspace.

Ben-Menahem and Singh (1968) presented a formulation using multipolar expansions of the displacement Hansen vectors. We use a similar multipolar expansion of the scalar potentials for P, SV and SH waves. Since numerical finite difference simulations of complex source or source region radiation routinely use the divergence and curl of the displacement

field to separate P- and S-wave radiation and since these are easily related to P- and S-wave potentials, this type of expansion was a natural one for this class of problem. This was the original motivation for using potential expansions (Bache and Harkrider, 1976). In addition, it allowed us to use the theoretical results of Harkrider (1964) for Rayleigh and Love waves in multilayered media by means of a trivial generalization. For theoretical problems, the choice between multipolar expansion of Hansen vectors and potentials is a matter of convenience. In fact, we use the Hansen vector representation of the displacement field for a cavity initiated tectonic release as our fundamental source and then convert it into potentials.

This formulation, either in preliminary drafts of this manuscript or as a part of technical reports, has been referenced and/or used by Bache and Harkrider (1976), Bache et al (1978), Harkrider (1981), and Stevens (1982). The prestress fields discussed in this paper are restricted to homogeneous pure shear fields. More complicated cases can be found in Stevens (1982).

In the next section we present the displacement fields and potentials for the tectonic release source and the various approximations to it which have appeared in the literature including the point double couple. In addition we give the displacements and potentials for the explosion model corresponding to a step pressure applied to a spherical cavity. The sources are discussed in terms of their equivalent moment tensor forms and we presents illustrative comparisons of their far field time functions. In the following sections we present the multipole extension to Harkrider (1964) and then evaluate it to obtain surface wave expressions for the sources mentioned above and also the second order moment tensor for comparison with Mendiguren (1975). Finally we calculate Rayleigh and Love wave seismograms for canonical orientations of the pure shear stress field (Harkrider, 1977) and discuss them in terms of their P- and S-wave excitation.

TECTONIC RELEASE SOURCE MODELS

The tectonic release source model used in this paper is the instantaneous creation of a spherical cavity of radius R_0 in the presence of pure shear, $\tau_{12}^{(0)}$, at infinity. Details on the behavior and the literature of this and other tectonic release sources can be found in Stevens (1980). The form of the solution used here and the notation is from Ben-Menahem and Singh (1981, p228).

$$\bar{u}(\mathbf{x}, \omega) = \gamma_{22}^s L_{22}^s(k_o R) + \beta_{22}^s N_{22}^s(k_p R) \quad (1)$$

where the Hansen vectors are

$$L_{22}^s(k_o R) = \frac{dH_2^{(0)}(k_o R)}{d(k_o R)} P_{22}^s + \frac{H_2^{(0)}(k_o R)}{(k_o R)} \sqrt{6} B_{22}^s \quad (2)$$

$$N_{22}^s(k_p R) = 0 \frac{H_2^{(0)}(k_p R)}{(k_p R)} P_{22}^s + \left[\frac{dH_2^{(0)}(k_p R)}{d(k_p R)} + \frac{H_2^{(0)}(k_p R)}{(k_p R)} \right] \sqrt{6} B_{22}^s$$

and the vector spherical harmonics are

$$P_{22}^s = P_2^2(\cos\theta) \sin 2\phi \mathbf{e}_R \quad (3)$$

$$\sqrt{6} B_{22}^s = 2 P_2^1(\cos\theta) \sin 2\phi \mathbf{e}_\theta + 6 P_1^1(\cos\theta) \cos 2\phi \mathbf{e}_\phi$$

The coefficients are given by

$$\beta_{22}^s = - \frac{\tau_{12}^{(0)}}{6\mu k_p} g(\omega) \frac{[2F_{2,1}(k_o R_0) - F_{2,2}(k_o R_0)]}{\Delta_2} \quad (4)$$

$$\gamma_{22}^s = - \frac{\tau_{12}^{(0)}}{6\mu k_o} g(\omega) \frac{[6F_{2,1}(k_p R_0) - F_{2,2}(k_p R_0)]}{\Delta_2}$$

where

$$F_{l,1}(\xi) = \frac{(l-1)}{\xi^2} h_l^{(0)}(\xi) - \frac{1}{\xi} h_{l+1}^{(0)}(\xi)$$

$$F_{l,2}(\xi) = \left[\frac{2}{\xi^2} (l^2 - 1) - 1 \right] h_l^{(0)}(\xi) + \frac{2}{\xi} h_{l+1}^{(0)}(\xi) \quad (5)$$

$$F_{l,l}(\xi) = \left[\frac{1}{\xi^2} l(l-1) - \frac{1}{2} \left(\frac{\alpha}{\beta} \right)^2 \right] h_l^{(0)}(\xi) + \frac{2}{\xi} h_{l+1}^{(0)}(\xi)$$

$$\Delta_l = 2l(l+1) F_{l,1}(k_p R_0) F_{l,1}(k_o R_0) - F_{l,2}(k_p R_0) F_{l,2}(k_o R_0)$$

and

$$g(\omega) = \frac{1}{i\omega}$$

In Cartesian coordinates, the Hansen vectors are given by

$$L_{22}^2(k_o R) = \frac{1}{k_o} \nabla \left[h_2^{(0)}(k_o R) P_2^2(\cos\theta) \sin 2\phi \right]$$

and

(6)

$$N_{22}^2(k_p R) = -\frac{2}{k_p} \nabla \left[h_2^{(0)}(k_p R) P_2^2(\cos\theta) \sin 2\phi \right] + 6 h_1^{(0)}(k_p R) P_1^1(\cos\theta) \left(\sin\phi \mathbf{e}_1 + \cos\phi \mathbf{e}_2 \right)$$

Using the following relations

$$\frac{\partial A_o}{\partial x_1} = ik_o^2 h_1^{(0)}(k_o R) P_1^1(\cos\theta) \cos\phi$$

$$\frac{\partial A_o}{\partial x_2} = ik_o^2 h_1^{(0)}(k_o R) P_1^1(\cos\theta) \sin\phi \quad (7)$$

$$\frac{\partial^2 A_o}{\partial x_1 \partial x_2} = -ik_o^2 h_2^{(0)}(k_o R) P_2^2(\cos\theta) \sin 2\phi$$

where

$$A_o = -ik_o h_0^{(0)}(k_o R) = \frac{\exp(-ik_o R)}{R}$$

we have

$$L_{22}^2(k_o R) = i \frac{6}{k_o^4} \left\{ \nabla \frac{\partial^2 A_o}{\partial x_1 \partial x_2} \right\} \quad (8)$$

$$N_{22}^2(k_p R) = -i \frac{6}{k_p^4} \left\{ 2 \nabla \frac{\partial^2 A_p}{\partial x_1 \partial x_2} + k_p^2 \left(\frac{\partial A_p}{\partial x_2} \mathbf{e}_1 + \frac{\partial A_p}{\partial x_1} \mathbf{e}_2 \right) \right\}$$

and we can write the cartesian components of displacement as

$$\bar{u}_i(\mathbf{x}, \omega) = i \left[\frac{K_o}{k_o^4} 2 \frac{\partial^2 A_o}{\partial x_1 \partial x_1 \partial x_2} - \frac{K_p}{k_p^4} \left\{ 2 \frac{\partial^2 A_p}{\partial x_1 \partial x_1 \partial x_2} + k_p^2 \left(\frac{\partial A_p}{\partial x_2} \delta_{i1} + \frac{\partial A_p}{\partial x_1} \delta_{i2} \right) \right\} \right] \quad (9)$$

where

$$K_\alpha = \frac{3}{k_\alpha} \gamma_{22}^2$$

and

$$K_\rho = \frac{6}{k_\rho} \beta_{22}^2$$

(10)

This solution in spectral moment tensor form is

$$\bar{u}_i(\mathbf{x}, \omega) = - \left[\bar{M}_{12} (\bar{G}_{i1,2} + \bar{G}_{i2,1}) + \frac{1}{6} \bar{M}_{1112} \bar{G}_{i\rho,12} \right] \quad (11)$$

where the moment tensor components are

$$\begin{aligned} \bar{M}_{12}(\omega) &= \bar{M}_{21}(\omega) \\ &= i 4\pi\rho\omega^2 \frac{K_\rho}{k_\rho^3} \end{aligned} \quad (12)$$

$$\begin{aligned} \bar{M}_{1112}(\omega) &= \bar{M}_{2212}(\omega) = \bar{M}_{3312}(\omega) \\ &= -i \frac{48\pi\rho\omega^2}{k_\alpha^2} \left(\frac{K_\alpha}{k_\alpha^3} - \frac{K_\rho}{k_\rho^3} \right) \end{aligned} \quad (13)$$

since

$$\bar{G}_{ij,k}(\omega) = \frac{1}{4\pi\rho\omega^2} \left\{ \frac{\partial^2 (A_\rho - A_\alpha)}{\partial x_i \partial x_j \partial x_k} + \delta_{ij} k_\rho^2 \frac{\partial A_\rho}{\partial x_k} \right\} \quad (14)$$

and

$$\begin{aligned} \bar{G}_{i\rho,12}(\omega) &= \frac{\partial^2}{\partial x_1 \partial x_2} \left(\bar{G}_{i1,1} + \bar{G}_{i2,2} + \bar{G}_{i3,3} \right) \\ &= \frac{1}{4\pi\rho\omega^2} k_\alpha^2 \frac{\partial^2 A_\alpha}{\partial x_i \partial x_1 \partial x_2} \end{aligned} \quad (15)$$

and

$$\bar{G}_{i1,2} + \bar{G}_{i2,1} = \frac{1}{4\pi\rho\omega^2} \left\{ 2 \frac{\partial^2 (A_\rho - A_\alpha)}{\partial x_i \partial x_1 \partial x_2} + k_\rho^2 \left(\delta_{i1} \frac{\partial A_\rho}{\partial x_2} + \delta_{i2} \frac{\partial A_\rho}{\partial x_1} \right) \right\} \quad (16)$$

Thus the lowest rank of moment tensor, which this source can be expressed as, is a second rank plus a fourth rank moment tensor (David Cole, personal communication, 1982).

From Ben-Menahem and Singh (1981), as $\omega \rightarrow 0$

$$\frac{K_p}{k_p^3} \rightarrow -\frac{1}{\omega} \frac{\pi \tau_{12}^{(0)}}{4\pi\rho\omega^2} R_0^3 \frac{(1-\sigma)}{(7-5\sigma)} \left\{ 20 + \frac{(1-3\sigma)}{(1-2\sigma)} \frac{\omega^2}{\alpha^2} R_0^2 \right\} \quad (17)$$

where σ is Poisson's ratio. Substituting this limit, we have

$$\bar{M}_{12}(\omega) \rightarrow \frac{1}{i\omega} 20\pi \tau_{12}^{(0)} R_0^3 \frac{(1-\sigma)}{(7-5\sigma)} \quad (18)$$

From the definition of scalar moment

$$M_0 = \lim_{\omega \rightarrow 0} \{i\omega \bar{M}_{12}(\omega)\} = 20\pi \tau_{12}^{(0)} R_0^3 \frac{(1-\sigma)}{(7-5\sigma)} \quad (19)$$

which is the same result obtained from the approximate solutions to this problem given by Randall (1966) and Archambeau (1972) (Aki and Tsai 1972, Randall 1973, Harkrider 1976),

Minster and Suteau 1977, Minster 1979)

Also

$$\frac{K_\sigma}{k_\sigma^3} \rightarrow -\frac{1}{\omega} \frac{\pi \tau_{12}^{(0)}}{4\pi\rho\omega^2} R_0^3 \frac{(1-\sigma)}{(7-5\sigma)} \left\{ 20 + \frac{3}{2} \frac{\omega^2}{\beta^2} R_0^2 \right\} \quad (20)$$

and

$$\begin{aligned} \bar{M}_{1112}(\omega) &= -i 48\pi\rho\alpha^2 \left\{ \frac{K_\sigma}{k_\sigma^3} - \frac{K_p}{k_p^3} \right\} \\ &\rightarrow \frac{1}{i\omega} 24\pi \tau_{12}^{(0)} R_0^5 \frac{(1-\sigma)}{(1-2\sigma)(7-5\sigma)} \end{aligned} \quad (21)$$

as $\omega \rightarrow 0$.

This higher order moment tensor complexity is simply due to the P wave time history being different than the S wave. This difference in time histories is not unusual and is typically due to source finiteness as here. Because of the source volume symmetry, it is not a function of takeoff angle and azimuth such as is in the case of fault plane directivity. We can keep the double couple and more generally the second order moment tensor formulation if we separate the Green's function into its P wave and S wave contributions and define separate P and S wave moment tensor components. For this case $\bar{M}_{12}^{(P)}(\omega)$ and

$\bar{M}_{12}^{(s)}(\omega)$ respectively where

$$\bar{M}_{12}^{(p)}(\omega) = i 4\pi\rho\omega^2 \frac{K_\alpha}{k_\alpha^3} \quad (22)$$

and

$$\bar{M}_{12}^{(s)}(\omega) = i 4\pi\rho\omega^2 \frac{K_\alpha}{k_\rho^3}$$

as in equation (12), with corner frequencies

$$f_c^{(p)} = \frac{\alpha}{2\pi R_0} \left[\frac{(7-5\sigma)}{5(1-\sigma)} \right]^{1/2}$$

and

$$f_c^{(s)} = \frac{\beta}{2\pi R_0} \left[\frac{(7-5\sigma)}{5(1-\sigma)} \right]^{1/2}$$

and their respective whole space Green's functions

$$\bar{G}_{i1,2}^{(p)} + \bar{G}_{i2,1}^{(p)} = - \frac{1}{4\pi\rho\omega^2} 2 \frac{\partial^2 A_\alpha}{\partial x_i \partial x_1 \partial x_2} \quad (23)$$

and

$$\bar{G}_{i1,2}^{(s)} + \bar{G}_{i2,1}^{(s)} = \frac{1}{4\pi\rho\omega^2} \left\{ 2 \frac{\partial^2 A_\beta}{\partial x_i \partial x_1 \partial x_2} + k_\beta^2 \left(\delta_{i1} \frac{\partial A_\beta}{\partial x_2} + \delta_{i2} \frac{\partial A_\beta}{\partial x_1} \right) \right\}$$

For the elastic whole space, this is trivial. This Green's function separation can also be done for a vertically homogeneous halfspace using the the multipole potential formulation of the next sections.

We could obtain the desired source description in terms of the scalar compression potential, $\bar{\Phi}$, and the shear rotation vector potentials, $\bar{\Psi}$, by the following operations:

$$\bar{\Phi} = - \frac{1}{k_\alpha^2} \nabla \cdot \mathbf{u}(\mathbf{x}, \omega)$$

and

$$\bar{\Psi} = \frac{1}{k_\beta^2} \nabla \times \mathbf{u}(\mathbf{x}, \omega) \quad (24)$$

on the displacement expressions, equation (1), as was done for the second rank seismic moment tensor in APPENDIX C

But equations (1) and (2) are already in the form of the general quadrupole of Harkrider (1976)

$$\begin{aligned}\bar{u}_R &= \sin^2\theta \sin 2\phi \left\{ K_o \frac{d}{dR} H_2^{(2)}(k_o R) + 3K_\rho \frac{H_2^{(2)}(k_\rho R)}{R} \right\} \\ \bar{u}_\theta &= \sin 2\theta \sin 2\phi \left\{ K_o \frac{H_2^{(2)}(k_o R)}{R} + \frac{1}{2} K_\rho \left[\frac{d}{dR} H_2^{(2)}(k_\rho R) + \frac{H_2^{(2)}(k_\rho R)}{R} \right] \right\} \\ \bar{u}_\phi &= \sin\theta \cos 2\phi \left\{ 2K_o \frac{H_2^{(2)}(k_o R)}{R} + K_\rho \left[\frac{d}{dR} H_2^{(2)}(k_\rho R) + \frac{H_2^{(2)}(k_\rho R)}{R} \right] \right\}\end{aligned}\quad (25)$$

Comparing equation (25) with equations (49) and (50) of Harkrider (1976), we can write down the cartesian displacement potentials (Harkrider, 1976, equation (47)) for this class of source as

$$\begin{aligned}\bar{\Phi} &= K_o \sin^2\theta \sin 2\phi H_2^{(2)}(k_o R) \\ \bar{\Psi}_1 &= K_\rho \cos\theta \sin\theta \cos\phi H_2^{(2)}(k_\rho R) \\ \bar{\Psi}_2 &= -K_\rho \cos\theta \sin\theta \sin\phi H_2^{(2)}(k_\rho R) \\ \bar{\Psi}_3 &= -K_\rho \sin^2\theta \cos 2\phi H_2^{(2)}(k_\rho R)\end{aligned}\quad (26)$$

or

$$\begin{aligned}\bar{\Phi} &= \frac{K_o}{3} P_2^2(\cos\theta) \sin 2\phi H_2^{(2)}(k_o R) \\ \bar{\Psi}_1 &= \frac{K_\rho}{3} P_2^1(\cos\theta) \cos\phi H_2^{(2)}(k_\rho R) \\ \bar{\Psi}_2 &= -\frac{K_\rho}{3} P_2^1(\cos\theta) \sin\phi H_2^{(2)}(k_\rho R) \\ \bar{\Psi}_3 &= -\frac{K_\rho}{3} P_2^2(\cos\theta) \cos 2\phi H_2^{(2)}(k_\rho R)\end{aligned}\quad (27)$$

For a pure shear dislocation or double couple fault model (Harkrider, 1976)

$$K_o = -i \frac{\bar{M}(\omega)}{4\pi\rho\omega^2} k_o^3$$

For the dislocation slip history, we use the Ohnaka (1973) ' ω -square model' (Aki 1967), which is the minimum phase ' ω -square model'. In terms of moment history it is given by

$$\bar{M}(\omega) = \frac{k_f^2 M_0}{i\omega (k_T + i\omega)^2}$$

with corner frequency

$$f_c = \frac{1}{2\pi T_0}$$

and

$$K_s = -\frac{M_0}{4\pi\rho\omega^2} \frac{1}{v} \frac{k_f^2}{(k_T + i\omega)^2} k_s^2 \quad (28)$$

For both P and S waves the far field rise time is given by $T_0 = 1/k_T$

For the Randall-Archambeau approximate tectonic release model (Harkrider, 1976), after correcting a sign error in the stress definition,

$$K_s = \frac{3M_0}{4\pi\rho\omega^2} \frac{\omega^2}{v} \frac{D(k_s R_0)}{\omega^2 R_0^2} \quad (29)$$

where M_0 is given by equation (19) and

$$D(x) = \cos x - \frac{\sin x}{x}$$

with corner frequencies

$$f_c^{(P)} = \frac{\sqrt{3} \alpha}{2\pi R_0}$$

and

$$f_c^{(S)} = \frac{\sqrt{3} \beta}{2\pi R_0}$$

For the tectonic release sources, the far-field rise times for P and S are given by $T_0^{(P)} = R_0/\alpha$ and $T_0^{(S)} = R_0/\beta$ respectively.

The time histories of explosions are usually expressed in terms of their reduced displacement potentials $\psi(t)$ which is implicitly defined by the explosions linear displacement radiation field as

$$u_R = - \frac{\partial}{\partial R} \frac{\Psi(t - R/\alpha)}{R}$$

Since

$$\bar{u}_R = \frac{\partial}{\partial R} \bar{\Phi}$$

we have

$$\bar{\Phi} = i \bar{\Psi}(\omega) k_\alpha H_0^{(2)}(k_\alpha R) \quad (30)$$

For consistency with the second order moment tensor, we have

$$\begin{aligned} \bar{M}(\omega) &= \bar{M}_{11} = \bar{M}_{22} = \bar{M}_{33} \\ &= 4\pi\rho\alpha^2 \bar{\Psi}(\omega) \end{aligned}$$

We will only consider two explosion time histories

$$\bar{M}(\omega) = \frac{M_0}{i\omega} \quad (31)$$

and

$$\bar{M}(\omega) = \frac{M_0}{i\omega} \frac{e^{i(k_\alpha R_0 - \theta_B)}}{\left[\left(1 - k_\beta^2 R_0^2 / 4 \right)^2 + k_\alpha^2 R_0^2 \right]^{1/2}} \quad (32)$$

where

$$\theta_B = \tan^{-1} \frac{k_\alpha R_0}{\left(1 - k_\beta^2 R_0^2 / 4 \right)}$$

with corner frequency

$$f_c = \frac{\beta}{\pi R_0}$$

which corresponds to a step pressure applied to the walls of a cavity of radius R_0 .

In Figure 1, we show the far-field radial (P) and tangential (S) displacement time histories for the exact tectonic cavity release, for the Randall-Archambeau approximate cavity release, and for the 'ω-square' double couple model. The cavity radius is the same for the first two models and the P and S rise times for the double couple are chosen to be

the same as the cavity release S rise times. This is more evident in Figure 2 where we show the corresponding P- and S-wave velocity fields. The moment is the same for all the sources. The S-wave velocity fields for the cavity release and the double couple are very similar. The basic difference is in the time duration and amplitude of their P-wave fields. In Figure 3, we compare the P- and S-wave displacement fields in detail for these three sources by overlaying them and having the same moment for each comparison. The moments for the P-waves are greater than the S-waves in order to better display the differences in wave form.

In Figure 4, we compare the P-wave, ie. radial, displacement and velocity fields for the tectonic cavity release and the cavity step pressure explosion for the same moment and cavity radius. The time histories are quite similar with the basic difference being the distortion or bump on the cavity release time history which corresponds in arrival time to a Rayleigh wave traveling around the cavity. The far field displacement spectra for all four sources are shown in Figure 5 with their corresponding corner frequencies.

AN ELASTODYNAMIC SOURCE IN A VERTICALLY INHOMOGENEOUS HALF-SPACE FORMULATION

As our source in a locally homogeneous region, we take the slightly modified elastodynamic source form of Archambeau (1968).

$$\bar{\Phi}_j = -\frac{1}{k_v^2} \sum_{n=0}^{\infty} \sum_{m=0}^n \{A_{nm} \cos m\phi + B_{nm} \sin m\phi\} P_n^m(\cos\theta) h_n^{(3)}(k_v R) \quad (33)$$

$$\bar{\Psi}_{ij} = \frac{2}{k_j^2} \sum_{n=0}^{\infty} \sum_{m=0}^n \{C_{nm}^{(j)} \cos m\phi + D_{nm}^{(j)} \sin m\phi\} P_n^m(\cos\theta) h_n^{(2)}(k_j R)$$

where $\bar{\Phi}_j$ and $\bar{\Psi}_{ij}$ are the Fourier-time transformed compressional and Cartesian shear potentials ($j=1, 2$ and 3) respectively. In order to express these potentials in terms of the separable solutions to the Helmholtz equation in cylindrical coordinates, we use the Erdelyi integral (Harkrider, 1976, Ben-Menahem and Singh, 1981).

$$h_n^{(3)}(k, R) P_n^m(\cos\theta) = \frac{(i)^{1-n}}{k_v} [\operatorname{sgn}(h-z)]^{n+\frac{1}{2}} \int_0^{\infty} \bar{P}_n^m(\tilde{\nu}_v/k_v) F_n J_m(kr) k dk \quad (34)$$

where

$$F_n = k \frac{\exp(-i\tilde{\nu}_v |z-k|)}{i\tilde{\nu}_v}$$

$$\tilde{\nu}_v = k r_v = \begin{cases} (k_v^2 - k^2)^{1/2} & ; \quad k < k_v \\ -i(k^2 - k_v^2)^{1/2} & ; \quad k > k_v \end{cases}$$

$$P_n^m(\xi) = (1-\xi^2)^{m/2} P_n^{(m)}(\xi)$$

$$\bar{P}_n^m(\xi) = (\xi^2-1)^{m/2} P_n^{(m)}(\xi)$$

$$k_v = \frac{\omega}{v}$$

v is either α or β , the compression or shear velocity respectively and $(r, s) = (0, h)$ is the source location.

Making use of this relation, we can rewrite equations (33) as

$$\bar{\Phi}_z = i \sum_{n=0}^{\infty} \int_0^{\infty} \{ \bar{A}_n \cos m\phi + \bar{B}_n \sin m\phi \} F_n J_m(kr) dk \quad (35a)$$

$$\bar{\Psi}_\phi = \sum_{n=0}^{\infty} \int_0^{\infty} \{ \bar{C}_n^{(j)} \cos m\phi + \bar{D}_n^{(j)} \sin m\phi \} F_\rho J_m(kr) dk \quad (35b)$$

where

$$\begin{aligned} \bar{A}_n &= - \sum_{\alpha=-\infty}^{\infty} \frac{(i)^{-\alpha}}{k_\alpha^3} [\operatorname{sgn}(k-z)]^{m+\alpha} A_{n\alpha} \bar{P}_\alpha^m \{ \tilde{v}_\alpha / k_\alpha \} \\ \bar{B}_n &= - \sum_{\alpha=-\infty}^{\infty} \frac{(i)^{-\alpha}}{k_\alpha^3} [\operatorname{sgn}(k-z)]^{m+\alpha} B_{n\alpha} \bar{P}_\alpha^m \{ \tilde{v}_\alpha / k_\alpha \} \\ \bar{C}_n^{(j)} &= 2 \sum_{\alpha=-\infty}^{\infty} \frac{(i)^{-\alpha}}{k_\rho^3} [\operatorname{sgn}(k-z)]^{m+\alpha} C_{n\alpha}^{(j)} \bar{P}_\alpha^m \{ \tilde{v}_\rho / k_\rho \} \\ \bar{D}_n^{(j)} &= 2 \sum_{\alpha=-\infty}^{\infty} \frac{(i)^{-\alpha}}{k_\rho^3} [\operatorname{sgn}(k-z)]^{m+\alpha} D_{n\alpha}^{(j)} \bar{P}_\alpha^m \{ \tilde{v}_\rho / k_\rho \} . \end{aligned} \quad (36)$$

Next we obtain expressions for the cylindrical SV potential, ψ , and the cylindrical SH potential, χ , which are convenient potentials for our cylindrical coordinate system, in terms of Cartesian SV and SH potentials given in equation (35). The vertical displacement integrand, w , of its k integral is related to the compressional and Cartesian SV potential integrands by

$$\bar{w} = \frac{\partial \bar{\Phi}}{\partial z} + \frac{\partial \bar{\Psi}_2}{\partial z} - \frac{\partial \bar{\Psi}_1}{\partial y} \quad (37)$$

and in terms of the compressional and SV potential integrands by

$$\bar{w} = \frac{\partial \bar{\Phi}}{\partial z} + k^2 \bar{\psi} \quad (38)$$

which by inspection yields the relation

$$\bar{\psi} = \frac{1}{k^2} \left(\frac{\partial \bar{\Psi}_2}{\partial z} - \frac{\partial \bar{\Psi}_1}{\partial y} \right) \quad (39a)$$

From Harkrider (1976), the integrands of the cylindrical and Cartesian SH potential are

related by

$$\bar{\chi} = \frac{1}{k^2} (k_\rho^2 \bar{\psi}_s) \quad (39b)$$

Performing the above operation and comparing with the cylindrical SV potential

$$\bar{\psi}_s = i \sum_{m=0}^{\infty} \int_0^{\infty} \{ \bar{E}_m \cos m\phi + \bar{F}_m \sin m\phi \} F_\rho J_m(kr) dk \quad (40)$$

we obtain the following relation between coefficients as derived in Appendix A.

$$\begin{aligned} 2k\bar{E}_m &= \left(\bar{C}_{m+1}^{(2)} - \bar{C}_{m-1}^{(2)} \right) - \left(\bar{D}_{m+1}^{(1)} + \bar{D}_{m-1}^{(1)} \right) \\ 2k\bar{F}_m &= \left(\bar{C}_{m+1}^{(1)} + \bar{C}_{m-1}^{(1)} \right) + \left(\bar{D}_{m+1}^{(2)} - \bar{D}_{m-1}^{(2)} \right) \end{aligned}$$

where

$$\bar{C}_m^{(j)} \text{ and } \bar{D}_m^{(j)} \text{ are zero for } m > n$$

and in addition

$$\bar{C}_0^{(2)} = \bar{D}_0^{(1)}, \quad \bar{C}_0^{(1)} = -\bar{D}_0^{(2)}$$

and

$$\bar{F}_0 = 0.$$

For the cylindrical SH potential, we have using equation (39b)

$$\bar{\chi}_s = \sum_{m=0}^{\infty} \int_0^{\infty} \frac{k_\rho^2}{k^2} \{ \bar{C}_m^{(3)} \cos m\phi + \bar{D}_m^{(3)} \sin m\phi \} F_\rho J_m(kr) dk \quad (41)$$

The cylindrical source potentials given by equations (35), (40), and (41) may now be substituted into the multilayer formulation by Harkrider (1964). But first we note that alternating terms in the infinite series in equations (36) are of opposite sign depending on where z is greater or lesser than h . We separate the series such that

$$\bar{A}_m = \bar{A}_m^e + \bar{A}_m^o \quad (42)$$

where the e superscript denotes a new series made up of the terms with $m + n$ even and the o , a series formed by terms with $m + n$ odd. A similar separation is done for the

other source coefficients. The new coefficients have the following property

$$\bar{A}_m^e(z > h) = \bar{A}_m^e(z < h)$$

and

$$\bar{A}_m^e(z > h) = -\bar{A}_m^e(z < h) \quad (43)$$

Defining

$$\begin{aligned} \delta U_m &= \delta \left(\frac{\dot{u}_e}{c} \right)_m^e \cos m\phi + \delta \left(\frac{\dot{u}_e}{c} \right)_m^s \sin m\phi \\ \delta W_m &= \delta \left(\frac{\dot{w}_e}{c} \right)_m^e \cos m\phi + \delta \left(\frac{\dot{w}_e}{c} \right)_m^s \sin m\phi \\ \delta Z_m &= \delta \sigma_m^e \cos m\phi + \delta \sigma_m^s \sin m\phi \\ \delta X_m &= \delta \tau_{Rm}^e \cos m\phi + \delta \tau_{Rm}^s \sin m\phi \\ \delta V_m &= \delta \left(\frac{\dot{v}_e}{c} \right)_m^e \cos m\phi + \delta \left(\frac{\dot{v}_e}{c} \right)_m^s \sin m\phi \\ \delta Y_m &= \delta \tau_{Lm}^e \cos m\phi + \delta \tau_{Lm}^s \sin m\phi \end{aligned} \quad (44)$$

and comparing our source potential relations with equations (30) and (37) in Harkrider (1964), we obtain

$$\begin{aligned} \delta \left(\frac{\dot{u}_e}{c} \right)_m^e &= 2k^2 \left[\frac{\bar{A}_m^e}{r_a} - ik \frac{\bar{E}_m^e}{r_a} \right] \\ \delta \left(\frac{\dot{u}_e}{c} \right)_m^s &= 2k^2 \left[\frac{\bar{B}_m^e}{r_a} - ik \frac{\bar{F}_m^e}{r_a} \right] \\ \delta \left(\frac{\dot{w}_e}{c} \right)_m^e &= 2k^2 \left[\bar{A}_m^e + ik \frac{\bar{E}_m^e}{r_\rho} \right] \\ \delta \left(\frac{\dot{w}_e}{c} \right)_m^s &= 2k^2 \left[\bar{B}_m^e + ik \frac{\bar{F}_m^e}{r_\rho} \right] \\ \delta \sigma_m^e &= 2\rho c^2 k^2 \left[(\gamma - 1) \frac{\bar{A}_m^e}{r_a} - ik \gamma \frac{\bar{E}_m^e}{r_a} \right] \\ \delta \sigma_m^s &= 2\rho c^2 k^2 \left[(\gamma - 1) \frac{\bar{B}_m^e}{r_a} - ik \gamma \frac{\bar{F}_m^e}{r_a} \right] \end{aligned} \quad (45)$$

$$\delta\tau_{km}^e = 2\rho c^2 k^2 \left[-\gamma \bar{A}_m^e - ik(\gamma - 1) \frac{\bar{E}_m^e}{r_\rho} \right]$$

$$\delta\tau_{km}^i = 2\rho c^2 k^2 \left[-\gamma \bar{B}_m^i - ik(\gamma - 1) \frac{\bar{F}_m^i}{r_\rho} \right]$$

$$\delta \left(\frac{\dot{v}_e}{c} \right)_m^e = i2k_\rho^2 \frac{\bar{C}_m^{(s)e}}{r_\rho}$$

$$\delta \left(\frac{\dot{v}_i}{c} \right)_m^i = i2k_\rho^2 \frac{\bar{D}_m^{(s)i}}{r_\rho}$$

$$\delta\tau_{Lm}^e = -i2k_\rho^2 \mu \bar{C}_m^{(s)e}$$

$$\delta\tau_{Lm}^i = -i2k_\rho^2 \mu \bar{D}_m^{(s)i}$$

where

$$\gamma = \frac{2\beta^2}{c_R}$$

and where we have used the following relations between coefficients representing the down-going and upgoing source radiation or the strength of the source potentials just below and above the source

$$2 \bar{A}_m^e = \bar{A}_m^+ - \bar{A}_m^-$$

$$2 \bar{A}_m^i = \bar{A}_m^+ + \bar{A}_m^-$$

A more modern notation would be to use D for downgoing and U for upgoing instead of the + and - notation of Harkrider (1964).

Following Harkrider (1964) we obtain as our integral solution for the vertical displacement at the surface of our inhomogeneous half-space

$$\langle \bar{w}_e \rangle = \sum_{m=0}^{\infty} \int_0^{\infty} \left(\frac{1}{ik} \right) \frac{R_{11}[A]_m + R_{12}[B]_m + R_{13}Z_m}{F_e} J_m(kr) dk \quad (46)$$

where

$$F_e = -R_{11} - [T]R_{12}$$

$$[T] = \left[\frac{\sigma_e}{\dot{w}_e/c} \right]$$

$$\begin{aligned}
[A]_m &= \left[-(A_{RS})_{43} \delta U_m + (A_{RS})_{33} \delta W_m - (A_{RS})_{23} \delta Z_m + (A_{RS})_{13} \delta X_m \right] \\
[B]_m &= \left[(A_{RS})_{42} \delta U_m - (A_{RS})_{32} \delta W_m + (A_{RS})_{22} \delta Z_m - (A_{RS})_{12} \delta X_m \right]
\end{aligned} \quad (47)$$

and

$$Z_m = \left[-(A_{RS})_{41} \delta U_m + (A_{RS})_{31} \delta W_m - (A_{RS})_{21} \delta Z_m + (A_{RS})_{11} \delta X_m \right]$$

(For symbols used without definition here, refer to Harkrider (1964), (1970) and Harkrider and Flinn (1970).

The matrix A_{RS} as defined in Harkrider (1964) is the layer product matrix which gives the displacement-stress vector associated with P-SV motion at source depth in terms of the surface displacement-stress vector. The integral solution given by equation (47) is also valid for a vertically inhomogeneous half-space where A_{RS} is the propagator matrix of the P-SV displacement stress vector from the surface down to the source depth, h , i.e., $A_{RS} = A_R(h)$ and $A_R = A_R(z_{i-1})$. The only restriction on this form of the solution is that at some depth the media is terminated by a homogeneous half-space commencing at depth z_{i-1} .

The surface azimuthal displacement due to SH waves is given by

$$\langle \bar{v}_s \rangle = - \sum_{m=0}^{\infty} \int_0^{\infty} \left(\frac{1}{ik} \right) \frac{N_m^{(1)} N_m^{(2)}}{F_L} \frac{dJ_m(kr)}{d(kr)} dk \quad (48)$$

where

$$\begin{aligned}
F_L &= -(A_L)_{21}^* - (A_L)_{11} \mu_i \tau_{pi}^* \\
N_m^{(1)} &= -i \left[(A_L)_{22} - (A_L)_{12}^* \mu_i \tau_{pi}^* \right] \left[(A_{LS})_{11} \delta Y_m - (A_{LS})_{21} \delta V_m \right] \\
N_m^{(2)} &= 1 + \frac{F_L}{N_m^{(1)}} \left[(A_{LS})_{12} \delta Y_m - (A_{LS})_{22} \delta V_m \right]
\end{aligned} \quad (49)$$

and

$$x = ix^*$$

The A_{LS} is the propagator matrix for the displacement stress vector associated with SH

motion down from the surface to the source depth, h . A_L is the propagator matrix from the surface down to the depth at which the terminating homogeneous half-space begins with elastic properties denoted by subscript l i.e., $A_{LS} = A_L(h)$ and $A_L = A_L(z_{l-1})$.

Evaluating the residue contributions of equations (46) and (48), in order to obtain the surface displacements due to Rayleigh and Love waves respectively, yields

$$\{\bar{w}_s\}_R = i \frac{\pi}{k_R} A_R \sum_{m=0}^{\infty} \left\{ -\delta U_m \frac{1}{k_R} \bar{y}_1^R(h) - \delta W_m \frac{i}{k_R} \bar{y}_2^R(h) + \delta Z_m \bar{y}_1^R(h) - i \delta X_m \bar{y}_2^R(h) \right\} \cdot H_m^{(2)}(k_R r)$$

$$\{\bar{q}_s\}_R = -\frac{1}{k_R} \bar{y}_3^R(0) \frac{\partial}{\partial r} \{\bar{w}_s\}_R \quad (50)$$

where

$$A_R = -\frac{R_{12}'}{\left[\frac{\partial F_e}{\partial k} \right]_R}$$

or equivalently in terms of energy integrals

$$A_R = \frac{1}{2c_R U_R I_1^R} \quad (51)$$

where

$$I_1^R = \int_0^{\infty} \rho [(\bar{y}_1^R)^2 + (\bar{y}_2^R)^2] dz$$

and

$$\{\bar{v}_s\}_L = -i \frac{\pi}{k_L^2} A_L \sum_{m=0}^{\infty} \left\{ \delta Y_m \bar{y}_1^L(h) - \delta V_m \frac{i}{k_L} \bar{y}_2^L(h) \right\} \frac{dH_m^{(2)}(k_L r)}{dr}$$

where

$$A_L = \frac{1}{(A_L)_{11} \left[\frac{\partial F_L}{\partial k} \right]_L}$$

or

$$A_L = \frac{1}{2c_L U_L I_1^L} \quad (52)$$

where

$$I_1^L = \int_0^\infty \rho (\bar{y}_1^L)^2 dz$$

and the correspondence between the Saito (1967) and Haskell (Harkrider, 1964, 1970) notation for the eigenfunctions or the homogeneous, i.e. no source, displacement-stress vector components evaluated at the residue eigenvalues is given by

$$\begin{aligned} \bar{y}_3^R(h) &= \left[\frac{u^*(h)}{w_o} \right]_H = (A_{RS})_{11} \left[\frac{u_o^*}{w_o} \right]_H + (A_{RS})_{12} + (A_{RS})_{13} [T^*] \\ \bar{y}_1^R(h) &= \left[\frac{w(h)}{w_o} \right]_H = - (A_{RS})_{21} \left[\frac{u_o^*}{w_o} \right]_H + (A_{RS})_{22} - (A_{RS})_{23} [T^*] \\ \bar{y}_2^R(h) &= k_R \left[\frac{\sigma^*(h)}{\dot{w}_o/c_R} \right]_H = k_R \left\{ (A_{RS})_{31} \left[\frac{u_o^*}{w_o} \right]_H + (A_{RS})_{32} + (A_{RS})_{33} [T^*] \right\} \\ \bar{y}_4^R(h) &= -k_R \left[\frac{\tau_R(h)}{\dot{w}_o/c_R} \right]_H = -k_R \left\{ - (A_{RS})_{41} \left[\frac{u_o^*}{w_o} \right]_H + (A_{RS})_{42} - (A_{RS})_{43} [T^*] \right\} \\ \bar{y}_1^L(h) &= \left[\frac{v(h)}{v_o} \right]_H = (A_{LS})_{11} \\ \bar{y}_2^L(h) &= k_L \left[\frac{\tau_L^*(h)}{\dot{v}_o/c_L} \right]_H = k_L (A_{LS})_{21} \end{aligned} \quad (53)$$

and

$$\dot{s}/c = ikx$$

Using equations (45) the solutions can be written as

$$\{\bar{w}_o\}_R = -4\pi k_R \mu A_R \{K_R \Phi_R^* - k_R L_R \psi_R^* + \frac{k_R}{2\mu\nu_o} M_R \Phi_R^* - \frac{k_R^2}{2\mu\nu_\rho} N_R \psi_R^*\} \quad (54)$$

and

$$\{\bar{v}_o\}_L = -2\pi\mu A_L \left\{ \chi_L^* \bar{y}_1^L(h) - \frac{\chi_L^*}{\mu\nu_\rho} \bar{y}_2^L(h) \right\} \quad (55)$$

where

$$\nu_0 = i \bar{\nu}_0$$

$$\nu_0^2 = k^2 - k_0^2$$

$$K_R = \bar{y}_3^R(h) - \frac{1}{2\mu k_R} \bar{y}_2^R(h)$$

$$L_R = \bar{y}_1^R(h) - \frac{1}{2\mu k_R} \bar{y}_4^R(h) \quad (56)$$

$$M_R = \rho c_R^2(\gamma - 1) \bar{y}_1^R(h) - \frac{1}{k_R} \bar{y}_4^R(h)$$

$$N_R = \rho c_R^2(\gamma - 1) \bar{y}_3^R(h) - \frac{1}{k_R} \bar{y}_2^R(h)$$

$$\Phi_R^s = \sum_{m=0}^{\infty} \left(\bar{A}_m^s \cos m\phi + \bar{B}_m^s \sin m\phi \right) H_m^{(2)}(k_R r)$$

$$\psi_R^s = \sum_{m=0}^{\infty} \left(\bar{E}_m^s \cos m\phi + \bar{F}_m^s \sin m\phi \right) H_m^{(2)}(k_R r) \quad (57)$$

$$\chi_L^s = \sum_{m=0}^{\infty} \frac{k_\theta^2}{k_L^2} \left(\bar{C}_m^{(s)s} \cos m\phi + \bar{D}_m^{(s)s} \sin m\phi \right) \frac{dH_m^{(2)}(k_L r)}{dr}$$

and the o superscripted variables defined similarly. The elastic parameters μ and ρ which appear in all the previous equations, except inside of integrals, are for the media at source depth h .

SURFACE WAVES

In order to demonstrate the utility of this formulation once the multipole coefficients of the potentials have been determined, we first obtain surface wave expressions for a second order moment tensor.

The cylindrical coefficients for a second order moment tensor are (Appendix C and equations (57))

$$\begin{aligned}
 \Phi_R^* &= \frac{i}{4\pi\rho\omega^2} \left\{ \left[\frac{k_R^2}{2} (\bar{M}_{11} + \bar{M}_{22}) + (k_\phi^2 - k_R^2) \bar{M}_{33} \right] H_0^{(2)}(k_R r) \right. \\
 &\quad \left. + \frac{k_R^2}{2} [(\bar{M}_{22} - \bar{M}_{11}) \cos 2\phi - 2\bar{M}_{12} \sin 2\phi] H_2^{(2)}(k_R r) \right\} \\
 \Phi_R^* &= -\frac{i}{4\pi\rho\omega^2} 2k_R \nu_\alpha [\bar{M}_{13} \cos \phi + \bar{M}_{23} \sin \phi] H_1^{(2)}(k_R r) \\
 \psi_R^* &= \frac{i}{4\pi\rho\omega^2} \frac{(k_\phi^2 - 2k_R^2)}{k_R} [\bar{M}_{13} \cos \phi + \bar{M}_{23} \sin \phi] H_1^{(2)}(k_R r) \\
 \psi_R^* &= \frac{i}{4\pi\rho\omega^2} \frac{\nu_\rho}{2} \left\{ (\bar{M}_{11} + \bar{M}_{22} - 2\bar{M}_{33}) H_0^{(2)}(k_R r) \right. \\
 &\quad \left. + [(\bar{M}_{22} - \bar{M}_{11}) \cos 2\phi - 2\bar{M}_{12} \sin 2\phi] H_2^{(2)}(k_R r) \right\} \\
 \chi_L^* &= \frac{i}{4\pi\rho\omega^2} \frac{k_\phi^2}{2} [2\bar{M}_{12} \cos 2\phi + (\bar{M}_{22} - \bar{M}_{11}) \sin 2\phi] \frac{dH_2^{(2)}(k_L r)}{dr} \\
 \chi_L^* &= \frac{i}{4\pi\rho\omega^2} k_\phi^2 \frac{\nu_\rho}{k_L} [\bar{M}_{23} \cos \phi - \bar{M}_{13} \sin \phi] \frac{dH_1^{(2)}(k_L r)}{dr}
 \end{aligned} \tag{58}$$

Substituting these generalised cylindrical potential coefficients into equation (54), we have

$$\begin{aligned}
 \{\bar{\psi}_0\}_R &= -ik_R A_R \left\{ \frac{\beta^2}{\alpha^2} \frac{(\bar{M}_{11} + \bar{M}_{22} + \bar{M}_{33})}{3} K_R - \frac{(\bar{M}_{11} + \bar{M}_{22} - 2\bar{M}_{33})}{12} B_\phi \right\} H_0^{(2)}(k_R r) \\
 &\quad + \frac{C_\phi}{2} (\bar{M}_{13} \cos \phi + \bar{M}_{23} \sin \phi) H_1^{(2)}(k_R r) \\
 &\quad + \frac{A_\phi}{4} \left\{ (\bar{M}_{11} - \bar{M}_{22}) \cos 2\phi + 2\bar{M}_{12} \sin 2\phi \right\} H_2^{(2)}(k_R r) \tag{59}
 \end{aligned}$$

where

$$A_\phi = -\bar{y}_2^R(k)$$

$$B_\phi = -\left\{ \left(3 - 4 \frac{\beta^2}{\alpha^2} \right) \bar{y}_2^R(k) + \frac{2}{\rho \alpha^2 k_R} \bar{y}_2^R(k) \right\}$$

and

$$C_\phi = \frac{1}{\mu k_R} \bar{y}_2^R(k)$$

From equation (55), we obtain

$$\begin{aligned} \{\bar{v}_\phi\}_L = & -\frac{i}{2} A_L \left\{ \frac{\bar{y}_1^L(k)}{2} \left[2\bar{M}_{12} \cos 2\phi + (\bar{M}_{22} - \bar{M}_{11}) \sin 2\phi \right] \frac{dH_2^{(2)}(k_L r)}{dr} \right. \\ & \left. - \frac{1}{\mu k_L} \bar{y}_2^L(k) (\bar{M}_{22} \cos \phi - \bar{M}_{12} \sin \phi) \frac{dH_1^{(2)}(k_L r)}{dr} \right\} \end{aligned} \quad (60)$$

The far field forms of the above displacement fields are identical with Mendiguren (1975).

For a general quadrupole seismic source of arbitrary orientation (Appendix B and equations (57))

$$\begin{aligned} \Phi_R^\circ &= -i \frac{\bar{M}^{(P)}(\omega)}{4\pi\rho\omega^2} \left\{ (k_R^2 + 2\nu_\phi^2) \Lambda_0 H_0^{(2)}(k_R r) + k_R^2 \Lambda_2 H_2^{(2)}(k_R r) \right\} \\ \Phi_R^\circ &= i \frac{\bar{M}^{(P)}(\omega)}{2\pi\rho\omega^2} k_R \nu_\phi \Lambda_1 H_1^{(2)}(k_R r) \\ \psi_R^\circ &= -i \frac{\bar{M}^{(S)}(\omega)}{4\pi\rho\omega^2} \frac{(k_\theta^2 - 2k_R^2)}{k_R} \Lambda_1 H_1^{(2)}(k_R r) \\ \psi_R^\circ &= -i \frac{\bar{M}^{(S)}(\omega)}{4\pi\rho\omega^2} \nu_\theta \left\{ 3 \Lambda_0 H_0^{(2)}(k_R r) + \Lambda_2 H_2^{(2)}(k_R r) \right\} \\ \chi_L^\circ &= i \frac{\bar{M}^{(S)}(\omega)}{4\pi\rho\omega^2} \frac{k_\theta^2}{2} \frac{\partial \Lambda_2}{\partial \phi} \frac{dH_2^{(2)}(k_L r)}{dr} \\ \chi_L^\circ &= -i \frac{\bar{M}^{(S)}(\omega)}{4\pi\rho\omega^2} k_\theta^2 \frac{\nu_\theta}{k_L} \frac{\partial \Lambda_1}{\partial \phi} \frac{dH_1^{(2)}(k_L r)}{dr} \end{aligned} \quad (61)$$

where we use the P and S wave moment definitions

$$\bar{M}^{(P)}(\omega) = i 4\pi\rho\omega^2 \frac{K_\phi}{k_\phi^3}$$

$$\bar{M}^{(s)}(\omega) = i 4\pi\rho\omega^2 \frac{K_\alpha}{k_\beta^3}$$

, where $\tau_{12}^{(0)}$ has been replaced by $\tau^{(0)}$, the pure shear field of arbitrary orientation (Harkrider, 1977), and

$$\Lambda_0 = \frac{1}{2} \sin \lambda \sin 2\delta$$

$$\Lambda_1 = \cos \lambda \cos \delta \cos \phi_f - \sin \lambda \cos 2\delta \sin \phi_f$$

$$\Lambda_2 = \frac{1}{2} \sin \lambda \sin 2\delta \cos 2\phi_f + \cos \lambda \sin \delta \sin 2\phi_f$$

$$\frac{\partial \Lambda_1}{\partial \phi} = -\sin \lambda \cos 2\delta \cos \phi_f - \cos \lambda \cos \delta \sin \phi_f$$

$$\frac{\partial \Lambda_2}{\partial \phi} = 2 \cos \lambda \sin \delta \cos 2\phi_f - \sin \lambda \sin 2\delta \sin 2\phi_f$$

$$\phi_f = \phi - \phi_s$$

with ϕ_s the fault strike azimuth. These coefficients were defined in Harkrider (1976), Sato (1972) and used in Langston and Helmberger (1975) as A_3 , A_2 , A_1 , A_0 , and $2A_4$, respectively.

Again substituting the coefficients into equations (54) and (55), we have

$$\begin{aligned} \{\bar{u}_s\}_R = i k_R A_R \frac{1}{k_\beta^2} \left\{ \left[\bar{M}^{(p)} (k_R^2 + 2\nu_\alpha^2) K_R - 3 \bar{M}^{(s)} \frac{k_R^2}{2\mu} N_R \right] \Lambda_0 H_0^{(2)}(k_R r) \right. \\ \left. - \left[\bar{M}^{(p)} \frac{k_R^2}{\mu} M_R + \bar{M}^{(s)} (k_\beta^2 - 2k_R^2) L_R \right] \Lambda_1 H_1^{(2)}(k_R r) \right. \\ \left. + k_R^2 \left[\bar{M}^{(p)} K_R - \bar{M}^{(s)} \frac{1}{2\mu} N_R \right] \Lambda_2 H_2^{(2)}(k_R r) \right\} \quad (62) \end{aligned}$$

and

$$\{\bar{u}_s\}_L = -i \frac{\bar{M}^{(s)}(\omega)}{4} A_L \left\{ \bar{y}_1^L(k) \frac{\partial \Lambda_2}{\partial \phi} \frac{dH_2^{(2)}(k_L r)}{dr} + \frac{2}{\mu k_L} \bar{y}_2^L(k) \frac{\partial \Lambda_1}{\partial \phi} \frac{dH_1^{(2)}(k_L r)}{dr} \right\} \quad (63)$$

For a double couple,

$$\bar{M}^{(p)}(\omega) = \bar{M}^{(s)}(\omega) = \bar{M}(\omega)$$

and we obtain

$$\{\bar{w}_o\}_R = -i \frac{\bar{M}(\omega)}{2} k_R A_R \left\{ B_\phi \Lambda_0 H_0^{(2)}(k_R r) - C_\phi \Lambda_1 H_1^{(2)}(k_R r) + A_\phi \Lambda_2 H_2^{(2)}(k_R r) \right\} \quad (64)$$

and

$$\{\bar{v}_o\}_L = -i \frac{\bar{M}(\omega)}{4} A_L \left\{ \bar{y}_1^L(h) \frac{\partial \Lambda_2}{\partial \phi} \frac{dH_2^{(2)}(k_L r)}{dr} + \frac{2}{\mu k_L} \bar{y}_2^L(h) \frac{\partial \Lambda_1}{\partial \phi} \frac{dH_1^{(2)}(k_L r)}{dr} \right\} \quad (65)$$

In the far field these expressions reduce to the double couple expressions in Ben-Menahem and Harkrider (1964) and correct the sign error in the Love wave coefficient $G(h)$ in Harkrider (1970).

For an explosion,

$$\Phi^e = \frac{i}{4\pi\rho\omega^2} k_\alpha^2 \bar{M}(\omega) H_0^{(2)}(k_R r) \quad (66)$$

and

$$\{\bar{w}_o\}_R = -ik_R A_R \frac{\beta^2}{\alpha^2} \bar{M}(\omega) K_R H_0^{(2)}(k_R r) \quad (67)$$

which can be obtained by either setting the diagonal components of the stress tensor equal to $\bar{M}(\omega)$ in equations (58) and (59) or by direct substitution in equation (54).

For all cases, the radial displacement is obtained from the vertical by using

$$\{\bar{q}_o\}_R = -\frac{1}{k_R} \bar{y}_3^R(0) \frac{\partial}{\partial r} \{\bar{w}_o\}_R \quad (68)$$

For shallow sources, the source depth dependent terms reduce to

$$K_R \rightarrow \bar{y}_3^R(0)$$

$$L_R \rightarrow 1$$

$$M_R \rightarrow \rho c_R^2(\gamma - 1)$$

$$N_R \rightarrow \rho c_R^2(\gamma - 1) \bar{y}_3^R(0)$$

as $h \rightarrow 0$. Using

$$\rho c_R^2(\gamma - 1) = \mu (2k_R^2 - k_\beta^2)/k_R^2$$

we have for the shallow general quadrupole source

$$\begin{aligned} \{\bar{w}_s\}_R \rightarrow i k_R A_R \frac{1}{k_\rho^2} & \left\{ \left[\bar{M}^{(p)} (3k_R^2 - 2k_\rho^2) - \frac{3}{2} \bar{M}^{(s)} (2k_R^2 - k_\rho^2) \right] \bar{y}_3^R(0) \Lambda_0 H_0^{(2)}(k_R r) \right. \\ & - (2k_R^2 - k_\rho^2) \left[\bar{M}^{(p)} - \bar{M}^{(s)} \right] \Lambda_1 H_1^{(2)}(k_R r) \\ & \left. + \frac{1}{2} \left[2 k_R^2 \bar{M}^{(p)} - \bar{M}^{(s)} (2k_R^2 - k_\rho^2) \right] \bar{y}_3^R(0) \Lambda_2 H_2^{(2)}(k_R r) \right\} \quad (69) \end{aligned}$$

and

$$\{\bar{v}_s\}_L \rightarrow -i \frac{\bar{M}^{(s)}}{4} A_L \frac{\partial \Lambda_2}{\partial \phi} \frac{dH_2^{(2)}(k_L r)}{dr} \quad (70)$$

For the shallow explosion

$$\{\bar{w}_s\}_R \rightarrow -ik_R A_R \frac{\beta^2}{\alpha^2} \bar{M}(\omega) \bar{y}_3^R(0) H_0^{(2)}(k_R r) \quad (71)$$

DISCUSSION

Vertical Rayleigh and transverse Love waves were calculated for an exact supersonic cavity shear release source model. Orientations of the prestress pure shear field correspond to the three canonical or "fundamental" double couple faults: the vertical strike slip, the vertical dip slip, and the 45° dip thrust faults. Rayleigh and Love waves for two earth structures at a range of 2000 km. are shown in Figure 6. The source orientations with respect to the receiver are specified by their fault equivalents; dip (δ), rake (λ), and azimuth (ϕ). The propagation paths are for the Western US (WUS) and Central US (CUS) velocity and attenuation models determined by Herrmann, Mitchell and colleagues at Saint Louis University (Table 1). The synthetics included a WWSSN LP instrument. The failure radius and source depth are both 0.8 km. This radius corresponds to P and S wave rise times of 0.23 and 0.39 sec for the WUS models and 0.16 and 0.28 sec for the CUS model respectively. For comparison we also show a cavity explosion with the same source depth, cavity radius and seismic moment as the tectonic release model.

The most obvious features seen in the synthetics are the difference in period content between the two crust-upper mantle models and the poor excitation of the prestress field orientation associated with vertical dip slip mechanisms. The longer period Rayleigh and Love waves seen in the WUS model are somewhat due to the longer source rise times but are primarily caused by the greater attenuation of that model. Although the poor excitation of Rayleigh and Love waves by a near surface vertical or horizontal dip slip point dislocation, which are identified in the figure by (90°, 90°, 90°) and (90°, 90°, 0°) respectively, and the \bar{M}_{12} or \bar{M}_{13} moment tensor equivalent can be explained mathematically by their spectral amplitude being proportional to a stress eigen-function which approaches zero as source depth is reduced, this is not a very intuitive explanation. It would be instructive to be able to explain the observation in terms of the source vertical radiation pattern and waves generated by the free surface. For example, a frequently used ray explanation for Love and teleseismic body waves is the destructive interference

between the free surface reflected waves from this shallow source and its downgoing radiation.

In order to explore the possibility of a more intuitive explanation for this near surface effect on Rayleigh waves and to better understand the effect of differing P and SV wave time histories, we separated the Rayleigh wave into its contribution due to the P and SV wave separately. The resulting synthetics for the three tectonic release source orientations in the two structures are shown in Figure 7. Not only do the P and SV contributions appear to be out of phase for all the mechanisms but the P wave contribution is larger for all mechanisms except the vertical dip slip where it is essentially the same. The P contribution for the strike slip orientation is even larger than that due to an explosion of equal moment. This is particularly evident in the CUS structure. The enhancement of the P wave generated Rayleigh waves for the strike slip over the explosion is probably due to the vertical radiation pattern or amplitude variation over the source wave front. This effect should be similar to that of the interaction of wave front curvature with the free surface used to explain the excitation of the Rayleigh wave on a homogeneous halfspace.

As mentioned above, the Rayleigh wave generated by the P wave radiation from the shallow vertical dip slip fault model is almost equal and opposite to the Rayleigh wave excited by the SV source radiation. Their individual amplitudes are similar to the vertical strike slip generated Rayleigh waves. In order to demonstrate this analytically, we separate the expressions for the vertical Rayleigh wave displacement due to this mechanism into its contribution from the P and SV source radiation. The P and SV potentials from equations (61) reduce to

$$\Phi^s = i \frac{\bar{M}^{(p)}(\omega)}{2\pi\rho\omega^2} k_R \nu_0 \sin \phi_f H_1^{(2)}(k_R r)$$

$$\psi^s = -i \frac{\bar{M}^{(s)}(\omega)}{4\pi\rho\omega^2} \frac{(k_p^2 - 2k_R^2)}{k_R} \sin \phi_f H_1^{(2)}(k_R r)$$

Substituting the above individually into the vertical Rayleigh displacement and recalling M_R

and L_R from equations (56), we have for the vertical displacement excited by the P source potential

$$\{\bar{w}_z\}_R^{(P)} = i \frac{\bar{M}^{(P)}(\omega)}{k_\beta^2} k_R \Delta_R \left[(k_\beta^2 - 2k_R^2) \bar{y}_1^R(k) + \frac{k_R^2}{\mu k_R} \bar{y}_4^R(k) \right] \sin \phi_f H_1^{(2)}(k_R r) \quad (72a)$$

and the vertical displacement excited by the SV source potential

$$\{\bar{w}_z\}_R^{(SV)} = -i \frac{\bar{M}^{(S)}(\omega)}{k_\beta^2} k_R \Delta_R (k_\beta^2 - 2k_R^2) \left[\bar{y}_1^R(k) - \frac{1}{2\mu k_R} \bar{y}_4^R(k) \right] \sin \phi_f H_1^{(2)}(k_R r) \quad (72b)$$

if

$$\bar{M}^{(P)}(\omega) = \bar{M}^{(S)}(\omega) = \bar{M}(\omega)$$

as in a point double couple, the sum of the P wave and SV wave excited Rayleigh waves reduces to the usual expression

$$\{\bar{w}_z\}_R = i \frac{\bar{M}(\omega)}{2\mu} \Delta_R \bar{y}_4^R(k) \sin \phi_f H_1^{(2)}(k_R r)$$

which approaches zero as the source depth, $k \rightarrow 0$ since $\bar{y}_4^R(k) \rightarrow 0$ whereas

$$\{\bar{w}_z\}_R^{(P)} \rightarrow i \frac{\bar{M}^{(P)}(\omega)}{k_\beta^2} k_R \Delta_R (k_\beta^2 - 2k_R^2) \sin \phi_f H_1^{(2)}(k_R r)$$

and

$$\{\bar{w}_z\}_R^{(SV)} \rightarrow -i \frac{\bar{M}^{(S)}(\omega)}{k_\beta^2} k_R \Delta_R (k_\beta^2 - 2k_R^2) \sin \phi_f H_1^{(2)}(k_R r)$$

and their sum approaches

$$\{\bar{w}_z\}_R \rightarrow i \frac{\bar{M}^{(P)}(\omega) - \bar{M}^{(S)}(\omega)}{k_\beta^2} k_R \Delta_R (k_\beta^2 - 2k_R^2) \sin \phi_f H_1^{(2)}(k_R r)$$

which does not vanish at zero source depth.

This surprising result for tectonic release models should be considered only as an analytic artifact since any pure shear prestress field for this equivalent double couple orientation, such as $\tau_{13}^{(0)}$ or $\tau_{23}^{(0)}$ where 3 is in the s direction, will be proportional to the depth

below the free surface. Thus, although the displacement field for this tectonic release mechanism is not zero at the free surface for a finite moment, it is impossible for the moment to be uniform and not approach zero at shallow source depths in a realistic prestress model. In the case of the tectonic release models, the separated expressions are actually double couples with P and SV time histories, which differ primarily by their P to SV velocity ratios in spectral amplitude and by their respective velocities in time scale (Figures 1-5). We use this tectonic release model as one way to investigate the interaction of P and SV generated Rayleigh waves.

The displacement expressions obtained individually for a P and a SV source, equations (72), are identical to those one would obtain by separating the displacement equation (69) into the terms which contain $\bar{M}^{(P)}$ and those that contain $\bar{M}^{(S)}$. By this means it is possible to separate the P and SV source contributions for the other orientations of the double couple as well as the tectonic release source directly from equation (69).

Similar conclusions can be reached for the case of a homogeneous halfspace using the classical potential formulation where we include P wave source and SV wave source potentials separately and satisfy the boundary conditions at infinity and the free surface for each source. For the three fundamental faults defined by $(\delta^\circ, \lambda^\circ, \phi^\circ)$ and the explosion, we have for the P and SV source generated vertical surface displacements.

Vertical Strike Slip: $(90^\circ, 0^\circ, 45^\circ)$

$$\langle w_s^{(P)} \rangle = \frac{\bar{M}^{(P)}}{2\pi\rho\omega^3} \int_0^\infty \frac{k^3(\gamma-1)}{F_R} e^{-iQ} J_2(kr) dk$$

$$\langle w_s^{(SV)} \rangle = \frac{\bar{M}^{(S)}}{2\pi\rho\omega^3} \int_0^\infty \frac{k^3\gamma}{F_R} e^{-iQ} J_2(kr) dk$$

with

$$F_R = -\{(\gamma - 1)^2 + \gamma^2 r_\alpha r_\beta\}, P_\alpha = k r_\alpha h, Q_\alpha = k r_\beta h, (k r_\alpha)^2 = k_\alpha^2 - k^2, \text{ and } \gamma = 2k^2 \beta^2 / \omega^2.$$

Vertical Dip Slip: (90°, 90°, 90°)

$$\langle w_\alpha^{(p)} \rangle = \frac{\bar{M}^{(p)}}{\pi \rho \omega^2} \int_0^\infty \frac{k^2 (i k r_\alpha) (\gamma - 1)}{F_R} e^{-i P_\alpha} J_1(k r) dk$$

$$\langle w_\alpha^{(sv)} \rangle = -\frac{\bar{M}^{(s)}}{\pi \rho \omega^2} \int_0^\infty \frac{k^2 (i k r_\alpha) (\gamma - 1)}{F_R} e^{-i Q_\alpha} J_1(k r) dk$$

45° Dip Thrust: (45°, 90°, 45°)

$$\langle w_\alpha^{(p)} \rangle = \frac{\bar{M}^{(p)}}{4\pi \rho \omega^2} \int_0^\infty \frac{k (3k^2 - 2k_\alpha^2) (\gamma - 1)}{F_R} e^{-i P_\alpha} J_0(k r) dk$$

$$\langle w_\alpha^{(sv)} \rangle = \frac{\bar{M}^{(s)}}{4\pi \rho \omega^2} \int_0^\infty \frac{3k^2 \gamma r_\alpha r_\beta}{F_R} e^{-i Q_\alpha} J_0(k r) dk$$

Explosion:

$$\langle w_\alpha^{(p)} \rangle = -\frac{\bar{M}^{(p)}}{2\pi \rho \alpha^2} \int_0^\infty \frac{k (\gamma - 1)}{F_R} e^{-i P_\alpha} J_0(k r) dk$$

Evaluating the residue for the homogeneous halfspace expressions given above, we obtain

Vertical Strike Slip: (90°, 0°, 45°)

$$\{\bar{w}_\alpha\}_R^{(p)} = i \frac{k_R}{2} \bar{M}^{(p)} \gamma \bar{y}_3^R(0) A_R H_2^{(2)}(k_R r) e^{-|P_\alpha|}$$

$$\{\bar{w}_\alpha\}_R^{(sv)} = -i \frac{k_R}{2} \bar{M}^{(s)} (\gamma - 1) \bar{y}_3^R(0) A_R H_2^{(2)}(k_R r) e^{-|Q_\alpha|}$$

Vertical Dip Slip: (90°, 90°, 90°)

$$\{\bar{w}_\alpha\}_R^{(p)} = -i k_R \bar{M}^{(p)} (\gamma - 1) A_R H_1^{(2)}(k_R r) e^{-|P_\alpha|}$$

$$\{\bar{w}_\alpha\}_R^{(sv)} = i k_R \bar{M}^{(s)} (\gamma - 1) A_R H_1^{(2)}(k_R r) e^{-|Q_\alpha|}$$

45° Dip Thrust: (45°, 90°, 45°)

$$\{\bar{w}_s\}_R^{(P)} = i k_R \bar{M}^{(P)} \frac{1}{2k_\beta^2} (3k_R^2 - 2k_\alpha^2) \bar{y}_s^R(0) A_R H_0^{(2)}(k_R r) e^{-|P_s|}$$

$$\{\bar{w}_s\}_R^{(SV)} = -i k_R \bar{M}^{(SV)} \frac{1}{2k_\beta^2} \frac{3}{2} (2k_R^2 - k_\beta^2) \bar{y}_s^R(0) A_R H_0^{(2)}(k_R r) e^{-|Q_s|}$$

Explosion:

$$\{\bar{w}_s\}_R^{(P)} = i k_R \frac{\beta^2}{\alpha^2} \bar{M}^{(P)} \bar{y}_s^R(0) A_R H_0^{(2)}(k_R r) e^{-|P_s|}$$

where the halfspace Rayleigh response is (Harkrider, 1970, Harkrider *et al.*, 1974, Hudson and Douglas, 1975)

$$A_R = \omega \frac{1}{4\rho} \frac{r_\alpha^*}{c_R} \left\{ (\gamma - 1) + \frac{1}{2} \frac{\gamma^2}{\alpha^2} \frac{[2c_R^2 - \alpha^2 - \beta^2]}{(\gamma - 1)^2} \right\}^{-1}$$

,and the free surface ellipticity is

$$\bar{y}_s^R(0) = \frac{(\gamma - 1)}{\gamma r_\alpha^*} = \frac{r_\beta^* \gamma}{(\gamma - 1)}$$

with $r_\alpha^* = - \left(1 - \frac{c_R^2}{\alpha^2} \right)^{1/2}$ and $r_\beta^* = - \left(1 - \frac{c_R^2}{\beta^2} \right)^{1/2}$. These expressions agree with the Raleigh wave displacements, which one would obtain from the P and SV separated equation (69).

As the source depth, h , approaches zero and thus P_s and Q_s approach zero, an inspection of the above expressions show that the P and SV contributions to the Rayleigh wave are of opposite sign for all the orientations and of equal amplitude for the vertical dip slip. As stated earlier, this also can be seen for the more realistic earth models in Figure 7. Since the predicted reduction in Rayleigh wave amplitude as a function of source depth for the vertical dip slip source orientation is caused by a delicate balance of P and S wave source histories, the application of the double couple model to shallow earthquake observations with its inherent assumption of equal P and S wave time histories should be

done with care.

Near the surface the stress eigenfunctions \bar{y}_2^R , \bar{y}_4^R and \bar{y}_2^L are proportional to source depth and thus vanish as the source approaches the free surface. All that remains is the \bar{y}_1^R or vertical displacement eigenfunction which controls the source depth excitation of Rayleigh waves from a vertical point force. In the excitation of Rayleigh waves, its role is similar to \bar{y}_3^R or ellipticity eigenfunction which governs the excitation of the horizontal point force, the shallow vertical dipole and explosions. Thus as the vertical dip slip oriented tectonic release source approaches the free surface, the non-vanishing part of the Rayleigh amplitude wave can be considered as the sum of Rayleigh waves from two vertical point forces of opposite polarity; one with the P wave time history and the other with the S wave history. Of course, unlike azimuthally independent vertical point force Rayleigh waves, this Rayleigh wave has a sine dependence on azimuth.

The spectra for the non vanishing Rayleigh displacement field for the shallow tectonic release sources with a vertical dip slip orientation have a spectral minimum or hole. The spectral hole is due to the destructive interference of the P and S wave generated Rayleigh waves and depends on the differences in their time functions. Spectra for this difference in time functions, $|\bar{M}^{(P)} - \bar{M}^{(S)}|$ is shown in Figure 8 for a P wave velocity of 6.2 km/sec, S wave velocity of 3.5 km/sec, and a density of 2.7 gm/cc for our two cavity tectonic release models. The cavity radius is 0.8 km. The P wave and S wave moments are both 10^{26} dyne-cm. The low frequency asymptote for the exact supersonic cavity release model is

$$\bar{M}^{(P)} - \bar{M}^{(S)} \rightarrow \frac{1}{i\omega} M_0 \frac{1}{10} \left(\frac{\omega R_0}{\alpha} \right)^2 \frac{1}{(1-2\sigma)}$$

The high frequency asymptote for the same model is

$$\bar{M}^{(P)} - \bar{M}^{(S)} \rightarrow \frac{1}{i\omega} M_0 \frac{1}{5} \left(\frac{\alpha}{\omega R_0} \right)^2 \frac{(7-5\sigma)}{(1-\sigma)} \left[\exp(i k_\alpha R_0) - \frac{\beta^2}{\alpha^2} \exp(i k_\beta R_0) \right]$$

The peak and the overall shape of spectrum are controlled by the rise times or corner

frequencies of the individual P and S wave histories. The shift to longer periods is proportional to the failure radius and inversely proportional to the body velocities. Increasing the radius also increases the peak value of this moment difference function even if we keep the seismic moments constant.

Rayleigh waves were also calculated for the vertical dip slip orientation of the exact supersonic cavity release for source depths of 0.8, 0.4, 0.2 and 0. km depths for a variety of cavity radii from 10. to 0.2 km for the WUS and CUS models. Reducing the source depth while keeping the failure dimensions finite should be considered an analytic construction used only to demonstrate the point vertical dip slip double couple orientations dependence on the difference in source P and SV wave time histories as the source approaches the free surface. This is particularly true for this mechanism since, as discussed earlier, the prestress field necessary for this type of mechanism also vanishes as one approaches the free surface. Even when the source radius is not larger than the source depth, the prestress will not be vertically uniform over the source dimensions. These were compared with vertical dip slip point double couple S wave rise times of the tectonic release model for all the source depths except the free surface. The synthetics included a WWSSN LP instrument.

For the vertical strike slip and dip slip orientations of tectonic release, we measured maximum peak to peak amplitudes for various release surface radii at zero source depth. As the radius was reduced, the amplitudes for the dip slip orientation decreased monotonically. For the strike-slip model the amplitudes increased to a maximum value and then showed a slight decrease with smaller radii for both the CUS and WUS models. This moderate maximum in the Rayleigh wave values was felt to be due to the presence of the peak in the moment-rate spectra of the P and S waves. For rise times corresponding to the release rise times, we also measured amplitudes for the vertical strike-slip double couple at zero source depth. Since the assumed double couple spectral history does not have a peak, decreasing the rise time or increasing the corner frequency increased the amplitude of

the Rayleigh wave for both crustal models to point at which it was the same as for a step history. As one might expect, this monotonic increase in amplitude was also observed for the dip slip double couple at the other three source depths.

As the release radius was reduced for the various depths, the larger Rayleigh wave amplitudes approached that of the double couple until some minimum rise time of the S wave at which point the double couple and tectonic release were identical for smaller rise times. This occurred at a S wave rise time of about 0.5 second for the CUS model at a source depth of 0.2 km. As expected, reducing the double couple source depths by a factor of 2 reduced the Rayleigh wave amplitude factors similarly for the vertical dip slip model.

In addition, as the radius was decreased in the CUS model, there was a minimum amplitude at intermediate radii, which gave values less than the double couple at corresponding rise times. This was present at all depths below the surface. For the WUS model, the tectonic release values were larger for all radii and rise times. This minimum in amplitude was associated with a spectral hole present only in the tectonic release models, which was expected because of the difference in P and SV source time functions.

A more complete study of these effects would require many different source and propagation elastic structures and is beyond the scope of this paper. Although a convenient way to approximate the effect of differencing shot point velocities and source dimensions is to run a suite of double couple time history calculations for the P and SV sources separately and then sum the different combinations. This would also allow one to efficiently check the range of source dimensions and shot point conditions for which the double couple is a valid approximation to tectonic release.

ACKNOWLEDGMENTS

This research was supported by the Defense Advanced Research Projects Agency(DARPA) of the U. S. Department of Defense and was monitored in part by the Air Force Office of Scientific Research under Contract F49620-83-C-0025 and the Air Force Geophysics Laboratory under Contracts F19628-85-K-0017 and F19628-87-K-0028. In addition, while at the Center of Seismic Studies, D.G.H. and C.B.A. received support from DARPA through the Defense Supply Service-Washington under Contract No. MDA903-84-C-0020.

Contribution No. 4363, Division of Geological and Planetary Sciences, California Institute of Technology, Pasadena, California.

SEISMOLOGICAL LABORATORY
CALIFORNIA INSTITUTE OF TECHNOLOGY
PASADENA, CALIFORNIA 91125
(D.G.H.)

S-CUBED, DIVISION OF
MAXWELL LABORATORIES, INC.
P. O. BOX 1620
LA JOLLA, CALIFORNIA 92038-1620
(J.L.S.)

UNIVERSITY OF COLORADO/CIRES
CAMPUS BOX 449
BOULDER, COLORADO 80309
(C.B.A.)

REFERENCES

- Archambeau, C. B. (1968). General theory of elastodynamic source fields, *Rev. Geophys. Space Phys.* **6**, 241-288.
- Archambeau, C. B. (1972). The theory of stress wave radiation from explosions in prestressed media, *Geophys. J. R. astr. Soc.* **39**, 329-366.
- Bache, T. C. and D. G. Harkrider (1976). The body waves due to a general seismic source in a layered earth model: 1. Formulation of the theory, *Bull. Seism. Soc. Am.* **66**, 1805-1819.
- Ben-Menahem, A. and D. G. Harkrider (1964). Radiation patterns of surface waves from buried dipolar point-sources in a flat stratified earth, *J. Geophys. Res.* **69**, 2605-2620.
- Ben-Menahem, A. and S. J. Singh (1968). Eigenvector expansions of Green's Dyads with applications to geophysical theory, *Geophys. J. R. astr. Soc.* **16**, 417-452.
- Ben-Menahem, A. and S. J. Singh (1968). Multipolar elastic fields in a layered half-space, *Bull. Seism. Soc. Am.* **58**, 1519-1572.
- Ben-Menahem, A. and S. J. Singh (1981). *Seismic Waves and Sources*, Springer-Verlag, New York.
- Burridge, R. (1975). The pulse shapes and spectra of elastic waves generated when a cavity expands in an initial shear field, *J. Geophys. Res.* **80**, 2606-2607.
- Burridge, R. and Z. Alterman (1972). The elastic radiation from an expanding spherical cavity, *Geophys. J. R. astr. Soc.* **30**, 451-477.
- Douglas, A., J. A. Hudson, and V. K. Kambhavi (1971). The analysis of surface wave spectra using a reciprocity theorem for surface waves, *Geophys. J. R. astr. Soc.* **23**, 207-223.
- Dunkin, J. W. (1965). Computation of modal solutions in layered, elastic media at high frequencies, *Bull. Seism. Soc. Am.* **55**, 335-358.
- Gilbert, F. and G. E. Backus (1966). Propagator matrices in elastic wave and vibration problems, *Geophysics* **31**, 326-332.
- Harkrider, D. G. (1964). Surface waves in multilayered elastic media, I. Rayleigh and Love waves from buried sources in a multilayered elastic half-space, *Bull. Seism. Soc. Am.* **54**, 627-679.
- Harkrider, D. G. (1970). Surface waves in multilayered elastic media, Part II. Higher mode

- spectra and spectral ratios from point sources in plane layered earth models, *Bull. Seism. Soc. Amer.* **60**, 1937-1987.
- Harkrider, D. G. (1976). Potentials and displacements for two theoretical seismic sources, *Geophys. J. R. Astr. Soc.* **47**, 97-133.
- Harkrider, D. G. (1977). Elastic relaxation coefficients for a spherical cavity in a prestressed medium of arbitrary orientation, *Research Note, Geophys. J. R. Astr. Soc.* **50**, 487-491.
- Harkrider, D. G. and E. A. Flinn (1970). Effect of crustal structure on Rayleigh waves generated by atmospheric explosions, *Rev. Geophys. Space Phys.* **8**, 501-516.
- Harkrider, D. G., C. A. Newton, and E. A. Flinn (1974). Theoretical effect of yield and burst height of atmospheric explosions on Rayleigh wave amplitudes, *Geophys. J. R. Astr. Soc.* **36**, 191-225.
- Harvey, D. J. (1981). Seismogram synthesis using normal mode superposition: the locked mode approximation, *Geophys. J. R. astr. Soc.* **66**, 37-69.
- Haskell, N. A. (1964). Radiation pattern of surface waves from point sources in a multilayered medium, *Bull. Seism. Soc. Am.* **54**, 377-393.
- Hirasawa, T. and R. Sato (1963). Propagation of elastic waves from a spherical origin: parts 1 and 2 (in Japanese), *Zisin* **16**, 52-77.
- Hudson, J. A. (1969). A quantitative evaluation of seismic signals at teleseismic distances-I Radiation from point sources, *Geophys. J. R. astr. Soc.* **18**, 233-249.
- Hudson, J. A. and A. Douglas (1975). On the amplitude of seismic waves, *Research Note, Geophys. J. R. astr. Soc.* **42**, 1039-1044.
- Kind, R. and R. I. Odom (1983). Improvements to layer matrix methods, *J. Geophys.* **53**, 127-130.
- Koyama, J., S. E. Horiuchi, and T. Hirasawa (1973). Elastic waves generated from sudden vanishing of rigidity in a spherical region, *J. Phys. Earth* **21**, 213-226.
- Mendiguren, J. A. (1977). Inversion of surface wave data in source mechanism studies, *J. Geophys. Res.* **82**, 889-894.
- Minster, J. B. (1979). Near-field waveforms from an arbitrarily expanding transparent spherical

- cavity in a prestressed medium, *Geophys. J. R. astr. Soc.* **56**, 81-96.
- Minster, J. B. and A. Suteau (1977). Far-field waveforms from an arbitrarily expanding transparent spherical cavity in a prestressed medium, *Geophys. J. R. astr. Soc.* **61**, 215-233.
- Sesawa, K. and K. Kanai (1941). Transmission of arbitrary elastic waves from a spherical source, solved with operational calculus. I and II, *Bull. Earthq. Res. Inst.* **19**, 151-161 and 417-442.
- Sesawa, K. and K. Kanai (1942). Transmission of arbitrary elastic waves from a spherical source, solved with operational calculus. III, *Bull. Earthq. Res. Inst.* **20**, 1-19.
- Stevens, J.L. (1980). Seismic radiation from the sudden creation of a spherical cavity in an arbitrary prestressed elastic medium, *Geophys. J. R. astr. Soc.* **61**, 303-328.
- Stevens, J. L. (1982). A mode for tectonic strain release from explosions in complex prestress fields applied to anomalous seismic waves from NTS and Eastern Kazakh explosions, , SCUBED Technical Report, (SSS-R-82-5358) and (VSC-TR-82-20), Contract No. F08606-79-C-0007 submitted to DARPA, La Jolla, California.
- Wang, C. Y. and R. B. Herrmann (1985). Synthesis of coda waves in layered medium, *Lg Wave Excitation*, Saint Louis University Final Technical Report, Contract No. F49620-83-C-0087 submitted to DARPA.
- Woodhouse, J. H. (1974). Surface waves in a laterally varying layered structure, *Geophys. J. R. astr. Soc.* **37**, 461-490.

Appendix A

In this Appendix, we drop the double bar superscript notation in equations (37) through (39a) and rewrite as

$$w = \frac{\partial \Phi}{\partial x} + \frac{\partial \Psi_2}{\partial x} - \frac{\partial \Psi_1}{\partial y} \quad \text{where} \quad \langle w \rangle = \int_0^\infty w dk$$

and

$$w = \frac{\partial \Phi}{\partial x} + k^2 \psi$$

or

$$\psi = \frac{1}{k^2} \left(\frac{\partial \Psi_2}{\partial x} - \frac{\partial \Psi_1}{\partial y} \right)$$

In terms of cylindrical coordinate derivatives

$$k^2 \psi = \left[\cos \phi \frac{\partial \Psi_2}{\partial r} - \frac{\sin \phi}{r} \frac{\partial \Psi_2}{\partial \phi} - \sin \phi \frac{\partial \Psi_1}{\partial r} - \frac{\cos \phi}{r} \frac{\partial \Psi_1}{\partial \phi} \right]$$

where the cartesian potential integrands are

$$\Psi_1 = i \sum_{m=0}^{\infty} \left[\bar{C}_m^{(1)} \cos m\phi + \bar{D}_m^{(1)} \sin m\phi \right] J_m F_\rho$$

$$\Psi_2 = i \sum_{m=0}^{\infty} \left[\bar{C}_m^{(2)} \cos m\phi + \bar{D}_m^{(2)} \sin m\phi \right] J_m F_\rho$$

or

$$k \psi = i \sum_{m=0}^{\infty} \left\{ \left[\bar{C}_m^{(2)} \cos \phi \cos m\phi + \bar{D}_m^{(2)} \cos \phi \sin m\phi - \bar{C}_m^{(1)} \sin \phi \cos m\phi - \bar{D}_m^{(1)} \sin \phi \sin m\phi \right] \frac{dJ_m}{kdr} + \left[\bar{C}_m^{(2)} \sin \phi \sin m\phi - \bar{D}_m^{(2)} \sin \phi \cos m\phi + \bar{C}_m^{(1)} \cos \phi \sin m\phi - \bar{D}_m^{(1)} \cos \phi \cos m\phi \right] m \frac{J_m}{kr} \right\} F_\rho$$

and

$$\frac{dJ_m}{d(kr)} = 1/2 (J_{m-1} - J_{m+1})$$

$$m \frac{J_m}{kr} = 1/2 (J_{m-1} + J_{m+1})$$

then

$$2k\psi = i \left\{ \sum_{m=0}^n \left[\bar{C}_m^{(2)} \cos(m-1)\phi + \bar{D}_m^{(2)} \sin(m-1)\phi + \bar{C}_m^{(1)} \sin(m-1)\phi - \bar{D}_m^{(1)} \cos(m-1)\phi \right] J_{m-1} + \left[-\bar{C}_m^{(2)} \cos(m+1)\phi - \bar{D}_m^{(2)} \sin(m+1)\phi + \bar{C}_m^{(1)} \sin(m+1)\phi - \bar{D}_m^{(1)} \cos(m+1)\phi \right] J_{m+1} \right\} F_\theta$$

Collecting and identifying with

$$\psi = i \sum_{m=0}^n (\bar{E}_m \cos m\phi + \bar{F}_m \sin m\phi) J_m F_\theta$$

We have the following recurrence relation

$$\begin{aligned} 2k \bar{E}_m &= (\bar{C}_{m+1}^{(2)} - \bar{C}_{m-1}^{(2)}) - (\bar{D}_{m+1}^{(1)} + \bar{D}_{m-1}^{(1)}) \\ 2k \bar{F}_m &= (\bar{C}_{m+1}^{(1)} + \bar{C}_{m-1}^{(1)}) + (\bar{D}_{m+1}^{(2)} - \bar{D}_{m-1}^{(2)}) \end{aligned} \quad 1 \leq m \leq n$$

where $\bar{C}_m^{(j)}$ and $\bar{D}_m^{(j)}$'s are zero for $m > n$ and $m < 0$ and

$$\bar{C}_0^{(2)} = \bar{D}_0^{(1)} \quad \text{and} \quad \bar{C}_0^{(1)} = -\bar{D}_0^{(2)}$$

and

$$\bar{F}_0 = 0$$

As an example when $n=6$, we have

$$\begin{aligned} 2k \bar{E}_0 &= \bar{C}_1^{(2)} - \bar{D}_1^{(1)} & 2k \bar{F}_0 &= 0 \\ 2k \bar{E}_1 &= \bar{C}_2^{(2)} - \bar{D}_2^{(1)} - 2\bar{C}_0^{(2)} & 2k \bar{F}_1 &= \bar{C}_2^{(1)} + \bar{D}_2^{(2)} + 2\bar{C}_0^{(1)} \\ 2k \bar{E}_2 &= \bar{C}_3^{(2)} - \bar{D}_3^{(1)} - \bar{C}_1^{(2)} - \bar{D}_1^{(1)} & 2k \bar{F}_2 &= \bar{C}_3^{(1)} + \bar{D}_3^{(2)} + \bar{C}_1^{(1)} - \bar{D}_1^{(2)} \\ 2k \bar{E}_3 &= \bar{C}_4^{(2)} - \bar{D}_4^{(1)} - \bar{C}_2^{(2)} - \bar{D}_2^{(1)} & 2k \bar{F}_3 &= \bar{C}_4^{(1)} + \bar{D}_4^{(2)} + \bar{C}_2^{(1)} - \bar{D}_2^{(2)} \\ 2k \bar{E}_4 &= \bar{C}_5^{(2)} - \bar{D}_5^{(1)} - \bar{C}_3^{(2)} - \bar{D}_3^{(1)} & 2k \bar{F}_4 &= \bar{C}_5^{(1)} + \bar{D}_5^{(2)} + \bar{C}_3^{(1)} - \bar{D}_3^{(2)} \\ 2k \bar{E}_5 &= -\bar{C}_6^{(2)} - \bar{D}_6^{(1)} & 2k \bar{F}_5 &= +\bar{C}_6^{(1)} - \bar{D}_6^{(2)} \\ 2k \bar{E}_6 &= -\bar{C}_6^{(2)} - \bar{D}_6^{(1)} & 2k \bar{F}_6 &= +\bar{C}_6^{(2)} - \bar{D}_6^{(1)} \end{aligned}$$

Appendix B

Cartesian and cylindrical multiple coefficients for quadruple sources of arbitrary orientation.

Comparing Harkrider (1976) equations (A8) with this paper's equations (33), we obtain the Cartesian coefficients:

$$\begin{aligned}
 A_{20} &= -K_\alpha k_\alpha^2 \sin \lambda \sin 2\delta \\
 A_{21} &= \frac{2}{3} K_\alpha k_\alpha^2 \cos \lambda \cos \delta & B_{21} &= -\frac{2}{3} K_\alpha k_\alpha^2 \sin \lambda \cos 2\delta \\
 A_{22} &= -\frac{1}{6} K_\alpha k_\alpha^2 \sin \lambda \sin \delta & B_{22} &= -\frac{1}{3} K_\alpha k_\alpha^2 \cos \lambda \sin \delta \\
 C_{20}^{(1)} &= \frac{1}{2} K_\beta k_\beta^2 \sin \lambda \cos 2\delta & C_{21}^{(1)} &= \frac{1}{6} K_\beta k_\beta^2 \cos \lambda \sin \delta \\
 D_{21}^{(1)} &= -\frac{1}{3} K_\beta k_\beta^2 \sin \lambda \sin 2\delta & C_{22}^{(1)} &= \frac{1}{12} K_\beta k_\beta^2 \sin \lambda \cos 2\delta \\
 D_{22}^{(1)} &= \frac{1}{12} K_\beta k_\beta^2 \cos \lambda \cos \delta & C_{20}^{(2)} &= \frac{1}{2} K_\beta k_\beta^2 \cos \lambda \cos \delta \\
 C_{21}^{(2)} &= \frac{1}{6} K_\beta k_\beta^2 \sin \lambda \sin 2\delta & D_{21}^{(2)} &= -\frac{1}{6} K_\beta k_\beta^2 \cos \lambda \sin \delta \\
 C_{22}^{(2)} &= -\frac{1}{12} K_\beta k_\beta^2 \cos \lambda \cos \delta & D_{22}^{(2)} &= \frac{1}{12} K_\beta k_\beta^2 \sin \lambda \cos 2\delta \\
 C_{21}^{(3)} &= -\frac{1}{6} K_\beta k_\beta^2 \sin \lambda \cos 2\delta & D_{21}^{(3)} &= -\frac{1}{6} K_\beta k_\beta^2 \cos \lambda \cos \delta \\
 C_{22}^{(3)} &= -\frac{1}{6} K_\beta k_\beta^2 \cos \lambda \sin \delta & D_{22}^{(3)} &= \frac{1}{12} K_\beta k_\beta^2 \sin \lambda \sin 2\delta
 \end{aligned} \tag{B1}$$

The resultant cylindrical coefficients using Appendix A are

$$\begin{aligned}
 \bar{A}_0 &= \frac{1}{2k_\alpha} K_\alpha (k^2 + 2\nu_\alpha^2) \sin \lambda \sin 2\delta \\
 \bar{A}_2 &= \frac{1}{2k_\alpha} K_\alpha k^2 \sin \lambda \sin 2\delta & \bar{B}_2 &= \frac{1}{k_\alpha} K_\alpha k^2 \cos \lambda \sin \delta \\
 \bar{A}_1 &= -\frac{2}{k_\alpha} K_\alpha k \nu_\alpha \cos \lambda \cos \delta & \bar{B}_1 &= \frac{2}{k_\alpha} K_\alpha k \nu_\alpha \sin \lambda \cos 2\delta
 \end{aligned}$$

$$\bar{E}_0^* = \frac{3}{2k_\rho} K_\rho \nu_\rho \sin \lambda \sin 2\delta \quad (\text{B2})$$

$$\bar{E}_2^* = \frac{1}{2k_\rho} K_\rho \nu_\rho \sin \lambda \sin 2\delta$$

$$\bar{F}_2^* = \frac{1}{k_\rho} K_\rho \nu_\rho \cos \lambda \sin \delta$$

$$\bar{E}_1^* = \frac{1}{k_\rho} K_\rho \frac{(k_\rho^2 - 2k^2)}{k} \cos \lambda \cos \delta$$

$$\bar{F}_1^* = -\frac{1}{k_\rho} K_\rho \frac{(k_\rho^2 - 2k^2)}{k} \sin \lambda \cos 2\delta$$

$$\bar{C}_1^{(s)*} = -\frac{1}{k_\rho} K_\rho k \nu_\rho \sin \lambda \cos 2\delta$$

$$\bar{D}_1^{(s)*} = -\frac{1}{k_\rho} K_\rho k \nu_\rho \cos \lambda \cos \delta$$

$$\bar{C}_2^{(s)*} = -\frac{1}{k_\rho} K_\rho k^2 \cos \lambda \sin \delta$$

$$\bar{D}_2^{(s)*} = \frac{1}{2k_\rho} K_\rho k^2 \sin \lambda \sin 2\delta$$

Appendix C

The definition of the second order seismic moment tensor is

$$u_i(x, t) = M_{pi} \frac{\partial}{\partial \xi_j} G_{ij}$$

$$u_i(x, t) = -M_{pi} G_{ip,i}$$

or

$$\bar{u}_i(x, \omega) = -\bar{M}_{pi}^{(\omega)} \bar{G}_{ip,i}$$

where the comma denotes differentiation with respect to the observer coordinates, x , rather than the source coordinates, ξ .

Now

$$\bar{G}_{ip,i} = \frac{1}{4\pi\rho\omega^2} \left\{ \frac{\partial^2}{\partial x_i \partial x_p \partial x_i} (A_p - A_\infty) + k_p^2 \delta_{ip} \frac{\partial}{\partial x_i} A_p \right\}$$

Now from Harkrider (1976), equations(32) and (33), we have that

$$\bar{\Phi} = -\frac{1}{k_\omega^2} \frac{\partial \bar{u}_i}{\partial x_i}$$

and

$$\bar{\Psi}_i = \frac{1}{k_p^2} c_{ip} \frac{\partial \bar{u}_k}{\partial x_j}$$

or

$$\bar{\Phi} = \frac{1}{k_\omega^2} \bar{M}_{pi} \bar{G}_{ip,i}$$

and

$$\bar{G}_{ip,i} = \frac{1}{4\pi\rho\omega^2} \left\{ \frac{\partial^2}{\partial x_p \partial x_i} \frac{\partial^2}{\partial x_i^2} (A_p - A_\infty) + k_p^2 \delta_{ip} \frac{\partial^2}{\partial x_i \partial x_i} A_p \right\}$$

and since

$$\frac{\partial^2}{\partial x_i^2} A_i = -k_\omega^2 A_i \quad \text{and} \quad \delta_{ip} \frac{\partial^2}{\partial x_i \partial x_i} A_p = \frac{\partial^2}{\partial x_i \partial x_p} A_p$$

we have

$$\bar{G}_{\phi,\phi} = \frac{1}{4\pi\rho\omega^2} k_z^2 \frac{\partial^2}{\partial z_1 \partial z_1} A_\phi$$

Thus

$$\begin{aligned} \bar{\Phi} &= \frac{1}{4\pi\rho\omega^2} \bar{M}_{\phi\phi} \frac{\partial^2}{\partial z_1 \partial z_1} A_\phi \\ &= \frac{1}{4\pi\rho\omega^2} \left\{ \bar{M}_{11} \frac{\partial^2}{\partial z_1^2} + \bar{M}_{22} \frac{\partial^2}{\partial z_2^2} + \bar{M}_{33} \frac{\partial^2}{\partial z_3^2} + 2\bar{M}_{12} \frac{\partial^2}{\partial z_1 \partial z_2} \right. \\ &\quad \left. + 2\bar{M}_{13} \frac{\partial^2}{\partial z_1 \partial z_3} + 2\bar{M}_{23} \frac{\partial^2}{\partial z_2 \partial z_3} \right\} A_\phi \end{aligned}$$

From Erdelyi (1937)

$$H_2^{(0)}(k, R) P_2^{(0)}(\cos\theta) e^{im\phi} = i^{-m} (D_z)^m P_2^{(m)}(\partial/\partial i k_z, z) H_0^{(0)}(k, R) \quad (C1)$$

where the differential operator D_z is defined as

$$D_z = \frac{1}{ik_z} \left(\frac{\partial}{\partial z_1} + i \frac{\partial}{\partial z_2} \right)$$

Combining equation (C1) with

$$H_2^{(0)}(k, R) P_2^{(0)}(\cos\theta) = \frac{i}{2k_z} \left[\frac{3}{k_z^2} \frac{\partial^2 A_\phi}{\partial z_1^2} + A_\phi \right]$$

and

$$A_\phi = -i k_z H_0^{(0)}(k, R)$$

We have

$$\begin{aligned} \frac{\partial^2 A_\phi}{\partial z_1^2} &= i \frac{k_z^2}{3} \left\{ H_0^{(0)}(k, R) - 2H_2^{(0)}(k, R) P_2^{(0)}(\cos\theta) \right\} \\ \frac{\partial^2 A_\phi}{\partial z_1^2} &= i \frac{k_z^2}{3} \left\{ H_0^{(0)}(k, R) + H_2^{(0)}(k, R) \left[P_2^{(0)}(\cos\theta) - \frac{1}{2} P_2^{(2)}(\cos\theta) \cos 2\phi \right] \right\} \\ \frac{\partial^2 A_\phi}{\partial z_2^2} &= i \frac{k_z^2}{3} \left\{ H_0^{(0)}(k, R) + H_2^{(0)}(k, R) \left[P_2^{(0)}(\cos\theta) + \frac{1}{2} P_2^{(2)}(\cos\theta) \cos 2\phi \right] \right\} \\ \frac{\partial^2 A_\phi}{\partial z_1 \partial z_2} &= -i \frac{k_z^2}{6} H_2^{(0)}(k, R) P_2^{(2)}(\cos\theta) \sin 2\phi \end{aligned}$$

$$\frac{\partial^2 A_r}{\partial x_1 \partial x_3} = -i \frac{k_\alpha^5}{3} H_2^{(0)}(k_\alpha R) P_2^1(\cos\theta) \cos\phi$$

$$\frac{\partial^2 A_r}{\partial x_2 \partial x_3} = -i \frac{k_\alpha^5}{3} H_2^{(0)}(k_\alpha R) P_2^1(\cos\theta) \sin\phi$$

Comparing with the definition of the cartesian multipole coefficients we have

$$A_{00} = -\frac{1}{4\pi\rho\omega^2} i \frac{k_\alpha^5}{3} (\bar{M}_{11} + \bar{M}_{22} + \bar{M}_{33})$$

and

$$A_{20} = -\frac{1}{4\pi\rho\omega^2} i \frac{k_\alpha^5}{3} (\bar{M}_{11} + \bar{M}_{22} - 2\bar{M}_{33}) \quad (C2)$$

$$A_{21} = +\frac{1}{4\pi\rho\omega^2} i \frac{k_\alpha^5}{3} 2\bar{M}_{13} \quad B_{21} = +\frac{1}{4\pi\rho\omega^2} i \frac{k_\alpha^5}{3} 2\bar{M}_{23}$$

$$A_{22} = +\frac{1}{4\pi\rho\omega^2} i \frac{k_\alpha^5}{6} (\bar{M}_{11} - \bar{M}_{22}) \quad B_{22} = +\frac{1}{4\pi\rho\omega^2} i \frac{k_\alpha^5}{3} \bar{M}_{12}$$

Now

$$e_{ijk} \frac{\partial \bar{u}_k}{\partial x_j} = -\bar{M}_{ji} e_{ijk} \bar{G}_{kp,ij}$$

and

$$\bar{G}_{kp,ij} = \frac{1}{4\pi\rho\omega^2} \left\{ \frac{\partial^2}{\partial x_p \partial x_i} \frac{\partial^2}{\partial x_k \partial x_j} (A_p - A_\alpha) + k_p^2 \delta_{kp} \frac{\partial^2}{\partial x_i \partial x_j} A_p \right\}$$

Operating with e_{ijk} , the first term is zero since it is symmetric in (j,k) and

$$e_{ijk} \bar{G}_{kp,ij} = \frac{1}{4\pi\rho\omega^2} k_p^2 e_{ijp} \frac{\partial^2}{\partial x_i \partial x_j} A_p$$

thus

$$\bar{\Psi}_i = -\frac{1}{4\pi\rho\omega^2} e_{ijp} \bar{M}_{ji} \frac{\partial^2}{\partial x_i \partial x_j} A_p$$

which yields

$$\bar{\Psi}_1 = -\frac{1}{4\pi\rho\omega^2} \left\{ (\bar{M}_{22} - \bar{M}_{23}) \frac{\partial^2}{\partial x_2 \partial x_3} + \bar{M}_{23} \left(\frac{\partial^2}{\partial x_3^2} - \frac{\partial^2}{\partial x_1^2} \right) \right. \\ \left. + \bar{M}_{12} \frac{\partial^2}{\partial x_1 \partial x_2} - \bar{M}_{13} \frac{\partial^2}{\partial x_1 \partial x_3} \right\} A_p$$

$$\bar{\Psi}_2 = -\frac{1}{4\pi\rho\omega^2} \left\{ (\bar{M}_{11} - \bar{M}_{22}) \frac{\partial^2}{\partial x_1 \partial x_2} + \bar{M}_{12} \left(\frac{\partial^2}{\partial x_1^2} - \frac{\partial^2}{\partial x_3^2} \right) \right. \\ \left. + \bar{M}_{13} \frac{\partial^2}{\partial x_2 \partial x_3} - \bar{M}_{23} \frac{\partial^2}{\partial x_1 \partial x_3} \right\} A_p$$

$$\bar{\Psi}_3 = -\frac{1}{4\pi\rho\omega^2} \left\{ (\bar{M}_{22} - \bar{M}_{11}) \frac{\partial^2}{\partial x_1 \partial x_2} + \bar{M}_{12} \left(\frac{\partial^2}{\partial x_1^2} - \frac{\partial^2}{\partial x_3^2} \right) \right. \\ \left. + \bar{M}_{23} \frac{\partial^2}{\partial x_1 \partial x_3} - \bar{M}_{13} \frac{\partial^2}{\partial x_2 \partial x_3} \right\} A_p$$

Comparing as before we have

$$C_{20}^{(1)} = -\frac{1}{8\pi\rho\omega^2} i \frac{k_p^5}{3} \bar{M}_{23}$$

$$C_{21}^{(1)} = -\frac{1}{8\pi\rho\omega^2} i \frac{k_p^5}{3} \bar{M}_{12}$$

$$C_{22}^{(1)} = -\frac{1}{8\pi\rho\omega^2} i \frac{k_p^5}{6} \bar{M}_{23}$$

$$C_{20}^{(2)} = +\frac{1}{8\pi\rho\omega^2} i \frac{k_p^5}{3} \bar{M}_{13}$$

$$C_{21}^{(2)} = +\frac{1}{8\pi\rho\omega^2} i \frac{k_p^5}{3} (\bar{M}_{11} - \bar{M}_{22})$$

$$C_{22}^{(2)} = -\frac{1}{8\pi\rho\omega^2} i \frac{k_p^5}{6} \bar{M}_{13}$$

$$C_{20}^{(3)} = 0$$

$$C_{21}^{(3)} = +\frac{1}{8\pi\rho\omega^2} i \frac{k_p^5}{3} \bar{M}_{23}$$

$$C_{22}^{(3)} = +\frac{1}{8\pi\rho\omega^2} i \frac{k_p^5}{3} \bar{M}_{12}$$

$$D_{21}^{(1)} = -\frac{1}{8\pi\rho\omega^2} i \frac{k_p^5}{3} (\bar{M}_{22} - \bar{M}_{23})$$

$$D_{22}^{(1)} = +\frac{1}{8\pi\rho\omega^2} i \frac{k_p^5}{6} \bar{M}_{13}$$

$$D_{21}^{(2)} = +\frac{1}{8\pi\rho\omega^2} i \frac{k_p^5}{3} \bar{M}_{12}$$

$$D_{22}^{(2)} = -\frac{1}{8\pi\rho\omega^2} i \frac{k_p^5}{6} \bar{M}_{23}$$

$$D_{21}^{(3)} = -\frac{1}{8\pi\rho\omega^2} i \frac{k_p^5}{3} \bar{M}_{13}$$

$$D_{22}^{(3)} = -\frac{1}{8\pi\rho\omega^2} i \frac{k_p^5}{6} (\bar{M}_{11} - \bar{M}_{22})$$

(C3)

The resulting cylindrical coefficients using Appendix A are

$$\bar{A}_0 = + \frac{1}{4\pi\rho\omega^2} \frac{i}{2} \left[k^2(\bar{M}_{11} + \bar{M}_{22}) + 2\bar{M}_{33}(k_\rho^2 - k^2) \right]$$

$$\bar{A}_1 = + \frac{1}{4\pi\rho\omega^2} 2\epsilon k \bar{v}_\rho \bar{M}_{13} \quad \bar{B}_1 = + \frac{1}{4\pi\rho\omega^2} 2\epsilon k \bar{v}_\rho \bar{M}_{23}$$

$$\bar{A}_2 = + \frac{1}{4\pi\rho\omega^2} \frac{i}{2} k^2(\bar{M}_{22} - \bar{M}_{11}) \quad \bar{B}_2 = - \frac{1}{4\pi\rho\omega^2} i k^2 \bar{M}_{12}$$

$$\bar{C}_0^{(s)} = 0$$

$$\bar{C}_1^{(s)} = - \frac{1}{4\pi\rho\omega^2} \epsilon k \bar{v}_\rho \bar{M}_{23} \quad \bar{D}_1^{(s)} = + \frac{1}{4\pi\rho\omega^2} \epsilon k \bar{v}_\rho \bar{M}_{13}$$

$$\bar{C}_2^{(s)} = + \frac{i}{4\pi\rho\omega^2} k^2 \bar{M}_{12} \quad \bar{D}_2^{(s)} = - \frac{i}{8\pi\rho\omega^2} k^2 (\bar{M}_{11} - \bar{M}_{22}) \quad (C4)$$

and

$$\bar{E}_0 = - \frac{1}{8\pi\rho\omega^2} \epsilon \bar{v}_\rho (\bar{M}_{11} + \bar{M}_{22} - 2\bar{M}_{33})$$

$$\bar{E}_1 = - \frac{i}{4\pi\rho\omega^2} \frac{(2k^2 - k_\rho^2)}{k} \bar{M}_{13} \quad \bar{F}_1 = - \frac{i}{4\pi\rho\omega^2} \frac{(2k^2 - k_\rho^2)}{k} \bar{M}_{23}$$

$$\bar{E}_2 = + \frac{1}{8\pi\rho\omega^2} \epsilon \bar{v}_\rho (\bar{M}_{11} - \bar{M}_{22}) \quad \bar{F}_2 = + \frac{1}{4\pi\rho\omega^2} \epsilon \bar{v}_\rho \bar{M}_{12}$$

where

$$\epsilon = \text{sgn}(z-h)$$

Thus coefficients involving ϵ are odd and the other coefficients are even in the sense of equations(43).

TABLE 1

Western United States Model (WUS)					
Thickness (km)	α (km/sec)	β (km/sec)	ρ (gm/cm ³)	Q_α	Q_β
2.0	3.55	2.06	2.20	170.	85.
3.0	6.15	3.27	2.79	300.	150.
18.0	6.15	3.57	2.79	300.	150.
8.0	6.70	3.93	2.97	1000.	500.
6.0	6.70	3.73	2.97	1000.	500.
0.0	7.80	4.41	3.35	2000.	1000.

Central United States Model (CUS)					
Thickness (km)	α (km/sec)	β (km/sec)	ρ (gm/cm ³)	Q_α	Q_β
1.0	5.00	2.89	2.5	600.	300.
9.0	6.10	3.52	2.7	600.	300.
10.0	6.40	3.70	2.9	600.	300.
20.0	6.70	3.87	3.0	4000.	2000.
0.0	8.15	4.70	3.4	4000.	2000.

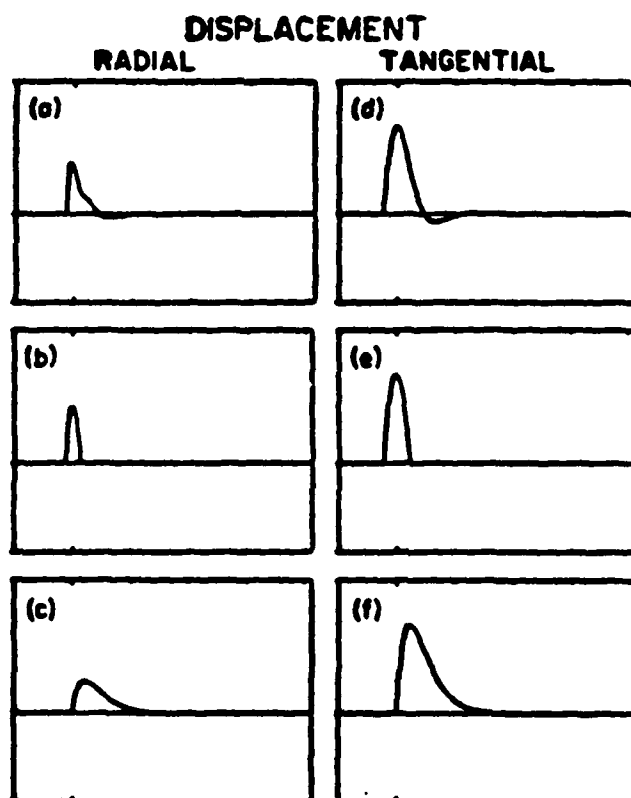


Figure 1. Far-field radial (P) and tangential (S) displacement time histories for the exact tectonic cavity release (Fig. 1a and 1d), for the Randall-Archambeau approximate cavity release (Fig. 1b and 1e), and for the ' u -square' double couple model (Fig. 1c and 1f).

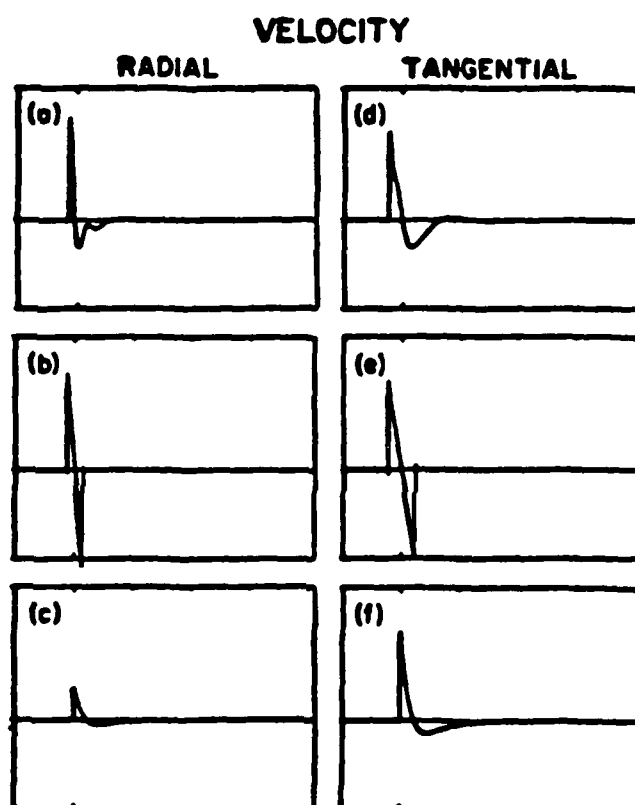


Figure 2. Far-field radial (P) and tangential (S) velocity time histories for the exact tectonic cavity release (Fig. 2a and 2d), for the Randall-Archambeau approximate cavity release (Fig. 2b and 2e), and for the 'U-square' double couple model (Fig. 2c and 2f).

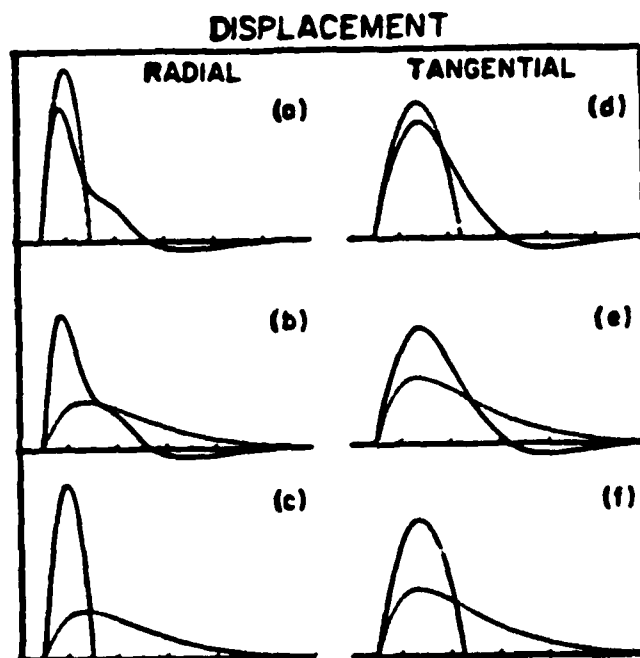


Figure 3. Far-field radial (P) and tangential (S) displacement time histories for the exact tectonic cavity release (solid line) superimposed on the Randall-Archambeau approximate cavity release (dashed line)(Fig. 3a and 3d), for the exact tectonic cavity release (solid line) superimposed on the ' ψ -square' double couple model (dashed line)(Fig. 3b and 3e), and for the Randall-Archambeau approximate cavity release (solid line) superimposed on the ' ψ -square' double couple model (dashed line)(Fig. 3c and 3f).

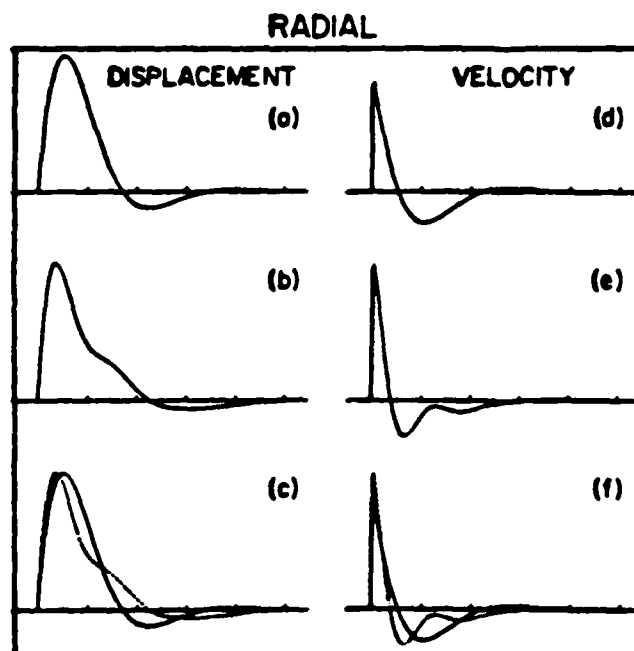


Figure 4. Far-field radial (P) displacement and velocity time histories for the step pressure on a cavity explosion (Fig. 4a and 4d), for the exact tectonic cavity release (Fig. 4b and 4e), and the two sources time histories superimposed (Fig. 4c and 4f).

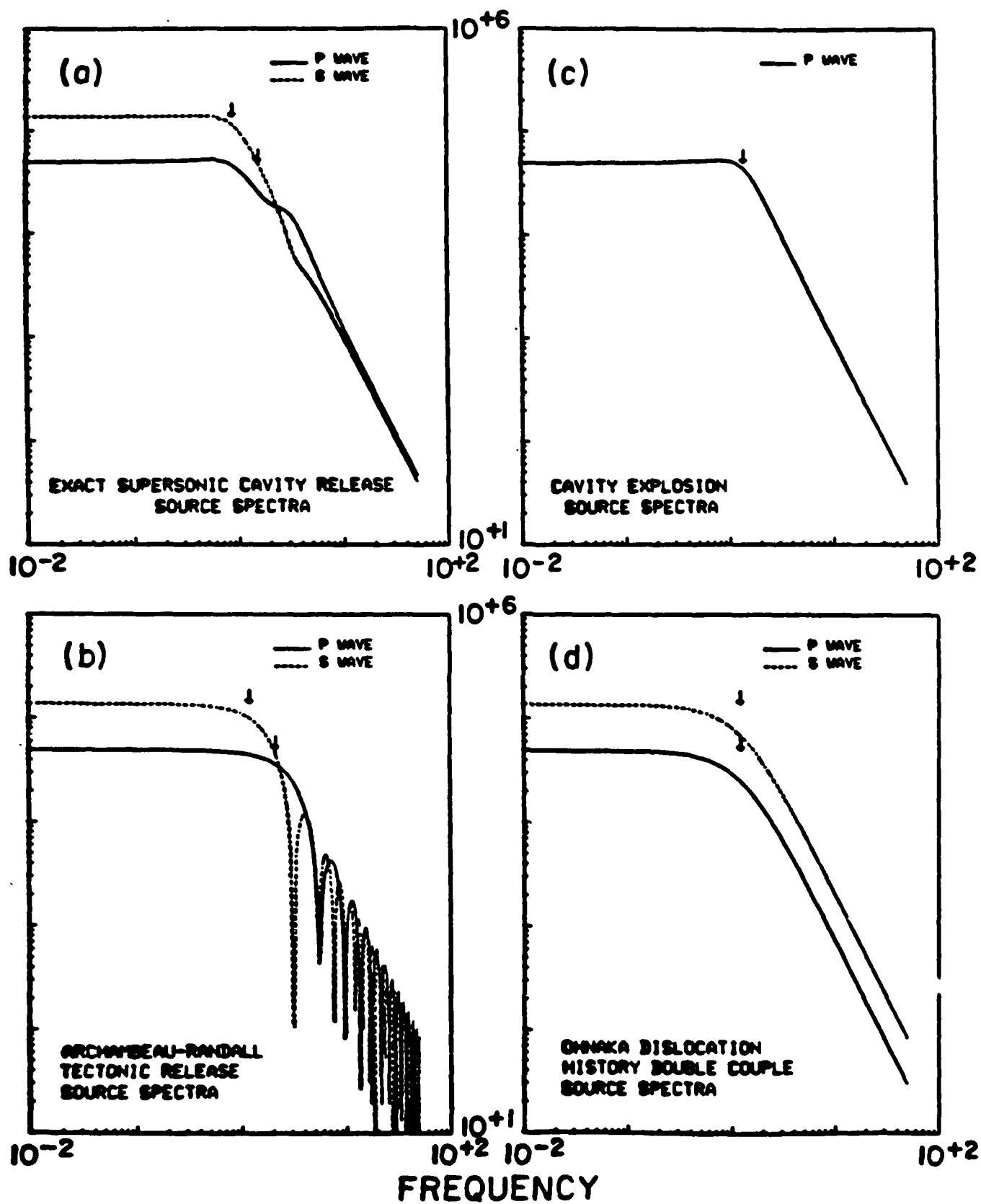


Figure 5. Far-field source displacement spectra.

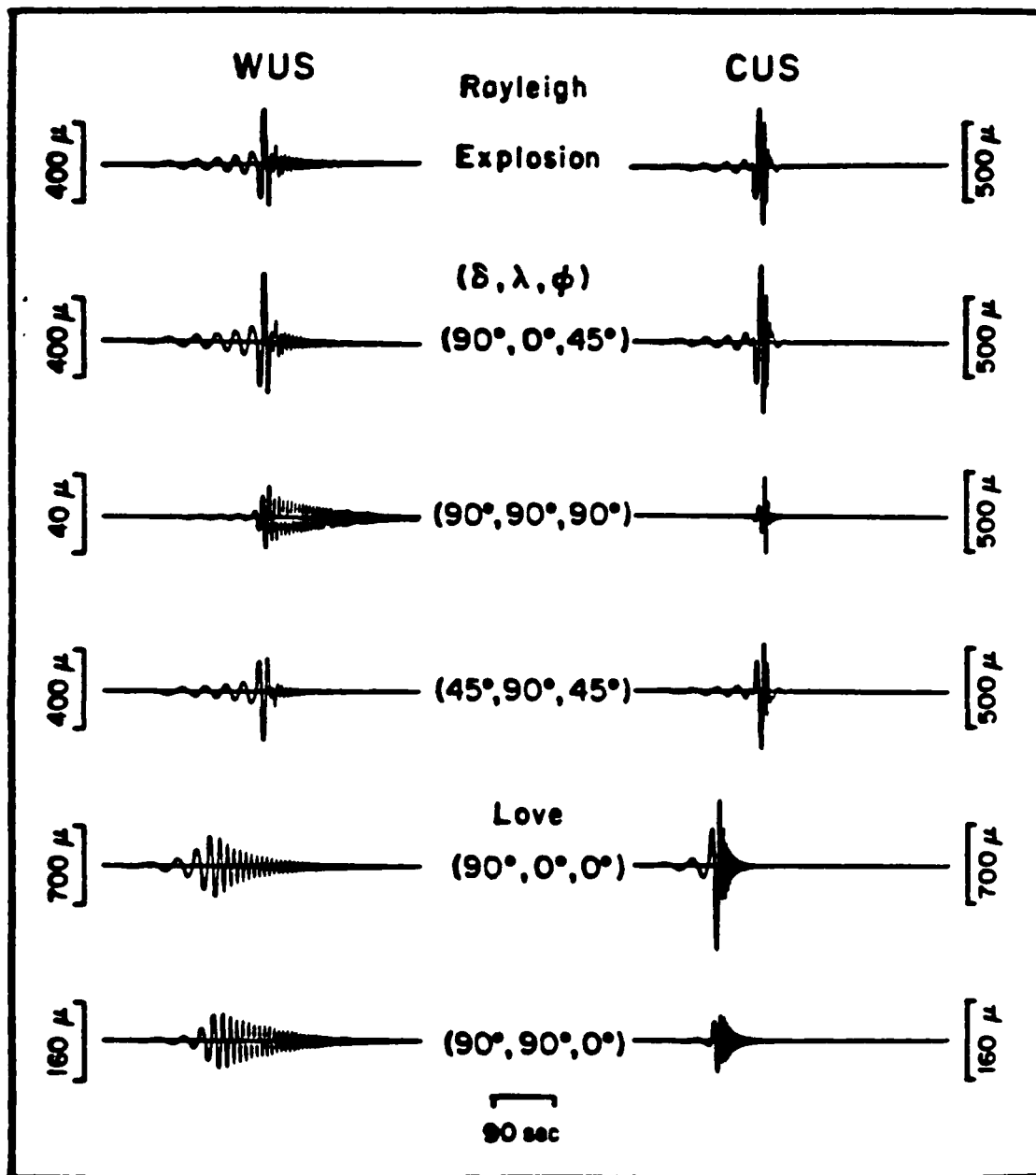


Figure 6. Vertical Rayleigh and horizontal Love waves at a range of 2000 km as observed on a WSSN LP seismograph.

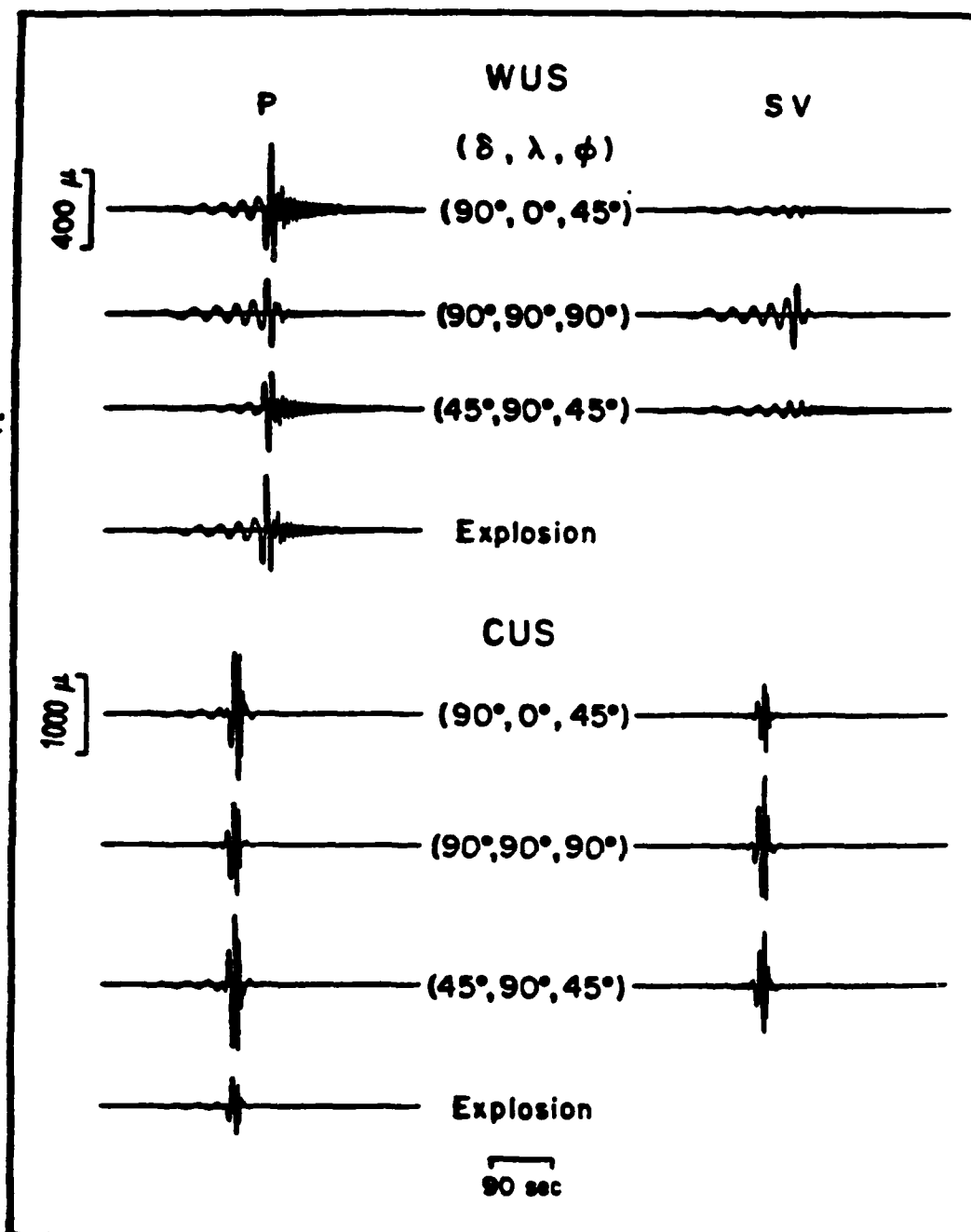


Figure 7. Vertical Rayleigh waves at a range of 2000 km as observed on a WSSN LP seismograph. The contributions to the Rayleigh wave by the P and SV source radiation are shown separately.

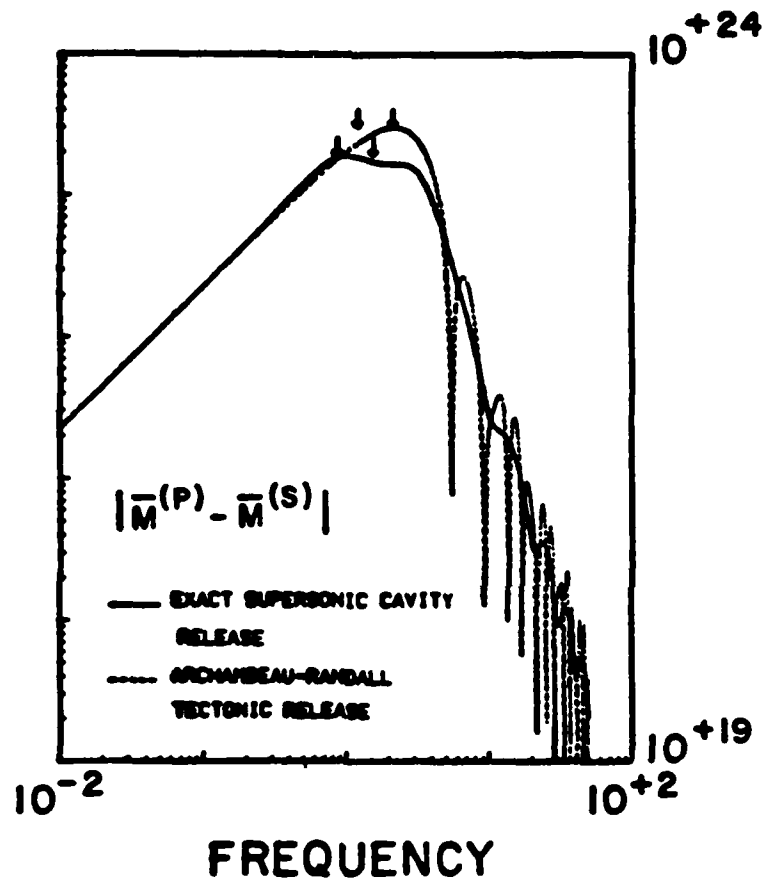


Figure 8. Spectral difference between P and S wave moments for the exact supersonic cavity release and the approximate Randall-Archambeau equivalent. The arrows mark the P and S corner frequencies.

CONTRACTORS (United States)

Prof. Thomas Ahrens
Seismological Lab, 252-21
Division of Geological & Planetary Sciences
California Institute of Technology
Pasadena, CA 91125

Prof. Charles B. Archambeau
CIRES
University of Colorado
Boulder, CO 80309

Prof. Muawia Barazangi
Institute for the Study of the Continent
Cornell University
Ithaca, NY 14853

Dr. Douglas R. Baumgardt
ENSCO, Inc
5400 Port Royal Road
Springfield, VA 22151-2388

Prof. Jonathan Berger
IGPP, A-025
Scripps Institution of Oceanography
University of California, San Diego
La Jolla, CA 92093

Dr. Lawrence J. Burdick
Woodward-Clyde Consultants
566 El Dorado Street
Pasadena, CA 91109-3245

Dr. Karl Coyner
New England Research, Inc.
76 Olcott Drive
White River Junction, VT 05001

Prof. Vernon F. Cormier
Department of Geology & Geophysics
U-45, Room 207
The University of Connecticut
Storrs, CT 06268

Prof. Steven Day
Department of Geological Sciences
San Diego State University
San Diego, CA 92182

Dr. Zoltan A. Der
ENSCO, Inc.
5400 Port Royal Road
Springfield, VA 22151-2388

Prof. John Ferguson
Center for Lithospheric Studies
The University of Texas at Dallas
P.O. Box 830688
Richardson, TX 75083-0688

Prof. Stanley Flatte
Applied Sciences Building
University of California
Santa Cruz, CA 95064

Dr. Alexander Florence
SRI International
333 Ravenswood Avenue
Menlo Park, CA 94025-3493

Prof. Henry L. Gray
Vice Provost and Dean
Department of Statistical Sciences
Southern Methodist University
Dallas, TX 75275

Dr. Indra Gupta
Teledyne Geotech
314 Montgomery Street
Alexandria, VA 22314

Prof. David G. Harkrider
Seismological Laboratory
Division of Geological & Planetary Sciences
California Institute of Technology
Pasadena, CA 91125

Prof. Donald V. Helmberger
Seismological Laboratory
Division of Geological & Planetary Sciences
California Institute of Technology
Pasadena, CA 91125

Prof. Eugene Herrin
Institute for the Study of Earth and Man
Geophysical Laboratory
Southern Methodist University
Dallas, TX 75275

Prof. Robert B. Herrmann
Department of Earth & Atmospheric Sciences
St. Louis University
St. Louis, MO 63156

Prof. Bryan Isacks
Cornell University
Department of Geological Sciences
SNEE Hall
Ithaca, NY 14850

Dr. Rong-Song Jih
Teledyne Geotech
314 Montgomery Street
Alexandria, VA 22314

Prof. Lane R. Johnson
Seismographic Station
University of California
Berkeley, CA 94720

Prof. Alan Kafka
Department of Geology & Geophysics
Boston College
Chestnut Hill, MA 02167

Prof. Fred K. Lamb
University of Illinois at Urbana-Champaign
Department of Physics
1110 West Green Street
Urbana, IL 61801

Prof. Charles A. Langston
Geosciences Department
403 Deike Building
The Pennsylvania State University
University Park, PA 16802

Prof. Thorne Lay
Department of Geological Sciences
1006 C.C. Little Building
University of Michigan
Ann Arbor, MI 48109-1063

Prof. Arthur Lerner-Lam
Lamont-Doherty Geological Observatory
of Columbia University
Palisades, NY 10964

Dr. Christopher Lynnes
Teledyne Geotech
314 Montgomery Street
Alexandria, VA 22314

Prof. Peter Malin
University of California at Santa Barbara
Institute for Crustal Studies
Santa Barbara, CA 93106

Dr. Randolph Martin, III
New England Research, Inc.
76 Olcott Drive
White River Junction, VT 05001

Dr. Gary McCartor
Mission Research Corporation
735 State Street
P.O. Drawer 719
Santa Barbara, CA 93102 (2 copies)

Prof. Thomas V. McEvilly
Seismographic Station
University of California
Berkeley, CA 94720

Dr. Keith L. McLaughlin
S-CUBED
A Division of Maxwell Laboratory
P.O. Box 1620
La Jolla, CA 92038-1620

Prof. William Menke
Lamont-Doherty Geological Observatory
of Columbia University
Palisades, NY 10964

Stephen Miller
SRI International
333 Ravenswood Avenue
Box AF 116
Menlo Park, CA 94025-3493

Prof. Bernard Minster
IGPP, A-025
Scripps Institute of Oceanography
University of California, San Diego
La Jolla, CA 92093

Prof. Brian J. Mitchell
Department of Earth & Atmospheric Sciences
St. Louis University
St. Louis, MO 63156

Mr. Jack Murphy
S-CUBED, A Division of Maxwell Laboratory
11800 Sunrise Valley Drive
Suite 1212
Reston, VA 22091 (2 copies)

Dr. Bao Nguyen
GL/LWH
Hanscom AFB, MA 01731-5000

Prof. John A. Orcutt
IGPP, A-025
Scripps Institute of Oceanography
University of California, San Diego
La Jolla, CA 92093

Prof. Keith Priestley
University of Nevada
Mackay School of Mines
Reno, NV 89557

Prof. Paul G. Richards
Lamont-Doherty Geological Observatory
of Columbia University
Palisades, NY 10964

Dr. Wilmer Rivers
Teledyne Geotech
314 Montgomery Street
Alexandria, VA 22314

Dr. Alan S. Ryall, Jr.
Center for Seismic Studies
1300 North 17th Street
Suite 1450
Arlington, VA 22209-2308

Prof. Charles G. Sammis
Center for Earth Sciences
University of Southern California
University Park
Los Angeles, CA 90089-0741

Prof. Christopher H. Scholz
Lamont-Doherty Geological Observatory
of Columbia University
Palisades, NY 10964

Prof. David G. Simpson
Lamont-Doherty Geological Observatory
of Columbia University
Palisades, NY 10964

Dr. Jeffrey Stevens
S-CUBED
A Division of Maxwell Laboratory
P.O. Box 1620
La Jolla, CA 92038-1620

Prof. Brian Stump
Institute for the Study of Earth & Man
Geophysical Laboratory
Southern Methodist University
Dallas, TX 75275

Prof. Jeremiah Sullivan
University of Illinois at Urbana-Champaign
Department of Physics
1110 West Green Street
Urbana, IL 61801

Prof. Clifford Thurber
University of Wisconsin-Madison
Department of Geology & Geophysics
1215 West Dayton Street
Madison, WS 53706

Prof. M. Nafi Toksoz
Earth Resources Lab
Massachusetts Institute of Technology
42 Carleton Street
Cambridge, MA 02142

Prof. John E. Vidale
University of California at Santa Cruz
Seismological Laboratory
Santa Cruz, CA 95064

Prof. Terry C. Wallace
Department of Geosciences
Building #77
University of Arizona
Tucson, AZ 85721

Dr. Raymond Willeman
GL/LWH
Hanscom AFB, MA 01731-5000

Dr. Lorraine Wolf
GL/LWH
Hanscom AFB, MA 01731-5000

Prof. Francis T. Wu
Department of Geological Sciences
State University of New York
at Binghamton
Vestal, NY 13901

OTHERS (United States)

Dr. Monem Abdel-Gawad
Rockwell International Science Center
1049 Camino Dos Rios
Thousand Oaks, CA 91360

Dr. Stephen Bratt
Science Applications Int'l Corp.
10210 Campus Point Drive
San Diego, CA 92121

Prof. Keiiti Aki
Center for Earth Sciences
University of Southern California
University Park
Los Angeles, CA 90089-0741

Michael Browne
Teledyne Geotech
3401 Shiloh Road
Garland, TX 75041

Prof. Shelton S. Alexander
Geosciences Department
403 Deike Building
The Pennsylvania State University
University Park, PA 16802

Mr. Roy Burger
1221 Serry Road
Schenectady, NY 12309

Dr. Ralph Archuleta
Department of Geological Sciences
University of California at Santa Barbara
Santa Barbara, CA 93102

Dr. Robert Burridge
Schlumberger-Doll Research Center
Old Quarry Road
Ridgefield, CT 06877

Dr. Thomas C. Bache, Jr.
Science Applications Int'l Corp.
10210 Campus Point Drive
San Diego, CA 92121 (2 copies)

Dr. Jerry Carter
Rondout Associates
P.O. Box 224
Stone Ridge, NY 12484

J. Barker
Department of Geological Sciences
State University of New York
at Binghamton
Vestal, NY 13901

Dr. W. Winston Chan
Teledyne Geotech
314 Montgomery Street
Alexandria, VA 22314-1581

Dr. T.J. Bennett
S-CUBED
A Division of Maxwell Laboratory
11800 Sunrise Valley Drive, Suite 1212
Reston, VA 22091

Dr. Theodore Cherry
Science Horizons, Inc.
710 Encinitas Blvd., Suite 200
Encinitas, CA 92024 (2 copies)

Mr. William J. Best
907 Westwood Drive
Vienna, VA 22180

Prof. Jon F. Claerbout
Department of Geophysics
Stanford University
Stanford, CA 94305

Dr. N. Biswas
Geophysical Institute
University of Alaska
Fairbanks, AK 99701

Prof. Robert W. Clayton
Seismological Laboratory
Division of Geological & Planetary Sciences
California Institute of Technology
Pasadena, CA 91125

Dr. G.A. Bollinger
Department of Geological Sciences
Virginia Polytechnical Institute
21044 Derring Hall
Blacksburg, VA 24061

Prof. F. A. Dahlen
Geological and Geophysical Sciences
Princeton University
Princeton, NJ 08544-0636

Prof. Anton W. Dainty
Earth Resources Lab
Massachusetts Institute of Technology
42 Carleton Street
Cambridge, MA 02142

Prof. Adam Dziewonski
Hoffman Laboratory
Harvard University
20 Oxford St
Cambridge, MA 02138

Prof. John Ebel
Department of Geology & Geophysics
Boston College
Chestnut Hill, MA 02167

Eric Fielding
SNEE Hall
INSTOC
Cornell University
Ithaca, NY 14853

Prof. Donald Forsyth
Department of Geological Sciences
Brown University
Providence, RI 02912

Prof. Art Frankel
Mail Stop 922
Geological Survey
790 National Center
Reston, VA 22092

Dr. Anthony Gangi
Texas A&M University
Department of Geophysics
College Station, TX 77843

Dr. Freeman Gilbert
Inst. of Geophysics & Planetary Physics
University of California, San Diego
P.O. Box 109
La Jolla, CA 92037

Mr. Edward Giller
Pacific Sierra Research Corp.
1401 Wilson Boulevard
Arlington, VA 22209

Dr. Jeffrey W. Given
Sierra Geophysics
11255 Kirkland Way
Kirkland, WA 98033

Prof. Stephen Grand
University of Texas at Austin
Department of Geological Sciences
Austin, TX 78713-7909

Prof. Roy Greenfield
Geosciences Department
403 Deike Building
The Pennsylvania State University
University Park, PA 16802

Dan N. Hagedorn
Battelle
Pacific Northwest Laboratories
Battelle Boulevard
Richland, WA 99352

Kevin Hutchenson
Department of Earth Sciences
St. Louis University
3507 Laclede
St. Louis, MO 63103

Prof. Thomas H. Jordan
Department of Earth, Atmospheric
and Planetary Sciences
Massachusetts Institute of Technology
Cambridge, MA 02139

Robert C. Kemerait
ENSCO, Inc.
445 Pineda Court
Melbourne, FL 32940

William Kikendall
Teledyne Geotech
3401 Shiloh Road
Garland, TX 75041

Prof. Leon Knopoff
University of California
Institute of Geophysics & Planetary Physics
Los Angeles, CA 90024

Prof. L. Timothy Long
School of Geophysical Sciences
Georgia Institute of Technology
Atlanta, GA 30332

Prof. Art McGarr
Mail Stop 977
Geological Survey
345 Middlefield Rd.
Menlo Park, CA 94025

Dr. George Mellman
Sierra Geophysics
11255 Kirkland Way
Kirkland, WA 98033

Prof. John Nabelek
College of Oceanography
Oregon State University
Corvallis, OR 97331

Prof. Geza Nagy
University of California, San Diego
Department of Ames, M.S. B-010
La Jolla, CA 92093

Prof. Amos Nur
Department of Geophysics
Stanford University
Stanford, CA 94305

Prof. Jack Oliver
Department of Geology
Cornell University
Ithaca, NY 14850

Prof. Robert Phinney
Geological & Geophysical Sciences
Princeton University
Princeton, NJ 08544-0636

Dr. Paul Pomeroy
Rondout Associates
P.O. Box 224
Stone Ridge, NY 12484

Dr. Jay Pulli
RADIX System, Inc.
2 Taft Court, Suite 203
Rockville, MD 20850

Dr. Norton Rimer
S-CUBED
A Division of Maxwell Laboratory
P.O. Box 1620
La Jolla, CA 92038-1620

Prof. Larry J. Ruff
Department of Geological Sciences
1006 C.C. Little Building
University of Michigan
Ann Arbor, MI 48109-1063

Dr. Richard Sailor
TASC Inc.
55 Walkers Brook Drive
Reading, MA 01867

Thomas J. Sereno, Jr.
Science Application Int'l Corp.
10210 Campus Point Drive
San Diego, CA 92121

John Sherwin
Teledyne Geotech
3401 Shiloh Road
Garland, TX 75041

Prof. Robert Smith
Department of Geophysics
University of Utah
1400 East 2nd South
Salt Lake City, UT 84112

Prof. S. W. Smith
Geophysics Program
University of Washington
Seattle, WA 98195

Dr. Stewart Smith
IRIS Inc.
1616 North Fort Myer Drive
Suite 1440
Arlington, VA 22209

Dr. George Sutton
Rondout Associates
P.O. Box 224
Stone Ridge, NY 12484

Prof. L. Sykes
Lamont-Doherty Geological Observatory
of Columbia University
Palisades, NY 10964

Prof. Pradeep Talwani
Department of Geological Sciences
University of South Carolina
Columbia, SC 29208

Prof. Ta-liang Teng
Center for Earth Sciences
University of Southern California
University Park
Los Angeles, CA 90089-0741

Dr. R.B. Tittmann
Rockwell International Science Center
1049 Camino Dos Rios
P.O. Box 1085
Thousand Oaks, CA 91360

Dr. Gregory van der Vink
IRIS, Inc.
1616 North Fort Myer Drive
Suite 1440
Arlington, VA 22209

William R. Walter
Seismological Laboratory
University of Nevada
Reno, NV 89557

Dr. Gregory Wojcik
Weidlinger Associates
4410 El Camino Real
Suite 110
Los Altos, CA 94022

Prof. John H. Woodhouse
Hoffman Laboratory
Harvard University
20 Oxford Street
Cambridge, MA 02138

Dr. Gregory B. Young
ENSCO, Inc.
5400 Port Royal Road
Springfield, VA 22151-2388

GOVERNMENT

Dr. Ralph Alewine III
DARPA/NMRO
1400 Wilson Boulevard
Arlington, VA 01731-5000

Mr. James C. Battis
GL/LWH
Hanscom AFB, MA 22209-2308

Dr. Robert Blandford
DARPA/NMRO
1400 Wilson Boulevard
Arlington, VA 87185

Eric Chael
Division 9241
Sandia Laboratory
Albuquerque, NM 01731-5000

Dr. John J. Cipar
GL/LWH
Hanscom AFB, MA 01731-5000

Mr. Jeff Duncan
Office of Congressman Markey
2133 Rayburn House Bldg.
Washington, D.C. 20515

Dr. Jack Evernden
USGS - Earthquake Studies
345 Middlefield Road
Menlo Park, CA 94025

Art Frankel
USGS
922 National Center
Reston, VA 22092

Dr. T. Hanks
USGS
Nat'l Earthquake Research Center
345 Middlefield Road
Menlo Park, CA 94025

Dr. James Hannon
Lawrence Livermore Nat'l Laboratory
P.O. Box 808
Livermore, CA 94550

Paul Johnson
ESS-4, Mail Stop J979
Los Alamos National Laboratory
Los Alamos, NM 87545

Janet Johnston
GL/LWH
Hanscom AFB, MA 01731-5000

Dr. Katharine Kadinsky-Cade
GL/LWH
Hanscom AFB, MA 01731-5000

Ms. Ann Kerr
IGPP, A-025
Scripps Institute of Oceanography
University of California, San Diego
La Jolla, CA 92093

Dr. Max Koontz
US Dept of Energy/DP 5
Forrestal Building
1000 Independence Avenue
Washington, DC 20585

Dr. W.H.K. Lee
Office of Earthquakes, Volcanoes,
& Engineering
345 Middlefield Road
Menlo Park, CA 94025

Dr. William Leith
U.S. Geological Survey
Mail Stop 928
Reston, VA 22092

Dr. Richard Lewis
Director, Earthquake Engineering & Geophysics
U.S. Army Corps of Engineers
Box 631
Vicksburg, MS 39180

James F. Lewkowicz
GL/LWH
Hanscom AFB, MA 01731-5000

Mr. Alfred Lieberman
ACDA/VI-OA State Department Bldg
Room 5726
320 - 21st Street, NW
Washington, DC 20451

Stephen Mangino
GL/LWH
Hanscom AFB, MA 01731-5000

Dr. Frank F. Pilotte
HQ AFTAC/TT
Patrick AFB, FL 32925-6001

Dr. Robert Masse
Box 25046, Mail Stop 967
Denver Federal Center
Denver, CO 80225

Katie Poley
CIA-OSWR/NED
Washington, DC 20505

Art McGarr
U.S. Geological Survey, MS-977
345 Middlefield Road
Menlo Park, CA 94025

Mr. Jack Rachlin
U.S. Geological Survey
Geology, Rm 3 C136
Mail Stop 928 National Center
Reston, VA 22092

Richard Morrow
ACDA/VI, Room 5741
320 21st Street N.W.
Washington, DC 20451

Dr. Robert Reinke
WL/NTESG
Kirtland AFB, NM 87117-6008

Dr. Keith K. Nakanishi
Lawrence Livermore National Laboratory
P.O. Box 808, L-205
Livermore, CA 94550

Dr. Byron Ristvet
HQ DNA, Nevada Operations Office
Attn: NVCG
P.O. Box 98539
Las Vegas, NV 89193

Dr. Carl Newton
Los Alamos National Laboratory
P.O. Box 1663
Mail Stop C335, Group ESS-3
Los Alamos, NM 87545

Dr. George Rothe
HQ AFTAC/TGR
Patrick AFB, FL 32925-6001

Dr. Kenneth H. Olsen
Los Alamos Scientific Laboratory
P.O. Box 1663
Mail Stop C335, Group ESS-3
Los Alamos, NM 87545

Dr. Michael Shore
Defense Nuclear Agency/SPSS
6801 Telegraph Road
Alexandria, VA 22310

Howard J. Patton
Lawrence Livermore National Laboratory
P.O. Box 808, L-205
Livermore, CA 94550

Donald L. Springer
Lawrence Livermore National Laboratory
P.O. Box 808, L-205
Livermore, CA 94550

Mr. Chris Paine
Office of Senator Kennedy, SR 315

United States Senate
Washington, DC 20510

Dr. Lawrence Turnbull
OSWR/NED
Central Intelligence Agency, Room 5G48
Washington, DC 20505

Colonel Jerry J. Perrizo
AFOSR/NP, Building 410
Bolling AFB
Washington, DC 20332-6448

Dr. Thomas Weaver
Los Alamos National Laboratory
P.O. Box 1663, Mail Stop C335
Los Alamos, NM 87545

J.J. Zucca
Lawrence Livermore National Laboratory
Box 808
Livermore, CA 94550

Defense Technical Information Center
Cameron Station
Alexandria, VA 22314 (5 copies)

GL/SULL
Research Library
Hanscom AFB, MA 01731-5000 (2 copies)

Defense Intelligence Agency
Directorate for Scientific &
Technical Intelligence
Washington, DC 20301

Secretary of the Air Force (SAFRD)
Washington, DC 20330

AFTAC/CA
(STINFO)
Patrick AFB, FL 32925-6001

Office of the Secretary Defense
DDR & E
Washington, DC 20330

TACTEC
Battelle Memorial Institute
505 King Avenue
Columbus, OH 43201 (Final Report Only)

HQ DNA
Attn: Technical Library
Washington, DC 20305

Mr. Charles L. Taylor
GL/LWH

Hanscom AFB, MA 01731-5000

DARPA/RMO/RETRIEVAL
1400 Wilson Boulevard
Arlington, VA 22209

DARPA/RMO/Security Office
1400 Wilson Boulevard
Arlington, VA 22209

Geophysics Laboratory
Attn: XO
Hanscom AFB, MA 01731-5000

Geophysics Laboratory
Attn: LW
Hanscom AFB, MA 01731-5000

DARPA/PM
1400 Wilson Boulevard
Arlington, VA 22209

CONTRACTORS (Foreign)

Dr. Ramon Cabre, S.J.
Observatorio San Calixto
Casilla 5939
La Paz, Bolivia

Prof. Hans-Peter Harjes
Institute for Geophysik
Ruhr University/Bochum
P.O. Box 102148
4630 Bochum 1, FRG

Prof. Eystein Husebye
NTNF/NORSAR
P.O. Box 51
N-2007 Kjeller, NORWAY

Prof. Brian L.N. Kennett
Research School of Earth Sciences
Institute of Advanced Studies
G.P.O. Box 4
Canberra 2601, AUSTRALIA

Dr. Bernard Massinon
Societe Radiomana
27 rue Claude Bernard
75005 Paris, FRANCE (2 Copies)

Dr. Pierre Mecheler
Societe Radiomana
27 rue Claude Bernard
75005 Paris, FRANCE

Dr. Svein Mykkeltveit
NTNF/NORSAR
P.O. Box 51
N-2007 Kjeller, NORWAY

FOREIGN (Others)

Dr. Peter Basham
Earth Physics Branch
Geological Survey of Canada
1 Observatory Crescent
Ottawa, Ontario, CANADA K1A 0Y3

Dr. Eduard Berg
Institute of Geophysics
University of Hawaii
Honolulu, HI 96822

Dr. Michel Bouchon
I.R.I.G.M.-B.P. 68
38402 St. Martin D'Heres
Cedex, FRANCE

Dr. Hilmar Bungum
NTNF/NORSAR
P.O. Box 51
N-2007 Kjeller, NORWAY

Dr. Michel Campillo
Observatoire de Grenoble
I.R.I.G.M.-B.P. 53
38041 Grenoble, FRANCE

Dr. Kin Yip Chun
Geophysics Division
Physics Department
University of Toronto
Ontario, CANADA M5S 1A7

Dr. Alan Douglas
Ministry of Defense
Blacknest, Brimpton
Reading RG7-4RS, UNITED KINGDOM

Dr. Roger Hansen
NTNF/NORSAR
P.O. Box 51
N-2007 Kjeller, NORWAY

Dr. Manfred Henger
Federal Institute for Geosciences & Nat'l Res.
Postfach 510153
D-3000 Hanover 51, FRG

Ms. Eva Johannisson
Senior Research Officer
National Defense Research Inst.
P.O. Box 27322
S-102 54 Stockholm, SWEDEN

Dr. Fekadu Kebede
Seismological Section
Box 12019
S-750 Uppsala, SWEDEN

Dr. Tormod Kvaerna
NTNF/NORSAR
P.O. Box 51
N-2007 Kjeller, NORWAY

Dr. Peter Marshal
Procurement Executive
Ministry of Defense
Blacknest, Brimpton
Reading FG7-4RS, UNITED KINGDOM

Prof. Ari Ben-Menahem
Department of Applied Mathematics
Weizman Institute of Science
Rehovot, ISRAEL 951729

Dr. Robert North
Geophysics Division
Geological Survey of Canada
1 Observatory Crescent
Ottawa, Ontario, CANADA K1A 0Y3

Dr. Frode Ringdal
NTNF/NORSAR
P.O. Box 51
N-2007 Kjeller, NORWAY

Dr. Jorg Schlittenhardt
Federal Institute for Geosciences & Nat'l Res.
Postfach 510153
D-3000 Hannover 51, FEDERAL REPUBLIC OF GERMANY

Prof. Daniel Walker
University of Hawaii
Institute of Geophysics
Honolulu, HI 96822